UNIVERSITÀ DEGLI STUDI DI PADOVA

DIPARTIMENTO DI SCIENZE CHIMICHE

CORSO DI LAUREA MAGISTRALE IN SCIENZA DEI MATERIALI

TESI DI LAUREA MAGISTRALE

Electrochemical Scanning Tunnelling Microscopy investigations of Fe@N-based macrocyclic molecules adsorbed on Au(111) and their implications in Oxygen Reduction Reaction

Relatore: Prof. Christian Durante

Controrelatore: Dott. Denis Badocco

LAUREANDO: Alessandro Facchin

ANNO ACCADEMICO 2017 / 2018

Abstract

Fuel-cells can be a valuable alternative to fossil-fuel non-renewable energy sources since H_2 and O_2 are used as fuel and comburant, respectively, and H_2O is the main product. O_2 is entailed at the cathode of the cell and it undergoes a reduction reaction, which however reveals to be the bottle neck step in a common proton exchange membrane fuel cell. High costs and scarcity make Pt-based materials no longer desirable catalysts for ORR. Among many non-platinum group materials, metal-coordinating nitrogen atoms dispersed in mesoporous carbonaceous matrix (MN_x) exhibit remarkable catalytic activity. In the Volcano-like plot describing the correlation between the number of *d* electrons and the reduction potential of MN_4 metal centre, iron lays at the top in accordance with Sabatier's principle of catalysis. There is however a general lack in understanding the O_2 reduction mechanism occurring at FeN_x sites so that collecting information about the Fe-N active sites holds a primary relevance in understanding the O_2 reduction reaction pathway. On this regard, Metal-centred phthalocyanines and porphyrins are known to act as catalysts for ORR since 1960's. They are indeed good model systems for mimicking a specific class of MN_x sites, namely MN_4. In this thesis project, FeN_4 macrocycles were used to functionalise an Au(111) single crystal, which allowed to evaluate their performance towards ORR thanks to the well-known inertness of Au towards oxygen chemistry.

Fe(II)-phthalocyanine, Fe(III)-phthalocyanine chloride and Fe(III)-tetramethoxyphenyl porphyrin chloride were examined in their ability to promote the O_2 reduction reaction by means of electrochemical scanning tunnelling microscopy (EC-STM), as well as by cyclic voltammetry (CV).

From CV investigations in Ar purged electrolyte, the redox behaviour of the Fe centres was pointed out as a basic step in the active site formation, which was assigned to the low-oxidation state Fe(II). By further registering cyclic voltammograms of FeN_4/Au electrodes in O_2 saturated electrolyte, a clear reduction peak was observed at potentials close to the previously found Fe(III)→Fe(II) peak potentials. Therefore, a "redox-catalysis" mechanism holds, in which the reduction of the metal centre from (III) oxidation state to (II) is first required to then allow the O_2 reduction**.**

EC-STM revealed to be a powerful tool to explore the self-assembly processes at the solid/liquid interface characterising the studied systems. Moreover, the O_2 adsorption step will be actually visualised, succeeding in distinguishing the *end-on* and/or the *side-on* adsorption geometry. *Potentiodynamic imaging* enabled to correlate the intense reductive current revealed by CV at a definite applied potential to the system response at single sites provided by EC-STM.

The effect of chloride in altering the adsorption behaviour of FeN_4 molecules, as well as in modifying the O_2 catalytic activity, was encountered by comparing Fe(II)Pc and Fe(III)Pc-Cl, and dedicated CV investigation were carried out to gather further information.

INDEX

List of Abbreviations

PEMFC	Proton Exchange Membrane Fuel Cell
ORR	Oxygen Reduction Reaction
HER	Hydrogen Evolution Reaction
OER	Oxygen Evolution Reaction
NPMCs	Non-Precious Metal Catalysts
MC	Mesoporous carbonaceous
HOR	Hydrogen Oxidation Reaction
EC-STM	Electrochemical Scanning Tunneling Microscopy
CV	Cyclic Voltammetry
UHV	Ultra-High Vacuum
Non-PGM	non-Platinum group metal
DOS	Density of State
WKB	Wentzel-Kramers-Brillouin
NHE	Normal Hydrogen Electrode
RHE	Reversible Hydrogen Electrode
SCE	Saturated Calomel Electrode
WE	Working Electrode
RE	Reference Electrode
CE	Counter Electrode
TE	Tip Electrode
OCP	Open Circuit Potential
CVD	Chemical Vapour Deposition
DMF	N,N-Dimethylformamide
SAM	Self-Assembled Monolayer
FCC	Face Centred Cubic
HCP	Hexagonal Close-Packed
FFT	Fast Fourier Transform
DC	Direct Current

PZC	Point of Zero Charge
Fe(II)Pc	Fe(II)-Phthalocyanine
Fe(III)Pc-Cl	Fe(III)-Phthalocyanine chloride
Fe(III)TMPP-Cl	Fe(III)-tetramethoxyphenyl-Porphyrin chloride
OPG	Oriented Pyrolytic Graphite
HOPG	High-Oriented Pyrolytic Graphite
DFT	Density Functional Theory

Chapter 1

Introduction

Metal-phthalocyanines and -porphyrins are macrocyclic transition metal complexes which are widely regarded as catalysts both for homogeneous and heterogeneous reactions [1]. If some conductive surfaces, i.e.: metals, are functionalised with those compounds, an electrode surface is obtained and a catalytic activity towards an electrochemical reaction should arise. In this way, metal-phthalocyanines were found to catalyse electro-oxidation of nitrogen-containing compounds, such as hydrazine and hydroxylamine [1]. Electrocatalytic effects were also discovered towards electrochemical reactions involving sulphur compounds, like mercaptoethanol, cysteine, gluthanione, as well as thionyl chloride and sulphuryl chloride. Other reactions of interest promoted by metal-N_4 macrocycles are the electroreduction of CO_2, NO_3^- and NO [1].

A vital reaction, on which life on earth is based, is the reduction of molecular oxygen through respiration. Food, i.e. glucose, is oxidised by an environmental oxidant, i.e. di-oxygen, to carbon dioxide and water, and the free energy produced by respiration is captured in the form of protons by enzymatic species like NADH and $FADH_2$. However, O_2 is kinetically inert at ambient conditions [2] due to low affinity for H^+ or electrophiles in general, and it possesses a triplet electronic ground state, which hinders reactions with most organic matter in a singlet ground state [2]. Energy metabolism of mammalians thus requires catalysis, which is ensured by enzymes. It is not surprising that these enzymes are based on *heme* groups, which actually feature FeN_4 sites in the form of iron-porphyrins [3]. Much interest has been exerted on these systems, since they provide a consolidated technology for clean energy production and supply. It is the case of metal-air batteries and especially fuel cells.

Fuel-cells can be a valuable alternative to fossil-fuel non-renewable energy sources, since H_2 and O_2 are used as fuel and combustive, respectively, and the product of their combustion is H_2O, even if a real combustion does not take place. O_2 is entailed at the cathode of the cell, since it undergoes the reduction reaction, contrarily to H_2 which is subjected to oxidation. Actually, various types of fuel cells are nowadays a common reality, but each typology needs particular operating conditions to be fulfilled to return the best performances for which they have been projected.

In this regard, Proton Exchange Membrane Fuel Cell (PEMFCs) are herein considered as the target of the present work, which aims to characterise macrocyclic molecules with FeN_4 centres deposited on an Au(111) electrode as model system for ORR occurring at the cathode electrocatalyst surface. The half-cell reactions can be written as [4]:

$$Anode: H_2 \rightarrow 2H^+ + 2e^- \qquad (1.1)$$

$$Cathode: \frac{1}{2}O_2 + 2H^+ + 2e^- \rightarrow H_2O \qquad (1.2)$$

The global reaction is:

$$H_2 + \frac{1}{2}O_2 \rightarrow H_2O \qquad (1.3)$$

Therefore, protons (H^+) are generated by hydrogen oxidation reaction (HOR) at the anode. Then, combined with molecular oxygen supplied at the cathode, they undergo oxygen reduction reaction (ORR) at the cathode. A PEMFC is mainly characterised by a quasi-solid electrolyte [4], namely a polymeric membrane frequently based on Nafion® polymer. The membrane is embedded between anode and cathode and allows migration of H^+ from anode to cathode, which mainly occurs via Grotthus mechanism [5–8]. H^+ jumps from one H_2O molecule to a new one thanks to linear chains of water molecules formed by hydrogen bonding.

PEMFCs operate at low temperature, generally < 100 °C, to avoid dehydration of the membrane, which represents an advantage in terms of cell fabrication and handling. However, oxygen reduction reaction (ORR) is widely recognised as a low efficiency-process, especially at low temperatures like PEMFCs require, and a significant overpotential is needed for oxygen reduction to occur at satisfactory rate. The overpotential request turns into loss of cell voltage: for this reason, ORR needs to be catalysed. Pt-based electrodes exhibit the highest catalytic activity towards ORR [9]. Nonetheless, Pt and Pt-based materials suffer of scarcity and unequal distribution over the Earth's surface, and therefore implies high-costs, which hinder the widespread of PEMFC.

Non-Precious Metal Catalysts (NPMCs) are therefore needed as alternative materials to Pt and it was found that metal coordinating nitrogen groups on mesoporous carbon material (M-N-MC) show a catalytic activity almost comparable to the most performing Pt catalysts [10]. In M-N-MC catalysts, a pyrolyzed mesoporous carbonaceous (MC) matrix embeds the actives sites, represented by metal centres (M) coordinated by a various number of nitrogen atoms (N). Indeed, a plurality of active sites had been identified through analytical methods like XPS, XANES, TOF-SIMS, Mössbauer spectroscopy [11]. Metals can in fact be coordinated by 2 to 4 nitrogen atoms and notwithstanding many investigations are currently ongoing on M-N-MC catalysts [12], there is still a general lack of understanding on the main factors that govern electro-catalysis of ORR promoted by MN_x centres. Gathering information about the Fe-N active site(s) holds a primary relevance in understanding the O_2 reduction reaction pathway, which is known to proceed according to two main mechanisms, recognised as "$2e^-$-" or "$4e^-$ mechanism" [13]. Indeed, the $2e^-$ pathway involves two electrons in the electrocatalytic action, leading to hydrogen peroxide formation as the main reaction product. On the contrary, the $4e^-$ mechanism involves four electrons in the O_2 electroreduction, with water being produced as the main reaction product. The latter is then the most desirable reaction mechanism, since it makes the M-N-MC suitable for employment in possibly commercial PEMFCs, which would quickly worsen their performance due to hydrogen peroxide oxidising action onto the exchange membrane if the $2e^-$ pathway was followed. It is therefore clear that having the ability to study the ORR mechanism at the single-site level would allow to discriminate different types of MN_x sites in terms both of the electrocatalytic activity towards ORR and of the preferential reaction pathway. On this regard, Metal-centred phthalocyanines and porphyrins are known to act as catalysts for ORR since 1960's [14]. They are indeed good model systems for mimicking a specific class of MN_x sites, namely MN_4 [1,15–17].

Not only Metal-porphyrins and -phthalocyanines are good examples of FeN_4 single sites, but the entire experimental conditions adopted in the present work try to reproduce those of a real PEMFC. Indeed, 0.1 M perchloric acid provides an acidic pH for the FeN_4-based

electrode, since for PEMFCs the polymeric membrane is designed for H^+ mobility and H^+ must be the product of HOR at the anode. The FeN_4-based electrode is obtained by proper functionalisation of an Au(111) single crystal with FeN_4 solutions. The FeN_4/Au(111) electrode is kept at room temperature, and PEMFCs require reasonably low temperature to maintain a proper hydration level for the polymeric membrane. Of course, fuel cells do not deal with single crystals, nor with self-assembled monolayers of molecules adsorbed on it. Nonetheless, Au is almost inactive towards ORR [18–22], allowing to clearly evidence an eventual electrocatalytic effect of the functionalisation layer. In addition, dealing with a monolayer of well-defined FeN_4 molecular species allows to distinctively determine the role of a single active centre.

Certainly, there are also differences between FeN_4/Au electrodes and PEMFCs. The electrochemical environment recreated with an electrochemical cell cannot mimic the quasi-solid electrolytic membrane. Larger areas and higher electroactive material amounts characterise a standard fuel cell. Reactants are continuously supplied in gaseous phase with proper input flow systems, and the products are pulled out with adequate output flow systems, which allows recycling of non-reacted species.

In the present work, three FeN_4-based molecular systems are examined in their ability to promote the O_2 reduction reaction. This task will be accomplished by means of electrochemical scanning tunnelling microscopy (EC-STM), as well as by cyclic voltammetry (CV). Cyclic voltammetry will provide a standard electrochemical characterisation of the FeN_4 samples at macroscopic level. EC-STM allows to characterise each molecular system at the solid/electrolyte interface, furnishing a powerful tool to probe the structure of the FeN_4/Au electrode at single molecular level. This will offer first of all the possibility to analyse the result of the substrate functionalisation, which will be represented by self-assembled monolayers. Moreover, EC-STM performs imaging under electrochemical conditioning of the FeN_4/Au electrode. This becomes an extraordinary relevant aspect, since EC-STM then provides a direct correlation between the macroscopic electrochemical response shown by the FeN_4/Au electrode during a CV characterisation to its behaviour at the microscopic scale probed by means of STM. Indeed, the O_2 adsorption step will be actually visualised, succeeding in distinguishing the *end-on* and/or the *side-on* adsorption geometry. Furthermore, *potentiodynamic imaging* will demonstrate the O_2 disappearance from the Fe site at applied potentials close to the peak potential assigned to ORR process, therefore correlating the intense reductive current revealed at a definite applied potential to the system response at single sites.

The present works aims to provide an advanced understanding of the O_2 reduction reaction on specific FeN_4 sites by means of cyclic voltammetry and, above all, of EC-STM. In particular, the adsorption process and adsorption geometry will be taken into account. Three molecular systems will be compared to extract information about the effect of the chemical environment on the ORR electrocatalysis. They also serve as mean of evaluation for characterising the self-assembly process at the solid/liquid interface.

In chapter 2, theoretical concepts linked to STM tunnelling are outlined, trying to discriminate the general tunnelling theory developed for UHV with multiple approaches to the treatment of tunnelling at the solid/liquid interface. The STM basic working principles will be enucleated. Theoretical concepts regarding the electrical double-layer and its modifications during a cyclic voltammetry experiment will also be pointed out. In chapter 3, experimental setup and methods will be elucidated, from glassware cleaning to Au preparation and functionalisation, as well as for CV experimental setting up. Chapter 4 describes the Au(111) single crystal, being the substrate for the FeN_4 functionalisation. The electrochemical response

of three different FeN_4/Au(111) electrodes will be taken into exam in chapter 5. Finally, in chapter 6, EC-STM analysis of the three FeN_4 systems will be thoroughly described.

References

[1] J.H. Zagal, *Metallophthalocyanines as catalysts in electrochemical reactions*, Coord. Chem. Rev., **1992**, *119*, 89–136.

[2] J.H. Zagal, F. Bedioui, J.P. Dodelet, *N_4-Macrocyclic Metal Complexes*, Springer, **2006.**

[3] M. Shao, *Electrocatalysis in Fuel Cells*, **2015**.

[4] J. Zhang, ed., *PEM Fuel Cell Electrocatalysts and Catalyst Layers Fundamentals and Applications*, Springer, **2008**.

[5] T. Okada, G. Xie, O. Gorseth, S. Kjelstrup, N. Nakamura, T. Arimura, *Ion and water transport characteristics of Nafion membranes as electrolytes*, Electrochim. Acta., **1998**, *43*, 3741–3747.

[6] D.N. Son, H. Kasai, *Proton transport through aqueous Nafion membrane*, Eur. Phys. J. E., **2009**, *29*, 351–361.

[7] G.A. Ludueña, T.D. Kühne, D. Sebastiani, *Mixed Grotthuss and vehicle transport mechanism in proton conducting polymers from Ab initio molecular dynamics simulations*, Chem. Mater., **2011**, *23*, 1424–1429.

[8] http://www1.lsbu.ac.uk/water/grotthuss.html.

[9] Y. Nie, L. Li, Z. Wei, *Recent advancements in Pt and Pt-free catalysts for oxygen reduction reaction*, Chem. Soc. Rev., **2015**, *44*, 2168–2201.

[10] G. Wu, K.L. More, C.M. Johnston, P. Zelenay, *High-Performance Electrocatalysts for Oxygen Reduction Derived from Polyaniline, Iron, and Cobalt*, Science, **2012**, *332*, 443–448.

[11] K. Artyushkova, A. Serov, S. Rojas-Carbonell, P. Atanassov, *Chemistry of Multitudinous Active Sites for Oxygen Reduction Reaction in Transition Metal-Nitrogen-Carbon Electrocatalysts*, J. Phys. Chem. C., **2015**, *119*, 25917–25928.

[12] W. Xu, Z. Wu, S. Tao, *Recent progress in electrocatalysts with mesoporous structures for application in polymer electrolyte membrane fuel cells*, J. Mater. Chem. A., **2016**, *4*, 16272–16287.

[13] S. Kattel, P. Atanassov, B. Kiefer, *A density functional theory study of oxygen reduction reaction on non-PGM Fe-N_x-C electrocatalysts*, Phys. Chem. Chem. Phys., **2014**, *16*, 13800–13806.

[14] R. Jasinski, *A New Fuel Cell Cathode Catalyst*, Nature., **1964**, *201*, 1212–1213.

[15] J.H. Zagal, M.A. Paez, A.A. Tanaka, J.R.J. dos Santos, C.A. Linkous, *Electrocatalytic activity of metal phthalocyanines for oxygen reduction*, J. Electroanal. Chem., **1992**, *339*, 13–30.

[16] J.H. Zagal, M.T.M. Koper, *Reactivity Descriptors for the Activity of Molecular MN_4*

Catalysts for the Oxygen Reduction Reaction, Angew. Chemie - Int. Ed., **2016**, *55*, 14510–14521.

[17] J.H. Zagal, S. Griveau, J.F. Silva, T. Nyokong, F. Bedioui, *Metallophthalocyanine-based molecular materials as catalysts for electrochemical reactions*, Coord. Chem. Rev., **2010**, *254*, 2755–2791.

[18] P. Quaino, N.B. Luque, R. Nazmutdinov, E. Santos, W. Schmickler, *Why is gold such a good catalyst for oxygen reduction in alkaline media?*, Angew. Chemie - Int. Ed., **2012**, *51*, 12997–13000.

[19] P. Rodriguez, M.T.M. Koper, *Electrocatalysis on gold*, Phys. Chem. Chem. Phys., **2014**, *16*, 13583–13594.

[20] J.Y. Gu, Z.F. Cai, D. Wang, L.J. Wan, *Single Molecular Imaging of Iron-Phthalocyanine Catalyzed Oxygen Reduction Reaction by in situ Scanning Tunneling Microscopy*, ACS Nano., **2016**, 1–10.

[21] S. Yoshimoto, A. Tada, K. Suto, R. Narita, K. Itaya, *Adlayer Structure and Electrochemical Reduction of O_2 on Self-Organized Arrays of Cobalt and Copper Tetraphenyl Porphines on a Au (111) Surface*, Langmuir., **2003**, *19*, 672–677.

[22] S. Yoshimoto, J. Inukai, A. Tada, T. Abe, T. Morimoto, A. Osuka, H. Furuta, K. Itaya, *Adlayer Structure of and Electrochemical O_2 Reduction on Cobalt Porphine-Modified and Cobalt Octaethylporphyrin-Modified Au(111) in $HClO_4$*, J. Phys. Chem. B., **2004**, *108*, 1948–1954.

Chapter 2

2 Theory

The presented work certainly finds its basis on the presence of an interface between a solid and a liquid. Solid/liquid interfaces are indeed omnipresent and therefore extensively studied, representing one the major topics of physical chemistry. They are involved in wetting properties of surfaces, adsorption/desorption phenomena, corrosion, heterogeneous catalysis, etc. Frequently, more than one of the aforementioned aspects take part to a physical chemical transformation. A more specific case is represented by electrified interfaces, which provide powerful tools to investigate potential-induced effects but also to directly manipulate a surface. For this reason, a dedicated section (2.2.2) will take into exam the most relevant models for electrified interfaces. A quantitative treatment of the current-time response for a quiescent electrolyte system is provided with the aim to extend the obtained results to the Cyclic Voltammetry technique, whose main aspects are also pointed out. Then the Scanning Tunnelling technique is examined in its theoretical aspects, elucidating the most relevant formulae for tunnelling phenomenon. A specific section will concern tunnelling phenomena at the solid/electrolyte interface, since EC-STM deals with this special interface. More practical details will also be furnished for the instrumental operating principles.

2.1 Scanning Tunnelling Microscopy

Scanning Tunnelling Microscopy (STM) was first introduced by Gerd Binning and Heinrich Rohrer from IBM's research laboratory in Rüschlikon near Zürich [1] [2]. It was further implemented by G. Binning, H. Rohrer, C. Gerber and E. Weibel, who successfully managed to obtain atomic resolution images of 7x7 reconstructed Si(111) crystals and of Au(110) crystals [3]. This was therefore a powerful demonstration that "There's Plenty of Room at the Bottom", as Richard Feynman argued [4], since the goals of "seeing" individual atoms and arrange them in any desired way became possible by exploitation of electron tunnelling effect. Indeed, in 1986, four years later from the introduction of STM, G. Binning and H. Rohrer won the Nobel Prize in Physics**.**

Scanning Tunnelling Microscopy makes use of a tunnelling tip of metallic material to probe the surface of a conductive sample. Upon application of a bias voltage between the tip and the sample, given their metallic nature, tunnelling events occur, and a tunnelling current is generated. Thanks to a positioning and approaching/retracting system based on piezoelectric materials, the tip is scanned over the sample surface and a series of topographic profiles are collected. These profiles are digitalised within a dedicated software, whose aim is to convert them in a topographic image of the scanned area. Given the high sensitivity and accuracy of the instrumentation, atomic resolution imaging is easily accessible, allowing to understand fundamental processes occurring at the microscopic scale of matter.

It must be remarked that STM was originally developed to work in Ultra High Vacuum (UHV) environment, since the first subject of investigation were mainly represented by single crystal surfaces. Therefore, to avoid contamination from atmosphere gases, pressures of less than 10^{-9} mbar were and are needed. Simple calculations can be carried out considering quantities like incident flux and sticking coefficient [5]**.** The incident flux is proportional to the gas density and the average molecular velocity: $F = \frac{1}{4}\rho\bar{v}$. ρ can be calculated by the ideal gas law, being the number of molecules per volume: $pV = Nk_BT$, leads to $\frac{N}{V} = \rho = \frac{p}{k_BT}$. The mean velocity is given by Maxwell speed distribution, as: $\bar{v} = \sqrt{\frac{8k_BT}{\pi m}}$. Therefore, the flux of incident molecules becomes:

$$F = \frac{1}{4}\rho\bar{v} = \frac{1}{4}\left(\frac{p}{k_BT}\right)\left(\sqrt{\frac{8k_BT}{m\pi}}\right) = \frac{p}{\sqrt{2\pi m k_BT}} \qquad (2.1)$$

The result is a number of molecules impacting the surface per square meter per second. A flux of $10^{27}\,\frac{molecules}{m^2 s}$ is attainable at environmental pressure (~760 Torr), while a flux of $10^{15}\,\frac{molecules}{m^2 s}$ is obtained at $\sim 10^{-9}\ Torr$ ($\sim 10^{-9} mbar$).

A lower time limit for surface contamination (i.e. formation of a monolayer of adsorbed species) can be calculated in the simple case of unitary sticking coefficient. The sticking coefficient *S* is a measure of the tendency of a species to adsorb (stick) onto a surface, and it is defined as the ratio of molecules impacting on the surface versus the number of molecules that stick on it. Sticking coefficients therefore vary from 0 (no adsorption) to 1 (maximum adsorption). Since the surface concentration is typically in the order of $10^{15}\,\frac{atoms}{cm^2}$, and upon assuming *S=1*, for a pressure of 760 Torr the corresponding time for monolayer contamination is $3.44\ 10^{-9}\ s$. For a pressure of $10^{-9}\ Torr$ ($\sim 10^{-9} mbar$), the monolayer formation time is $2.61\ 10^{3}\ s$.

The sticking coefficient is strongly dependent of many factors, like temperature, surface coverage, exposed crystallographic face and of course it changes on the basis of the adsorbing molecule. Considering Au(111) single crystal, which is the only substrate used in this work, the problem of contamination seems to represent a minor issue. Indeed, Au(111) is known to exhibit low tendency to contamination [6].

A major advantage of Scanning Probe Microscopy techniques, like STM, is that they can be and have been extended to environments different from UHV, i.e. air or, more interestingly, a liquid phase. This opened the route to extensive solid/liquid interface studies, and to all phenomena linked to this special interface. Sonnenfeld and Hansma managed to atomically resolve the surface structure of HOPG samples at the solid/water interface [7], unveiling the potentialities of imaging in a liquid, thus mimicking the conditions for important biological processes (DNA replication, enzymatic catalysis, membrane transport) [7]. Not only biological processes, but also corrosion of metals, etching of semiconductors, electrodeposition and dissolution of minerals can be potentially studied as solid/liquid interface phenomena [8].

However, additional considerations must be made when working at the solid/liquid interface. The solid/liquid interface defines in fact a region of finite thickness, in which different properties with respect to the bulk phase can arise [8]. For this reason, this finite thickness region is often termed as interphase, being the interface the exact place where the two phases

come in contact. The solid phase can in fact perturb the liquid one, for example due to excess charges that metals frequently exhibit at their surfaces [8]**.** Alternatively, the liquid phase can modify the solid surface, since it could provide anions able to specifically adsorb on the solid surface. Furthermore, organic molecules accidentally or intentionally present in the liquid phase can adsorb on the solid surface, opening the route to the wide varieties of self-assembly processes.

A schematic but realistic representation of the solid/liquid interphase features and phenomena is provided in figure 2.1

Surface atoms are often highly mobile, thus a solid will never exhibit a perfect surface, but a great number of defects will always be present. Step edges, adatoms, vacancies and islands are indeed common surface defects. Substitutional defects can also occur, as well as specific adsorption of anions: for example, halides do present specific adsorption patterns on Au(111) [9]**.** Of course, organic molecules can intentionally be introduced in the liquid phase, with the aim to induce self-assembly processes during their adsorption on the solid surface. Self-assembly plays a significant role in understanding the role of intermolecular forces and molecule/substrate forces on the adsorption event. Its result, i.e. a self-assembled layer, enables an easier scanning capability, since molecules are more tightly arranged and therefore more resistant to the perturbations induced by tunnelling events [10].

Solid/liquid interface is therefore crucial for combining the macroscopic world to the microscopic nature of matter, since single-molecular imaging is achievable through *in situ* STM [7, 11, 8]**.**

A special case arises when the liquid is represented by an electrolytic solution. The idea is to perform *in situ* STM in electrochemical environment, therefore under potential control of the sample, which plays at the same time as working electrode of a "Four-Electrode Setup". This gives the possibility to *in situ* investigate a system at a peculiar solid/liquid interface, offering in addition the ability to tune its behaviour upon proper polarisation of the sample as working electrode. In this way, essential information can be obtained for the electrode/electrolyte interface, and electrochemical processes can be can be controlled, induced or inhibited. For this work, the particular electrochemical process of Oxygen Reduction Reaction (ORR) will be taken into exam, studying the influence that FeN_4 macrocycles exert on ORR as models of some of the most performing non-PGM ORR electrocatalysts.

2.1.1 Electron Tunnelling

The Scanning Tunnelling Microscopy is based on the quantum tunnelling effect. The concept is that an electron can tunnel through a potential barrier that exists between two metallic surfaces, even if it does not possess a sufficiently high energy to overcome that barrier. For this purpose, consider a one-dimensional potential barrier [12], as depicted in figure 2.1.

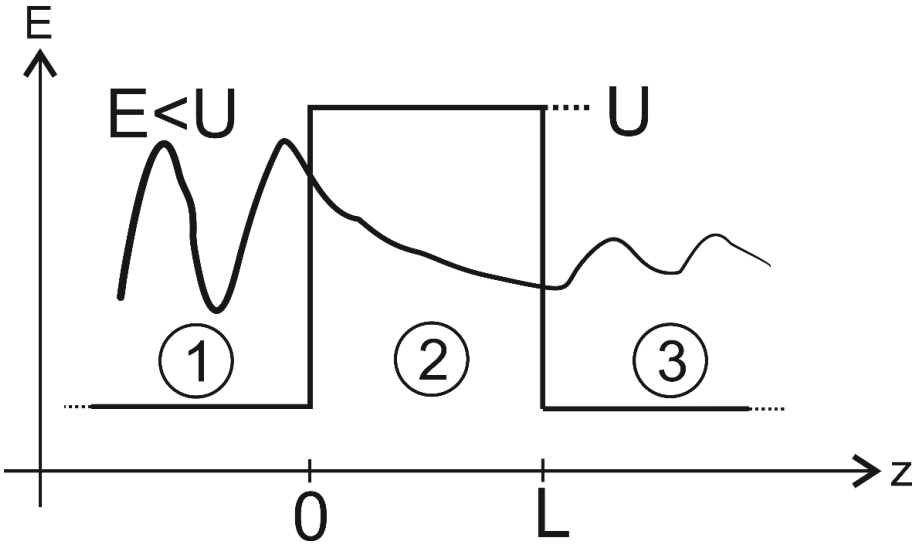

Figure 2.1: Scheme of the one-dimensional potential barrier.

The barrier is represented by a constant finite potential energy *U* between the positions *z=0* and *z=L*. Classically, electrons moving with energy *E* greater than U are able to overcome the retarding force exerted by the potential barrier at *z=0*. They suffer a reduction in energy in the barrier (*E-U*), but at *x=L* they continue moving with their original speed. Conversely, electrons moving with energy *E* lower than *U* are reflected by the barrier: between *z=0* and *z=L* a classically forbidden region is established.

In quantum mechanics field, there exists a finite probability for the electron to be reflected by the barrier, even if its energy is higher than the barrier itself. Alternatively, there also exists a finite probability for the electron to penetrate through the potential barrier, even if its energy is lower (*E<U*). The process of penetrating the barrier is called *tunnelling* and it is a concept in complete disagreement with classical physics. A mathematical description of the tunnelling phenomenon [12] [13] can be provided by the solution of Schrödinger equation.

$$-\frac{\hbar^2}{2m}\frac{d^2}{dz^2}\psi(z) + U(z)\psi(z) = E\psi(z) \qquad (2.2)$$

for *z<0* (region 1) and *z>L* (region 3), i.e. when *E>U*, solutions of Schrödinger equation are: $\psi(z) = \psi(0)e^{\pm ikz}$, wit $k = \frac{\sqrt{2m(E-|U|)}}{\hbar}$. Within the barrier, solution is provided by $\psi(z) = \psi(0)e^{-\chi z}$, with $\chi = \frac{\sqrt{2m(|U|-E)}}{\hbar}$. Notice that within the barrier (region 2), the electron is described by an exponentially attenuating wave, propagating along $+z$ direction. The probability density of finding an electron within the barrier at position *z* is given by the square modulus of the wavefunction: $|\psi(z)|^2 = |\psi(0)|^2 e^{-2\chi z}$.

The wave function in region 1, where *z<0*, is given by: $\psi_1 = A_1 e^{ikz} + B_1 e^{-ikz}$.

The wave function for region 2, within the potential barrier, is given by: $\psi_2 = A_2 e^{\chi z} + B_2 e^{-\chi z}$.

The weave function for region 3, where *z>L*, is given by: $\psi_3 = A_3 e^{ikz}$.

The coefficients A_1, A_2, A_3, B_1, B_2 account for reflection and transmission of the wave functions, therefore proper boundary conditions are needed for the wave functions of each

region to join at the barrier edges. This translates into wave functions (and their derivatives) that should be continuous everywhere:

$$\begin{matrix} \psi_1(0) = \psi_2(0) & \psi_2(z) = \psi_3(z) \\ \psi_1'(0) = \psi_2'(0) & \psi_2'(z) = \psi_3'(z) \end{matrix} \tag{2.3}$$

As a result, these equations are obtained:

$$\begin{aligned} A_1 + B_1 &= A_2 + B_2 \\ A_2 e^{\chi z} + B_2 e^{-\chi z} &= A_3 e^{ikz} \\ ikA_1 - ikB_1 &= \chi A_2 + \chi B_2 \\ A_2 e^{\chi z} + \chi B_2 e^{\chi z} &= ikA_3 e^{ikz} \end{aligned} \tag{2.4}$$

The current density is defined as: $J(z) = -i\frac{\hbar}{2m}\left(\psi^* \frac{d\psi(z)}{dz} - \psi \frac{d\psi(z)}{dz}\right)$

The incident current is given by:

$$J_{inc} = -i\frac{\hbar}{2m}\left(\psi_1^*(z)\frac{d\psi_1(z)}{dz} - \psi_1(z)\frac{d\psi_1(z)}{dz}\right) = \frac{\hbar k}{m}|A_1|^2 \tag{2.5}$$

whereas the transmitted current is:

$$J_{tr} = -i\frac{\hbar}{2m}\left(\psi_3^*(z)\frac{d\psi_3(z)}{dz} - \psi_3(z)\frac{d\psi_3(z)}{dz}\right) = \frac{\hbar k}{m}|A_3|^2 \tag{2.6}$$

Hence, a transition probability can be defined as the ratio between the transmitted current density and the incident current density, as follows:

$$T = \frac{J_{tr}}{J_{inc}} = \frac{|A_3|^2}{|A_1|^2} = \frac{1}{1+\frac{(k^2+\chi^2)^2}{4k^2\chi^2}\sinh^2(\chi s)} \tag{2.7}$$

since $k = \frac{\sqrt{2m(E-|U|)}}{\hbar}$ and $\chi = \frac{\sqrt{2m(|U|-E)}}{\hbar}$, and upon assuming a high (i.e. $E \ll U$) and large (i.e. $\sinh^2(\chi s) \gg 1$) potential barrier, the following expression for *T* is obtained:

$$T \approx \frac{16k^2\chi^2}{(k^2+\chi^2)^2} \cdot e^{-2\chi s} \tag{2.8}$$

where *s* defines the location of electrode in region 3 (see figure 2.1: One-dimensional potential barrier with region 1,2,3).

A general theory of the tunnelling phenomenon is now presented, showing the fundamental equation that link the tunnelling current to the tip-sample distance. It is the case of Bardeen's approach to electron tunnelling [13]. A planar tunnelling junction (see fig. 2.1. one-dimensional potential barrier with regions 1 2 3.) is considered and electron tunnelling is treated as a one-particle process, therefore neglecting mutual interactions among electrons during tunnelling. A direct interaction of tip and sample is excluded. The Bardeen's approach makes use of an important result of first order time-dependent perturbation theory, that is the Fermi Golden Rule. This allows to evaluate the probability of an electron, described by wave function ψ with associated energy E_ψ, to tunnel into a state described by wave function χ, with corresponding energy E_χ [14].

$$W_{ij}(t) = \frac{2\pi}{\hbar}\delta\left(E_i^S - E_j^T\right)\left|M_{ij}\right|^2 \tag{2.9}$$

$|M_{ij}|^2$ is the tunnelling matrix element, and it is mathematically described by the integral: $<\psi_j^T|U_T|\psi_i^S>$, with $U_T = U_T(t) = e^{\frac{\eta t}{\hbar}}$, and $\eta > 0$. $U_T(t)$ is the time-dependent potential adiabatically turned on at the tip-electrode. It is easy to associate E_i^S to an occupied state of the sample, and E_j^T to an unoccupied state of the tip, or vice versa. Nonetheless, tip and sample are metals and for this reason a most suitable reasoning can be based on energy bands, as continuous spectra of states. Therefore, the mathematical sum Σ over i-ths tip states ψ_i^T and j-ths sample states ψ_j^S is considered. At *T*=0 K, the Fermi level is sharply separating occupied states from unoccupied states, whilst at $T > 0\,K$ the edge is smeared out. Fermi-Dirac distribution well described fermions (i.e. electrons) state occupation.

Occupied states are indeed given by: $f(E - E_F) = \frac{1}{\left(1+e^{\frac{E-E_F}{k_B T}}\right)}$;

unoccupied states are given by: $1 - f(E - E_F)$.

Upon application of a bias voltage *V*, at thermal equilibrium, a tunnelling current from sample to tip $I_{S\to T}$ is established, as well as the counterpart from tip to sample $I_{T\to S}$:

$$I_{S\to T} = \frac{4\pi e}{\hbar}\sum_{ij} f\left(E_i^S - E_F^S\right)\left[1 - f\left(E_j^T - E_F^T\right)\right]\left|M_{ij}\right|^2 \delta\left(E_j^T - E_i^S - eV\right) \quad (2.10)$$

$$I_{T\to S} = \frac{4\pi e}{\hbar}\sum_{ij} f\left(E_j^T - E_F^T\right)\left[1 - f\left(E_j^S - E_F^S\right)\right]\left|M_{ij}\right|^2 \delta\left(E_j^T - E_i^S - eV\right) \quad (2.11)$$

The net total current is given by difference between the two tunnelling current contributions:

$$I = \frac{4\pi e}{\hbar}\sum_{ij}[f\left(E_i^S - E_F^S\right) - f\left(E_j^T - E_F^T\right)\left|M_{ij}\right|^2 \delta\left(E_j^T - E_i^S - eV\right) \quad (2.12)$$

Summation over discrete states turns into an integral over energies, in which the density of states *n(E)* appears:

$$I = \frac{4\pi e}{\hbar}\int dE\left[f(E_F^T - eV + E) - f\left(E_F^S + E\right)\right] n^T(E_F^T - eV + E) n^S\left(E_F^S + E\right)\left|M\left(E_F^S + E, E_F^T - eV + E\right)\right|^2 \quad (2.13)$$

n^S and n^T are the density of states (DOS) of, respectively, the sample and the tip. For the simple case of $T = 0\,K$, the tunnelling current expression simplifies to:

$$I = \frac{4\pi e}{\hbar}\int_0^{eV} dE\; n^T(E_F^T - eV + E) n^S\left(E_F^S + E\right)|M|^2 \quad (2.14)$$

which in the limit of small bias voltages becomes:

$$I = \frac{4\pi e}{\hbar} V n^T(E_F^T) n^S\left(E_F^S\right)|M|^2\,. \quad (2.15)$$

The tunnelling matrix element is treated by many theories, starting by Bardeen's approach and going to Tersoff-Hamann model or to Chen's expansion [13].

However, the key-point is the dependence of the matrix element on the sample-tip gap *s*. Indeed, by applying the Wentzel-Kramers-Brillouin (WKB) approximation, the matrix element can be express as:

$$|M|^2 = e^{-2\gamma} \quad (2.16)$$

where

$$\gamma = \int_0^s \sqrt{\frac{2m\phi}{\hbar^2}}dx = \frac{s}{\hbar}\sqrt{2m\phi_{eff}} \qquad (2.17)$$

m is the mass of the electron, *s* represents the sample-tip separation, and ϕ_{eff} is the effective height of the barrier, namely a combination of work functions of tip and sample. For the sake of simplification, ϕ_{eff} can be written [15] as the average work function of tip and sample, that is: $\phi_{eff} = \frac{(\phi^T - \phi^S)}{2}$.

This gives access to a simple tunnelling current expression [16], as follows:

$$I = \frac{4\pi e}{\hbar} n^T(E_F^T) n^S\left(E_F^S\right) V \cdot e^{-s\sqrt{\frac{8m\phi}{\hbar^2}}} \qquad (2.18)$$

which shows a linear dependence of the tunnelling current to the bias voltage and an exponential dependence to the tip-sample distance. This exponential dependence turns into high vertical resolution, since large differences in tunnelling current are detected for relatively small sample-tip distances variations.

2.1.2 Tunnelling through an electrolyte

When passing from UHV environment to solid/liquid interface, STM imaging becomes more difficult to describe. Several differences arise, and a unique tunnelling theory has not been developed yet. Some quantitative approaches have in any case been explored, providing at least experimental evidences as starting points for theoretical considerations.

One solid point is that water exerts an effect in the tunnelling phenomenon between tip and substrate. As a result, variations of the tunnelling current with the sample/tip distance are detected [17]. In other words, the effective barrier height for electron tunnelling has changed. When tunnelling at the solid/liquid interface, the tip has to certainly deal with an easier contamination, since the high fields applied between tip and sample can attract and accumulate impurities in the tunnelling gap [17] [18].

Schmickler and Henderson [19][17] modelized a flat metal electrode surface as jellium, the tip as a jellium sphere, and water as dielectric mean. The result is a reduced effective barrier height (~2-3 eV), if compared to common barrier heights detected in vacuo (~3-5 eV).

Another approach concerns tunnelling via intermediate states. This means that electrons tunnel from tip to sample (or vice versa) passing through a certain number of intermediate states, which can be represented by hydrated electrons [17] [20] or dipole resonances [17] [21]. This last point was developed by Halbritter [21] and will be further elucidated. In general, tunnelling through these intermediate states causes the barrier height to reduce. The following Gamov-like expression for the tunnelling probability via an i-th intermediate state can be formulated:

$$P_t^i = \frac{P_t(m-i)P_t(i-t)}{P_t(m-i)+P_t(i-t)} \qquad (2.19)$$

$P_t(m-i)$ represents the tunnelling probability from the metal electrode to an i-th intermediate state, while $P_t(i-t)$ accounts for the tunnelling probability from the i-th state to the tip. P_t^i is mostly affected by the smaller of the two probabilities and the most favourable case occurs

when the two are equal. If the tunnelling gap is changed by a quantity ΔL, the position of the intermediate state is mostly unchanged, resulting in a reduction of the tunnelling barrier, since it can be conveniently expressed as follows:

$$\phi = -\frac{\hbar^2}{8m}\left(\frac{d\ln i}{dL}\right)^2 \tag{2.20}$$

Schmickler [17] and Mosyak, Nitzan and Kosloff [22] modelized the sample and the tip as semi-infinite jellium, and the gap between the jellium edges is filled with water molecules. Its thickness is set to 9.6 Å in order to host three layers of water molecules. The calculation of the interaction of these three layers with a tunnelling electron resulted in a three-dimensional potential energy hypersurface. Maxima are localised at the positions of oxygen atoms, whereas deep minima are found near hydrogen atoms. The presence of minima near hydrogen atoms increases the tunnelling probability [17]. It must be remarked that the configuration of water molecules varies, but does it on a much longer time scale if compared to the electron tunnelling event: an electron basically experiences a static tunnelling barrier [11], leading to an effective barrier height of ~2 eV.

An overview of intermediate states theory proposed by Halbritter [21] is now provided. He performed systematic Distance Tunnelling Spectroscopy and Voltage Tunnelling Spectroscopy to modelise the tunnelling phenomenon in the presence of a solid/electrolyte interface. He assigned a primary role to intermediate states localised in the tunnelling gap. Their presence has to be correlated with dipole resonances originated by oriented water molecules within the tunnelling gap. In vacuo tunnelling current exhibits an exponential decay [21] (as previously described):

$$I_T(d) \propto e^{-2kd} \tag{2.21}$$

If one intermediate state is located within the tunnelling barrier, a "resonance" phenomenon occurs, namely the electron tunnels from tip to sample (or vice versa) passing through the intermediate state in between the sample/tip gap. The tunnelling current dependence upon the sample/tip separation *d* changes accordingly:

$$I_{T_1}(d) \propto \rho_{l,0}\, e^{-\frac{2kd}{2}} \tag{2.22}$$

where, $\rho_{l,0}$ is stands for a uniform distribution of localised states. k is the inverse decay length and it features a dependence upon the effective tunnelling barrier ϕ_{eff}:

$$k \propto \left(\phi_{eff}\right)^{\frac{1}{2}} \tag{2.23}$$

$I_{T_1}(d)$ exhibits a slower decay with *d*, i.e. a weaker distance dependence if compared to $I_T(d)$. If *n* intermediate states are considered, this dependence would be further weakened, leading to a reduced effective tunnel distance:

$$d_{eff} = \frac{d}{n+1} \tag{2.24}$$

which turns into a reduction of the tunnelling barrier height:

$$\phi_{eff} = \frac{\phi_0}{(n+1)^2} \tag{2.25}$$

Intermediate states are interpreted as dipole resonances related to water molecules, which form layers uniformly covering the tip electrode surface, as well as the working electrode surface. The orientation of the molecules and the thickness of the resulting layers can be influenced by chemical nature of the electrolyte, crystallographic orientation of the sample, defects on the tip and/or on the sample, together with the presence of adsorbed species. The tip potential also exerts a major role, since at the very-end tip a strong and inhomogeneous electric field is originated when the bias potential is applied. Tunnelling mechanism are generally associated to a low number of intermediate states ($n \sim 2-3$): higher numbers would lead to a strong signal decrease and therefore a worse signal/noise ratio.

Hugelmann and Schindler [23, 18] also investigated the effect on the tunnelling current induced by the presence of water layers within the sample/tip gap, showing that a substantially non-exponential decay of the tunnelling current (with respect to the sample/tip separation *d*) occurs at the solid/liquid interface. Their Distance Tunnelling Spectroscopy studies led to the observation of an oscillatory tunnelling probability (with a period of ~0.35 nm), whose origination was attributed to the presence of definite water layers in the tunnelling gap. The oscillation period is close to the predicted distance of water molecules in the Helmholtz layer of the solid/liquid interface [18, 23]. After the jump to contact of the tunnelling current revealed at *z=0* (i.e. the sample surface), the tunnelling phenomenon should behave with a vacuum-like mechanism, since the gap is still too small to accommodate any molecule. A different mechanism is involved (and the tunnelling barrier height starts to decrease) when a gap of ~0.15 nm is reached, since water molecules start to enter the gap and tunnelling is expected to involve hydrogen atoms. If a gap of 0.35 nm is realised, a complete layer of water molecules is formed, and the tunnelling barrier height experiences its first minimum. Upon further increasing the gap, the barrier height increases since a vacuum-like situation is again established. At ~0.55 nm, new water molecules are able to accommodate in the gap, thereby lowering the barrier height up to a new minimum at ~0.70 nm. Therefore, it has experimentally been found that the tunnelling barrier height is minimum when electron tunnelling is maximised across the electronic states of hydrogen [18]**.** Tunnelling barrier minima occur each time a water layer is completed within the tunnelling gap.

2.1.3 Modes of Operation

In the constant current mode, the tunnelling current that flows between tip and sample is held constant. Since the tunnelling current is exponentially linked to the tip-sample distance, as already shown in section 2.1.1., maintaining a constant current requires the tip/sample distance to be fixed. Due to surface roughness, the tip nominal height must continuously be corrected in order not to vary the tip/sample distance. This can be accomplished thanks to a feedback loop circuit. The tunnelling current is manually set thanks to a dedicated knob, as explained in section 3.2. If the feedback loop detects an increase of the current (i.e. the tip finds a surface protrusion), a voltage response is sent to the piezoelectric scanner with the purpose to increase the tip/sample distance, therefore opposing to the tunnelling current increase and restoring its desired value. As a result, the vertical movement, along Z direction, of the tip due to surface roughness generates a topographic profile. A colour hue is assigned to each Z value and consecutive topographic profiles are collected: in this way, topographic profiles turn into topographic images. Images are then 2D projections of consecutives topographic profiles.

In constant-height mode the initial vertical position Z of the tip is held constant, thus allowing the tip/sample distance and consequently the tunnelling current to vary. The tunnelling current becomes a function of the lateral position and an apparent topographic image of the surface is obtained. Image acquisition through constant-height mode is a faster process compared with constant-current imaging. Nonetheless, it represents a riskier mode of operation, since surface protrusions can easily lead to tip crash. This mode should in fact be used in the case of atomically flat surfaces.

Constant-current mode is therefore a slower but safer image acquisition technique, that should be used for samples with rough topography in order to minimise tip crashes. It is convenient also for samples with unknown topography and for samples whose topography may vary during scanning, if for example a different polarisation is applied to a functionalised working electrode, like in the present work with FeN_4-functionalised Au(111) crystal.

2.1.3.1 Positioning

The tip is scanned onto the sample thanks to two positioners. A coarse positioner controls the coarse approach (or retraction) of the tip with respect to the sample, allowing the tip to quickly cover large distances (0.3 mm). A coarse positioner can be distinguished basically in three types: Mechanical, Louse or Beetle. The STM unit herein described features a Beetle-type coarse positioner, also known as Besocke positioner, as it was firstly introduced by K. Besocke in 1987 [24]**.** It consists of three piezoelectric tubes (Piezolegs) mounted on a fixed plate, together with the holder containing the PEEK cell with the sample. A depiction of the piezoleg system is shown in figure 2.2.

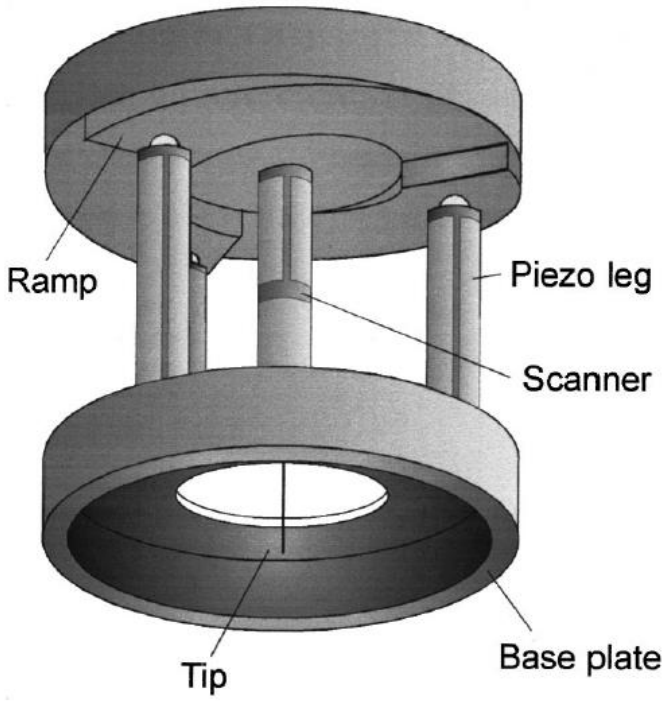

Figure 2.2: Image of the piezoleg system [25].

The tip is mounted on a cylindrical ramp, which is leaned onto the three piezolegs. Each piezoleg terminates with a 2 mm radius stainless steel sphere, which is glued to the piezoelectric tube in order to provide electrical isolation. Upon application of a proper voltage, the piezoelectric tubes oscillate, and the cylindrical plate starts rotating, thus pulling the tip forward (or backward). The voltage is then quickly reduced and the balls return to their original positions. Due to inertia of the ramp, the balls slip on it when returning to their original position, being now ready to a new voltage application. This "stick-and-slip" procedure is repeated until the feedback loop reaches a set-point tunnelling current. From there on, the approaching must be manually accomplished by forcing the stick-and-slip mechanism up to a tunnelling current value in the range [-300; +300] arbitrary units. The arbitrary units derive from instrumental calibration and a value belonging to the [-300; +300] a.u. range guarantees stable tunnelling conditions.

A fine positioner is made out of a piezoceramic tube, also called Piezotube. This material exhibits piezoelectric effect, which means that if a mechanical stress is applied to the piezoceramic material, an electric field is generated. The corresponding electric polarisation is given by:

$$P_i = d_{ijk}\,\sigma_{jk} \tag{2.26}$$

The stress σ_{jk} is a second rank tensor, while the piezoelectric modulus d_{ijk} is a third rank tensor, but it is symmetric in the last two indexes (i.e.: $d_{ijk} = d_{ikj}$).

Alternatively, if an electric field is applied, the piezoceramic material undergoes a mechanical strain (inverse piezoelectric effect):

$$\varepsilon_{jk} = d_{ijk}E_i \tag{2.27}$$

Symmetry properties of crystals play a major role in determining piezoelectricity [26]**.** The piezoelectric tensor should in fact vanish in centro-symmetric crystals. Of the remaining 21 non-centro-symmetric crystallographic classes, 20 are compatible with piezoelectricity: despite being non-centro-symmetric, the 432 crystallographic class does not exhibit piezoelectricity due to annihilation of charges along the <111> polar axes.

To further elucidate piezoelectric properties, the following figure 2.3. is taken into exam.

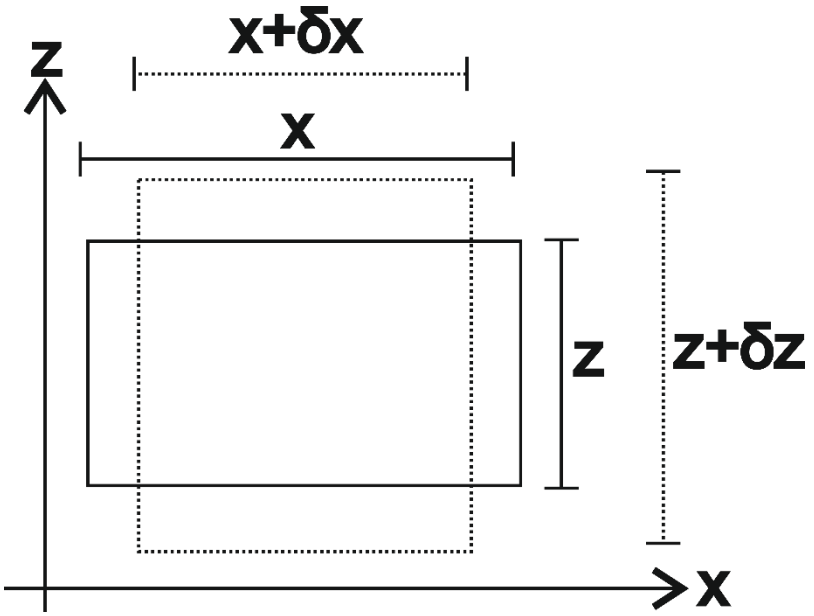

Figure 2.3: Scheme of a two-dimensional piezoelectric slab.

For the sake of convenience, a two-dimensional system is taken into account, with only *x* and *z* directions. If a voltage V is applied to a piezoelectric slab of thickness *z*, the corresponding uniform and stationary electric field will be defined as $E_z = \frac{V}{z}$. As a result, a strain in the *xz* plane is generated: $\varepsilon_x = \frac{\delta x}{x}$, $\varepsilon_z = \frac{\delta z}{z}$.

Typical values for piezoelectric coefficients are meters/Volts. These materials are therefore extremely sensitive, since a 1 V change in the applied voltage can turn into tens of nanometres difference in the tube length. Hence, these materials are suitable for STM imaging, which requires precise movements of the scanning tip with an accuracy of less than 0.1 Å.

Focusing on the experimental setup, the case of a piezoelectric tube must now be considered., since the tip is fitted into a piezoelectric tube, namely a tube made out of piezoelectric material. In particular, the inverse piezoelectric effect is exploited, obtaining a tube able to deform upon electric field application. For this purpose, four electrodes are realised on the external side of the tube and one contact is realised inside the tube itself. The four outer electrodes allow displacements of the tip in a parallel plane with respect to the sample surface. In this way, the tip can be swept over the surface sample, covering areas from 1 x 1 nm up to 1000 x 1000 nm. The inner electrode enables tip extension/retraction of ±100 nm along the perpendicular direction with respect to the sample surface.

Displacements in the *xy* plane are achieved by voltage application to two opposite electrodes. For example, a lateral displacement Δx along *x* direction is given by applying voltages of $-U_x$ and $+U_x$, respectively, to the two opposite electrodes placed along *x* direction: $\Delta x = \frac{2\sqrt{2}d_{xz}l^2U_x}{\pi Dh}$, with *l* length of the tube, *h* wall thickness, *D* the diameter of the tube.

A displacement in the vertical direction Z is accomplished by applying a voltage between the inner electrode and the four outer electrodes. The vertical displacement is then: $\Delta z = \frac{d_{xz}lU_z}{h}$ [27].

2.1.3.2 Tip

The tunnelling tip has a major role in determining the resolution capability of the STM unit. Indeed, if the tip is properly prepared, atomic resolution is readily achievable [28]. As already described, there exist an exponential dependency of the tunnelling current with respect to the tip-sample distance. For this reason, an ideal tip should terminate with a single atom in order to determine a precise tunnelling condition. However, real tips may more often present more than one atom at the very end of the tip, thus causing a general worsening of the tunnelling events. As a result, atomically sharp tips will properly follow surface protrusions, trenches and pits, thus providing an accurate representation of the sample topography. Conversely, a pyramidal-shaped or blunt tip will only approximately follow the surface roughness, hence providing a poor representation of the sample topography. If the tip has a particularly large termination, the sample itself can act as imaging probe, thus leading to an effective imaging of the tip. These concepts are depicted in figure 2.4.

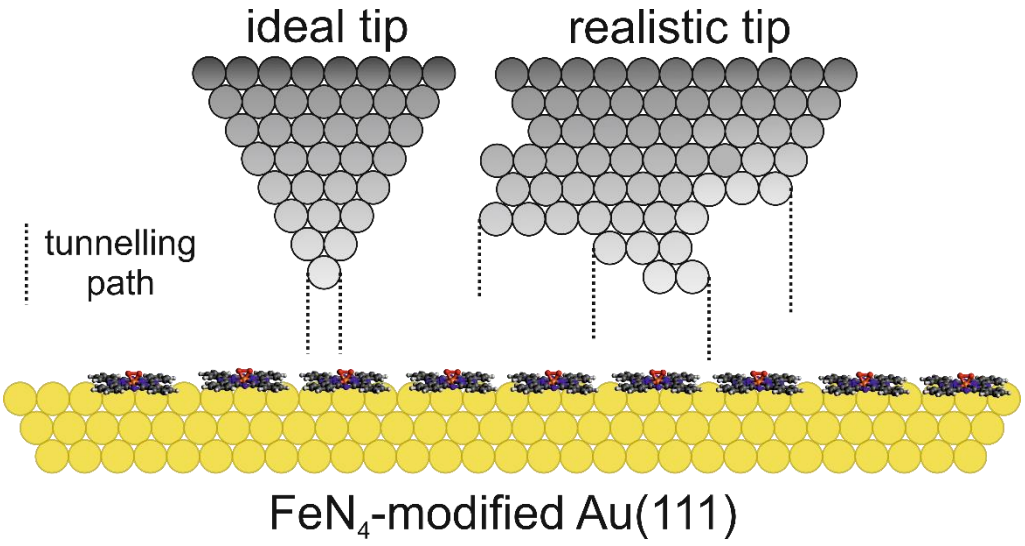

Figure 2.4: Visual representation of an ideal (left) and a realistic (right) tip.

Obtaining a high-radius-of-curvature tip is therefore essential. Tips can be fabricated by mechanical grinding or cutting of metal wires, but usually these procedures lead to large radius-of-curvature tips, double tips, or blunt tips. The most common and reliable method for obtaining sharp tips is electrochemical etching. This procedure is further described in section 3.2.2.

2.1.3.3 Vibration isolation

Topographic profiles measured in constant-current mode are usually in the range of 10^1 - 10^2 pm. This means that the instrumentation must be extremely sensitive and accurate, and that small vibrations of even few µm, not detectable by eye, would be deleterious for STM imaging. Therefore, every source of vibration must be eliminated, or at least reduced down to 0.001 pm (two orders of magnitude less than operation range of STM). The two major issues are external vibrations, not relied to the STM instrumentation, and inner vibrations, caused indeed by the

instrumentation itself. Vibrations commonly found in the laboratory environment span from 1 to 100 Hz. It is the case of ventilation ducts, transformers and motors (6-65 Hz), or simply walking and working (1-3 Hz) nearby the instrumentation. Conversely, inner vibrations usually possess higher frequencies, from 1 to 100 kHz, and are often associated to the internal resonance frequency of the particular STM unit.

Various strategies are adopted to reduce, at the same time, inner and external vibrations, like suspension springs, rubber feet, heavy platforms. One of the most significant mean of vibration minimisation is represented by suspension springs and a noteworthy mode of operation description is herein provided. The suspension spring system consists in the combination of four steel springs coupled with a heavy granite plate, on which the STM unit is fixed. The resonance frequencies for vertical and lateral motion are, respectively:

$$f_{vertical} = \frac{1}{2\pi}\sqrt{\frac{k}{m}}; \qquad f_{lateral} = \frac{1}{2\pi}\sqrt{\frac{g}{L}} \tag{2.28}$$

For vertical motion, the simple motion of a mass *m* attached to a spring with *k* spring constant is considered. For lateral motion, the case of a simple pendulum is considered: it is the case of a point mass suspended to a rod of negligible mass, which undergoes small amplitude oscillations.

2.2 Electrochemistry

2.2.1 Potential Differences

When a metal and an electrolyte are put to contact, microscopic changes take place at the interface. These phenomena are better described further on section 2.2.2. A charge q^M resides on the surface of the metal and it therefore originates an opposite charge in the liquid phase, $-q^S$. The two charges exactly compensate:

$$q^S = -q^M \tag{2.29}$$

In this case, the charge on the metal surface is assumed to have a negative value. The potential profile is depicted in figure 2.5.

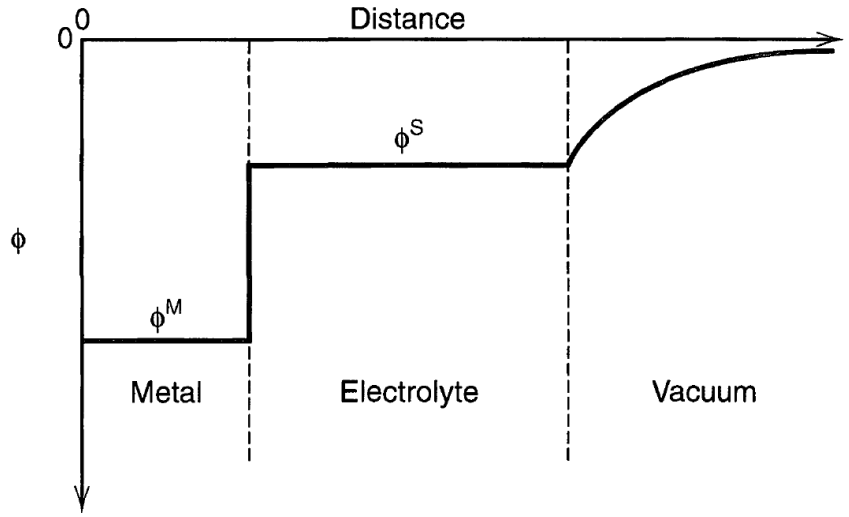

Figure 2.5: Potential profile through the system metal-electrolyte-vacuum [29].

Since a positive q^S charge appears at the interface, a negative charge $-q^M$ must reside at the outer surface of the electrolyte. If a positive test charge is now brought from an infinite distance to a definite distance, it will be attracted by the charge $-q^M$ on the outer surface of the electrolyte. A negative work is required for the test charge to cross any distance towards the electrolyte coming from the vacuum environment.

It is useful to recall the definition of potential difference between the point (x', y', z') and (x, y, z):

$$\phi(x', y', z') - \phi(x, y, z) = \int_{x,y,z}^{x',y',z'} -\boldsymbol{\epsilon} \cdot d\boldsymbol{l} \tag{2.30}$$

where $\boldsymbol{\epsilon}$ is the electric field vector, whereas $d\boldsymbol{l}$ is the infinitesimal path tangent to the direction of movement. Within the electrolyte, no electric field arises, and the potential is constant. This constant value is generally termed ϕ^S. At the metal/solution interface, negative work is done to take the test charge through it, resulting in a sharp change in potential from ϕ^S to ϕ^M. The potential then remains constant at ϕ^M within the metal, since no electric field appears. The difference $\Delta\phi = \phi^M - \phi^S$ is called interfacial potential difference and it depends on the charge density at the interface. However, $\Delta\phi$ cannot be measured for a single interface, since sampling electrical properties of the solution would introduce at least one more interface. Nevertheless, electrochemical potentials can conveniently be defined:

$$\bar{\mu}_i^\alpha = \mu_i^\alpha + z_i F \phi^\alpha \tag{2.31}$$

μ_i^α is the chemical potential, as shown in eq. (32), while z_i is the charge of the i-th species in phase α.

$$\mu_i^\alpha = \left(\frac{\partial G}{\partial n_i}\right)_T, p, n_{i \neq i} \tag{2.32}$$

n_i is the number of moles of *I* in phase α.

Let us consider the following cell:

$$Cu|Zn|ZnCl_2|AgCl|Ag|Cu' \tag{2.33}$$

The corresponding cell reaction is:

$$Zn + 2AgCl + 2e^{-}(Cu) \rightleftarrows Zn^{2+} + 2Ag + 2Cl^{-} + 2e^{-}(Cu') \qquad (2.34)$$

At equilibrium, making use of electrochemical potential definition, eq. (2.34) becomes:

$$\bar{\mu}_{Zn}^{Zn} + 2\bar{\mu}_{AgCl}^{AgCl} + 2\bar{\mu}_{e}^{Cu'} = \bar{\mu}_{Zn^{2+}}^{S} + 2\bar{\mu}_{Ag}^{Ag} + 2\bar{\mu}_{Cl^{-}}^{S} + 2\bar{\mu}_{e}^{Cu} \qquad (2.35)$$

Since $\Delta G = -nFE$, upon proper rearrangement of eq. (2.35), the result is:

$$E = E^{0} - \frac{RT}{2F}\ln\left(a_{Zn^{2+}}^{S}\right)\left(a_{Cl^{-}}^{S}\right)^{2} \qquad (2.36)$$

Nerst equation for the cell (eq. 2.33) has been obtained. This shows the utility for treating interfacial regions with electrochemical potentials, rather than with interfacial potentials.

A basic but quantitative approach is herein developed to describe the current-time response of a planar electrode used as working electrode in an unstirred electrolytic solution. The reaction $O + ne^{-} \rightarrow R$ is considered. If no stirring is performed on the solution, a variation of the concentration profile will occur, causing the current to depend upon this concentration variation:

$$C = C(x,t) \qquad i_d = C(E,t) \qquad (2.37)$$

The current is therefore governed by diffusion, and will be termed as diffusion-limited current, $i_d(t)$. The calculation of $i_d(t)$ and $C_O(x,t)$ requires the solution of 2nd Fick's law (linear diffusion equation):

$$\frac{\partial C_O(x,t)}{\partial t} = D_O \frac{\partial^2 C_O(x,t)}{\partial x^2} \qquad (2.38)$$

Proper initial and boundary conditions are required to solve equation (2.38):

$$C_O(x,0) = C_O^* \qquad (2.39)$$

$$\lim_{x\to\infty} C_O(x,t) = C_O^* \qquad (2.40)$$

$$C_O(0,t) = f(E) = 0 \qquad (2.41)$$

Eq. (2.39) expresses the homogeneity of the solution at *t=0*; eq. (2.40) defines the semi-infinite nature of diffusion, i.e. regions far from electrode surface are unperturbed by reactions at the electrode surface; eq. (2.41) expresses the dependence of the concentration at the electrode surface on the applied potential, which for the reversible case will be provided by Nerst equation. In this case, the applied potential is assumed to be $E_f \ll E^{\circ}$, thus realising a surface concentration equal to 0 if a large time span is considered. Finally, flux balance for mass conservation holds:

$$D_O\left(\frac{\partial C_O(x,t)}{\partial x}\right)_{x=0} + D_R\left(\frac{\partial C_R(x,t)}{\partial x}\right)_{x=0} = 0 \qquad (2.42)$$

The partial differential equation dictated by eq (2.38) can be solved upon Laplace transformation of eq (2.38) and its subsequent solution in Laplace space needs to undergo an inverse Laplace transformation, leading to the ultimate expression for $C(x,t)$.

By applying Laplace transformation, the following ordinary differential equation is obtained:

$$\frac{d^2\overline{C_O}(x,s)}{dx^2} - \frac{s}{D_O}\overline{C_O}(x,s) + \frac{C_O^*}{D_O} = 0 \qquad (2.43)$$

Its solution yields:

$$\overline{C_O}(x,s) = \frac{C_O^*}{s} + A(s)e^{-\sqrt{\frac{s}{D_O}}x} + D(s)e^{\sqrt{\frac{s}{D_O}}x} \tag{2.44}$$

Boundary conditions derive from (2.40) and (2.41) and are:

$$\overline{C_O}(0,s) = 0 \tag{2.45}$$

$$\lim_{x\to\infty} \overline{C_O}(x,s) = \frac{C_O^*}{s} \tag{2.46}$$

Hence,

$$\overline{C_O}(x,s) = \frac{C_O^*}{s} - \frac{C_O^*}{s}e^{-\sqrt{\frac{s}{D_O}}x} \tag{2.47}$$

By using similar calculations and upon application of flux balance, the following expression for *R* species is obtained:

$$\overline{C_R}(x,s) = \frac{C_O^*}{s}e^{-\sqrt{\frac{s}{D_R}}x} \tag{2.48}$$

The inverse Laplace transform can now be successfully applied, as follows:

$$C_O(x,t) = L^{-1}\{\overline{C_O}(x,s)\} = C_O^*\left(1 - erfc\left[\frac{x}{2\sqrt{D_O t}}\right]\right) \tag{2.49}$$

$$C_R(x,t) = L^{-1}\{\overline{C_R}(x,s)\} = C_O^*\frac{D_O}{D_R}\ erfc\left[\frac{x}{2\sqrt{D_R t}}\right] \tag{2.50}$$

The error function rapidly reaches its asymptote, which corresponds to the bulk values of the corresponding *O* and *R* species. Namely, $C_O(x,t) \to C_O^*$, while $C_R(x,t) \to 0$, since the reaction $O + ne^- \to R$ was previously considered.

The flux at the electrode is proportional to the current (if *O* and *R* are transported to or from the electrode purely by diffusion):

$$\frac{i(t)}{nFA} = J_O(0,t) = -D_O\left(\frac{\partial C_O(x,t)}{\partial x}\right)_{x=0} \tag{2.51}$$

If Laplace transform is applied to eq. (2.51), expression (2.52) is obtained:

$$\bar{\imath}(s) = -nFAD_O\left(\frac{\partial \overline{C_O}(x,s)}{\partial x}\right)_{x=0} \tag{2.52}$$

Substituting eq. (2.47) into eq. (2.52), after proper differentiation, the result is:

$$\bar{\imath}(s) = -nFAD_O\left\{\frac{C_O^*}{s}\sqrt{\frac{s}{D_O}}e^{-\sqrt{\frac{s}{D_O}}x}\right\}_{x=0} \tag{2.53}$$

Inverse Laplace transform can now be applied, returning:

$$i(t) = L^{-1}\{\bar{\imath}(s)\} = -\frac{nFAD_O^{\frac{1}{2}}C_O^*}{\pi^{\frac{1}{2}}t^{\frac{1}{2}}} = i_d(t) \tag{2.54}$$

Eq. (2.52) is also known as Cottrel equation, and it expresses the effect of electroactive species depletion near the surface with a characteristic $t^{-1/2}$ dependence, which is a distinctive mark of diffusion control rather than electron transfer kinetics.

A more general case occurs when the applied potential E_f is changed to any value on the cathodic wave of the reaction $O + ne^- \rightarrow R$, without the limitation of highly negative potentials as did before. Nerst equation, as well as eq. (2.30), (2.40) and (2.42) still hold. Nerst equation can be conveniently rewritten as:

$$\theta = \frac{C_O(0,t)}{C_R(0,t)} = e^{\frac{nF(E-E^{\circ\prime})}{RT}} \tag{2.55}$$

By applying boundary conditions to Laplace transforms, calculated with the same methods before employed, the following equations for concentration profiles in Laplace space are obtained:

$$\overline{C_O}(x,s) = \frac{C_O^*}{s} - \frac{C_O^*}{(1+\theta\xi)} e^{-\sqrt{\frac{s}{D_O}}x} \tag{2.56}$$

$$\overline{C_R}(x,s) = \frac{C_O^*\xi}{(1+\theta\xi)} e^{-\sqrt{\frac{s}{D_R}}x} \tag{2.57}$$

where $\xi = \sqrt{\frac{D_O}{D_R}}$

If the same calculations before employed are now used, a more general Cottrell-like equation is achieved:

$$i(t) = -\frac{nFAD_O^{1/2}C_O^*}{(1+\xi\theta)\pi^{1/2}t^{1/2}} \tag{2.58}$$

Eq. (2.58) is valid for whichever step experiment in a reversible system.

If the applied potential *E* is made vary with time with a definite scan rate, a variation of the flux with time will occur. For the sake of simplicity, a linear variation of potential with time is considered (eq. (2.59)). Assuming a rapid electron transfer at the electrode surface, the Nerst equation holds, but it requires proper substitution with the new time-dependent potential *E(t)*:

$$E(t) = E_i - vt \tag{2.59}$$

$$\frac{C_O(0,t)}{C_R(0,t)} = e^{\frac{nF(E_i-vt-E^{\circ\prime})}{RT}} \tag{2.60}$$

v is the scan rate expressed in V/s.

Eq. (2.60) can be rewritten as:

$$\frac{C_O(0,t)}{C_R(0,t)} = \theta S(t) \tag{2.61}$$

where $\theta = e^{\frac{nF}{RT}(E_i-E^{\circ\prime})}$ and $S(t) = e^{-\sigma t}$, with $\sigma = \frac{nF}{RT}v$.

Eq. (2.44) and (2.51) are still valid, and combining them together and making use of convolution theorem the result is:

$$C_O(0,t) = C_O^* - \frac{1}{nFAD_O^{1/2}\pi^{1/2}} \int_0^t (t-\tau)^{-1/2} \cdot i(\tau) d\tau \quad (2.62)$$

Similarly,

$$C_R(0,t) = \frac{1}{nFA\pi^{1/2}D_R^{1/2}} \int_0^t (t-\tau)^{-1/2} \cdot i(\tau) d\tau \quad (2.63)$$

By exploiting eq. (2.61), the integral contained in eq. (2.62) and eq. (2.63) becomes:

$$2. \int_0^t (t-\tau)^{-1/2} \cdot i(\tau) d\tau = \frac{nFA\pi^{1/2}D_O^{1/2}C_O^*}{(1+\theta S(t)\xi)} \quad (2.64)$$

However, a closed form of eq. (2.64) can only be numerically computed. Moreover, it is convenient to change the *i(t)* form to the *i(E)* one and to rewrite eq. (2.64) in a dimensionless form to simplify its numerical solution. This last point can be fulfilled by proper substitution, as follows:

$$\sigma t = \frac{nF}{RT} vt = \frac{nF}{RT} (E_i - E) \quad (2.65)$$

$$i(\tau) = g(z) \quad (2.66)$$

with $z = \sigma\tau$.

Eq. (2.64) then becomes:

$$\int_0^t (t-\tau)^{-1/2} \cdot i(\tau) d\tau = \int_0^z (\sigma t - z)^{-1/2} \sigma^{-1/2} \cdot g(z)\, dz = \frac{C_O^*(\pi D_O)^{1/2}}{1+S(\sigma t)\theta\xi} \quad (2.67)$$

Hence,

$$\int_0^t (t-\tau)^{-1/2} \cdot i(\tau) d\tau = \int_0^z (\sigma t - z)^{-1/2} \chi(z)\, dz = \frac{1}{1+S(\sigma t)\theta\xi} \quad (2.68)$$

with $\chi(z) = \frac{g(z)}{C_O^*(\pi D_O \sigma)^{1/2}}$

Finally,

$$i = nFAC_O^*(\pi D_O \sigma)^{1/2} \chi(\sigma t) \quad (2.69)$$

$\chi(\sigma t)$ is a pure number and it is the result of numerical solutions found for eq. (2.68). In particular, the quantity $\pi^{\frac{1}{2}}\chi(\sigma t)$ reaches its maximum at a value of 0.4463, allowing to express the corresponding peak current as:

$$i_p = 0{,}4463nFAC_O^* D_o^{1/2} \left(\frac{nF}{RT}\right)^{1/2} v^{1/2} \quad (2.70)$$

which is known as Randles-Sevcik equation.

The corresponding (cathodic) peak potential is given by:

$$E_p = E_{1/2} - 1{,}109\frac{RT}{nF} = -\frac{28{,}5}{n}\ mV \text{ at T=25 °C} \quad (2.71)$$

$E_{1/2}$ is the half-wave potential and it is given by:

$$E_{1/2} = E° - \frac{RT}{nF} \ln \left(\frac{D_O}{D_R}\right)^{1/2} \quad (2.72)$$

Cyclic voltammetry is now taken into exam. The applied potential is given by:

$$E(t) = E_i - vt, \text{ for } 0 < t \leq \lambda \tag{2.73}$$

$$E(t) = E_i - 2v\lambda + vt, \text{ for } t > \lambda \tag{2.74}$$

At time $t=\lambda$ the direction of scan is inverted: the corresponding potential E_λ is called switching potential. For equation (2.73), the mathematical treatment is the same of a linear scan voltammetry. For equation (2.74), similar arguments can be used in the mathematical description. For a Nerstian system, the following expression holds:

$$\frac{C_O(0,t)}{C_R(0,t)} = e^{\frac{nF(E_i - 2v\lambda + vt - E^\circ)}{RT}} = \theta S(\sigma t) \tag{2.75}$$

where $\theta = e^{\frac{nF(E_i - E^\circ)}{RT}}$ and $S(\sigma t) = e^{(\sigma t - 2\sigma\lambda)}$.

Nonetheless, the results are similar as already derived for a LSV experiment. A caveat concerns the switching potential E_λ, on which there exists a dependence for the curve if the cathodic peak is less than 35 mV to E_λ.

2.2.2 Models for double-layer

2.2.2.1 Helmholtz Model

If a metallic electrode is considered, then its metallic nature dictates that any excess charge should reside at its surface, since no electric fields can develop within itself at equilibrium. Helmholtz proposed that two sheets of charges exist, one due to excess charge of the metal at its surface, the other one formed by counterions from the liquid phase in contact with the electrode. From this concept arises the name of *double layer*. This configuration resembles a parallel plate capacitor, with charge density σ and voltage drop between the plates V linked together by:

$$\sigma = \frac{\varepsilon\varepsilon_0}{d}V \tag{2.76}$$

where ε is the dielectric constant of the medium, ε_0 is the permittivity of free space, d is the gap within the plates. A differential capacitance can be defined as:

$$C_d = \frac{\partial\sigma}{\partial V} = \frac{\varepsilon\varepsilon_0}{d} \tag{2.77}$$

This model predicts a constant differential capacitance, which is however different from what is experimentally observed. Namely, ε and/or d should depend on potential and concentration, and C_d also should.

2.2.2.2 Gouy-Chapman Theory

Charge carrier density can be small, especially if low electrolyte concentrations are realised. This causes the counter-charges to accumulate in a layer with definite thickness. As a result, a diffuse layer of charges in solution has formed to counterbalance the surface charge at the electrode surface. Greatest concentration of charges will be found near the electrode surface,

since electrostatic forces are most able to overcome thermal processes, while progressively lesser concentrations will be found farther from the electrode. Therefore, the average distance d of charge separation should show dependences on both potential and electrolyte concentration. Ions are considered as point charges, and for this reason the diffuse layer starts from the electrode surface.

Double-layer structure can be mathematically described by non-linear differential equation of Poisson-Boltzmann, which provides a link between electric potential, charge density and ion concentration:

$$\frac{d^2\phi}{dx^2} = -\frac{zen_0}{\varepsilon\varepsilon_0}\left(e^{-\frac{zen_0\phi(x)}{kT}} - e^{\frac{zex}{kT}}\right) \qquad (2.78)$$

where n_0 is the bulk concentration of ions with charge z.

Upon solving Poisson-Boltzmann equation, the resulting differential capacitance is:

$$C_d = \frac{d\sigma_M}{d\phi_0} = \left(\frac{2z^2e^2\varepsilon\varepsilon_0 n_0}{kT}\right)^{1/2}\cosh\left(\frac{ze\phi_0}{2kT}\right) \qquad (2.79)$$

Gouy-Chapman theory predicts a dependence of C_d on potential, concentration and temperature. However, experimental capacitance values are usually lower than predicted ones. The major limit of Gouy-Chapman model is related to the finite size of ions in the electrolyte.

2.2.2.3 Stern's Modification

Ions do possess finite size and cannot approach the electrode surface any closer than their ionic radius. If they are solvated, an extra thickness must be added to that radius. Moreover, a plane of closest approach is considered, namely a layer of anions that covers the electrode surface. Two main regions are therefore defined: Inner Helmholtz Plane (IHP) and Outer Helmholtz Plane (OHP). At IHP, the adsorption of species without hydration sphere is observed. At OHP, ion with hydration sphere are encountered. Ions in direct contact with the electrode surface are said to be specifically adsorbed on it (see section 2.2.2.4). The differential capacitance is conveniently expressed by two terms: Helmholtz Capacitance (C_H) and Diffuse Layer Capacitance (C_{DL}). The differential capacitance is then given by:

$$\frac{1}{C_d} = \frac{1}{C_H} + \frac{1}{C_{DL}} \qquad (2.80)$$

C_H contributes to C_d with charges held at the OHP, while C_{DL} is the capacitance of truly diffuse charge. C_d is governed by the smaller of the contributions: at large electrolyte concentrations, and/or at large polarisations in diluted medium, C_{DL} becomes very large and therefore $\frac{1}{C_{DL}}$ becomes neglectable.

The following figure 2.6 displays a visual representation of the three double-layer model.

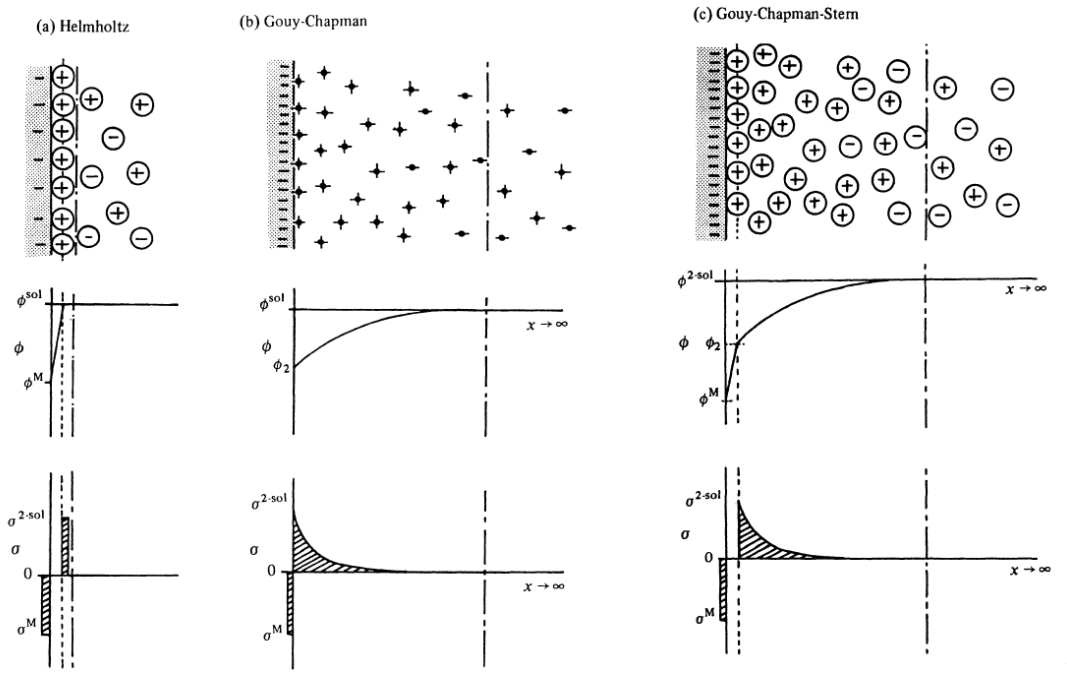

Figure 2.6: Schematic models of the ion, potential (**ϕ**) and charge (**σ**) distribution in a direction perpendicular to the plane of the electrode as described by (a) Helmholtz, (b) Gouy Chapman, and (c) Stern [30].

2.2.2.4 Specific Adsorption

Specifically, adsorbed ions are tightly bound to the electrode surface and therefore in direct contact with it. Hence, specific adsorption phenomena occur at IHP. SO_4^-, Cl^-, Br^-, I^- have weakly bound solvation water and they are prone to specific adsorb on clean electrode surfaces.

The amount of adsorbed species depends on its size and on its orientation on the electrode surface. Ions can in fact adsorb on sites in exact correspondence with surface atoms, giving a commensurate adsorption. Generally, ionic or molecular dimensions are too large to give this kind of adsorption, and an energetically more favourable packing occurs for higher spacings. If the required spacings prevent a fitting into vacant sites, rotations of the adsorbate unit cell can occur.

2.2.2.5 Self-Assembly at the solid/liquid interface

Self-Assembly deals with the process of spontaneous association of atomic or molecular entities, which under thermodynamic equilibrium conditions organise themselves into stable and well-defined structures joined by non-covalent bonds [31] [32] [33]. Despite this self-organisation process is based on weak interactions of single molecular units, it results in well-defined hierarchical macroscopic structures. It is worth to mention that the generated self-assembled structures occupy a thermodynamic minimum [31]**.** There exist examples of monolayers based on covalent bonds: thiolated groups easily form Self-Assembled Monolayers (SAM) on gold surfaces [34]. Nevertheless, the most riveting aspect of SAM formation lies in the ability to discard covalent bonds in favour of non-covalent interactions, which are notoriously weaker and lesser directional. It is the case of electrostatic interactions

(involving ions and/or dipoles), hydrogen bonds, hydrophobic interactions, π stacking and Van der Walls interactions [31]. An individual non-covalent interaction is weak, i.e. its binding energy is $\sim 0.1 - 5\ \frac{kcal}{mol}$. It is comparable to thermal energy: at $T = 300\ K$, the associated thermal energy is $kT \sim 0.6\ \frac{kcal}{mol}$. However, if an ensemble of units is attained, then a summation of weak interactions occurs, possibly leading to a system with sufficient stability, namely a self-assembled monolayer. Adverse phenomena must not be neglected. Indeed, competing interactions with solvent molecules can arise, preventing the desired species to interact among themselves. Moreover, entropy gained by eventual SAM disruption must be overwhelmed, since SAM formation is regarded as an energetically favourable process. A simple calculation can be provided: if two particles are brought together, the entropic contribution will be: $-T\Delta S \approx +5.5\ \frac{kcal}{mol}$. In addition, a conformational contribution must be considered, since freely rotating bonds are freezed when molecules are packed together: $-T\Delta S \cong +0.7\ \frac{kcal}{mol}$.

The self-assembly should result in a globally negative Gibbs free energy variation, meaning that good intermolecular contact (i.e. multipoint contact) must be fulfilled, and the assembling units should be sufficiently rigid enforce intermolecular interactions.

In the present work, extensive Self-Assembled Monolayers are successfully obtained for Fe(II)-Phthalocyanine and Fe(III)-tetramethoxyphenyl porphyrin chloride. An organised layer is also desirable for STM, since single molecules are often too mobile to be properly imaged [10]. The tunnelling tip can in fact perturbate molecular adsorption, causing removal or displacement of the molecule. The resolution may also worsen. Conversely, if molecules are packed in ordered domains, their mobility is reduced, and imaging is more efficient [10].

2.2.3 Reference Electrode

The reference electrode has the role to provide a fixed and constant potential, that does not vary during electrochemical characterisations. A reference electrode should in principle behave as an ideal non-polarisable electrode. Non-polarisable interface refers to an electrode surface, at which electron transfer is extremely fast. As a consequence, its potential should not change even if a current flows through it [35]. Since electron transfer process is fast, the electrode potential is calculated with Nerst equation. For this purpose, a special class of reference electrodes is considered, namely Hydrogen electrodes. These electrodes are based on platinised platinum foils, meshes or wires as active material able to exchange electrons in the redox process, on which hydrogen electrodes rely:

$$2H^+ + 2e^- \rightleftarrows H_2 \qquad (2.81)$$

with an associated potential, by convention, of: $E^\circ_{H_2,H^+} = 0\ V$ at all temperatures. This is strictly valid only if H_2 pressure is equal to 1 atm and if the solution contacting the Pt material possesses unitary activity, and the corresponding electrode is known as Normal Hydrogen Electrode (NHE). However, such conditions are not often attainable, but a convenient alternative can be employed, namely the Reversible Hydrogen Electrode (RHE). The glass electrode containing the Pt material is filled with the same electrolyte contained in the electrochemical cell and it is negatively polarised with respect to a counter-electrode, usually of Pt material. The negative polarisation enables Hydrogen Evolution Reaction at the RHE Pt surface, and gaseous H_2 accumulates in a bubble, which is trapped in the glass electrode. Therefore, the Pt mesh (or wire or foil) is in contact with both gaseous H_2 and hydronium (in

liquid phase), satisfying the equilibrium reaction (86). Of course, proper calculations need to be applied since deviations from Normal condition are introduced. This can be accomplished by the equation:

$$E_{H_2,H^+} = E^\circ{}_{H_2,H^+} + \frac{RT}{F}\ln\frac{a_{H^+}}{\sqrt{p_{H_2}}} \qquad (2.82)$$

Nonetheless, the RHE represents an actual practical advantage. The electrode is in fact filled with the same solution of the cell, and H_2 is generated *in situ*, with no need of an external hydrogen generator.

2.2.4 Working Electrode

The working electrode defines the interface under study [30]**.** Many classes of working electrodes have been used, but the present work only deals with a single-crystal electrode, namely a gold electrode exposing its (111) crystallographic face. Working electrode substrates should possess an even current and potential distribution and it should not chemically react with the electrolytic solution. Solid substrates can contaminate, oxidise and change in surface morphology with time, therefore they usually undergo pre-treatments before being mounted in the electrochemical cell. Pre-treatments can concern mechanical polishing or electropolishing techniques, chemical treatments with etching solutions or thermal annealing. This last procedure was largely employed in this work through a flame-annealing procedure in inert Ar atmosphere, as further described in section 3.2.3

2.2.5 Counter Electrode

The counter-electrode has the unique role to maintain the current required by the working electrode, without causing any limitation in the measured response of the cell [30]. Its potential is not matter of interest, and the only demanded feature is the ability to sustain the current developed at the working electrode. Oxidation/reduction reactions will occur at the counter-electrode surface when reduction/oxidation process occur at the working electrode surface. Therefore, reaction products developed at the counter-electrode should always be considered, aiming at the counter-electrode that introduces less contamination of the electrolytic environment as possible, in order not to interfere in the electrochemical response of the working electrode.

References

[1] G. Binnig, H. Rohrer, *Scanning tunneling microscopy*, Surf. Sci., **1983**, *126*, 236–244.

[2] G. Binnig, H. Rohrer, C. Gerber, E. Weibel, *Surface studies by scanning tunneling microscopy*, Phys. Rev. Lett., **1982**, *49*, 57–61.

[3] G. Binnig, H. Rohrer, C. Gerber, E. Weibel, T*unneling through a controllable vacuum gap*, Appl. Phys. Lett., **1982**, *40*, 178–180.

[4] http://calteches.library.caltech.edu/47/2/1960Bottom.pdf.

[5] http://faculty.virginia.edu/harrison/STM/tutorials/UHV.html.

[6] M.A. Lazaga, D.T. Wickham, D.H. Parker, G.N. Kastanas, B.E. Koel, *Reactivity of Oxygen Adatoms on the Au(111) Surface*, Acs Symp. Ser., **1993**, *523*, 90–109.

[7] R. Sonnenfeld, P.K. Hansma, *Atomic-resolution microscopy in water*, Science,**1986**, *232*, 211–213.

[8] A.J. Bard, F.-R. Fan, *Studies of the Liquid/Solid Interface by Scanning Tunnelling Microscopy and Scanning Electrochemical Microscopy*, Faraday Discuss., **1992**, *94*, 1–22.

[9] O.M. Magnussen, Ordered anion adlayers on metal electrode surfaces, Chem. Rev., **2002**, *102*, 679–725.

[10] A.J. Bard, L.R. Faulkner, *Electrochemical Methods, Fundamentals and Applications*, John Wiley & Sons,, **2001**.

[11] A.A. Gewirth, H. Siegenthaler, eds., *Nanoscale Probes of the Solid/Liquid Interface*, NATO Science Serie E: Applied Science, **1995,** *288.*

[12] R.A. Serway, C.J. Moses, C.A. Moyer, *Modern Physics*, 3rd edition, Thomson Learning, Inc., **2005**.

[13] S. Lounis, *Theory of Scanning Tunneling Microscopy*, in: Comput. Solids - Model. Ab Initio Methods Supercom- Puting, **2014**: p. 38.

[14] http://www2.fkf.mpg.de/ga/research/stmtutor/stmtheo.html, (n.d.).

[15] S.J. Altenburg, R. Berndt, *Local work function and STM tip-induced distortion of graphene on Ir(111)*, New J. Phys., **2014**, *16*, 053036.

[16] http://hoffman.physics.harvard.edu/research/STMtechnical.php.

[17] W. Schmickler, *Electronic Effects in the Electric Double Layer*, Chem. Rev., **1996**, *96*, 3177–3200.

[18] M. Hugelmann, W. Schindler, *Tunnel barrier height oscillations at the solid/liquid interface*, Surf. Sci., **2003**, *541*, L643–L648.

[19] W. Schmickler, D. Henderson, *A model for the scanning tunneling microscope operating in an electrolyte solution*, J. Electroanal. Chem., **1990,** *290*, 283–291.

[20] J.K. Sass, J.K. Gimzewski, *Solvent dynamical effects in STM with a polar liquid in the*

gap, J. Electroanal. Chem., **1991**, *308*, 333–337.

[21] J. Halbritter, G. Repphun, S. Vinzelberg, G. Staikov, W.J. Lorenz, *Tunneling Mechanisms in Electrochemical STM - Distance and Voltage Tunneling Spectroscopy*, Electrochim. Acta., **1995**, *40*, 1385–1394.

[22] A. Mosyak, A. Nitzan, R. Kosloff, *Numerical simulations of electron tunneling in water*, J. Chem. Phys., **1996**, *104*, 1549–1559.

[23] M. Hugelmann, W. Schindler, *In Situ Distance Tunneling Spectroscopy at Au(111)/0.02 M $HClO_4$: From Faradaic Regime to Quantized Conductance Channels*, J. Electrochem. Soc., **2004**, *151*, E97–E101.

[24] K. Besocke, *An Easily Operable Scanning Tunneling Microscope*, Surf. Sci., **1987**, *181*, 145–153.

[25] M. Wilms, M. Kruft, G. Bermes, K. Wandelt, *A new and sophisticated electrochemical scanning tunneling microscope design for the investigation of potentiodynamic processes*, Rev. Sci. Instrum., **1999**, *70*, 3641–3650.

[26] A.L. Kholkin, N.A. Pertsev, A. V. Goltsev, *Piezoelectricity and Crystal Symmetry*, chapter 2, **2008**.

[27] http://www.pi-usa.us/tutorial/4_39.html.

[28] M. Wilms, P. Broekmann, C. Stuhlmann, K. Wandelt, *In-situ STM investigation of adsorbate structures on Cu (111) in sulfuric acid electrolyte*, Surf. Sci., **1998**, *416*, 121–140.

[29] A.J. Bard, L.R. Faulkner, *Electrochemical Methods: Fundamentals and Applications*, 2nd Editio, Wiley, New York, 2001.

[30] D. Pletcher, R. Greff, R. Peat, L.M. Peter, J. Robinson, *Instrumental Methods in Electrochemistry*, **1985**.

[31] G.M. Whitesides, J.P. Mathias, C.T. Seto, *Molecular Self-Assembly and Nanochemistry : A Chemical Strategy for the Synthesis of Nanostructures*, Science, **1991**, *254*, 1312–1319.

[32] S. Zhang, *Molecular Self-Assembly*, Elsevier Science, **2001**.

[33] L. Jean-Marie, *Supramolecular Chemistry*, Science, **1993**, *260*, 1762–1763.

[34] C. Vericat, M.E. Vela, G. Benitez, P. Carro, R.C. Salvarezza, *Self-assembled monolayers of thiols and dithiols on gold: New challenges for a well-known system*, Chem. Soc. Rev., **2010**, *39*, 1805–1834.

[35] C.G. Zoski, *Handbook of Electrochemistry*, Elsevier, **2007**.

Chapter 3

3 Experimental

The experimental setups and the techniques used in this work are herein presented, detailing with a special attention the sequences of passages required for obtaining reproducible experiments and the theory and operational conditions of the employed instrumentations. First of all, cyclic voltammetry (CV) will be described as integrated part of the EC-STM technique because it provides information that mainly have a supporting character. In fact, from a mere experimental point of view, CV affords experimental features, on which EC-STM is also primarily based. Paramount relevance for EC-STM is possessed by the STM unit, since the results of an EC-STM measurement session actually are STM images at a defined electrochemical potential. Therefore, EC-STM can roughly be thought as an investigation technique that combines the imaging capability at the microscopic scale of STM to the macroscopic electrochemical knowledge provided by CV.

3.1 Cyclic Voltammetry "Ex-Situ" experimental setup

The cyclic voltammetry experiments were carried out both in a standard five necked glass reactor or in a special designed cell suitable also for EC-STM experiments. The required experimental setup is called "three-electrodes setup", because three electrodes are mounted. In a CV experiment, a potential difference is generated by mean of a potentiostat between a Working Electrode (WE) and the Reference Electrode (RE), that allows to trigger an electrochemical effect or process that is evidenced by the flowing of a current between the WE and the Counter Electrode (CE). The RE provides a constant potential, which in fact is used as a reference, for determining and/or intentionally varying (i.e.: polarising) the WE potential.

In the present work, a reversible hydrogen electrode (RHE) was employed and consists of a black Platinum (black-Pt) mesh supported inside a glass capillary. The capillary is sealed from one side where only a small portion of Pt wire protrudes for assuring the electric contact, whereas the other side is open, and the dangling black-Pt mesh is half-immersed in the electrolyte solution in equilibrium with an electrogenerated H_2 bubble. The RHE system involves the overall equilibrium reaction: $2H^+ + 2e^- \rightleftarrows H_2$.

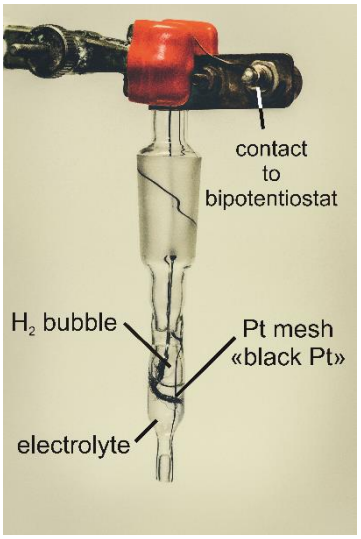

Figure 3.1: image of the RHE electrode used for EC-STM and cyclic voltammetry.

In the RHE, H_2 is not supplied but it is generated directly *in-situ*. For this purpose, the black-Pt mesh must be rinsed with MilliQ water and sonicated for 15 minutes, repeating the procedure for 5 times, then the capillary is filled with an Ar-purged 0.1 M $HClO_4$ solution, which is the same electrolyte used for STM measurements, as well as for CV. H_2 is generated in a two-electrodes circuit where RHE is polarized at negative potential, while a common Pt electrode acts as anode. Before electrolysis, the Pt wire is sonicated many times for 15 min inside a test tube filled with MilliQ and immersed for at least 10 hours in Piranha solution, repeating the procedure 2 times. The two extensively cleaned electrodes are connected to a power supply: RHE and the Pt-wire as the negative and the positive pole, respectively. Being negatively polarised, the aqueous solution contacting the black Pt mesh undergoes electrolysis, which affords the reduction of hydrogen ions to molecular hydrogen (hydrogen evolution reaction, HER). On the anode side, the aqueous solution contacting the Pt electrode undergoes oxidation, where of H_2O is oxidized to molecular oxygen (oxygen evolution reaction, OER). The optimal density current found for allowing HER to occur at the Pt-mesh surface was $j = 10\ mA\ cm^{-2}$. At this value a sufficiently large H_2 bubble can form in few minutes (< 10 min). The corresponding potential that allowed to maintain such a current was found to oscillate around 15 V. According to this procedure and because the system is in equilibrium with the external environmental pressure, the H_2 bubble pressure is close to 1 atm. The so generated $H_2|H_3O^+$ interface will afford a constant potential value as long as the H_2 reservoir remains disposable during electrochemical measurements. Once the potentiostat is switched off, the RHE is taken out from the beaker and quickly immersed in 0.1 M $HClO_4$ filled glass container end capped with a glass septum, which avoids any contaminants to be exchange with the main cell compartment. The glass container is in turn inserted in a glass holder with two capillary tubes at the bottom. These two capillary tubes allow the electrolyte to flow inside and outside, by keeping continuously immersed the RHE within the electrolyte and connected with the electrochemical system.

It is worth noting that an activation procedure was required because previous trials directly with 0.1 M $HClO_4$ did not enable the HER to occur at the RHE electrode. The procedure that helps to clean and activate the black-Pt mesh consists in a pre-electrolysis in sulfuric acid, briefly: the RHE capillary tip was rinsed with MilliQ water and then filled with 0.5 M H_2SO_4 electrolyte, after which it was immersed in a beaker containing the very same

electrolyte. As counter electrode, a Pt electrode was used, whereas an already calibrated RHE was used as reference electrode. A series of cyclic voltammetries were run limiting the scan range to [0; 1.2] V at 50 mV/s in order to avoid either extensive HER or OER, until ten equal consecutive scans were obtained. This procedure helps to clean and activate the black-Pt mesh. After that, the electrode was rinsed many times with MilliQ water and filled with 0.1 M $HClO_4$ solution to generate a H_2 bubble, as previously described. A saturated calomel electrode (SCE) was inserted in the same beaker containing the just prepared RHE, and the potential variations were evaluated in three days, even if after few hours it completely stabilised at a value of $E_{RHE/SCE}$= 0.260 V. The same measurement was repeated approximately after 1 month, but potential shifts were in all cases lower than 5 mV. This shift can be attributed to small differences in terms of electrodes positioning, ohmic drop, electrical connections and temperature.

The glass electrochemical cell is cleaned with Piranha solution (see section 3.2.4) to ensure complete elimination of organic contaminations. After that, it was thoroughly rinsed and sonicated with MilliQ water. This procedure was repeated before each experiment. Once rinsed, a 0.1 M $HClO_4$ solution is added as supporting electrolyte. The RHE reference electrode and the Pt counter-electrode, are inserted in two adjacent necks, while the central neck hosts the working electrode. The solution is deaerated by bubbling gaseous Ar or bubbled with O_2 gas when ORR is under investigation.

The Au working electrode is prepared by a thermal annealing treatment, as described in section 3.2.3. It is then subjected to the functionalisation with macrocyclic molecules, as described in section 3.2.7. Finally, it is mounted in a homemade PEEK holder, which easily fits the electrochemical cell and brings the working electrode at the same level of both the CE and the RHE tips. In this way, an optimal triangular arrangement is attained and the distances among electrodes are minimised. This is essential for reducing the magnitude of uncompensated resistance, which always afford a certain contribution to the whole cell overpotential. The uncompensated resistance is an ohmic drop caused by physical separation through an electrolyte among electrodes, specifically between WE and RE, and its main effect is a shift in the applied WE potential:

$$V_u = iR_u. \qquad (3.1)$$

Modern potentiostats, like the Metrohm Autolab PGStAT204 in use, feature positive feedback circuits, which allow to electronically compensate the ohmic drop. To accomplish this, an impedance spectrum is registered and the value of ohmic drop is determined from the resulting curve as the point where it changes shape or slope. The value is then multiplied by 0.8, and the resulting number is inserted as the ohmic drop compensation resistance. The ohmic drop is compensated by the safe limit of 80% to avoid any possible overcompensation effects that would result in instrumental noise and signal oscillations. In fact, if a positive oscillation sums to an already full compensated resistance, then undesirable reactions can harmfully lead to a damage of the working electrode surface. Moreover, impedance determination of ohmic drop is conducted at the open circuit potential, at which no Faradaic processes occur at the WE surface, but CV are collected for a certain potential window. Ohmic drop can therefore change accordingly to a change in WE applied potential, confirming that full compensation must be avoided.

3.2 EC-STM

The electrochemical scanning tunnelling microscope used to accomplish this work can defined as "Beetle-type" and the experimental setup was developed by the K. Wandelt group [1]. The term "beetle" refers to the tip-positioning and -approaching unit, as previously described in chapter 2. Investigating by means of EC-STM a sample means that a metallic tip scans the surface of a solid sample to obtain topographic profiles of it. In the meantime, the sample plays as working electrode in a "four-electrodes setup". Therefore, EC-STM provides a combination of information, i.e. the topographic mapping of the sample associated to the electrochemical response of the involved system. Surface scanning is in fact performed at the solid/liquid interface, where the liquid is an electrolytic solution of 0.1 M $HClO_4$. The sample is fitted in the centre of small cell, hereafter presented. The sample acts as WE and for this reason needs to be an electrical conductor. This property must be fulfilled also for the tunnelling event to occur, as already discussed in sections 2.1.1 and 2.1.2. As counter electrode, a Pt wire is chosen. Pt is a convenient choice because it is expected to not affect the good operation of the electroanalytical system [2]. It is in fact commonly regarded as an inert material towards many reactions, like oxidation. On the other hand, Pt is a sensitive material towards chemisorption of sulphur and nitrogen compounds, as well as CO. These contamination sources can be however excluded on the basis of reactants and compounds used in this work. As reference electrode, the instrumentation offers two possibilities, both with advantages and disadvantages to be evaluated in order to attain the best compromise for the examined system. The two choices concern a Pt wire as "pseudo-reference" electrode or an external RHE. It is worth noting that an external SCE ($KCl/Hg_2Cl_2/Cl^-$) or SSE ($K_2SO_4/Hg_2SO_4/SO_4^-$) can be employed as well, but RHE avoids any contaminations of chlorides or sulphate ions. A more detailed description of the pseudo-reference electrode is provided hereafter, while an extensive treatment of RHE has already been provided in section 2.2.3. Both typologies were explored, and the external RHE has been chosen as preferential reference electrode. A "three-electrodes setup" have been attained and it can actually be exploited to measure cyclic voltammetries. In this case, they are termed as "in situ cyclic voltammetries", because they are registered with the same experimental configuration used for EC-STM investigation, which presents some differences compared to a standard three-electrodes setup, previously described in section 3.1.

The fourth electrode is the tunnelling tip (tip electrode, TE), whose preparation is illustrated in section 3.2.2, while its operation principles have already been shown in section 2.1.3.2. The use of a bipotentiostat allows to control the potential difference between WE and CE (on the basis of the RE) and in the meantime the potential difference between WE and TE (or RE). A depiction of the Four-Electrodes setup is furnished in figure 3.2.

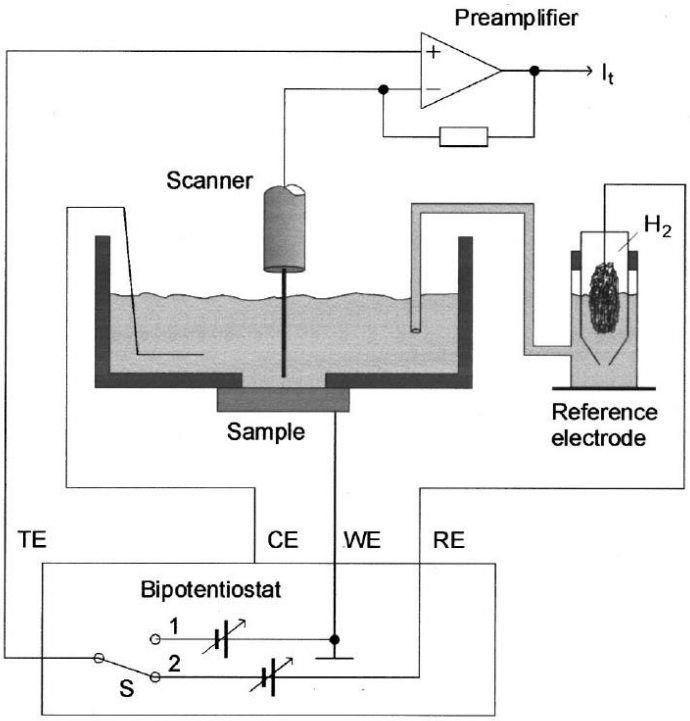

Figure 3.2: Schematisation of the four-electrodes setup [1]. The switch S in position 1 enables an internal bias control between TE and WE, whereas in position 2 enables an external bias control between TE and RE.

It must be remarked that, being the tip a polarised electrode with respect to the WE (or the RE), on its surface some Faradaic processes can occur if the polarisation of the WE is changed. The appearance of a Faradaic current is detrimental for EC-STM because its magnitude can overcome that of tunnelling current. Common value for tunnelling currents are in fact around 1 nA and in several cases also lower, therefore Faradaic currents of 1 μA, for example, will completely superimpose to the much smaller tunnelling current, making the STM imaging impossible to accomplish.

According to figure 3.2, if the switch *S* is in position 1, the bipotentiostat applies a constant potential difference between TE and WE (namely, a voltage *bias*). In this case, the EC-STM conveniently records *potentiostatic images* [1], since the WE potential is maintained constant during tip scanning and also among following images. This constant value can be manually selected by means of a knob (see figure 3.6). *Potentiostatic imaging* is useful at the beginning of an EC-STM measurement session, when tunnelling parameters (tunnelling current and *bias)* need to be optimised to achieve satisfactory image resolution. This optimisation essentially deals with two aspects: Faradaic current minimisation and tunnelling resonance conditions, as already illustrated in section 2.1.3.3. The procedure can be more efficiently performed if the WE is polarised at "safe" potentials, at which minimal electrochemical reactions occur on the WE surface. If the switch *S* is in position 2, the EC-STM unit more conveniently records *potentiodynamic images*. Now the TE potential is held constant against the RE, while it varies with respect to the WE. Therefore, once found the best tunnelling parameters in the *potentiostatic mode* that in the meantime minimise unwanted Faradaic current at the TE, the switch is set in position 2 to fix the minimal Faradaic current upon varying the WE potential (versus the RE). It must be pointed out that, in this way, tunnelling resonance may not be preserved [1] as the WE potential is changed from its starting

value. Nonetheless, in most cases that Faradaic current at TE produces a major impact on the final image compared to variations in tunnelling resonance. For this reason, *potentiodynamic imaging* had frequently been performed as previously described by fixing the TE potential versus RE, although each specific system can exhibit a different behaviour.
Figure 3.3 provides an image of the full EC-STM experimental setup.

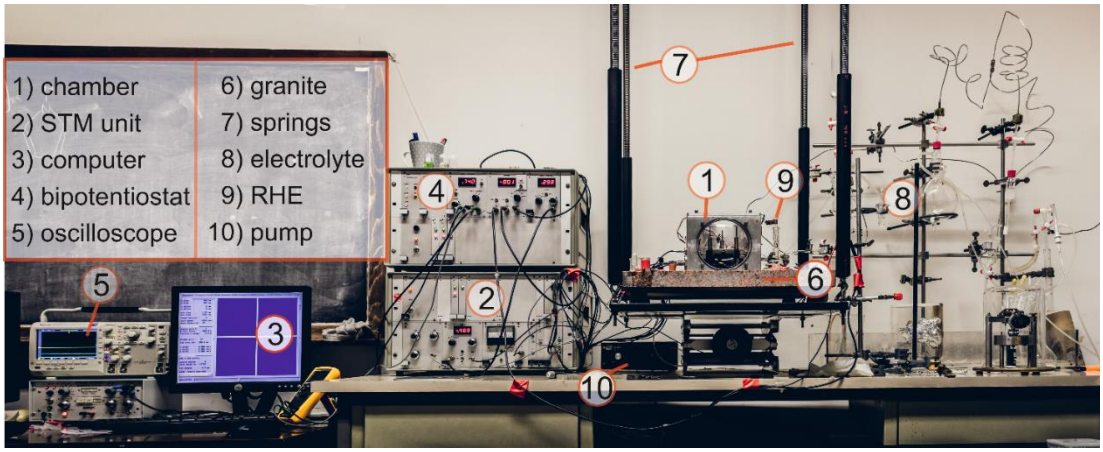

Figure 3.3: Image of the full EC-STM experimental setup.

The key-role is attributed to the aluminium chamber (1). It contains the STM amplifier and scanner, as well as the PEEK cell and the piezo-leg approaching system. The chamber is enclosed with a Plexiglas® slab on the front, to provide a direct visualisation of the inner components, and with an aluminium slab on the top. Both slabs can be tightened with screws to the chamber, exerting enough pressure on Viton® O-ring to guarantee a satisfactory sealing level. The chamber can be in fact filled with desired gas to condition the electrochemical analysis. In this work argon or oxygen, alternatively, were used. Tunnelling parameters are controlled thanks to the STM unit (2), which is interfaced to a computer (3) through a dedicated software. The bipotentiostat (4) allows to take *in situ* CV curves but it is also connected to the STM unit (2) to control the Four-Electrodes Setup. Another computer is assigned to the *in situ* CV recording. The oscilloscope (5) offers direct visualisation of tunnelling current and topographic profile for a quick adjustment of tunnelling parameters. The chamber (1) is mounted on a heavy granite plate (6). This plate is placed upon a brass stack through four rubber pieces, which damps high frequency (>100 Hz) vibrations. The brass stack, together with the granite plate, is suspended with four steel springs (7) from the ceiling. Electrolyte supply is provided by a glass flask (8) connected with Tygon® tubes to the cell. The RHE (9) is placed between the flask and the cell. A peristaltic pump (10) is connected as outlet to the cell. Ar or O_2 are supplied through suitable glassware connected with Tygon® tubings.

The aluminium chamber acts as Faraday cage to shield the scanner from electromagnetic and acoustic noises, which would inexorably make impossible STM image acquisition. The aluminium cage also provides an electrical connection among, the STM scanner, the cells and its electrodes and the steel springs providing a grounding circuit for dispersing charge accumulations.

A picture of the PEEK cell is provided in figure 3.4, where the Pt wire and the Au(111) single crystal are the CE and WE, respectively.

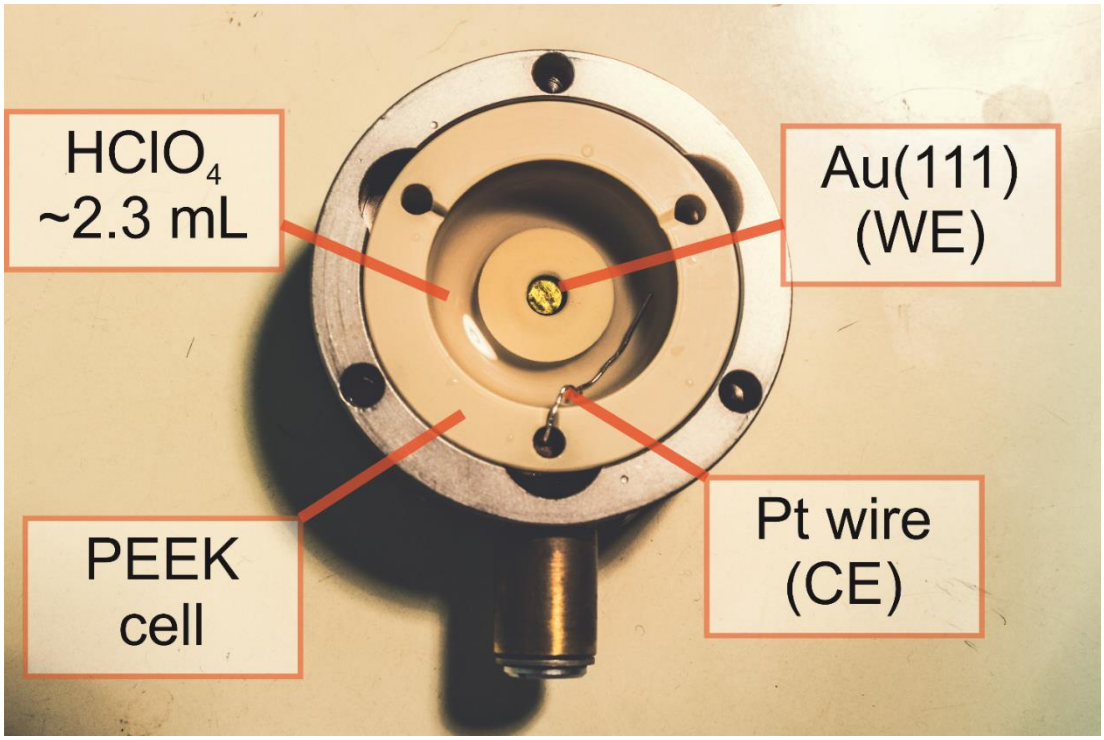

Figure 3.4: Image of Peek® cell with the Pt wire as counter electrode and the Au(111) crystal.

The Au exposed surface corresponds to an area of $Area_{Au_{exposed}} = 0.503\ cm^{-2}$, because the central hole exposes a disk of 0.4 cm diameter. Otherwise, the Au(111) crystal would expose a circular area of 0.8 cm diameter. The electrochemical cell and the electrodes are assembled outside the STM chamber, this procedure assures that all the components are precisely mounted avoiding any possible electrolyte leakage or declivity of the WE. A 0.4 mm diameter Viton® ring is mounted prior to insert the Au sample in a dedicated groove. The cell is then mounted into a dedicated aluminium housing, which embeds the electrical connections and terminates with a Lemo® plug. The housing features three screws to tighten the Au to the Viton® ring, providing sealing against electrolyte.

The piezo-legs system is shown in figure 3.5.

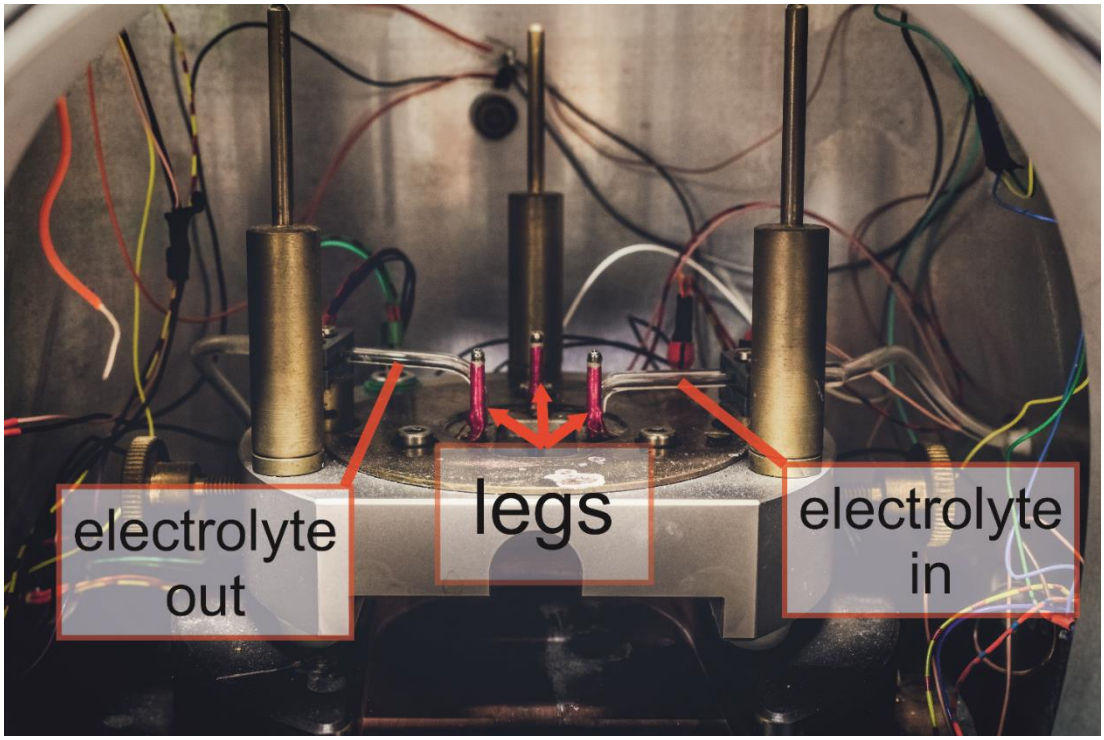

Figure 3.5: Piezo-legs system, on which the scanner undergoes a stick-and-slip mechanism.

Each leg consists of a piezoelectric tube with four electrodes. Upon applying proper polarisation among two or more electrodes of each leg and combining specific polarisation sequences at each leg, the piezo-leg system is then able to perform coarse approaching/retreating as well as lateral positioning along the four cardinal directions. By unscrewing a head screw, the STM scanner is released by a safety lock system and is free to lean on the three steel spheres that constitute the upper part of the three piezo-legs. The spheres rigidly transfer the leg oscillations to the scanner, allowing its rotation and therefore its approaching/retreating. The spheres must be properly isolated by the piezo-legs, otherwise undesired current would flow through the STM tip.

A coarse approaching is automatically accomplished and consists in a fast tip-sample distance reduction up to an initial tunnelling current set-point value. When the set-point tunnelling current is reached, a step-by-step manual approaching must be performed to achieve a stronger and more stable tunnelling signal.

The STM unit features two knobs to control the tunnelling current and voltage bias, respectively. Tunnelling current is held constant since the chosen mode of operation is the "constant current mode", whose details had already been introduced in section 2.1.3. The knob allows to manually set a constant I_t value in the range [0; 50] nA. Another knob allows to vary the voltage bias in terms of potential difference between TE and WE. This is also named "internal bias", as indicated by the switch in position "int." in figure 3.6, which realises the same condition of the switch in position 1 of figure 3.2.

The tunnelling tip is also part of the four-electrodes setup and the STM unit must be therefore interfaced with a bipotentiostat. The bipotentiostat permits to polarise the WE respect to the RE by closing the circuit with the counter electrode, but it is also able to polarise the TE versus the WE (internal bias) or to the RE. This last case is also termed as "external bias", since the switch in figure 3.6 can be exchanged to "ext." and it correspond to the switch in position 2, in accordance with figure 3.2.

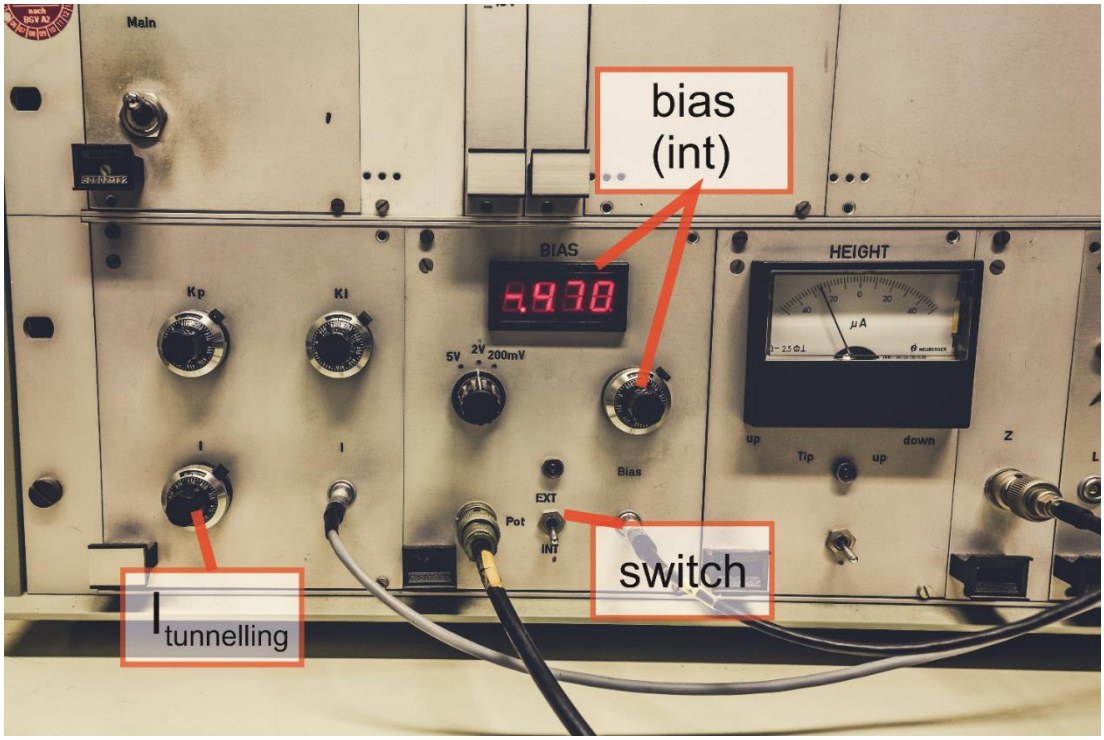

Figure 3.6: STM unit with indicated knobs for tunnelling current, internal bias control, as well as the switch for internal/external bias control.

Since the TE potential now relies on the RE, a different knob is required to vary the TE potential with respect to RE. This knob is indicated in figure 3.7 as “ext. bias control”, which offers an image of the bipotentiostat unit.

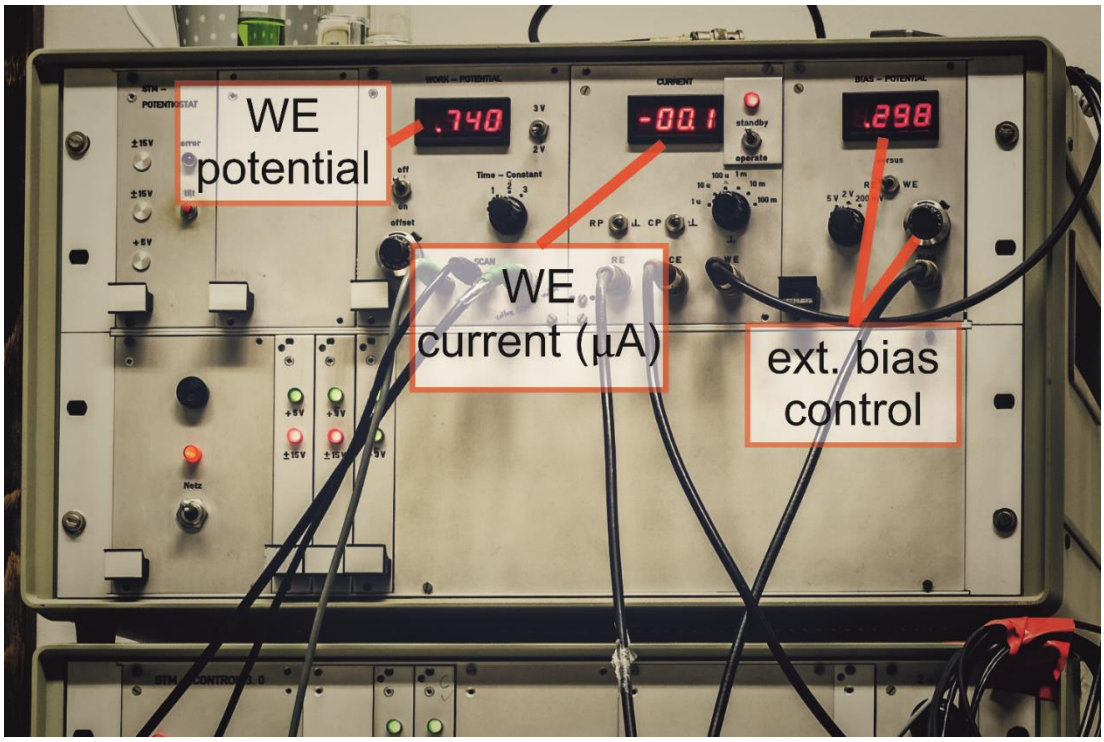

Figure 3.7: Picture of bipotentiostat for STM, with indicated knob for external bias control, as well as the displays for WE potential and WE current.

The bipotentiostat needs a voltage generator, featured in figure 3.3, which applies a voltage to the WE through the bipotentiostat. It is also able to generate saw-tooth voltage waves, from predefined upper and lower vertex potentials, allowing the recording of the so called *in situ* CVs with high sensitivity. However, this homemade instrumentation does not offer the possibility to compensate the *iR* ohmic resistance caused by the finite ionic conductivity of electrolyte and by the cell- and electrodes geometry.

As previously reported, a Pt wire can be used as pseudo-reference electrode (or quasi-reference electrode). This means that a Pt wire of the same dimensions and thickness of the CE Pt wire was fitted in a dedicated slot of the PEEK cell. In this way, the cleanness of the electrochemical environment can be more easily preserved and the *iR* ohmic drop can reach negligible values, generally $iR_{pseudo} < 5\ \Omega$, since the electrolyte volume is small (around 2.3 mL) and the electrode are in close proximity. Despite the low ohmic drop, the use of Pt as pseudo-reference electrode can in principle cause potential shifts up to 100 mV, especially when freshly saturated electrolyte is exchanged in the cell. For this reason, the most part of STM measurements were recorded using the RHE as reference electrode. Due to an excessively small cell volume, the RHE cannot be fitted directly in the cell, but needs to be mounted externally, and for this reason it is also called external reference electrode. The major disadvantage of external reference electrodes for EC-STM comes from the distance of the RE with respect to WE. Long tubes are required to establish an electrolytic connection between the RHE and the cell, thus increasing the ohmic drop up to 100 Ω. Another issue concerns the cleanness of additional glassware (the electrode itself and the glass holder terminating with a glass frit) and additional tubings. Nonetheless, satisfactory level of cleanness had been reached by Piranha etching for few hours the glassware, and by simple rinsing the Tygon tubings with at least 2 L MilliQ water. These drawbacks are balanced by noteworthy advantages. The RHE is in fact a reference electrode with a fixed and stable reference potential. It also avoids the Au(111) contamination from anions like Cl^- or SO_4^{2-}, whose presence is brought by many standard reference electrodes like Ag/AgCl, Cl^- $Hg/Hg_2Cl_2/Cl^-$, $Hg/Hg_2SO_4/SO_4^{2-}$ etc. These anions are indeed highly prone to specifically adsorb on Au(111) surface [3], thus interfering with desired Fe(II)Pc (or Fe(III)Pc-Cl or Fe(III)TMPP-Cl) adsorption.

The oscilloscope is a useful tool during a STM measurement session, because it gives the chance to instantly visualise a current signal and the topographic profile of the sample. The displayed current signal is comprehensive of the tunnelling current together with Faradaic current flowing through the tunnelling tip. The other displayed signal belongs to the topographic profile, i.e. the correction of the tip nominal height to maintain a constant current. An example of the two displayed signals is given in figure 3.8.

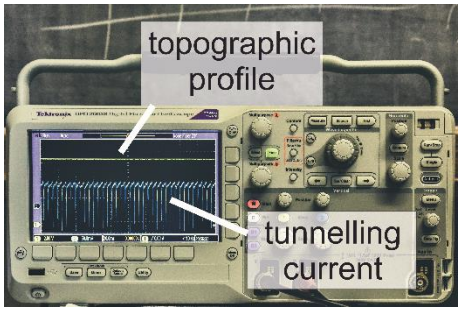

Figure 3.8: Picture of the oscilloscope with indicated signals for tunnelling current and topographic profile**.**

Their visualisation is particularly helpful when a new tip is mounted onto the scanner and in the early stages of image acquisition, when the instrumentation suffers of thermal and mechanical drift. The issue of instrumental drift will be later described in section 6.1. Through the use of the software dedicated to the STM control, shown in figure 3.2, the scanning direction is perpendicularly aligned with respect to the direction of maximum inclination of the sample. The aim is to reach a topographic profile as flat as possible on the oscilloscope, in order to get the maximum sensitivity and the least stroke for the tip scanning over the surface.

The heavy granite plate (7), together with the four rubber pieces and the four steel springs (8) are meant to damp high- and low-frequency vibrations, which would be detrimental to STM image recording. The granite plate serves as stable stand platform for the STM chamber and it rests on four rubber pieces attached to a steel square structure. Four steel springs (2.5 mm wire diameter) are connected to its edges. When acquiring STM images, the plate is suspended on the four springs, thus efficiently decoupling the STM chamber from external low-frequency vibrations (< 1 Hz) [1]. Isolation from >100 Hz frequency vibrations comes from a brass stack (three plates) separated by rubber pieces. The STM base carrying the cell is positioned on the brass stack through three rubber pieces.

A two-neck terminating flask is used as electrolyte reservoir. One neck is used for a gas dispersion tube, while the other neck is used for filling the flask with new electrolyte. This flask must be mounted at a higher position with respect to the RHE and the cell taking advantage from communicating vessels principle, so that when the valve of the flask is opened, the electrolyte flows to the cell, also filling the RHE glass container. A valve placed before the RHE allows to quickly stop the electrolyte flux and reduces bubbles formation. The peristaltic pump prevents overflow of electrolyte from the cell and allows to exchange the cell electrolyte with newly saturated one. Electrolyte entry and exit is performed with glass capillary tubes, which are visible in figure 5. The entry tube is maintained at a lower height with respect to the exit tube, since it must also provide continuous electrolytic connection with the external RHE. Therefore, the exit tube must lie at higher position to avoid excessive suction of electrolyte, that would result in the disconnection with RHE.

The gas dispersion tube is connected to a T-shaped valve, whose two remaining capillary glass tubes are connected to the O_2 and Ar cylinders. The electrolyte (0.1 M $HClO_4$) is bubbled (with Ar or with O_2) for at least 30 min. A second T-shaped valve enables to switch the Ar and O_2 lines for saturating the STM chamber. The two T-shaped valves are indicated in figure 3.2. Connections among glassware are made with Tygon® tubes, which are highly chemical resistant and are cleaned by filling the flask with MilliQ that is then allowed to flow inside the tubes up to a Teflon® cell (in lieu of the PEEK® cell). A continuous flow of 3 L of MilliQ water assures the proper tube cleaning.

3.2.1 STM “head”

The STM “head” is the most important part of the STM unit. It features the piezoelectric system for the tip approaching and scanning, as well as the Besocke ramp for coarse approaching/retracting [4]. It also serves as support for the electronic connections needed to properly interface the STM unit to the software. In particular, it contains a pre-amplifying element, needed to amplify the tunnelling current signal, which otherwise would be too small to be accurately determined. Analog-to-digital and digital-to-analog converters are widely exploited to provide full communication between the analogic STM unit and the digital standard PC. Nonetheless, the use of an analogic-based instrumentation simplifies and

enhances the STM images acquisition, since it increases frequency sampling rate and it reduces noise [1]**.** Moreover, tunnelling parameters can be directly varied during scanning, as aforementioned (section 3.2). An image of the STM head is provided in figure 3.9.

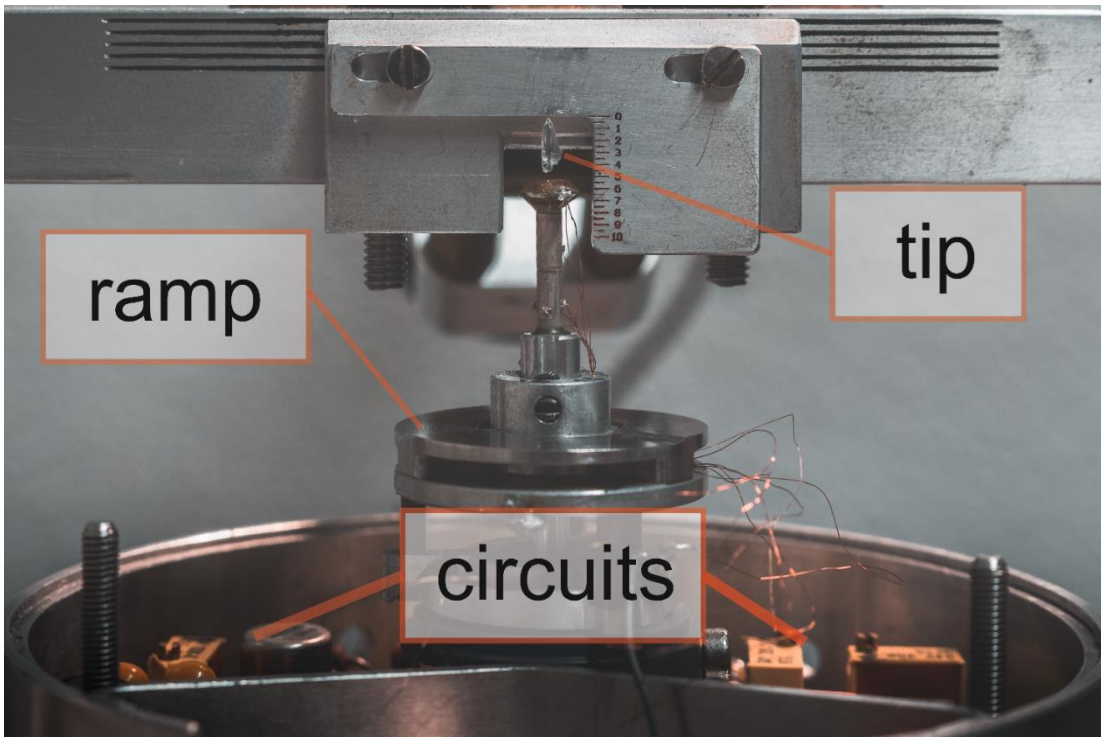

Figure 3.9: Image of STM scanner. The head is mounted upside down, with the ramp lying on the Piezolegs, allowing the coarse approaching for the tip.

3.2.2 Tunnelling Tip

Platinum/Iridium alloy (90:10) or tungsten are common materials for tunnelling tips. Pt/Ir are stable in a wide range of applied potentials and this enhanced stability would require longer and harsher etching procedures, while tungsten can be better handled but suffers of more instability [5,6]. Pt/Ir are also more difficult to prepare due to lower hardness and tend to deform mechanically. On the other hand, tungsten exhibits better mechanical properties and an easier preparation procedure. For this reason, only tungsten tips were employed for all EC-STM measurements reported in this work. Tunnelling tips can be prepared in different ways, ranging from mechanical procedures to electrochemical etching, as well as CVD or field ion microscopy onto pre-existing tips to improve the apex [7]. “Possibly there are as many tip-preparation procedures as there are people making tips” [8]. In this work, tip preparation is accomplished through an etching method. An electrochemical circuit is built with a platinum wire (0.5 mm thickness), a tungsten wire (0.25 mm thickness) and a 2M KOH solution as electrolyte.

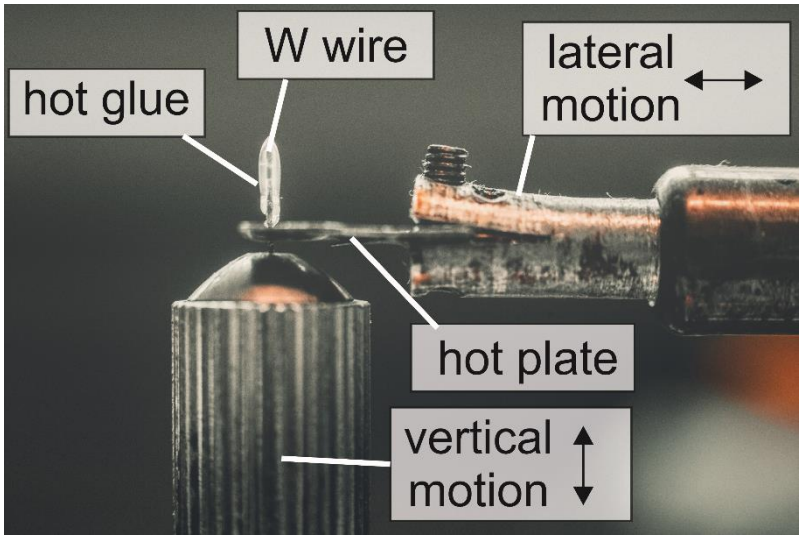

Figure 3.10: Picture of the tip coating station. Solid glue is placed on the hot-plate, where it melts. The tip is moved upwards through a slit, and the plate is withdrawn to remove the excess glue.

The Pt wire has a loop shape (6.5 mm inner diameter) and the tungsten wire is placed in its centre, using a calliper to reach ≈ 7 mm of tungsten wire length below the Pt ring. This will represent the final length of the tip. Positioning of the tungsten wire is carried out with clean tweezers. MilliQ water is used to rinse the Pt ring and the W wire after the positioning. The 2M KOH solution is poured in a small beaker and the W wire as well as the Pt ring are introduced in the KOH solution. A drop of KOH is retained by the ring in the form of a lamella. Bubbles instantly develop where the lamella embraces the W wire, since a square potential wave is applied between W and Pt. An AC voltage of 11.5 V (spike-spike) with a 100 Hz is initially applied for 2 minutes, going to 5.5 V for 30 seconds and then to 4 V up to falling of the tip. The tip drops off in a hole of a Teflon base and it is handled with clean tweezers; after rinsing it with MilliQ water it is placed in a dedicated box. This method is also regarded as "drop-off technique".

The aforementioned procedure accounts for an etching phenomenon induced by appropriate polarisation of the Pt/W circuit. Tungsten plays as anode because it is positively polarised, and it undergoes an oxidation reaction from metallic W to water-soluble tungstate anion WO_4^{2-}, thus reducing the thickness of the initial W wire. Platinum is chemically inert in this environment and acts only as an electron donor for the cathodic reaction, since it is subjected to negative polarisation. Anodic and cathodic reactions are widely recognised as [9], [10], [8]:

$$\begin{aligned} &Anode: \ W_{(s)} + 8OH^-_{(aq)} \rightarrow WO^{2-}_{4(aq)} + 4H_2O + 6e^- \\ &Cathode: \ 6H_2O + 6e^- \rightarrow \ 3H_{2(g)} + 6OH^-_{(aq)} \\ \hline &W_{(s)} + 2OH^-_{(aq)} + 2H_2O \rightarrow WO^{2-}_{4(aq)} + 3H_{2(g)} \end{aligned}$$

Having described the chemical aspects beyond tip etching allows to more deeply understand the *drop-off* phenomenon. When the W wire is inserted into the KOH drop, a meniscus is formed as consequence of capillary forces. A OH^- concentration gradient is established between the wire and the ring, due to OH^- depletion at the anode (W wire). Moreover, WO_4^{2-} possesses higher molar mass than the aqueous electrolyte, thus forming a denser layer that slowly moves alongside the W wire and diminishing, together with the OH^- depletion, the W

etching speed [7]. As a result, the upper part of the wire is subjected to a faster etching rate. A necking phenomenon occurs due to this anisotropic etching rate and the W wire *drops off* when its tensile strength cannot sustain its own weight anymore [7].

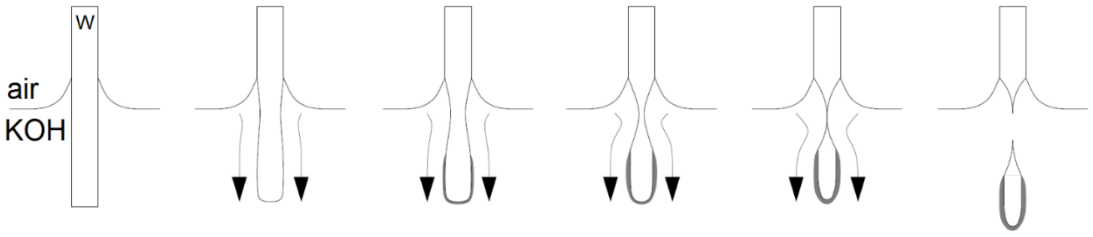

Figure 3.11: mechanism of tip etching [7].

After drying, which takes around 30 minutes, the tips can be coated with hot glue. UHU hot melt glue is cut in 3-4 mm pieces and they are put in a beaker with MilliQ water to remove dust particles in a sonication bath. Glue pieces must be dried with dust-free paper tissues before placing 1-3 pieces on a homemade hot-plate 0.7 mm slit derived by a soldering station. The plate is heated up to 160°C and 1-3 pieces of glue are melted on the plate. The tip is aligned with the slit and by rotating an endless micrometric screw, on which the tip is mounted, it passes through the hot glue, which attaches on it forming a solid polymeric coating. The very end tip remains uncovered by the glue due to its high curvature radius. Coated tips need to be left dry overnight to allow proper glue solidification. A picture of the tip coating station is shown in figure 3.10.

The glue-coated tip can now be mounted onto the STM scanner, which consists of a piezo-tube with a 4+1 electrodes design, as already presented in section 2.1.3.1. The non-coated lower part of the tip is squeezed with a needle-nose pliers for flattening the wire, so that the tip remains more firmly stacked inside the canula holder of the piezo-tube.

3.2.3 Au(111) sample preparation

In this work, an Au(111) single crystal (MaTeck) was used as substrate for FeN_4 molecules characterisation. In the case of EC-STM, the PEEK cell exposes only a central circular area with a 4 mm diameter, while for Ex-Situ Cyclic Voltammetry a home-built PEEK holder allowed to expose the full polished 8 mm diameter surface.

The crystal undergoes a flame annealing process before each functionalisation, i.e. before each experiment, both in the case of EC-STM and *ex-situ* CV. For this purpose, the Au is positioned on a Ceran® plate, which provides a heat-resistant flat surface. A butane gas flame is directed over the top surface of the crystal, which after 1/2 minutes gains a faint red glowing colour, since the flame reaches a temperature of 600-700°C. The thermal treatment is accomplished under continuous Argon flux realised with a narrow-neck glass funnel placed 3-4 cm above the Au surface. The crystal is first brought to red-glowing colour for 4 minutes, then it is cooled down to room temperature for 10 minutes keeping it under Ar atmosphere (the funnel is moved closer to the sample). Flame annealing is repeated for 3 minutes, as well as cooling down. Finally, the Au is heated to reach the red-glowing state and then it is cooled down for 15 minutes, after which it is ready to be functionalised by dipping it in the desired FeN_4 solution (see section 3.2.7 hanging meniscus). This procedure guarantees that the gold surface is clean and flat during the deposition and the following experiment. The reducing environment, provided by the Ar flux together with the butane flame, prevents the surface to be oxidised and indeed removes the passivating surface layer formed by oxide but also by any

other organic contaminants. Furthermore, the high temperatures (600-700°) lower the value for surface diffusion, so that wider atomic terraces with less defects are obtained [11,12].

A picture showing the flame annealing procedure is reported in figure 12.

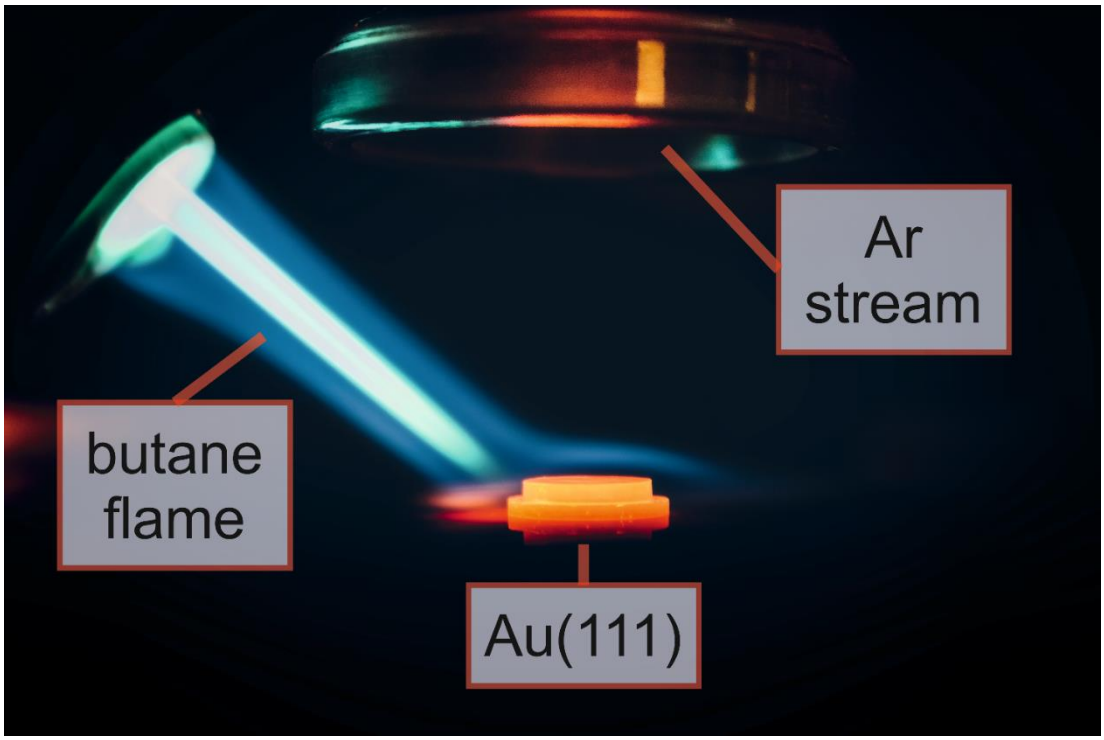

Figure 3.12: Flame-annealing procedure. A continuous Ar stream is maintained during flame-annealing. The glass tube is placed closer to Au when cooling down.

3.2.4 Glassware cleaning

Thorough care must be paid for an EC-STM experiment, as already anticipated. Every source of contamination must be minimised or possibly eliminated. Inorganic contaminants can be easily eliminated by copious rinsing and ultrasonic baths, but organic carbon might still represent an issue. Extensive organic carbon removal can be accomplished by exposing the glassware to Piranha solution. Piranha etching must be performed by slowly and carefully adding hydrogen peroxide to concentrated Sulphuric Acid (>95%) [13]. The reaction is exothermic and leads to *in situ* production of peroxymonosulphuric acid, also known as Caro's acid. Its Lewis structure is shown in figure 3.13.

$$H_2SO_4 + H_2O_2 \leftrightarrows HSO_3OOH + H_2O \qquad (3.2)$$

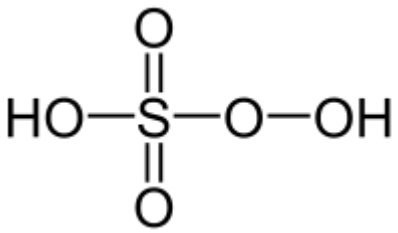

Figure 3.13: Lewis structure of Caro's acid, namely Peroxymonosulphuric acid.

Caro's acid had also been obtained by reaction of chlorosulfonic acid and 90% hydrogen peroxide [14]. However, the employment of high-test water peroxide requires thorough care and the mixing should be conducted at temperatures < 0°C, therefore this procedure was neglected. Although low-concentrated peroxymonosulphuric acid is known [15] to selectively oxidise some functional groups or to promote regioselective oxidative rearrangements, it is herein used as high-concentrated non-selective strong oxidising agent towards generic organic carbon. Despite the lack of extensive information about Caro's acid, its melting temperature was reported to be +45°C [16]. A qualitative verification can arise by direct observation of glassware filled with Piranha solution, since after few hours the solution turned opaque (especially if stirred, as the solid acid was probably precipitated).

3.2.5 Preparation of electrolyte

0.1 M $HClO_4$ was prepared using clean flasks (as described, sonication baths and Piranha solution). 67-72% Perchloric Acid (Fluka™ TraceSELECT™ Ultra, Honeywell) was properly diluted in MilliQ water (Specific Resistance > 18.2 MΩ cm, Total Organic Carbon < 5 ppb). This ensures the highest quality level for the final electrolytic solution and therefore the best conditions for running EC-STM experiments. Indeed, FeN_4 molecules possess dimensions at the nanometric scale and any other foreign molecule would interfere with the FeN_4 adsorption or would also adsorb on them, thus masking the functionalised Au surface from being scanned with the tip.

3.2.6 FeN_4 solutions preparation

Solutions of metal-phthalocyanines and -porphyrins were prepared using N,N-Dimethylformamide (DMF) to achieve a proper level of dissolution. Concentration plays a role in the achievement of a properly functionalised surface and it is strictly correlated with immersion time during functionalisation. Although the use of saturated solutions for similar purposes had already been reported [17], their use was avoided due to formation of precipitation that could negatively act on the adsorption of single molecules. According to limits of solubility of various metal-phthalocyanines [18], DMF is one of the best solvent for dissolving Fe(II)-Phthalocyanine. Furthermore, DMF possesses a reasonably low vapour pressure (293 Pa at 20°C [19]) and therefore it can be degassed with Ar without any significant loss.

Nonetheless, Fe(II)-Phthalocyanine was found to have the worst solubility if compared to Fe(III)-Phthalocyanine chloride and Fe(III)-tetrakismethoxyphenyl Porphyrin chloride. The difference in solubility can be explained in terms of the dipole moment characterising the molecule. It is in fact lower than the parent Fe(III)-Phthalocyanine chloride and the aprotic polar DMF is less effective in solubilising Fe(II)Pc.

The three molecules were subjected to UV-Vis spectrophotometry to monitor the evolution of the UV-Vis spectrum upon aging of the solutions (see Appendix). The main evidence is a decrease in absorbance for Fe(II)Pc bands, which can be attributed to precipitation, since large deposit was visible on the bottom of the flask. A change in colour was also noticeable in particular for Fe(III)Pc and FeTMPP, which are the other two molecules that together with Fe(II)-Phthalocyanine represent the FeN_4 macromolecules examined in the present work.

3.2.7 Au(111) functionalisation

The Au(111) surface was functionalised by hanging meniscus technique. This means that the sample surface is put in contact with the solution containing the FeN_4 macromolecules and then it is slightly withdrawn from the liquid level. However, due to capillary forces, the liquid remains in contact with the sample and a meniscus is formed. The choice of this method offers valuable advantages, such as the easy handling of the sample. It can be handled directly with clean tweezers, and indeed it allows better controlling of the immersion and retraction passages. Moreover, no particular holders are needed to fit the crystal, thus speeding up the insertion in the PEEK cell directly after functionalisation. The cleanness of the Au surface is maximised, since only the surface itself comes in contact with the FeN_4 solution.

The Au(111) sample is immersed (hanging meniscus) for 1 minute in the 0.1 mM FeN_4 solution and then quickly immersed (hanging meniscus) in a beaker containing MilliQ water to rinse the surface from DMF residues. The sample is then directly transferred into the PEEK® cell in order to avoid air exposure of the surface. Moreover, the water drop left on the surface helps better and full contact with the electrolyte when it is introduced in the cell with the glass capillary. The PEEK® cell is in fact characterised by a finite size border that encloses the crystal and, owing to the small diameter (4 mm) of the circular aperture and to the hydrophobicity of PEEK® as well as of the FeN_4-functionalised surface, a bubble of air tends to form and stick to the Au surface, thus preventing proper contact with the electrolyte. With a clean Pasteur pipette, a drop of 0.1 M $HClO_4$ is placed onto the Au surface after it had been mounted in the cell. The presence of the water drop facilitates the 0.1 M $HClO_4$ drop adhesion itself. From now on electrolyte (at least 15 mL) can allowed to flow in the cell through the glass capillary tube, to ensure complete removal of DMF and water traces.

As previously stated, concentration of FeN_4 solution and immersion time are key-factors for obtaining a good quality self-assembled monolayer (SAM). The optimisation of these two parameters lead to 1 minute and 0.1 mM as best immersion time and concentration, respectively, that guarantee the coverage of the entire Au surface, possibly without double- or multi-layer formation (i.e.: a molecule adsorbs on an already adsorbed one). Anyway, immersion time and concentration are just the macroscopic expression of a microscopic equilibrium among various interactions (electrostatic, hydrogen bonding, Van der Waals, hydrophobic, π-π), as already described in section 2.2.2.5.

3.2.8 Complete procedure for an EC-STM experiment

The complete procedure for an EC-STM experiment is outlined in figure 3.14.

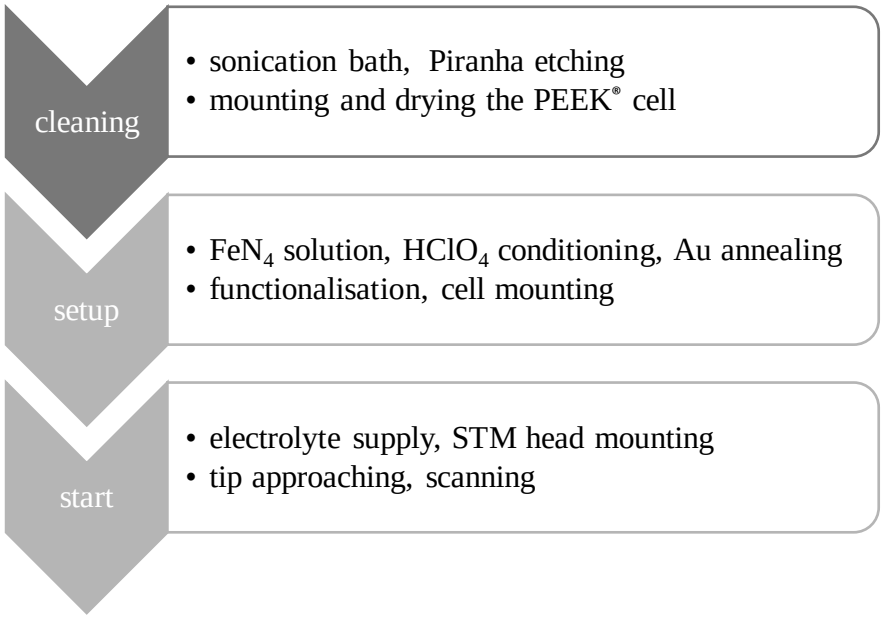

Figure 3.14: Complete procedure for an EC-STM experiments in a schematic way**.**

Glassware (beakers, flasks, Pasteur pipettes and also tweezers) is put into an ultrasonic cleaner and subjected to sonication baths of 15 minutes, rinsing and filling the glassware with bi-distillate water among each bath. The procedure is repeated 5-7 times. The glassware is then cleaned with Piranha solution, with a 1:1 mixture of H_2SO_4:H_2O_2. Only the beaker containing PEEK cell, Viton rings and Pt electrodes does not undergo this treatment. Piranha etching is performed until the peroxymonosulphuric acid H_2SO_5 in situ generated have decomposed the most part of organic contaminants (i.e. the solution has cooled down). The glassware must be thoroughly rinsed with MilliQ water, before letting it undergo at least other two sonication baths, using MilliQ water for rinsing and filling. PEEK® cell, Viton ring and Pt electrodes are let dry over dust-free paper tissues. The Pt wire is mounted and fixed with a screw in the dedicated slot. A dry beaker is used for weighing the molecules in the form of powder. The powder is pre-dissolved with DMF in a beaker and then transferred into a 25 mL graduated flask. A dry Pasteur pipette is used to bubble Ar in the FeN_4 solution for at least 30 minutes. The gas injection tube for $HClO_4$ is let fluxing Ar in the electrolyte. The Au(111) sample is subjected to flame annealing procedure, already described in section 3.2.3. After the final flash annealing, the RHE is prepared as described in 3.1. When the Au sample has cooled down, the Ar-saturated FeN_4 solution is poured in a beaker and the Au is functionalised with molecules by hanging meniscus method (see section 3.2.7). The Au is then placed in the PEEK cell and the latter is fixed to its aluminium housing; the three screws are tightened to seal the Au surface with the Viton ring. The cell is then mounted onto the STM base. The LEMO plug is connected to the STM unit. The peristaltic pump is turned on and freshly-saturated electrolyte is supplied to the cell thanks to the capillary tube. 10-20 mL of electrolyte are supplied before closing the valve to allow proper conditioning of the electrochemical environment. The bipotentiostat is

switched on and a potential is instantly applied to the WE. Generally, a potential close to OCP is selected as initial potential, in order not to develop high Faradaic current. The Plexiglass® plate is tightened to the chamber and the STM scanner is placed over the cell. Connections are made between the scanner and the STM unit, to allow remote control via software. The scanner is released by its safety lock position, leaning now onto the three piezo-legs. An aluminium plate with a central hole is tightened over the chamber and Ar (or O_2) is fluxed for few seconds to saturate the chamber, which is then closed with a rubber cap. The granite plate is suspended on the four springs and the tip approaching procedure is started via software. When the tunnelling current set-point is reached, manual approaching must be performed to reach stable tunnelling conditions. The EC-STM is now ready to acquire topographic profiles of the sample.

3.3 Image Analysis

The output of an STM measurement is a series of topographic profiles, and each one is the result of scanning with the tunnelling tip above the sample along a scan line with definite length. By assigning colour grades to the vertical scale *Z*, each point of every curved is coloured on the basis of its *Z* value. Assuming the tip is accurately following the surface roughness, then the latter can be visualised on the false-colours image produced by the registered topographic profiles. This can be accomplished thanks to dedicated software. The software that controls the STM unit actually realises a first image processing, returning raw images. These can be thought of as the original image registered by the instrumentation, and they are also said to be unfiltered. There exists several third-party software that allow to enhance images by applying specific filters. These filters increase the contrast and reduce noise or bad data points, and for this reason their employment must be moderated, otherwise artefacts are introduced in the final image. In this work, the two software WSxM [20] and Gwyddion [21] were extensively used.

3.3.1 WSxM

WSxM [20] was extensively employed thanks to its outstanding usability. With few quick operations it can indeed process an image and make it ready for advanced analysis, for example *Z* profile extracting, distances or angles measuring, etc. A procedure which revealed to be suitable in most of the cases is now described. First of all, the desired raw image is loaded into the program, and colour grades will automatically be attributed. Frequently, images present a slope, which is a direct consequence of a non-ideally horizontal tip scanning over the surface. This is often due to a sample declivity, since its mounting in the PEEK cell is susceptible of small variations, which however can determine large effects considering the exceptional STM sensitivity. To correct this effect, the function "global plane" can be used. It acts by subtracting a plane to the series of topographic profiles forming the image, correcting the non-horizontal position of the sample at the moment of scanning. If one or more step edges are present in the image, this automatic procedure can fail to give back a proper result, therefore the "local plane" function can be used. Small areas that must have the same *Z* height are manually selected to aid the software subtracting a proper plane to the raw image. Another essential feature is called "flatten". It exerts a smoothing effect on the image. STM images often present scars and stripes. Plenty of them are horizontal due to misalignment among consecutive scanning lines,

as a result of, for example, bad response of the piezoelectric materials or small vertical oscillations, which were not completely attenuated. As a consequence, successive topographic lines may present an offset, which moves the entire topographic profiles to lower or higher *Z* values if compared to previous and following scan lines, causing scars and stripes to appear with very bright or very dark colour. The "flatten" function acts with a flattening effect to reduce stripes and scars. "Equalise" is the mostly employed tool. It has the ability to tune image contrast, enhancing the colour difference between flat areas and protruded features. The "equalise" function allows to manually select a range of heights, excluding too short or too large height values, provoked by tunnelling disturbances. Those values are therefore not representative of the real system and can be considererd as artefacts. By contracting the range of heights, the colour grades are mone finely redistributed and the image appears more definite and easier to analyse. If a stripe is completely black or white, it can be eliminated by the "remove lines" tool.

The described filtering operations are always necessary to attain trustworthy images. The risk of introducing new artefacts in the image is minimum: filtering operations are manually accomplished and the effect of every parameter can be instantly displayed and therefore directly adjusted, if necessary.

Analysis of STM images is mostly performed by extraction of topographic profiles. The "profile" tools allows to trace any desired straight line on an image. This line will touch at least one point of the original topographic profiles registered during scanning. All the point that the line intersects will be retained and used to generate the corresponding topographic profile, as sequence of experimental data points. Straight lines are traced over regions of interest, like atoms, clusters, or molecules. This opens the possibility to gain fundamental information about surface morphology of the sample, especially if had been intentionally functionalised with particular molecules, as did for this work with macrocyclic FeN_4 compounds.

3.3.2 Gwyddion

Gwyddion [21] was also used for image analysis. Many features are in common with *WSxM*, even if different algorithms are used and a smaller level of manual actions is allowed, making image processing trickier. For image filtering, *WSxM* was preferred. Nonetheless, other actions are better performed or were no featured in the other software. A clear example is represented by profile extraction. A straight line can be drawn in whatever direction, and the software will return the corresponding topographic profile on the basis of the intersected data point. If, in the case of an oblique line, no points of a scanning line are intersected, then the software can perform an interpolation among the points that precede and follow the intermediate desired value. Moreover, many different interpolating functions are available: round, linear, Key, Nearest Neighbours Interpolation, etc. The main advantage is the possibility to select the "thickness" of the final topographic profile. If the thickness is increased, more points along the perpendicular direction of the drawn line will be averaged, originating a smoother and more definite final profile. This reveals to be a good a posteriori method for contrasting instrumental noise and to achieve more reliable morphological data. Images analysed with *WSxM* software were colour-mapped with blue tones, whereas those analysed with *Gwyddion* were colour-graded with grey-scale tones. Topographic profile appearance will slightly differ, but the displayed information is equal.

It is worth to mention that the *WSxM* software features many additional functions and analysis instruments, which however go out of the purposes of the present work. The only quantitative information obtained by the analysis of an STM image basically lies in topographic profiles. As already discussed in section 2.1.2, quantitative correlations of the tunnelling current with the tunnelling gap, for example, or with other quantities is still far from applicability [2]**.** The real and tangible capability of EC-STM lies in the structural and mechanistic information achieved by interpretation of the changes among multiple consecutive images, registered under potential control of the Working Electrode. As a matter of fact, information about surface structural order (or disorder) can also be extracted. Indeed, Self-Assembly was introduced in section 2.2.2.5 as one of the topics of this work. Chapter 6 will embrace symmetry considerations regarding Self-Assembled Monolayers of FeN_4 macrocycles.

3.3.3 CorelDRAW® X8

CorelDRAW® *X8* is a vector graphics editor. Despite its high potentiality, its use was limited to simple graphics drawing for determining unit cell parameters, angles, domain boundaries, etc. Anyway, it allowed to reach high precision levels and an appreciably fast workflow, giving the opportunity to repeat the same measures for different areas of the same image and for different images. Therefore, the resulting data possess a statistic-like nature.

3.4 UV-VIS

UV-Vis spectrophotometry was mainly employed as a qualitative mean to characterise the FeN_4 macrocyclic molecules. Phthalocyanines and Porphyrins can in fact undergo dimerization, precipitation and/or degradation if exposed to light and this photosensitivity should be taken into consideration when handling these compounds. A rough mean of detection for the aforementioned phenomena can come by directly watching the solution in the flasks. Indeed, Fe(II)-Phthalocyanine solution experiences after few hours a change in colour, from light-blue/green to yellowish, and it commences to precipitate. Fe(III)-Phthalocyanine appears intense blue and it maintains its colour as well as it solubilisation for more than 24 hours. Fe(III)-methoxyphenyl porphyrin maintains a brownish colour and full solubilisation for more than 24 hours.

For the solutions to undergo a spectrophotometric investigation, a proper concentration must be realised. Actually, 0.1 mM revealed to be a proper concentration for evaluating the Q-bands region, while it was too large for a correct determination of the B-bands region. B-bands were in fact revealed as saturated signals if the concentration was too high, therefore deviating from linear trend expected by Lambert-Beer law. Dilutions to $3.33 * 10^{-5} M$ for Fe(II)-phthalocyanine, and to $1 * 10^{-5} M$ for Fe(III)-phthalocyanine and Fe(III)-methoxyphenyl Porphyrin were prepared immediately after UV-Vis spectrophotometry of 0.1 mM solutions and stored in separate glass flasks. Each glass container was enveloped with aluminium foil before and after use to minimise light exposure. This precaution was needed since an aging experiment was conducted and photodegradation must be reduced.

References

[1] M. Wilms, M. Kruft, G. Bermes, K. Wandelt, *A new and sophisticated electrochemical scanning tunneling microscope design for the investigation of potentiodynamic processes*, Rev. Sci. Instrum., **1999**, *70*, 3641–3650.

[2] A.J. Bard, L.R. Faulkner, *Electrochemical Methods, Fundamentals and Applications*, John Wiley & Sons, inc., **2001**.

[3] O.M. Magnussen, *Ordered anion adlayers on metal electrode surfaces*, Chem. Rev., **2002**, *102*, 679–725.

[4] M. Wilms, P. Broekmann, C. Stuhlmann, K. Wandelt, *In-situ STM investigation of adsorbate structures on Cu (111) in sulfuric acid electrolyte*, Surf. Sci., **1998**, *416*, 121–140.

[5] B.L. Rogers, J.G. Shapter, W.M. Skinner, K. Gascoigne, *A method for production of cheap, reliable Pt-Ir tips, Rev. Sci. Instrum*., **2000**, *71*, 1702–1705.

[6] A.H. Sørensen, U. Hvid, M.W. Mortensen, K.A. Mørch, *Preparation of platinum/iridium scanning probe microscopy tips*, Rev. Sci. Instrum.,**1999**, *70*, 3059–3067.

[7] A. Lucier, *Preparation and Characterization of Tungsten Tips Suitable for Molecular Electronics Studies*, Thesis, **2004,** McGill University, Canada.

[8] I. Ekvall, E. Wahlström, D. Claesson, H. Olin, E. Olsson, *Preparation and Characterization of electrochemically etching W tips for STM*, Meas. Sci. Technol., **1999**, *10*, 11–18.

[9] J.P. Ibe, P.P. Bey, S.L. Brandow, R.A. Brizzolara, N.A. Burnham, D.P. DiLella, K.P. Lee, C.R.K. Marrian, R.J. Colton, *On the electrochemical etching of tips for scanning tunneling microscopy*, J. Vac. Sci. Technol. A., **1990**, *8*, 3570–3575.

[10] R. Kazinczi, E. Szocs, E. Kálmán, P. Nagy, Novel methods for preparing EC STM tips, Appl. Phys. A Mater. Sci. Process., **1998**, *66*, 535–538.

[11] J. Clavilier, K. El Achi, M. Petit, A. Rodes, M.A. Zamakhchari, *Electrochemical monitoring of the thermal reordering of platinum single-crystal surfaces after metallographic polishing from the early stage to the equilibrium surfaces*, J. Electroanal. Chem., **1990**, *295*, 333–356.

[12] P.J. Welford, B.A. Brookes, V. Climent, R.G. Compton, *The hanging meniscus contact: Geometry induced diffusional overpotential. The reduction of oxygen in dimethylsulphoxide at Au(111),* J. Electroanal. Chem., **2001**, *513*, 8–15.

[13] E.T. Fell, *US2789954A. United States Patent Office*, **1953**.

[14] D.L. Ball, J.O. Edwards, *The Kinetics and Mechanism of the Decomposition of Caro's Acid. I,* J. Am. Chem. Soc., **1956,** *78*, 1125–1129.

[15] G.R. Krow, *Monoperoxysulfuric Acid,* Encycl. Reagents Org. Synth., **2001**.

[16] J. D'Ans, W. Friederich, *Synthese der Caroschen Säure und der Überschwefelsäure*,

Eur. J. Inorg. Chem., **1910**, 1880–1882.

[17] J.Y. Gu, Z.F. Cai, D. Wang, L.J. Wan, *Single Molecular Imaging of Iron-Phthalocyanine Catalyzed Oxygen Reduction Reaction by in situ Scanning Tunneling Microscopy*, ACS Nano., **2016**, 1–10.

[18] F. Ghani, J. Kristen, H. Riegler, *Solubility Properties of Unsusbstituted Metal Phthalocyanines in Different Types of Solvents*, J. Chem. Eng. Data., **2012**, *57*, 439–449.

[19] www.sigmaaldrich.com dmf.pdf

[20] I. Horcas, R. Fernández, J.M. Gómez-Rodríguez, J. Colchero, J. Gómez-Herrero, A.M. Baro, *WSXM: A software for scanning probe microscopy and a tool for nanotechnology*, Rev. Sci. Instrum., **2007**, *78*.

[21] D. Nečas, P. Klapetek, *Gwyddion: An open-source software for SPM data analysis*, Cent. Eur. J. Phys., **2012**, *10*, 181–188.

Chapter 4

4 Au(111) properties and preparation

4.1 Au(111) surface

Gold has been one of the main materials which found applications both in science and arts. It had represented a valuable coinage metal, and still is a refined raw material for expensive jewellery. Many modern industrial applications concern dentistry and electronics. Its electronic configuration is $[Xe]4f^{14}5d^{10}6s^{1}$ and it therefore belongs to the 11th group and the 6th period of the period table of elements [1]. It melts at 1337.33 K and boils at 3129 K. Pure gold is non-magnetic and represents one of the most inert metallic elements: for this reason, it is also regarded as a noble metal [2]. It can be etched by *aqua regia*, as shown in the following reaction:

$$Au + 4HCl + HNO_3 \rightarrow H[AuCl_4] + 2H_2O + NO \qquad (4.1)$$

The mixture of hydrochloric and nitric acid oxidises gold, producing chloroauric acid. Alternatively, it can be dissolved in aqueous solutions containing an oxidising agent and a ligand (for example HCl and $FeCl_3$) [2]. It is however insoluble in nitric acid, while poor solubility is retained in mercury, with which it forms a solid solution up to 16% Hg [2].

Besides its decorative purposes, gold holds a primary role in nanoscience and nanotechnology, catalysis and self-assembled monolayers [3]. It is resistant towards oxidative corrosion [4] and it is widely regarded as an excellent thermal and electrical conductor.

Gold crystallises with a Face Centred Cubic (FCC) structure [3]. The unit cell for the bulk crystal has a lattice constant of 4.072 Å [5,6], whereas the atomic radius is 1.442 Å. The nearest-neighbours distance equals 2.884 Å. Being a single crystal, it was mostly studied for its low-indexes faces, namely (100), (110), (111). A representation of the three low-index faces is shown in figure 4.1 for a generic FCC crystal.

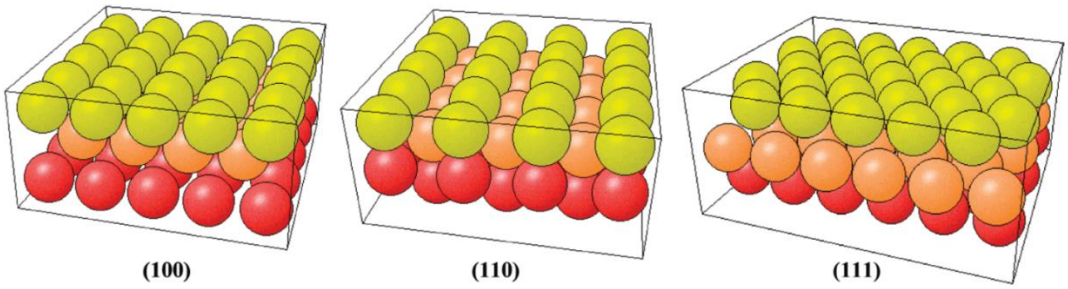

Figure 4.1: The three low-index crystallographic faces for a FCC crystal [3].

The top layer of a close-packed transition metal may present a change of the electronic structure, causing the top layer to have different properties with respect to the corresponding

bulk material [7]. Surface stress can appear and act as a driving force towards a surface reconstruction. In fact, all the three low-index gold surfaces exhibit a surface reconstruction. Au(100) is known to reconstruct with a (5 x 20) cell, producing a quasi-hexagonal top layer [3]. The missing row along the $< 1\bar{1}0 >$ direction causes the Au(110) to reconstruct into a (1 x 2) pattern [3]. The Au(111) face exhibits a remarkable reconstruction, called "herringbone reconstruction", and defined by a (22 x √3) unit cell [3,7–10]. This peculiar surface reconstruction is widely accepted to be the result of two opposing tendencies [3,7,9,10]. The coordination number for atoms at the surface is equal to 9, while it equals to 12 for the bulk phase, being a close-packed structure. For this reason, the top layer prefers to contract, trying to compensate for its reduced coordination. However, the bulk phase favours the surface atoms to occupy positions of minimum potential dictated by the underlying bulk atoms, thus forcing the growth of a commensurate layer. The misfit between the top layer and the bulk originates the (22 x √3) reconstruction. It is characterised by periodic arrays of pairs of partial dislocations, which act as domain walls among face-centred cubic FCC and hexagonal close-packed HCP domains. They are also termed as ridges. The compresence of both FCC and HCP domains is a consequence of the FCC bulk structure itself. Indeed, the stacking sequence along the <111> causes the atoms to occupy A, B, C positions with a …ABCAB… sequence for the bulk phase, whereby the surface atom can occupy either a FCC site (terminating the sequence with C, …ABCABC) or an HCP site (terminating the sequence with A, …ABCABA). The surface FCC and HCP positions both represent local minima of potential, but HCP are slightly higher in energy. This argument can justify the smaller width of HCP domains with respect to FCC domains. Alternating FCC and HCP domains are separated by domain walls, with a height of ~0.1 to 0.2 Å. These ridges are produced by the occupancy of bridge sites, which lie in between A and C sites. The (22 x √3) cell contains 23 atoms instead of 22. The extra atom relieves the tensile strength along the $< 1\bar{1}0 >$, causing in fact a 4.4 % contraction along that direction in the top layer. The outcome is then a surface superstructure made of alternating uniaxial domains arranged in a zig-zag pattern (herringbone) [9].

4.1.1 Au(111) in air (Ar)

Au(111) is known to reconstruct its surface with the (22 x √3) herringbone pattern, which remains stable even at room conditions. For this reason, the Au(111) sample was first characterised at the air/solid interface, without the presence of an electrolytic solution. A pre-treatment of the gold sample was necessary before alodging it in the STM cell, since organic contaminants, dust, or partial oxidation of the surface may prevent smooth and regular surface reconstruction. The pre-treatment consists of a flame annealing procedure, as previously described in section 3.2.3. After that, the sample is mounted in the PEEK cell, without assembling the Pt CE, and the cell is inserted in the aluminium chamber. Ar is pumped into the chamber, letting it flux for ~1 minute before sealing the chamber; the Ar flux is then immediately closed, in order to not produce a large excess pressure. The presence of Ar creates an inert atmosphere, even if gold is not expected to oxidise due to a higher reduction potential if compared to the O_2 one [11].

Tunnelling parameters used for investigating the bare Au(111) sample at the air/solid interface were usually more extreme than for the liquid/solid interface. A possible linkage can be found in the different behaviour of the tunnelling phenomenon at the two interfaces. As previously elucidated in section 2.1.2., the effective tunnelling barrier is expected to be lowered at the liquid/solid interface. Hence, since the air/solid case is now being examined,

electrons are supposed to seep into a wider tunnelling barrier. This means that a higher constant tunnelling current and/or a smaller Tip Electrode – Working Electrode bias are required to maximise the tunnelling events. The tunnelling current can be manually selected, as already described in section 3.2, as well as the bias voltage, as shown in section 3.2. If the applied bias V is thought to generate a uniform and stationary electric field with magnitude *E*, then bias and electric field will be connected by the following equation where a smaller bias voltage is linked with a closer tip-sample distance:

$$E = \frac{V}{z} \qquad (4.2)$$

where *z* is the tip-sample gap. Therefore, a lower voltage determines a smaller tip-sample distance *z*.

The obtained STM images are reported in figure 4.2a-e. The captions contain the tunnelling parameters (tunnelling current, bias) and the scan size. In this case, the applied bias is only "internal", as explained in section 3.2, since no electrochemical circuit is realised. Therefore, the voltage bias must necessarily be applied between tip and electrode.

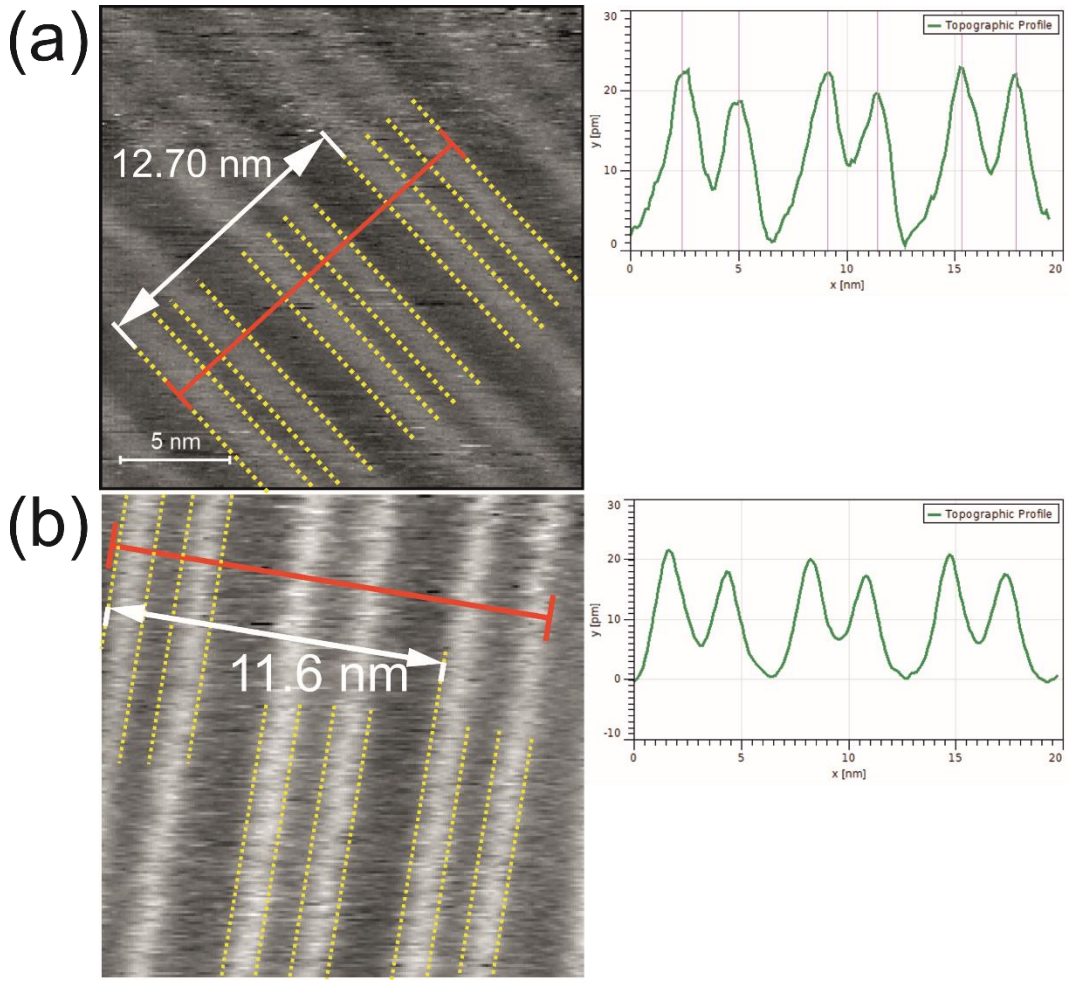

Figure 4.2: (a) Scan size: 21.9 nm x 21.9 nm, I_t =3.65 nA , U_b= –9 mV; (b) Scan size: 13.2 nm x 13.2 nm, I_t =3.65 nA, U_b = –9 mV.

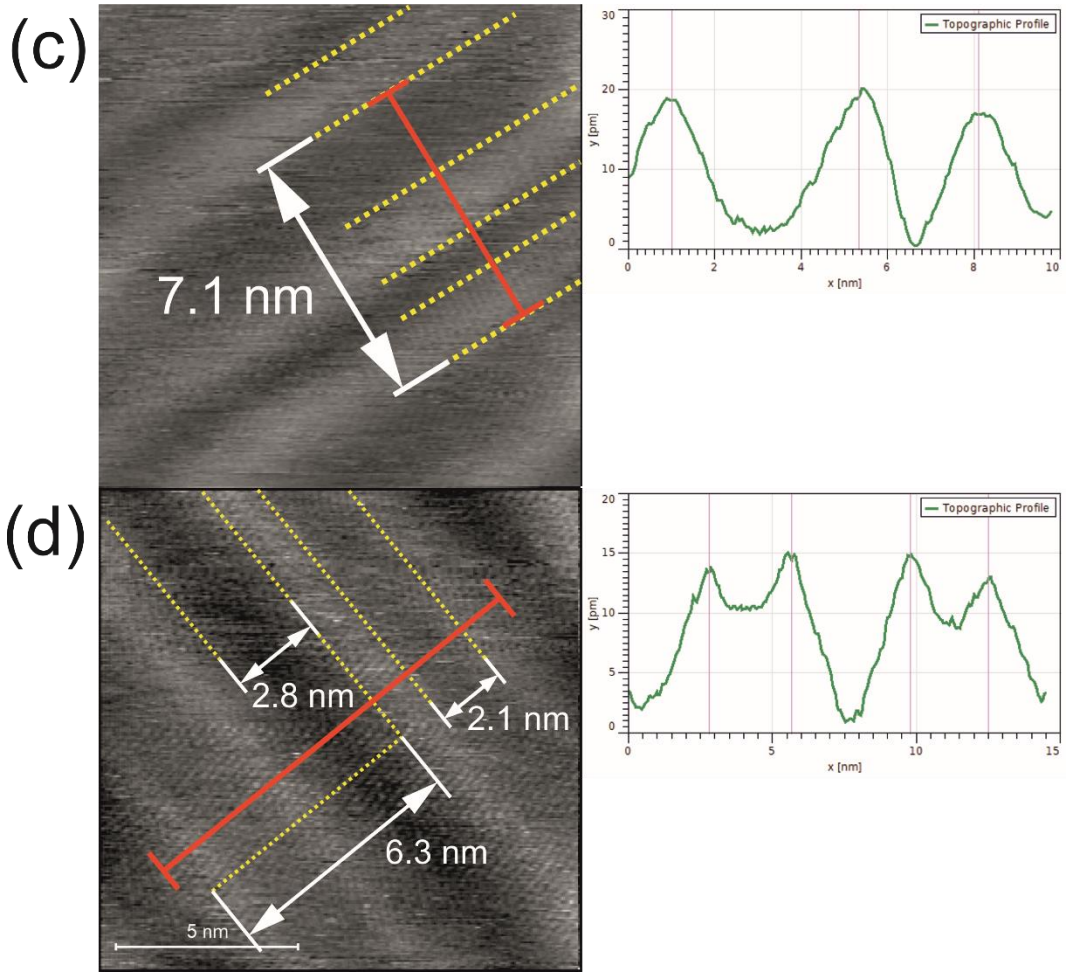

Figure 4.2: (c) Scan size: 13.2 nm x 13.2 nm, I_t =3.65 nA, U_b = –9 mV; (**d)** Scan size: 13.2 nm x 13.2 nm, I_t = 3.65 nA, U_b = 8 mV.

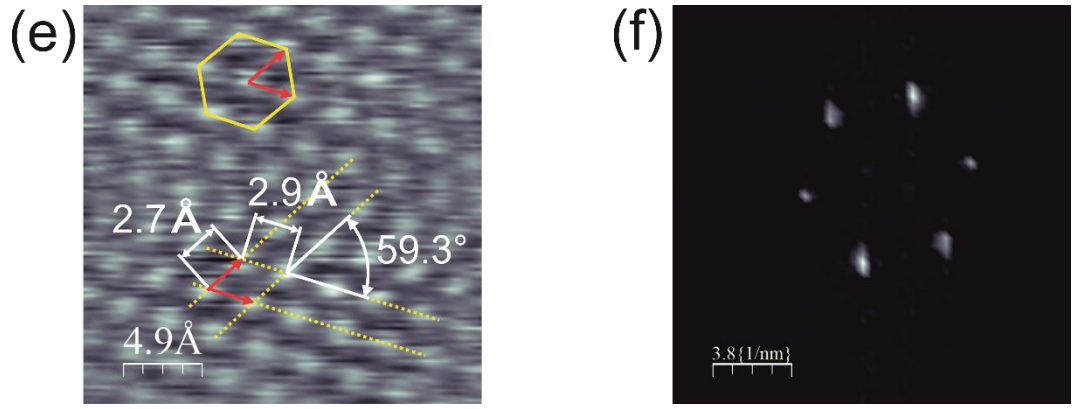

Figure 4.2: (e) Scan size: 2.5 nm x 2.5 nm, I_t = 3.65 nA, U_b = –9 mV; (f) Fast Fourier Transform of fig. 4.2e.

Fig. 4.2a-c clearly demonstrates that the Au(111) surface is not completely flat, but presents corrugations. This finds complete correspondence with well-known experimental data about Au(111) surface reconstruction [7–10,12]. The observation of this characteristic surface pattern is the proof that the Au single-crystal in use is definitely exposing the (111)

crystallographic face. Fig. 4.2d manages to provide a high-resolution image, showing close-packed atomic positions together with the long-range herringbone modulation. Topographic profiles were extracted by each image, to measure the height and the periodicity of the ridges. The typical height is expected to be collocated in the range of 0.1 – 0.2 Å [9]. For each extracted topographic profile, the height of each corrugation is calculated as the difference between one maximum (top of the corrugation) and the absolute minimum, which indicates the FCC domain. A local less deep minimum is found between each couple of corrugations and represents the HCP domain. The origin of larger and narrower domains is explained in section 4.1 as a difference in their thermodynamic stability.

The measured heights are reported for each image, as follows:

Fig. 4.2a: $h = 0.124$ Å.

Fig. 4.2b: $h = 0.130$ Å.

Fig. 4.2c: $h = 0.175$ Å.

Fig. 4.2d: $h = 0.065$ Å.

The final average value is:

$$\bar{h} = \frac{1}{N}\sum_{i=1}^{4} d_i = 0.124 \text{ Å} \tag{4.3}$$

The corresponding confidence interval has been calculated as standard error of the mean, by dividing the standard error of the sample to the square root of the number of observations, as follows:

$$s_{\bar{h}} = \frac{\sqrt{\frac{1}{N-1}\sum_{i=1}^{3}(h_i - \bar{h})^2}}{\sqrt{N}} = 0.023 \text{ Å} \tag{4.4}$$

Hence, the average periodicity of the imaged herringbone pattern is:

$$\bar{h} = (0.124 \pm 0.023) \text{ Å} \tag{4.5}$$

Since the expected value for herringbone corrugation (is fully included in the confidence interval of the measured one, the instrumentation is proved to reliably probe the sample surface, without significant deviations from reality.

Topographic profiles allowed to measure also the periodicity of herringbone reconstructed patterns. If more than one periodicity was present in an image, the maximum distance between two identical points (border of ridges) was measured and the resulting value was divided by the number of enclosed periodicities. An average periodicity is therefore obtained, providing a value with statistical relevance. The average associates a statistical confidence interval to a measured value (obtained as an average of measurements), which is affected by unavoidable random errors. Distances were measured with the dedicated measuring tool in the CorelDRAW software, trying to include as many periodicities as possible, thus providing more precise values. The measured distances are reported for each image, as follows:

Fig. 4.2a: $d = 6.4\ nm$.

Fig. 4.2b: $d = 5.8\ nm$.

Fig. 4.2c: $d = 7.1\ nm$.

Fig. 4.2d: $d = 6.3\ nm$.

The final average value is:

$$\bar{d} = \frac{1}{N}\sum_{i=1}^{3} d_i = 6.4\ nm \qquad (4.6)$$

The corresponding confidence interval has been calculated as standard error of the mean, by dividing the standard error of the sample to the square root of the number of observations, as follows:

$$s_{\bar{d}} = \frac{\sqrt{\frac{1}{N-1}\sum_{i=1}^{3}(d_i-\bar{d})^2}}{\sqrt{N}} = 1.8\ nm \qquad (4.7)$$

Hence, the average periodicity of the imaged herringbone pattern is:

$$\bar{d} = (6.4 \pm 1.8)\ nm \qquad (4.8)$$

This value can be compared with literature data obtained at the solid/UHV interface [13–15], revealing that the reference value is fully contained in the confidence interval of the experimental periodicity determination.

The above fig. 4.2 a-e are also an undeniable example of the cleanness of the Au single crystal surface, guaranteed by flame annealing. Moreover, it denotes a nearly null tendency to contamination by external gases. For this purpose, the chamber had been saturated with Ar gas, but the Au mounting in the PEEK cell and its transfer in the STM unit were performed by direct air exposure for few minutes, which for other surfaces would inevitably lead to extensive contamination, as theoretically calculated in section 2.1.

Fig. 4.2e is the example of the high-resolution capability of the instrumentation. In this case, it was pushed to its limits, by applying drastic tunnelling conditions: 3.65 nA as tunnelling current and –9 mV as voltage bias. In these conditions, the tip is extremely close to the sample, and the tunnelling current is close to the allowed full-scale. The tip is therefore exposed to high risk of damage, while the surface is heavily perturbated by the tunnelling phenomena, but the flame annealed Au(111) surface is smooth enough and defect-less providing quite satisfactory results. This high level of resolution was limited to a portion of a unique image, but a proper cropping was enough to point out the claimed atomic resolution. The corresponding Fast Fourier Transform is displayed in Figure 4.2.f. A Fourier transform is an integral transform that expresses a function as an infinite sum of amplitudes, wavelengths and phases. It is defined as:

$$f(\omega) = F\{g(x)\} = \frac{1}{\sqrt{2\pi}}\int_{-\infty}^{\infty} g(x)e^{-i2\pi x\omega}dx \qquad (4.8)$$

where $g(x)$ is the original function in the spatial domain [16]. $f(t)$ is the Fourier transform of $g(x)$ function and it is defined in the frequency ω domain. However, calculators deal with finite integrals, so the Fast Fourier Transform (FFT, also known as 2D-FFT) must be selected. The FFT is made of finite summations and defined as [17]:

$$F(k,l) = \sum_{i=0}^{N-1}\sum_{j=0}^{N-1} f(i,j)e^{-i2\pi\left(\frac{k_i}{N}+\frac{l_j}{N}\right)} \qquad (4.9)$$

where $f(i,j)$ is the image as defined in the spatial domain, whereas the exponential term is the linkage between a point (*i*;*j*) in the direct space (spatial domain) and the corresponding point (*k*;*l*) in the reciprocal space (frequency domain). *N* is the number of one-dimensional FT used to compute the integral of eq. (1). Eq. (2) states that Fast Fourier Transform $F(k,l)$ is obtained

by summating the result of the multiplication of the spatial image with the basis function. The basis function is a complex exponential function, and it can be expressed as sum of sine and cosine waves. At the end, the resulting FFT is a complex number, but it can be visualised thanks to its real and imaginary part. Indeed, one can define the Magnitude of the FFT as [18]:

$$Magnitude(f) = \sqrt{Re^2 + Im^2} \tag{4.10}$$

whereas the Phase as:

$$Phase(f) = \arctan\left(\frac{Im}{Re}\right) \tag{4.11}$$

The DC-component, also named 0 Hz term, is positioned at the centre of the Fourier Transform image and represents the average brightness of the picture. If the dynamic range of the resulting FFT is too large to be properly displayed, then it is more convenient to apply a logarithmic or a square root scale, as *WSxM* enables. Generally, Magnitude images are used due to an easier interpretation capability. *WSxM* then can display the real or imaginary part only, the modulus, a Power Spectrum, or the Root Mean Square of the FFT.

What is worth to remember is the reciprocal relation between direct space and Fourier space, for which the modulus of a reciprocal vector $\boldsymbol{r}$ is given by (for *WSxM* software):

$$|\boldsymbol{r}| = \frac{1}{|\boldsymbol{d}|} \tag{4.12}$$

where *d* is a direct-space vector. Hence, largely-spaced periodicities in the real space will become low-spaced in the reciprocal space, and vice versa. The reciprocal lattice vector modulus is obtained by measuring the distance between the centre (F(0,0)) and the centre of a bright spot in the FFT generated panel (a generic F(*k*,*l*) point). Bright spots arise if there exist objects with same dimensions which repeat with same distances and angles, so that they will be described by the same Fourier coefficients.

If reciprocal lattice vectors are measured on the FFT of Figure 4.2.f, which is calculated on the real image of Figure 4.2.e, the following three values are obtained (the software simultaneously measures pairs of symmetrical spots):

$|\boldsymbol{r_1}| = 2.79$ Å
$|\boldsymbol{r_2}| = 2.73$ Å
$|\boldsymbol{r_3}| = 2.95$ Å

The corresponding average value is:

$$|\bar{\boldsymbol{r}}| = \frac{1}{N}\sum_{i=1}^{3} r_i = 2.83 \text{ Å} \tag{4.13}$$

The confidence interval has been calculated as standard error of the mean, by dividing the standard error of the sample to the square root of the number of observations, as follows:

$$s_{\bar{r}} = \frac{\sqrt{\frac{1}{N-1}\sum_{i=1}^{3}(r_i - \bar{r})^2}}{\sqrt{N}} = 0.06 \text{ Å} \tag{4.14}$$

Hence, the average nearest neighbours distance of the imaged atomic distribution is:

$$\bar{r} = (2.83 \pm 0.06) \text{ Å} \tag{4.15}$$

The reported value for the Au-Au distance (nearest neighbours, 2.89 Å) is completely included in the confidence interval of the value obtained by the FFT of the registered image [8,10,13–15].

4.1.2 Au(111) in Ar purged electrolyte

Au(111) single-crystals are known to exhibit the (22 x √3) pattern even at the solid/electrolyte interface. There is however a significant effect of the applied electrode potential when the Au single crystal is mounted in an electrochemical cell and plays as working electrode. For a metal surface contacting an electrolytic solution in an electrochemical cell setup, a Point of Zero Charge PZC will always exist, at which no excess charge appears at the electrode surface [19]. If the electrode is intentionally polarised at whatever potential different from PZC, an excess charge will be present at the surface. The electrode potential in fact represents the electrochemical potential of electrons in the electrode and it is directly connected to the metal Fermi level, which in turn depends on its work function [19]. If the applied electrode potential is negative with respect to the PZC, then the surface is revealed to reconstruct with herringbone pattern. Conversely, if a more positive potential than PZC is applied, the reconstruction is lifted and the surface shows the unreconstructed (1 x 1) surface. This phenomenon is called *potential-induced reconstruction* and it is the evidence of the implication of surface charges in the reconstruction behaviour of surfaces. The lifting/reconstructing mechanisms are quickly accomplished, since few seconds are usually enough for the completion of reconstruction (or its lifting). However, the lifting/reconstruction phenomenon at the Au(111) surface is somewhat tricky. The herringbone pattern is in fact recognised as the energetically more stable state of the Au(111) surface. Thus, the (1 x 1) unreconstructed surface is a metastable state and the application of a definite negative potential (vs PZC) simply acts on the activation barrier for reconstruction, but not on the thermodynamic state of the surface [19].

When the original herringbone pattern is lifted, monoatomic-thick Au islands are formed. They are originated by the excess Au atoms that were fitted in the ridges of the more densely packed (22 x √3) surface, as previously explained in section 4.1. The Au islands also act as nucleation centres during the potential-induced reconstruction, since they are an easy source of extra Au atoms to be fitted in the compressed herringbone top layer. The potential-induced reconstruction is not completely innocent. A potential-induced reconstructed surface can be in fact distinguished by a more pronounced zig-zag pattern, and one terrace often presents more than one orientational domains of reconstruction rows.

The lifting/reconstruction phenomenon can be investigated by means of cyclic voltammetry.

The (22 x √3) → (1 x 1) transition causes the appearance of a positive current peak at $E_{p,lift}$~0,75 V $(vs\ RHE)$ if an anodic scan is performed from negative potentials with respect to PZC. Vice versa, a negative current peak appears at $E_{p,rec}$~0,70 V $(vs\ RHE)$ if a cathodic scan is performed starting by positive potentials with respect to PZC. These features are visible in the cyclic voltammetry shown in figure 4.3. The herringbone reconstruction/lifting is regarded as a reversible process [20] and it occurs each time the electrode potential overcomes the PZC potential in cathodic or anodic sweeps.

Let us now consider the entire cyclic voltammogram of Figure 4.3. Three main peaks are noticeable, and they are regarded as a finger print of an Au single crystal exposing the (111) crystallographic plane [28]. They are connected to the oxidation mechanism of the substrate, as well as its reduction [20]. Gold behaves like many other metals when inserted in an electrochemical cell and exposed to an electrolytic acid solution. If it is positively polarised, it undergoes oxidation through a two-electron mechanism formulated as:

$$\begin{gathered} M + H_2O \rightleftarrows MOH + H^+ + e^- \\ MOH \rightleftarrows MO + H^+ + e^- \\ \hline M + H_2O \rightleftarrows MO + 2H^+ + 2e^- \end{gathered} \qquad (4.16)$$

The two major oxidation peaks are labelled as OA3 ($E_{OA3} \approx 1{,}34\ V$) and as OA4 ($E_{OA4} \approx 1{,}56\ V$) [21]. Minor peaks or waves are found to precede E_{OA3} and are named as OA1 and OA2. OA1, OA2 and OA3 (figure 4.3) are concerned with the first electron transfer of reaction (1). In particular, OA1 and OA2 are related to OH deposition in between specifically adsorbed anions [21,22]. The $HClO_4$ solution provides perchlorate ClO_4^- anions, which are known for their low adsorption tendency on gold [21,23–26]. This is not true for any applied potential window. If a consistent positive excess charge is realised at the Au surface, even least adsorbing anions find favourable conditions for specific adsorption. This implies that large positive potentials need to be applied: in this case, $E_{app} > 1.2$ V is required to attain adsorption, whereas many other anions, like halides (I^-, Br^-, Cl^-) or even sulphate SO_4^- specifically adsorb at much lower applied potentials (frequently, $E_{app} < 0.7$ V) [27]. For ClO_4^-, H_2O molecules of the primary hydration shell are H-bonded to the O-atoms forming perchlorate [21,28]. Therefore, a significant part of the gold surface is hindered towards OH deposition by already adsorbed perchlorate anions. By positively rising the applied potential, a progressive discharge of the H-bonded water occurs, and the previously adsorbed anions are replaced by OH. This process is considered completed at OA3. At this stage, gold has been subjected to the first reaction of eq. (1). Now the surface is exposing M-OH dipoles, which may form 2 or 3 sublattice. Nonetheless, the most part of dipoles undergoes the following reconstruction mechanism (turn-over) [21][22]:

$$\begin{array}{ccc} HHH & & H\ \ H \\ OOO & \rightarrow & OMO \\ MMM & & MOM \\ & & H \end{array}$$

This first stage of gold oxidation is also referred as Under Potential Deposition of OH species between the adsorbed perchlorate anions [29].

Upon applying even more positive potentials, a second electron is transferred, and a monolayer-thick oxide film is formed, as showed in the second reaction of eq. (1). This justifies the presence of the anodic peak at $E_{OA4} \approx 1.60\ V$. This peak actually exhibits a higher current than expected by a simple one-electron transfer, and the claimed reason lies in an already not completed perchlorate desorption even when E_{OA3} was reached.

The oxide monolayer then undergoes complete reduction at $E_{OC} \approx 1.15\ V$, as proven by the intense peak in fig. 4.3. The reverse mechanism with respect to (2) is first required, namely the turn-over of the surface:

$$\begin{array}{ccc} H\ \ H & & HHH \\ OMO & \rightarrow & OOO \\ MOM & & MMM \\ H & & \end{array}$$

Now the actual reduction can take place, as:

$$MOH + H^+ + e^- \rightarrow M + H_2O \qquad (4.17)$$

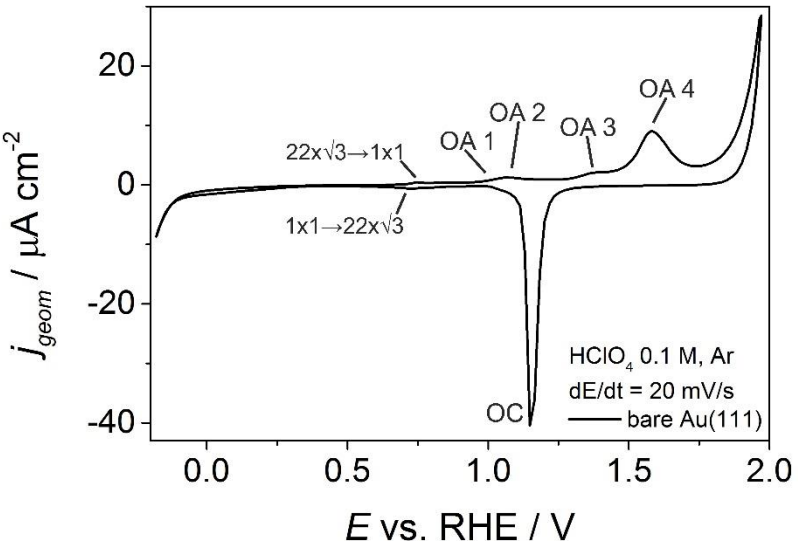

Figure 4.3: CV of Au(111) singe crystal in argon purged 0.1 M $HClO_4$ recorded at 0.2 V/s.

The obtained STM images are reported in Figure 4.4a-c. The captions contain the tunnelling parameters (tunnelling current, bias) and the scan size. Imaging was perfomed at the solid/electrolyte interface, with the primary aim to complete the characterisation of the Au(111) substrate and to evaluate eventual differences with the previously investigated solid/air interface of the same sample.

Distances were measured with the same procedure of the solid/air images. The measured distances are reported for each image, as follows:

Fig. 4.4a: $d = 6.7\ nm$.

Fig. 4.4b: $d = 6.9\ nm$.

Fig. 4.4c: $d = 6.3\ nm$.

The final average value is:

$$\bar{d} = \frac{1}{N}\sum_{i=1}^{3} d_i = 6.633 \text{ nm} \qquad (4.18)$$

The corresponding confidence interval has been calculated as standard error of the mean, by dividing the standard error of the sample to the square root of the number of observations, as follows:

$$s_{\bar{d}} = \frac{\sqrt{\frac{1}{N-1}\sum_{i=1}^{3}(d_i-\bar{d})^2}}{\sqrt{N}} = 0.178 \text{ nm} \qquad (4.19)$$

Hence, the average periodicity of the imaged herringbone pattern is:

$$\bar{d} = (6.63 \pm 0.18) \text{ nm} \qquad (4.20)$$

This value can be compared with literature data obtained at the solid/UHV interface [13–15], revealing that the reference value is fully contained in the confidence interval of the experimental periodicity determination.

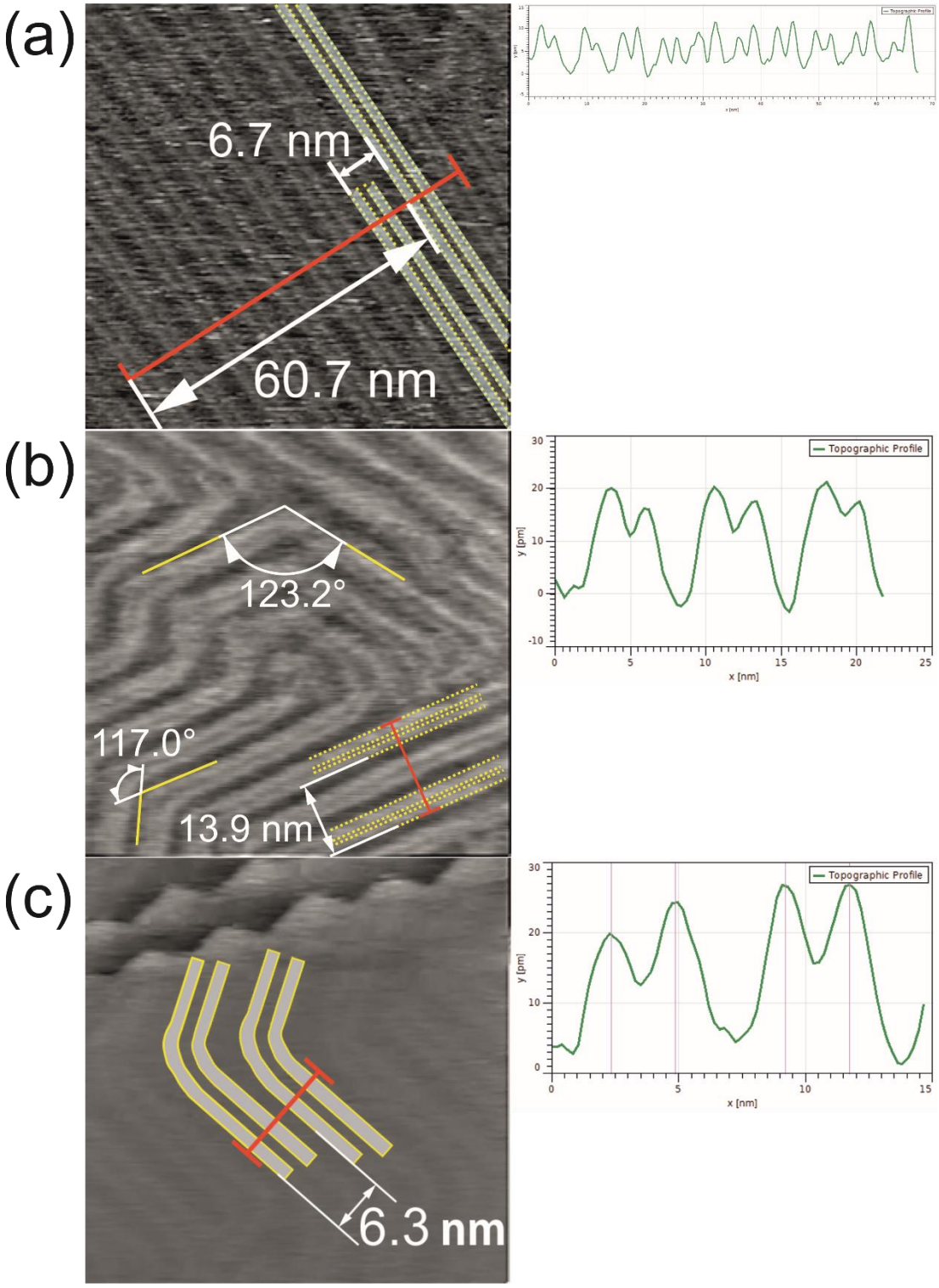

Figure 4.4: (a) Scan size: 70.6 nm x 70.6 nm, I_t = 1 nA, U_b= –122 mV, E_{app}= +401 mV, I= –0.6 µA; (b) Scan size: 79.5 nm x 79.5 nm, I_t=1.55 nA, U_b = –114 mV, E_{app} = 610 mV, I = –0.1 µA; (c) Scan size: 47.6 nm x 47.6 nm, I_t= 1 nA, U_b= –150 mV, E_{app}=, I= –0.1 µA.

Fig. 4.4.c features a sketch of a contour line for a triangular-shaped terrace edge. This however is an additional signature of the (111) surface symmetry, since such a surface orientation should result in hexagonal-like structures [30,31]. This is in accordance with the measured angles of $\alpha = 115.5°$ for the imaged triangles.

The same treatment can be extended to the herringbone zig-zag pattern. Figure 4.4.b demonstrates that the dislocation lines change their direction with angles of ~120°.

When the applied potential is swept to more positive values, the reconstruction undergoes the process of lifting [19]**.** The surface no more exhibits the (22 x √3) herringbone pattern, but rather a flat one with the simple (1 x 1) reconstruction, i.e. the top layer has the same symmetry of the bulk crystal. However, gold islands are formed due to release of extra Au atoms from the top layer [19], since the (22 x √3) was characterised by a 4% compression along the $< 1\bar{1}0 >$ direction. Figure 4.4.b shows that islands were detected when the applied potential was $E_{app} = +825\ mV$.

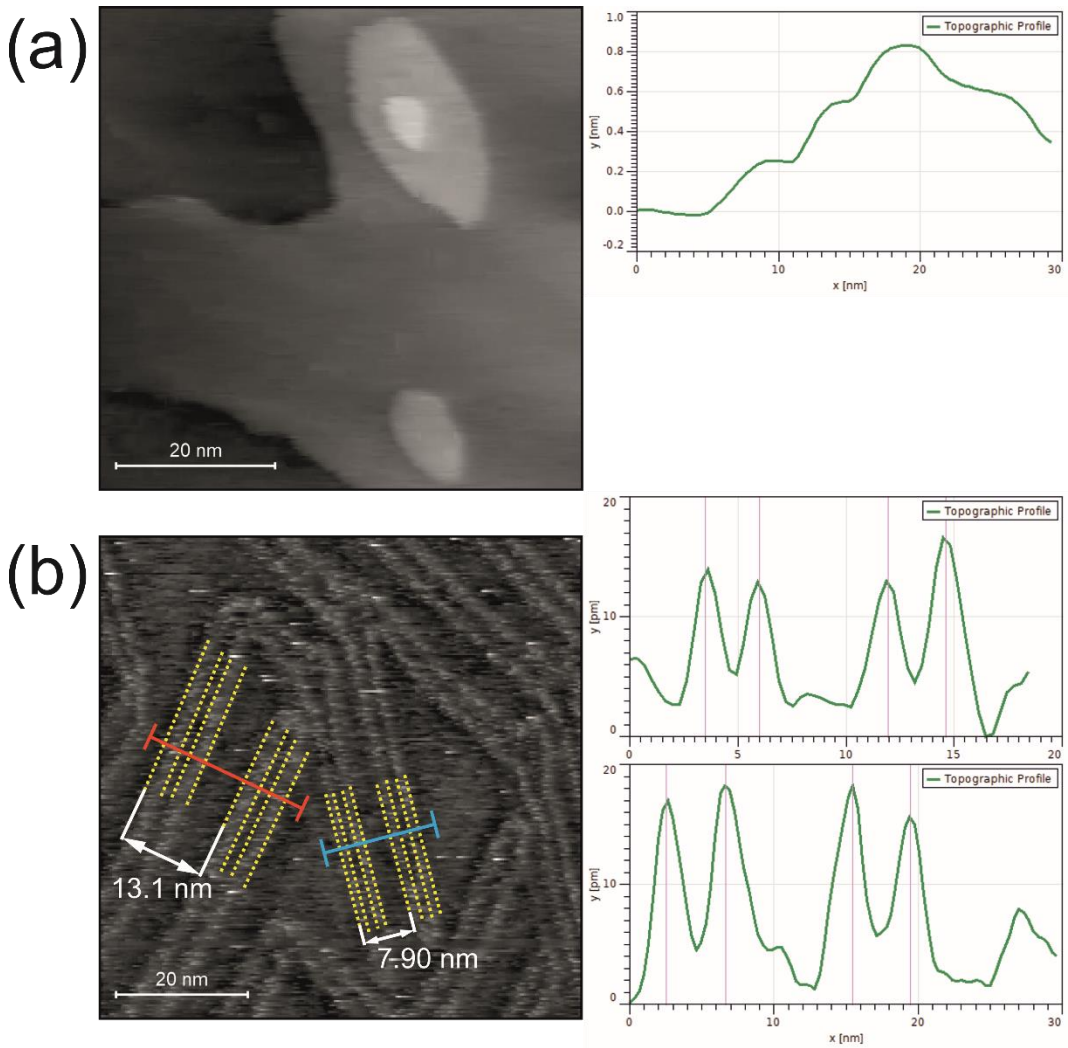

Figure 4.5: (a) Scan size: 60.3 nm x 60.3 nm, I_t= 1 nA, U_b= -112 mV, E_{app}= +850 mV, I = +0.6 μA; (b) Scan size: 72.8 nm x 72.8 nm, I_t = 1 nA, U_b = –122 mV, E_{app}= +500 mV, I = –0.2 μA.

The profile extracted by Figure 4.5a is another tool for evaluation of the resolving power of EC-STM instrumentation. The profile in fact shows characteristic steps of 0.24 nm, which is fully attributable to the expected step-edge height of Au(111) surface [13].

When the applied potential is swept back to sufficiently negative values, the (22 x √3) reconstructed surface is again stabilised, as shown in Figure 4.5b.

The gold island formed due to lifting of the reconstruction now serve as nucleation sites for the herringbone pattern formation, since extra atoms need to be fitted in a compressed top layer. As expected [19], the herringbone pattern appears more disordered, with zig-zag lines running along the three main crystallographic directions. The measured periodicity is in fact far from the previously measured distances, as reflected by the topographic profiles extracted the red and blue lines, in figure 4.5b.

References

[1] https://www.webelements.com/gold/.

[2] J.C. Yannopoulos, *The Extractive Metallurgy of Gold Extractive of Gold*, **1991**.

[3] J. Gong, *Structure and surface chemistry of gold-based model catalysts*, Chem. Rev., **2012**, *112*, 2987–3054.

[4] C.D. Bain, E.B. Troughton, Y.T. Tao, J. Evall, G.M. Whitesides, R.G. Nuzzo, *Formation of Monolayer Films by the Spontaneous Assembly of Organic Thiols from Solution onto Gold*, J. Am. Chem. Soc., **1989**, *111*, 321–335.

[5] https://www.webelements.com/gold/crystal_structure.html.

[6] A. Maeland, T.B. Flanagan, *Lattice Spacings of Gold-Palladium Alloys*, Can. J. Phys., **1964**, *42*, 2364–2366.

[7] Crljen, P. Lazić, D. Šokčević, R. Brako, *Relaxation and reconstruction on (111) surfaces of Au, Pt, and Cu*, Phys. Rev. B, **2003**, *68*, 1–8.

[8] F. Hanke, J. Björk, *Structure and local reactivity of the Au(111) surface reconstruction*, Phys. Rev. B, **2013**, *87*, 235422.

[9] Y. Hasegawa, P. Avouris, *Manipulation of the Reconstruction of the Au (111) Surface with the STM*, Science, **1992**, *258*, 5089, 1763–1765.

[10] S. Narasimhan, D. Vanderbilt, *Elastic Stress Domains and the Herringbone Reconstruction on Au(111)*, Phys. Rev. Lett., **1992**, *69*, 1564–1568.

[11] http://www2.ucdsb.on.ca/tiss/stretton/database/Standard_Reduction_Potentials.htm, (n.d.).

[12] T. Niu, *Surface strain mediated dipole alignment of ClAlPc on Au(111)*, Appl. Phys. Lett., **2015**, *106*, 1–6.

[13] J.V. V. Barth, H. Brune, G. Ertl, R.J. Behm, *Scanning tunneling microscopy observations on the reconstructed Au(111) surface: atomic structure, lon-range superstructure, rotational domains, and surface defects*, Phys. Rev. B., **1990**, *42*,

9307–9318.

[14] D.D. Chambliss, R.J. Wilson, S. Chiang, *Ordered nucleation of Ni and Au islands on Au(111) studied by scanning tunneling microscopy*, J. Vac. Sci. Technol. B., **1991**, *9*, 933–937.

[15] C. Wöll, S. Chiang, R.J. Wilson, P.H. Lippel, *Determination of atom positions at stacking-fault dislocations on Au(111) by scanning tunnelling microscopy*, Phys. Rev. B., **1989**, *39*, 7988–7991.

[16] https://www.encyclopediaofmath.org/index.php/Fourier_transform.

[17] https://homepages.inf.ed.ac.uk/rbf/HIPR2/fourier.htm.

[18] http://www.cs.unm.edu/~brayer/vision/fourier.html.

[19] D.M. Kolb, *Reconstruction Phenomena at Metal-Electrolyte Interfaces*, Progress., **1996**, *51*, 109–173.

[20] D.M. Kolb, J. Schneider, *Surface reconstruction in electrochemistry: Au(100-(5 × 20), Au(111)-(1 × 23) and Au(110)-(1 × 2)*, Electrochim. Acta., **1986**, *31*, 929–936.

[21] H. Angerstein-Kozlowska, B.E. Conway, A. Hamelin, L. Stoicoviciu, *Elementary steps of electrochemical oxidation of single-crystal planes of Au Part II. A chemical and structural basis of oxidation of the (111) plane,* J. Electroanal. Chem., **1987**, *228*, 429–453.

[22] H. Angerstein-Kozlowska, B.E. Conway, A. Hamelin, L. Stoicoviciu, *Elementary steps of electrochemical oxidation of single-crystal planes of Au-I. Chemical basis of processes involving geometry of anions and the electrode surfaces*, Electrochim. Acta., **1986**, *31*, 1051–1061.

[23] M. Hugelmann, W. Schindler, *Tunnel barrier height oscillations at the solid/liquid interface*, Surf. Sci., **2003**, *541*, L643–L648.

[24] A. Hamelin, S. Morin, J. Richer, J. Lipkowski, *Adsorption of pyridine on the (110) face of silver*, J. Electroanal. Chem., **1989**, *272*, 241–252.

[25] T. Vitanov, A. Popov, E.S. Sevastyanov, *Electrical double layer on (111) and (100) faces of silver single crystals in solutions containing ClO_4-and F-*, J. Electroanal. Chem., **1982**, *142*, 289–297.

[26] G. Valette, *Double layer on silver single crystal electrodes in contact with electrolytes having anions which are slightly specifically adsorbed. Part II. The (111) face*, J. Electroanal. Chem., **1989,** *269*, 191–203.

[27] O.M. Magnussen, *Ordered anion adlayers on metal electrode surfaces*, Chem. Rev., **2002**, *102*, 679–725.

[28] G. Brink, M. Falk, *Infrared spectrum of HDO in aqueous solutions of perchlorates and tetrafluoroborates*, Can. J. Chem., **1970**, *48*, 3019–3025.

[29] A. Hamelin, *Cyclic voltammetry at gold single-crystal surfaces. Part 1. Behaviour at low-index faces*, J. Electroanal. Chem., **1996**, *407*, 1–11.

[30] http://www.ntmdt-tips.com/contest/gallery/view/52770.

[31] H. Wolfschmidt, C. Baier, S. Gsell, M. Fischer, M. Schreck, U. Stimming, *STM, SECPM, AFM and electrochemistry on single crystalline surfaces*, Materials, **2010**, *3*, 4196–4213.

Chapter 5

5 Electrochemical characterisation

5.1 FeN_4 macrocycles in oxygen reduction reaction

In this chapter, the electrochemical properties of FeN_4-modified gold electrodes are examined. FeN_4 is an abbreviation to indicate macrocyclic molecules with planar geometry, which feature a number of Nitrogen atoms at least equal to four. Porphyrins, phthalocyanines and tetraaza-annulenes well represent classes of FeN_4 molecules. The four N atoms are placed in the middle of a circular-shaped molecular structure and a cavity is thereby originated. Metal-free phthalocyanine (free-base) was in fact found to have a diameter equal to 3.93 Å [1]**.** This makes it suitable for the coordination of metal ions. Indeed, Iron-porphyrins and iron-phthalocyanines are the macrocyclic compounds hereby exploited as source of FeN_4 sites. Iron has an atomic radius of 1.24 Å [2], but its ionic radius must be considered when thinking of metal-phthalocyanines and -porphyrins, resulting in a radius of 0.72 Å for Fe^{2+} and of 0.60 Å for Fe^{3+} [2].

In particular, Fe(II)-phthalocyanine (Fe(II)Pc), Fe(III)-phthalocyanine chloride (Fe(III)Pc-Cl) and Fe(III)-tetramethoxyphenyl-porphyrin chloride (Fe(III)TMPP-Cl) were used as FeN_4 macrocyclic molecules, being commercially available. They have been used without further purification, since the declared "dye content" (molecular purity) is > 90% (Fe(II)Pc > 90%; Fe(III)Pc-Cl > 99%; Fe(III)-TMPP > 99%). Belonging to the phthalocyanine or porphyrin classes, the aforementioned macrocyclic molecules possess a high number of aromatic rings and their extended conjugation produces a rigid structure with pronounced planar geometry. These FeN_4 compounds are therefore prone to non-covalent binding with the Au surface, which can be carried out by electrostatic interactions (involving ions and/or dipoles), hydrogen bonds, hydrophobic interactions, π stacking and Van der Walls interactions. This can lead to the formation of self-assembled monolayers (SAM) of FeN_4 molecules, whose nature will be extensively described in chapter 6.

Much interest has been exerted on metal phthalocyanines and porphyrins, since they provide good model systems for mimicking FeN_x sites, with a precisely defined x = 4. The latter retain a major role in O_2 reduction electrocatalysis, since they allow to avoid extensive Pt usage, therefore leading to Non-Platinum Groups catalysts for ORR.

The ORR is the most impacting issue in the fuel cell performance, on this regard, the FeN_4-functionalised electrodes reveal to be one of the best solutions for studying the effect of FeN_4-based macrocyclic compounds on ORR electrocatalysis. If a FeN_4-based species is found to be more active than others, then the causes can be directly ascribed to the particular FeN_4 molecule itself, i.e. substituents or metal centre, being equal the other experimental conditions.

FeN_4 chelates are therefore suitable for electrocatalytic activity modulation. Number of *d* electrons of the metal centre, formal potential of the M^{3+}/M^{2+} redox transition, donor-acceptor molecular hardness, pH (Pourbaix diagram), eventual axial ligands are among the most relevant aspects that may affect the MN_4 activity towards ORR [3,4].

The number of *d* electrons had been used in the construction of Volcano plots together with the measured potential for each MN_4 chelate at a given constant current density. Iron is at the top of the Volcano indicating its best catalytic activity based on this descriptor [3,4]. Anyway, Co, Mn and Cr are expected to exert a catalytic effect due to partially empty *d* orbitals, which can be occupied during O_2 adsorption [3,5].

A similar descriptor concerns the M^{3+}/M^{2+} redox formal potential, even if a more general notation $M^{n+}/M^{(n-1)+}$ would be preferred. In any case, the most common catalytic couple revels to be the M^{3+}/M^{2+} one [3,6–10]. A linear correlation had been found between the M^{3+}/M^{2+} redox potential and the M-O_2 binding energy [3], assuming that O_2 binds to the metal in the (II) oxidation state. The linear correlation shows that Fe-Phthalocyanine has an intermediate value of M-O_2 binding energy, in accordance with Sabatier's principle of catalysis, according to which a reaction proceeds at optimum rate when the reaction intermediate involved in the rate determining step binds not too strong nor too weak with the catalyst [3,5].

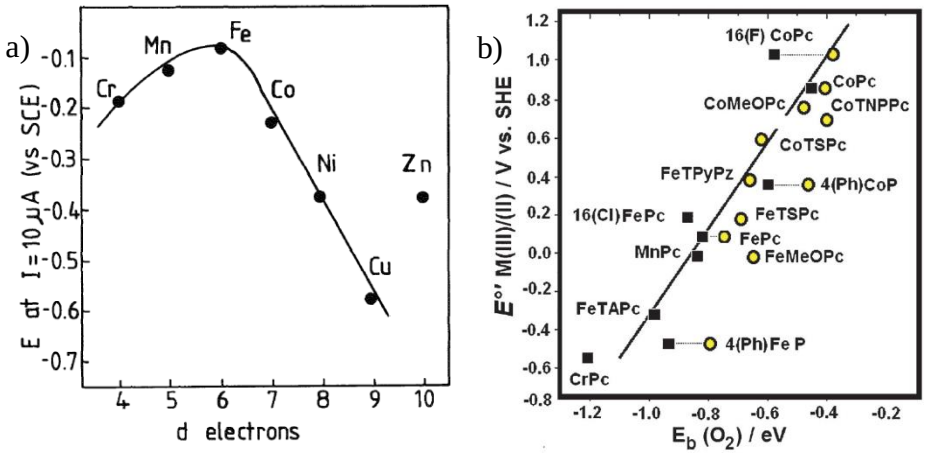

Figure 5.1: (a) Volcano plot activity of different M(II)-phthalocyanines in 0.1 M NaOH; (b) fitting from [3] obtained by [11] (back squares) and by [12] (yellow circles).

Donor-acceptor molecular hardness of the M-O_2 complex is another mean of comparison for electrocatalytic activity of MN_4 chelates. This concepts derives from Pearson's theory for catalysis [3,5,13,14]. Molecular hardness of a donor-acceptor complex is defined as:

$$\eta_{DA} = \frac{1}{2}(IP_D - EA_A) \qquad (5.1)$$

where IP_D is the ionisation potential of the donor species, i.e. the metal and EA_A is the electron affinity for the acceptor, i.e. oxygen. Making use of the Koopman's theorem, η_{DA} can be expressed as the difference between the energy of the LUMO of the acceptor and the energy of the HOMO of the donor [4,5,7], as follows:

$$\eta_{DA} = \frac{1}{2}(\varepsilon_A - \varepsilon_D) \qquad (5.2)$$

The larger is the HOMO-LUMO gap (hard donor-acceptor pair), the stronger is the bond between donor and acceptor, and this turns into low reactivity. Conversely, a narrow HOMO-LUMO gap pertains to "soft" molecules, and it provides a higher reactivity due to poorly bonded donor-acceptor species. The concept of molecular hardness suggests that if there is the possibility of tuning the HOMO and LUMO energy levels, then the reactivity could be modified as desired. Indeed, the nature of the metal centre as well as the typology and number of substituents on the macrocyclic ring are two fundamental and strictly correlated tools for altering electronic properties like HOMO/LUMO energies. Electron-withdrawing substituents act by depleting electron density from the metal centre, therefore lowering its HOMO level, resulting in a reduced HOMO-LUMO gap between donor (metal) and acceptor (oxygen). Electron-withdrawing substituents are expected to enhance electrocatalytic activity. The opposite is true for electron-donating groups: higher HOMO levels are expected for the metal centre, and the resulting "harder" molecule will exhibit lower electrocatalytic activity.

Ring substitution exerts a striking effect also on the redox potentials of the metal centre. Electron-withdrawing groups tend to attract electron density from the metal centre, making it easier for the metal to accept electrons and undergo reduction. Conversely, electron-donating groups provide electron density to the metal, making it prone to oxidation but hindering its reduction. This means that electron-withdrawing groups make the redox potential of the metal more positive, whereas electron-donating substituents shift it negatively. Of course, the entity of electron-withdrawal or -attraction reflects on the positive or negative shift amount of the metal redox potential.

The metal redox potential holds a major role in the ORR electrocatalysis. The $M^{n+}/M^{(n-1)+}$ redox formal potential has already been linearly correlated with O_2 adsorption energy, but it is also directly connected to the O_2 reduction mechanism. O_2 reduction occurring in the presence of MN_4 active sites is regarded as an inner-sphere reaction, namely at the Inner Helmholtz Plane of solid/liquid interface [4,7]. In other words, a number of electrons > 1 is transferred between the active site at the electrode surface and the reacting molecule, i.e. O_2. O_2 binds to the MN_4 active site thanks to the *d* orbitals of the metal [4,7,10], belonging to the transition metal series. This can be thought of as an adsorption process, but even if this step may be believed easy or obvious to occur, its real evidence can come only by experimental data provided by a scanning probe technique with considerably high imaging resolution: it is the case of EC-STM. It is thanks to its ability to work at the solid/liquid interface, in the presence of an O_2-saturated electrolyte, that oxygen adsorption had become something truly visible in STM images. It can be even stated whether the *end-on* or *side-on* adsorption geometry was characterising the O_2 adsorption step. The demonstration of this will be given in chapter 6. The *end-on* adsorption geometry, also known as Pauling model [10], implies that a σ interaction is established between the metal $3dz^2$ orbital, which is pointing perpendicularly outward the molecular plane, and the in-plane antibonding symmetric $1\pi_g^s$ orbital on the O_2 molecule [4,7,10]. Through this σ interaction, an electron transfer event has occurred from the metal to the O_2 molecule. A π interaction is also established and involves the metal *3dxy* orbital and the antisymmetric antibonding $1\pi_g^a$ orbital on the O_2 molecule. The π interaction acts as a back-bonding interaction. The visualisation of orbitals superimposition is given in figure 5.2a, while figure 5.2b shows a qualitative molecular orbital diagram for the complex formation between the metal (M) and the O_2 molecule. The *side-on* geometry, also known as Griffith model [10], is characterised by a σ type of bond formed by the overlap between the π oxygen orbital and the dz^2 (and *s*) orbitals of the metal centre. A π bond back-bond interaction

establishes between the $d\pi$ metal orbitals and the partially unoccupied π^* oxygen antibonding orbital.

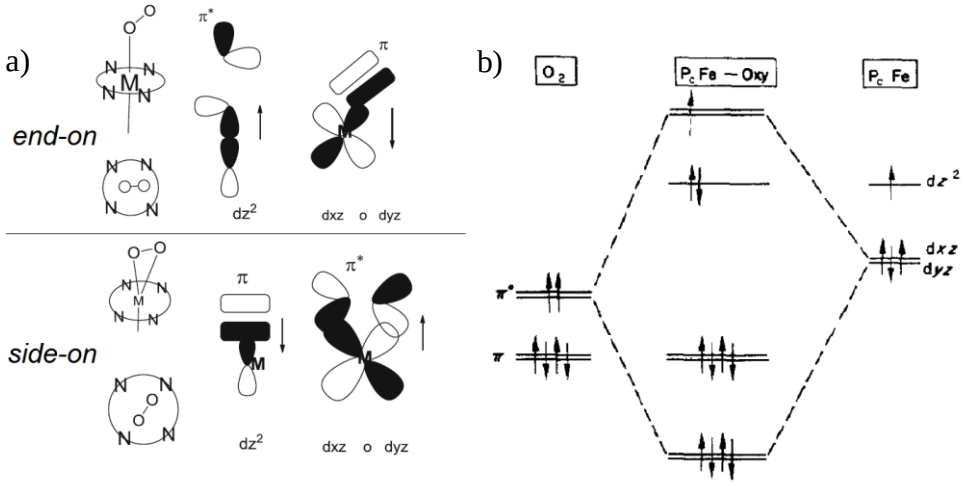

Figure 5.2: (a) *end-on* vs. *side-on* adsorption geometries and corresponding orbitals superpositions [7]; (b) orbital representation of the FePc-O_2 bond [15].

That of MN_4 is therefore a "redox-catalysis", in which the reduction of the metal centre from (III) oxidation state to (II) is first required to form the M-O_2 adduct [4,7,10,16]. The metal in the M-O_2 adduct regains the (III) oxidation state and reduces the O_2 molecule to water (preferably) or hydrogen peroxide, freeing the active site with its (III) oxidation state. In between the O_2 adsorption and H_2O releasing, several steps occur were electrons and hydrogen ions are transferred. The corresponding scheme is:

$$M(III)^+ + e^- \rightarrow M(II)$$
$$M(II) + O_2 \rightarrow [M(III)^+ O_2^-]$$
$$[M(III)^+ O_2^-] \rightarrow products + M(III)^+ \qquad (5.3)$$

According to this scheme, the potential at which O_2 reduction occurs should be close to the M(III)/M(II) redox potential. This is verified for MN_4 compounds, in which M = Mn, Fe, [8,9] but not for complexes based on cobalt, for which the Co(III)/Co(II) potential is far more positive than the O_2 reduction peak potential [3,4,7–10,16,17]. This interestingly indicates that the M(III)/M(II) formal potential should be as high as possible in a defined potential window. A higher formal potential determines a higher onset potential for O_2 reaction at the metal centre, but if the potential is too positive, like for many Co macrocycles, then a systematic worsening in the ORR activity will be observed. Too negative formal potentials are associated to a hardly reducible metal centre, while too positive formal potentials cause difficult oxidation of the metal centre [4,7]**.** Kind of volcano-shaped curves were obtained plotting the measured current at a constant potential (or the measured potential at a constant current) against the M(III)/M(II) formal potential [4,7,8,10,18–20] (figure 5.3). Fe and Fe-based compounds are often found at the vertex of the volcanos, indicating their better performances towards ORR.

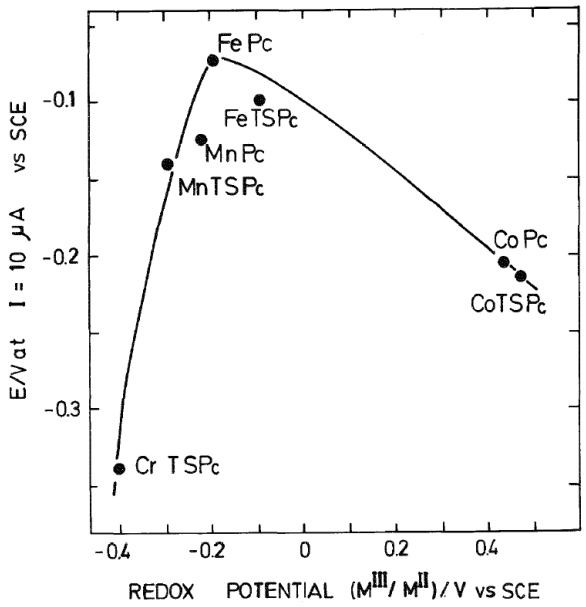

Figure 5.3: Electrocatalytic activity of metal-phthalocyanines for ORR vs. redox potential of the metal [10].

The mechanism for FePc-catalysed ORR in acidic media is reported according to the formulation of R. Baker at al. [21] and the literature cited therein. As first step, the reduction of the metal centre causes the iron to acquire the (II) oxidation state at sufficiently negatively polarised electrode surface:

$$Fe(III)Pc + e^- \rightarrow Fe(II)Pc \qquad (5.4)$$

The catalyst is now in its active form, namely the reduced iron atom at (II) oxidation state, and it is prone to adsorb an O_2 molecule from the oxygen-saturated electrolyte:

$$Fe(II)Pc + O_2 \rightarrow O_2 - Fe(II)Pc \qquad (5.5)$$

An adduct has been formed by the O_2 molecule and the Fe(II)Pc molecule. The Fe atom, being in its reduced (II) form, is prone to transfer an electron to the adsorbed O_2 molecule, contributing to its reduction:

$$O_2 - Fe(II)Pc + e^- + H^+ \rightarrow [HO_2 - Fe(III)Pc] \qquad (5.6)$$

This reaction is recognised as the rate determining step of the global ORR process. Three pathways are now possible. One route is a chemical reaction that brings to the formation of hydroperoxyl radicals:

$$[HO_2 - Fe(III)Pc] \rightarrow HO_2^{\bullet -} + Fe(III)Pc \qquad (5.7)$$

Alternatively, an additional electron transfer leads to hydrogen peroxide generation:

$$[HO_2 - Fe(III)Pc] + e^- + H^+ \rightarrow H_2O_2 + Fe(III)Pc \qquad (5.8)$$

If hydrogen peroxide is generated, two electrons were in total involved in ORR, from which the term "$2e^-$ mechanism". Finally and more interestingly, three electrons can be involved, leading to water as final reaction product [22]:

$$[HO_2 - Fe(III)Pc] + e^- + H^+ \rightarrow H_2O + [O - Fe(III)Pc]$$
$$[O - Fe(III)Pc] + e^- + H^+ \rightarrow [HO - Fe(III)Pc]$$
$$[HO - Fe(III)Pc] + e^- + H^+ \rightarrow Fe(II)Pc + H_2O \qquad (5.9)$$

For H_2O production, four electrons in total were needed, thus determining a "$4e^-$ mechanism".

The above mechanism is also regarded as an EC-like (electron transfer (E), followed by a chemical reaction (C)) mechanism, since the FePc, or in general the FeN_4 macrocycle, must be reduced before acting as catalyst for O_2 reduction [6].

The more desirable reduction mechanism is the "$4e^-$ pathway", since hydrogen peroxide generated via the "$2e^-$ pathway" is highly corrosive towards the proton exchange membrane [21,23]**.** Moreover, the highest energy conversion is achieved when O_2 is directly reduced to H_2O via the $4e^-$ mechanism [7,23].

5.2 Cyclic voltammetry investigation of FeN_4 macrocycles.

Cyclic voltammetry was conducted on the FeN_4-functionalised Au(111) electrodes. The primary aim was to extract basic information about peak potential, which serve as indicator parameters for redox processes occurring for the FeN_4 macrocycles. FeN_4 molecules are in fact expected to undergo the Fe(III)/Fe(II) redox process, which is regarded as a fundamental first step in the following O_2 reduction catalysis (chapter 6).

The functionalisation of the gold single crystal is performed by dipping the electrode surface in a 0.1 mM FeN_4 DMF solution, according to the hanging meniscus technique (section 3.2.7.). All cyclic voltammograms are recorded in 0.1 M $HClO_4$, prepared as described in section 3.2.5. The available potential window for the bare Au(111) electrode is of almost 2 V, but with remarkable limitations. Gold oxidation is quite a complex multi-step process, whose onset potential in anodic direction roughly coincides with $E_{app} \sim 1\ V\ (vs\ RHE)$. A full illustration has already been provided in section 4.1.2. Conversely, when performing the cathodic scan, HER starts to prevail at $E_{app} \sim -0.1/-0.2$ V (vs RHE), in accordance with literature data [24–28]**.** Therefore, the applied potential window for electrochemical characterisation of FeN_4-functionalised electrodes was limited in the range [–0.1-1 V vs. RHE], even if the coverage of the gold surface with organic molecule can lead to a different electrochemical response with respect to a bare Au electrode (Figure 5.1). The open circuit potential (OCP) for the FeN_4/Au(111) electrode immersed in Ar saturated 0.1 M $HClO_4$ was found to stabilise in the range [0.75; 0.80] V; whereas in the O_2 saturated electrolyte it was found in the range of [0.80; 0.86] V. This is in agreement with previously reported works [29,30]. Hence, all the cyclic voltammograms were recorded by starting at a potential close to the OCP and continuing the scan in cathodic direction.

5.2.1 Cyclic voltammetry of Fe(II)Pc in Ar purged electrolyte

Figure 5.4 shows cyclic voltammograms registered for FeN_4-functionalised Au(111) electrodes in Argon-saturated electrolyte (0.1 M $HClO_4$). CVs of bare Au electrode are also reported as mean of comparison for the evaluation of eventual electrochemical processes undergoing on the functionalised electrode in the surveyed potential windows. The vertical scale is expressed in geometrical current density $mA\ cm^{-2}$, obtained dividing the measured

current by the geometrical area of the Au(111) single crystal exposed to the electrolyte. CVs were shifted in the y axis direction for better evaluate the electrochemical features.

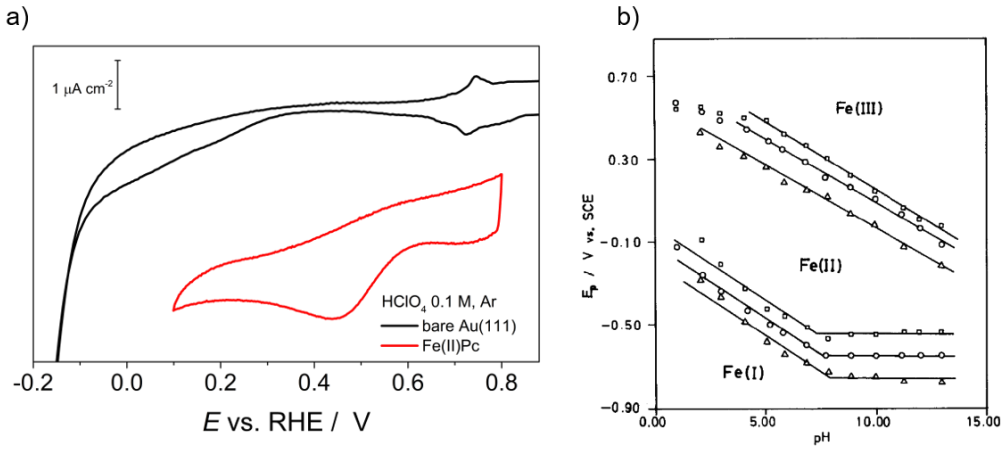

Figure 5.4 (a) CVs of Au(111) (black line) and Fe(II)Pc-functionalised Au(111) (red line) electrodes in argon purged 0.1 M $HClO_4$ recorded at 0.2 V/s; (b) Pourbaix diagram for the metal-centered processes of different iron phtalocyanines adsorbed on a OPG electrode (○) FePc, (□) FeTsPc, (△) FeMeOPc.

The electrochemical behaviour of Au(111) is widely explained in chapter 4, however it is worth to underline that the reversible redox couple at almost 0.7 V vs RHE is responsible for the lifting/reconstructing of the Au(111) surface and no other noticeable peaks are present and worth to be commented. The CV of FeN_4-functionalised Au(111) shows a reduction wave with an onset at $E_{onset} \cong 0.60$ V and culminating with a large asymmetric peak at $E_p = 0.44$ V. The inversion potential was set at $E_\lambda = 0.1$ V, since at more cathode potential hydrogen evolution reaction takes place, and it needs to be avoided. Organic monolayers are in fact very sensitive and labile to simultaneous reactions and surface changes. At this purpose, in the appendix it is reported the visual evidence of surface rearrangement of gold when consecutive scans involving the HER regime are performed. The anodic scan was continued up to $E_{app} = 0.80$ V to avoid the pre-oxidation regime of gold. Albeit the functionalisation of the Au(111) surface is known to modify the herringbone lifting/reconstruction potential [31], as directly visible in Au(111) CV the scan was prudentially stopped also to prevent gold island formation, which would interfere with the adsorbed molecules or would even cause their desorption.

The reduction wave and the corresponding peak at $E_p = 0.44$ V are ascribed to the reduction of Fe(III) to Fe(II), in accordance with literature data obtained for FePc-functionalised graphite (OPG, HOPG) [9,32] and Au [30,33] electrodes. A caveat for the oxidation states of the Fe centre is now provided. Iron-phthalocyanine is in fact supplied as Fe(II)-Pc, and even if no further purification was performed, iron is expected to retain its (II) oxidation state when dissolving the molecules in DMF. When the FePc-functionalised electrode is transferred in the electrochemical cell, either in the small PEEK cell for STM inspections and in a standard cell for ex-situ characterisation by cyclic voltammetry, it is exposed to a strongly acidic medium, i.e.: 0.1 M $HClO_4$. A qualitative information about iron oxidation state can be extracted by a Pourbaix diagram obtained for some FeN_4 species adsorbed on OPG electrodes, included Fe(II)Pc (Figure 5.4b) [3,9]. In the case of STM measurements, the bipotentiostat requires to apply a certain potential to the working electrode, and the chosen initial potential was in the range [+0.60; +0.75] V. In the case of ex-situ cyclic voltammetric characterisation, the scan was started by the OCP. In both cases, remembering

that the 0.1 M perchloric acid realises a pH=1, the applied potential lies at the limit of stability between Fe(II) and Fe(III). However, the Au(111) single crystal is quite a different substrate with respect to OPG, capable of different electrostatic interactions at the solid/liquid interface with respect to graphite. It is therefore inferred that iron was present mainly as Fe(III) at the aforementioned initial applied potentials, and its potential-induced reduction to Fe(II) is then the more plausible explanation for the detected reduction wave.

A tricky point concerns the anodic scan, in which no oxidation waves are clearly visible even in a wider potential window (Figure 5.4a). Actually, a very broad and low-current peak (O_1) may be perceived in the [+0.50; +0.65] V range. This would justify the re-oxidation step of Fe(II) to Fe(III), as expected by previous Fe(II)Pc/graphite measurements [3,9]. Owing to a different nature of the substrate, the oxidation wave is poorly resolved and fails to dissolve any doubts. Anyway it is not unusual that Au single crystals, and in particular Au(111), give similar results, as already observed for Fe-octaethylpoprhyrin [30] and Co- or Cu-phthalocyanines and -porphyrins [29,34,35]. The re-oxidation process is therefore considered slow and not fully resolvable through a potential variation with a defined scan rate. In fact, if consecutive scans are performed, a progressive loss in reduction wave current is attained, as shown in Figure 5.5a. At the second potential sweep, the current is almost halved; at the ninth consecutive scan, no substantial peak is revealed, indicating that no "reactants" are present at the electrode surface, namely Fe is still found almost exclusively in the (II) oxidation state when the cathodic scan has already begun. This agrees with previous experimental evidences for CoPc [29]. Furthermore, it is possible that in the wide potential window employed in figure 5.2a, Fe(II)Pc irreversibly desorbs so that it is no more possible evidences its redox behaviour in further cycles. Indeed, Fe(II)Pc monolayer is very sensitive to the applied potential since by subjecting the Fe(II)Pc-modified electrode to repeated potentials sweeps, the monolayer integrity was perturbed, and more negative peak potentials were recorded at each consecutive scan. Starting in fact by a peak potential at E_p= 0.44 V, the peak shifts to E_p= 0.41 V at the second scan.

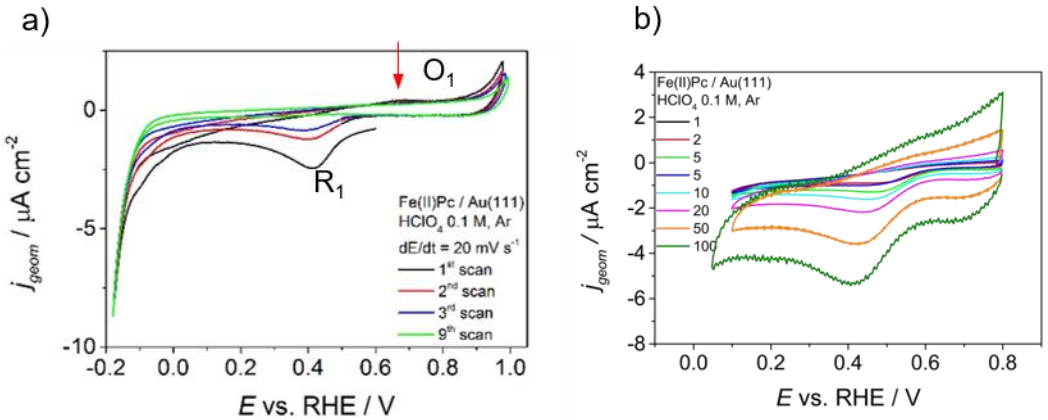

Figure 5.5: (a) Consecutive CVs and of Fe(II)Pc -functionalised Au(111) electrodes in argon purged 0.1 M $HClO_4$ recorded at 0.2 V/s; (b) CVs and of Fe(II)Pc -functionalised Au(111) electrodes in argon purged 0.1 M $HClO_4$ recorded at different scan rate.

Figure 5.5b reports the effect of the scan rate on the Fe(II)Pc -functionalised Au(111) electrode reduction peak. It is worth to mention that a linear correlation is expected between the peak current I_p and the scan rate when the molecular redox probe is adsorbed on the electrode surface since diffusive effects are absent, conversely a dependence by the root of the scan rate is expected for the diffusion-driven processes. In the present case because of the poor

reproducibility of the consecutive measurements at different scan rates, the plot of I_p vs dE/dt was built up considering 6 different points with a good linear correlation of the experimental points with respect to the interpolating line (R = 0.972). However a much better correlation (R = 0.996) was found for I_p vs (dE/dt)^0.5. Therefore, even though the redox process at Fe(II)Pc -functionalised Au(111) electrode is expected to not depend by diffusion, it is not possible to completely discharge the possibility that Fe(II)Pc adsorption is a dynamic process affected also by diffusion.

The E_p was also plotted versus log(dE/dt) giving a good linear correlation (R = 0.985). For a reversible Nernstian process, E_p does not depend from the scan rate, and its position should not change with respect to the variation of (dE/dt). In the present case the dependence of E_p from the scan rate clearly states that the reduction of Fe(III)Pc/Fe(II)Pc is an electrochemical irreversible process or at least a quasi-reversible electron transfer and this would also explain the absence or the clear evidence of a chemical reversibility on the anodic reverse scan.

5.2.2 Cyclic voltammetry of Fe(III)Pc-Cl in Ar purged electrolyte

Figure 5.6a compares the CV curve obtained for bare Au(111) with the voltammogram recorded for the gold electrode functionalised with Fe(III)-phthalocyanine chloride. The onset for the cathodic wave is at $E_{onset} \cong 0.65$ V and a broad reduction peak is centred at $E_p = 0.48$ V. In the case of Fe(III)Pc-Cl, iron centres retain their initial (III) oxidation state, due to the acidic environment and to the initial applied potential, as confirmed by the Pourbaix diagram (Fig. 5.4b). Along the anodic scan, it is not possible to detect a clear oxidation peak for the reversible oxidation of Fe(II) to Fe(III), but only a low-current smeared peak appears at [+0.55; +0.65] V. As did for the Fe(II)Pc case, this anodic wave is ascribed to the re-oxidation of the Fe(II) centre to the initial Fe(III) state in a slow and poorly detectable process. In fact, by safely restricting the scan in the range [+0.15; +0.65] V, the CVs of Fig. 5.6b are obtained.

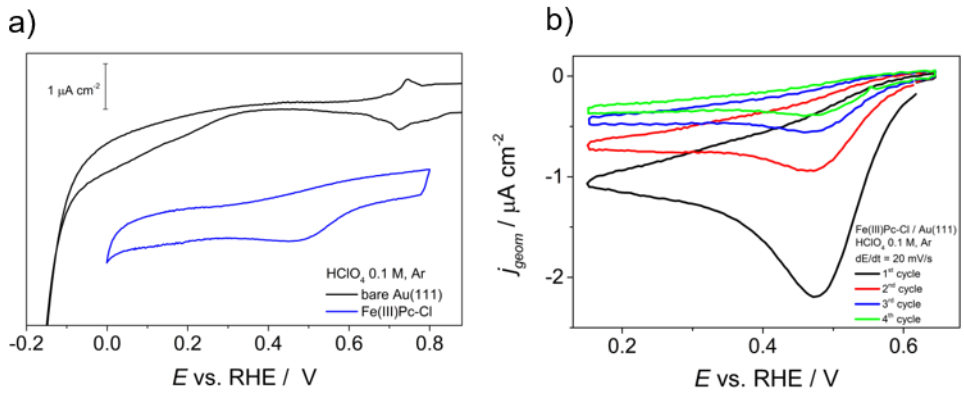

Figure 5.6: (a) CVs of Au(111) (black line) and Fe(III)Pc-Cl-functionalised Au(111) (blu line) electrodes in argon purged 0.1 M $HClO_4$ recorded at 0.2 V/s; (b) consecutive CVs and of Fe(III)Pc-Cl -functionalised Au(111) electrodes in argon purged 0.1 M $HClO_4$.

Figure 5.6b shows the consecutive scans recorded at Fe(III)Pc-Cl-functionalised Au(111), where it is visible a reduction in the current density peak by a factor ~2, upon consecutive cycling of the electrode and by the fourth cycle the Fe(III)/Fe(II) reduction peak has almost disappeared, similarly to what observed for Fe(II)-Phthalocyanine. Although the scan range had been prudentially limited at +0.15 V in the cathodic side, a decrease in the peak potential was revealed, even if its extent is smaller than what encountered for Fe(II)Pc.

The effect of the scan rate on the Fe(III)Pc-Cl functionalised Au(111) electrode is reported in Figure 5.7a and b; for the sake of simplicity, the obtained CVs were redistributed in two graphs: Figure 5.4a from 1 mV/s to 50 mV/s, whereas Figure 5.4.b accounts for the CVs registered with scan rates from 100 mV/s to 1000 mV/s.

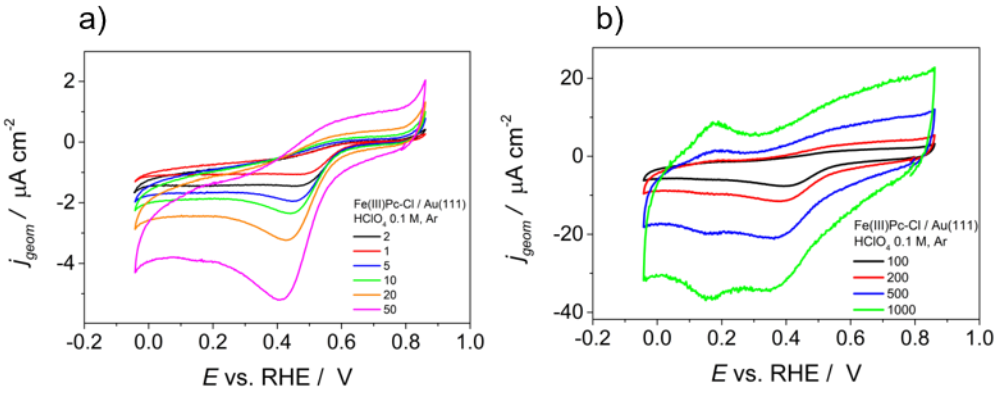

Figure 5.7: CVs at Fe(III)Pc-Cl-functionalised Au(111) electrodes in argon purged 0.1 M $HClO_4$ recorded at different scan rates (a) low values and (b) high values.

At low scan rates, up to 20 mV/s, the unique noticeable feature is the reduction wave of the Fe(III)/Fe(II) redox couple, as already explained. However, at higher scan rates, a new redox reversible couple can be observed at ~ 0.16-0.19 V. According to the Pourbaix diagram of Figure 5.4b, the stability interval of Fe(I) should begin at ~0.15 V (vs RHE) for Fe-phthalocyanine adsorbed on OPG electrode immersed in acidic medium. However, Alsudairi et al. shown that these peaks are actually related to the interaction of redox couple Fe(II)/Fe(I) with the phthalocyanine ligand, and not to the direct Fe(II)/Fe(I) redox process [36], since, Fe(I) would require a strong axial ligand as stabiliser. Hence, in the mechanism suggested by Alsudairi, the additional electron gained by iron when assuming the (I) oxidation state is spontaneously delocalised into an empty π^* orbital of the phthalocyanine ring, resulting in the formation of $[Fe(II)Pc]^-$. The electron is supposed to be shuttled from the Fe(I) species, formed at properly negative applied potential, to the ligand ring (phthalocyanine) thanks to its delocalised π system. The electron follows the opposite path when the electrode potential is anodically scanned, forming the transient Fe(I) species, which then oxidises to Fe(II). In this way, the corresponding anodic peak is generated.

It is worth noting, that in the present case Cl^- is available in the electrolyte solution, and whether neither ClO_4^- nor water molecule are sufficiently good ligands, Cl^- can actually be a sufficient strong ligand. Therefore it is also possible that Cl^- can coordinate Fe(I) in axial position, so that it cannot be excluded that the reversible redox couple can be also assigned to the Fe(II)/Fe(I) transition.

In both cases, the fact that significantly high scan rates (> 50 mV/s) up to 1 V/s, contrary to the most frequent experimental cases (at least for ORR studies), are needed to notice the reversible couple may be correlated with the rate of the involved reactions and/or with the nature of the mechanisms involved. At low scan rates, it is possible that the Fe(I) centres are not even formed due to its presumed instability or because are not fulfilled the conditions for a quick electron transfer to the ligand ring. Contrary, high potential sweep rates might detect the electron transfer from Fe(I) to phthalocyanine or for the Fe(II)/Fe(I) transition, since slow sideway reactions can be freezed.

5.2.3 Cyclic voltammetry of Fe(III)TMPP-Cl in Ar purged electrolyte

Figure 5.8a compares the CV curve obtained for bare Au(111) with the voltammogram recorded for the gold electrode functionalised with Fe(III)-tetramethoxyphenyl porphyrin chloride.

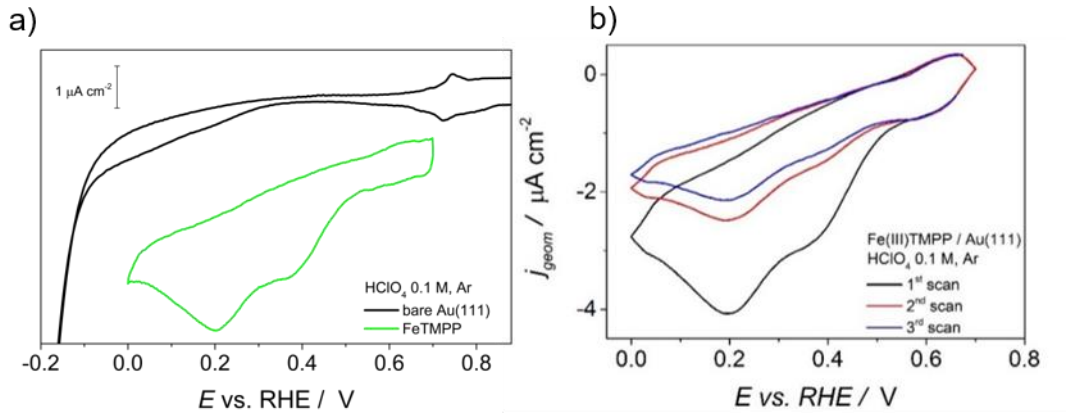

Figure 5.8: (a) CVs of Au(111) (black line) and Fe(III)TMPP-Cl -functionalised Au(111) (blu line) electrodes in argon purged 0.1 M $HClO_4$ recorded at 0.2 V/s; (b) consecutive CVs and of Fe(III)TMPP-Cl -functionalised Au(111) electrodes in argon purged 0.1 M $HClO_4$.

The cathodic scan exhibits two peaks with peak potentials at $E_p \cong 0.39$ V and at $E_p = 0.20$ V, respectively. The anodic side does not feature any particular voltammetric shape. The first cathodic wave is, like for Fe(II)Pc and Fe(III)Pc-Cl, attributed to the reduction of the iron centre from Fe(III) to Fe(II), even if the redox process occurs at more negative potential than what previously observed with phthalocyanines. Nonetheless, similar data were recorded by M. Fujihira et al. [37,38] for a Fe-porphyrin adsorbed on a carbon electrode and by Yoshimoto for a Fe-porphyrin adsorbed on Au(111) [30]. The meso-tetramethoxyphenyl substituents exert an electron donating effect on the Iron centre and it is expected to induce a cathodic shift on the reduction potentials of the Fe(III)/Fe(II) couple [5,21], in accordance with the obtained experimental evidences.

The more intense cathodic peak at $E_p = 0.20$ V is ascribed to reduction of the porphyrin ligand itself, similarly to what observed with Fe(III)-phthalocyanine chloride. Investigations on a free-base pyridyl porphyrin adsorbed on Au(111) electrodes showed that a peak potential close to the one observed in this work, can be related to redox properties of the ligand alone [39]. Zinc-porphyrin and -phthalocyanine were also revealed to exhibit redox properties related to the ligand framework [40].

When consecutive scans were repeated on the Fe(III)TMPP-Cl-modified Au(111) surface (Fig.5.8b), a progressive loss in cathodic current was noticeable. Considering the cathodic wave ascribed to the Fe(III)/Fe(II) redox process, the loss in current density justifies a slow re-oxidation of the iron centres, as hypothesised for the Fe-phthalocyanine systems (section 5.2.1). The diminution in current density for the more intense peak was detected also for Zinc(II)-tetraphenyl porphyrin adsorbed on Au(111) [40]**,** and it was associated not only to a redox behaviour of the ring ligand, but also to order-disorder phenomena of molecules on the Au(111) surface.

5.3 Cyclic voltammetry investigation of FeN_4 macrocycles in O_2 saturated electrolyte

The catalytic effect towards ORR was evaluated by bubbling the electrolytic solution with O_2 gas. Cyclic voltammograms were registered both with freshly-functionalised electrodes and for electrodes which already underwent CV investigation in deaerated electrolyte. No significant deviations were detected between the two experimental conditions if the potential sweeps in deaerated electrolyte were limited in number (< 10).

The examined FeN_4 molecules shown a catalytic effect towards O_2 reduction. The electrocatalytic activity was measured in terms of peak potential (E_p), at which the ORR process occurs. O_2 reduction should thermodynamically occur at a standard potential of $E°_{O_2} = 1.23\ V$ [41], and the rupture of the O-O bond should lead to the production of water. However, the O-O dissociation energy is 118 kcal/mol [10] and proper catalysts are required to increase the rate of the reaction [42]. The process of catalysis occurring at an electrode surface is regarded as a heterogeneous catalysis phenomenon, since the catalyst occupies a different phase from the reactants and products [43]. Au(111) is regarded as a bad catalyst toward ORR and a high overpotential is needed for the O_2 reduction to take place. The first step of O_2 reaction is stated as the adsorption at the gold surface in acidic environment:

$$O_2 + H^+ + e^- \rightarrow (HO_2)_{ads} \qquad (5.10)$$

At the equilibrium potential of $E = -0.046\ V$ neither oxygen nor hydrogen chemically adsorb on gold, leading to an overall bad oxygen reduction catalysis in acidic media [44,45].

5.3.1 Cyclic voltammetry of Fe(II)Pc in O_2 saturated electrolyte

The cyclic voltammogram obtained at bare Au(111) electrode in 0.1 M $HClO_4$ is reported in Figure 5.9a. The cyclic voltammogram of bare Au in O_2 saturated electrolyte features a cathodic wave with an onset potential at $E_{onset} \approx 0.4$ V, but it does not show any distinctive reduction peak. The O_2 reduction is therefore occurring in a not-defined and wide potential window, starting from the onset at 0.4 V and continuing up to the HER region at ≈ –0.2 V. This is the experimental evidence of a bad catalysis towards ORR, which makes Au(111) suitable for FeN_4 performances evaluation towards ORR in acidic medium.

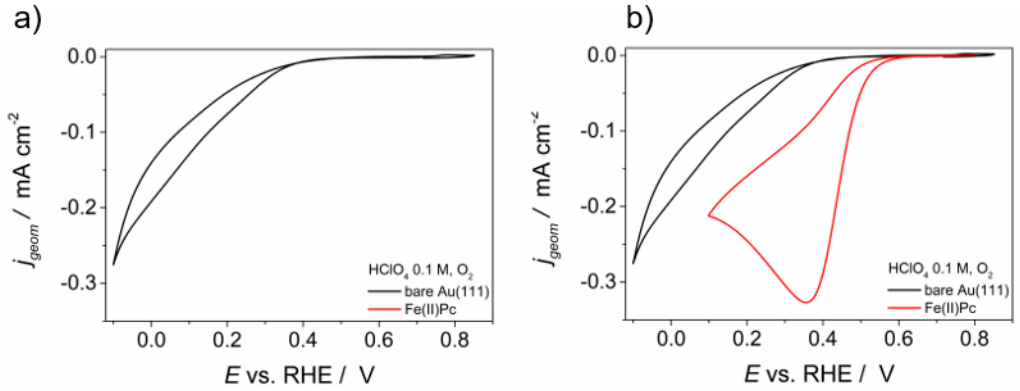

Figure 5.9: (a) CVs of Au(111) electrode in O_2 saturated 0.1 M $HClO_4$ recorded at 0.2 V/s; (b) comparison between Au(111) (black line) and Fe(II)PC -functionalised Au(111) (red line) electrodes in O_2 saturated 0.1 M $HClO_4$.

The comparison between Au(111) and Fe(II)Pc-functionalised Au(111) electrodes in O_2 saturated 0.1 M $HClO_4$ is reported in Figure 5.9b. Conversely to Au(111), Fe(II)Pc - functionalised Au(111) electrode shows a well-defined reduction peak for O_2 reduction. The cathodic peak onset is at E_{onset} ~0.6 V and the reduction peak potential at E_p = 0.37 V. The Fe(II)Pc adlayer is therefore showing an appreciable catalytic activity towards ORR with respect to bare gold of almost 0.3 V. It must be noted that the peak potential is close to the one observed in the absence of O_2 at the Fe(II)Pc adlayer and related to the reduction of Fe(III) to Fe(II), which creates the Fe(II) active sites, enabling O_2 adsorption and its further reduction. This is therefore in accordance with the expected behaviour of the FeN_4, where the Fe centre first undergoes an electron transfer, passing from the (III) oxidation state to the (II) reduced form, after which O_2 adsorbs to be reduced in a cascade steps of electron transfer and bond formation and breaking leading to H_2O or H_2O_2. Furthermore, the current density is two orders of magnitude higher than the previously recorded voltammograms in deaerated electrolyte.

The Randles-Sevcik equation describes the peak current for a reversible (Nerstian) system, showing a dependence on the square root of the scan rate according to the eq. 5.11:

$$i_{p_{rev}} = 0{,}4463nFAC_O^* \left(\frac{nF}{RT}\right)^{1/2} v^{1/2} \qquad (5.11)$$

The case of oxygen reduction reaction is however regarded as an irreversible process, and the shape of the obtained voltammogram for Fe(II)Pc (Fig. 5.9b) is a clear example of an irreversible system. Irreversibility occurs when the electron transfer is very slow. Therefore, to observe a net current, the process needs to be strongly activated by application of a large overpotential, which is defined as the extra potential to be added to the thermodynamic standard potential for the associated reaction to occur. The main feature of an irreversible system is the absence of counter peak in the reverse scan. The mathematical treatment of irreversible systems is similar to that of Nerstian system, but in the place of Nernst equation, the Butler-Volmer expression is required for linking the current to the potential. The final expression for the peak current of an irreversible system is given by:

$$i_{p_{irr}} = 0.4958nFAC_O^* D_o^{1/2} \left(\frac{\alpha F}{RT}\right)^{1/2} v^{1/2} \qquad (5.12)$$

The peak current is in both cases dependent on $v^{1/2}$, which is therefore not a discriminating criterion for reversibility. It is rather the signature of diffusion-controlled phenomena occurring at the electrode surface and it is opposed to the electrochemical response of adsorbed monolayer. The characteristic current-scan rate dependence would be given, for a system in which the oxidised species O is adsorbed and the reduced electroactive species R, by [46]:

$$i_{p,ads} = \frac{n^2F^2}{4RT} vA\Gamma_O^* \qquad (5.13)$$

where Γ_O^* is the amount of O species adsorbed at *t = 0*, *n* is the number of involved electrons, *v* is the scan rate. Note that adsorbed monolayers are in this case referred as the electroactive species subjected to oxidation or reduction processes. In the case of oxygen reduction reaction, the reacting species, i.e. O_2, is fully belonging to the liquid phase and its electrochemical response is expected to be properly described by that of a diffusion-controlled system, for which relations (5.11) or (5.12) hold for reversible or irreversible processes, respectively.

By fitting the experimental peak current against the corresponding square root of scan rate, a linear regression is obtained, (Figure 5.10). The corresponding fitting parameters

(intercept, slope and associated standard deviations, adjusted R square coefficient) are reported in the alleged table 5.1.

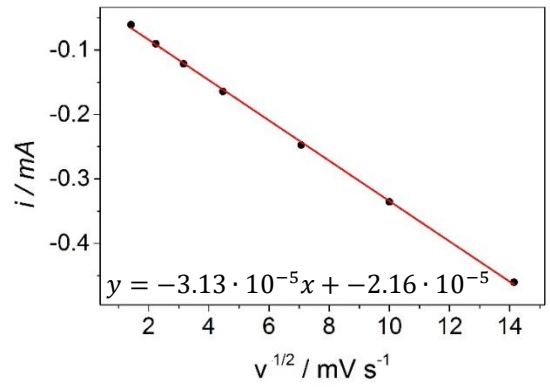

i_p vs $v^{1/2}$	a	Δa
Intercept	$-2.16 \cdot 10^{-5}$	$2.5 \cdot 10^{-6}$
	b	Δb
Slope	$-3.13 \cdot 10^{-5}$	$3 \cdot 10^{-7}$
R-Square	0.9993	

Figure 5.10: i_p vs $v^{1/2}$ plot of O_2 reduction at Fe(II)PC -functionalised Au(111) electrodes in 0.1 M $HClO_4$. **Table 5.1:** Fitting parameters of Figure 5.10.

The goodness of fit is expressed by a R square coefficient close to 1 (> 0.99), confirming that the experimental peak current has a linear dependence on the scan rate square root. This means that the O_2 molecules undergo a diffusion-controlled electrochemical process at the Fe(II)Pc-modified Au(111) electrodes.

The distinctive charateristic of an irreversible system with respect to reversible systems lies in the linear depency of the peak potential on the logarithm of the scan rate.The expression of the peak potential is mathematically derived by a similar procedure that led to determination of the peak potential for a Nerstian system (eq. 5.14). For the sake of simplicty, the result is reported:

$$E_p = E^{\circ\prime} - \frac{RT}{\alpha F}\left[0.78 + \ln\left(\frac{D_O^{\frac{1}{2}}}{k^\circ}\right) + \ln\left(\frac{\alpha F v}{RT}\right)^{\frac{1}{2}}\right] \qquad (5.14)$$

The experimental peak potential were therefore subjected to linear regression algorithm, leading to the fitting line of Figure 5.11 and the corresponding fitting parameters are reported in the Table 5.2. The very good correlation confirms the irreversible nature of the observed peaks for oxygen reduction reaction.

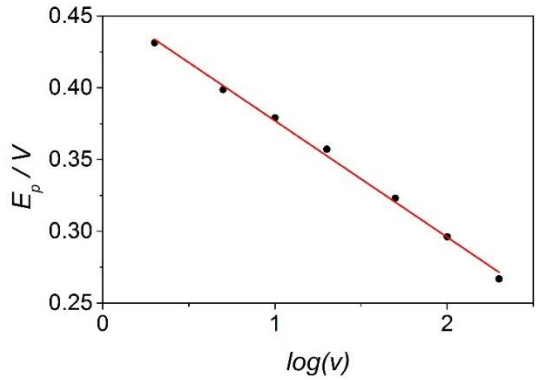

E_p vs Log$v$	a	Δa
Intercept	0.458	0.003
	b	Δb
Slope	-0.0811	0.0021
R-Square	0.9964	

Figure 5.11: E_p vs log$v$ plot of O_2 reduction at Fe(II)PC -functionalised Au(111) electrodes in 0.1 M $HClO_4$. **Table 5.2:** Fitting parameters of Figure 5.11.

5.3.2 *Cyclic voltammetry of Fe(III)Pc-Cl in O_2 saturated electrolyte*

Fe(III)-Phthalocyanine chloride is now taken into exam in its ability to reduce oxygen. The corresponding voltammogram registered in O_2 saturated electrolyte is reported in Figure 5.12a.

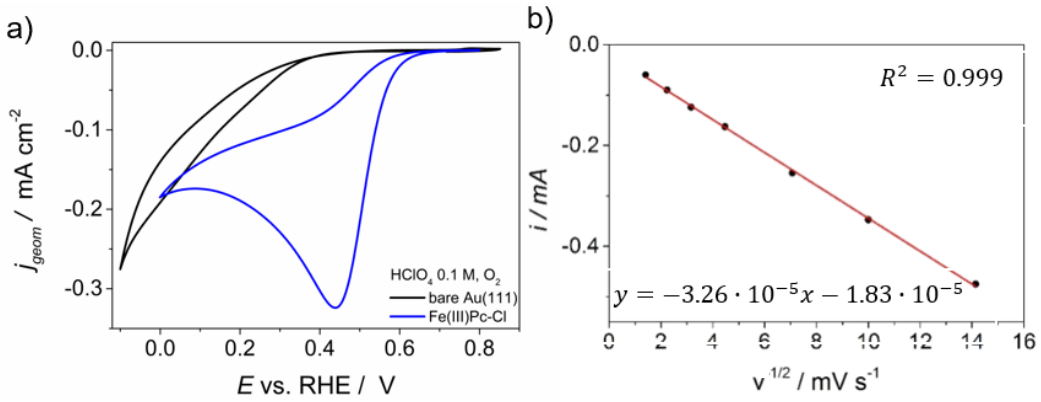

Figure 5.12: (a) comparison between Au(111) (black line) and Fe(III)PC-Cl-functionalised Au(111) (blue line) electrodes in O_2 saturated 0.1 M $HClO_4$; (b) i_p vs $v^{1/2}$ plot of O_2 reduction at Fe(III)PC-Cl-functionalised Au(111) electrodes in 0.1 M $HClO_4$.

Fe(III)-phthalocyanine chloride shown the most positive Fe(III)/Fe(II) peak potential among all the FeN_4 studied and it is therefore expected to exert the best catalytic activity towards ORR. The onset potential for the observed cathodic wave is at $E_{onset} \cong 0.67$ V and the corresponding peak potential is at $E_p = 0.44$ V. As did for Fe(II)Pc, the measured current peaks for Fe(III)-Phthalocyanine chloride were subjected to linear regression algorithm against the scan rate square root that proved the diffusion-controlled regime.

The nature of irreversibility was tested by a linear fitting of the experimental peak potentials against the calculated logarithm of the corresponding scan rates, as shown in Figure 5.13 which encloses the fitting parameters.

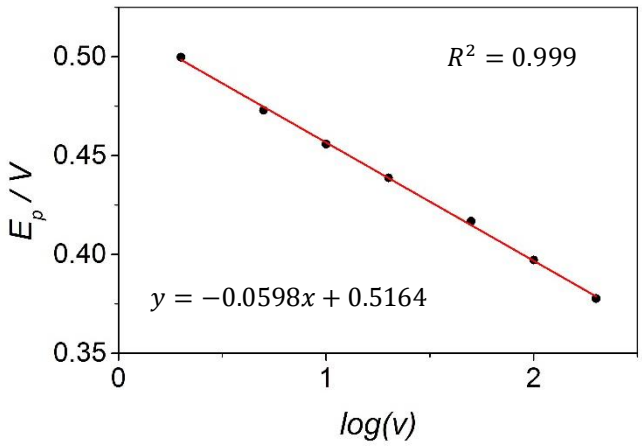

Figure 5.13: E_p vs log$v$ plot of O_2 reduction at Fe(III)PC-Cl-functionalised Au(111) electrodes in 0.1 M $HClO_4$.

5.3.3 Cyclic voltammetry of Fe(III)TMPP-Cl in O_2 saturated electrolyte

The cyclic voltammogram obtained for Fe-tetramethoxyphenyl porphyrin chloride in O_2 saturated electrolyte is reported in Figure 5.14.

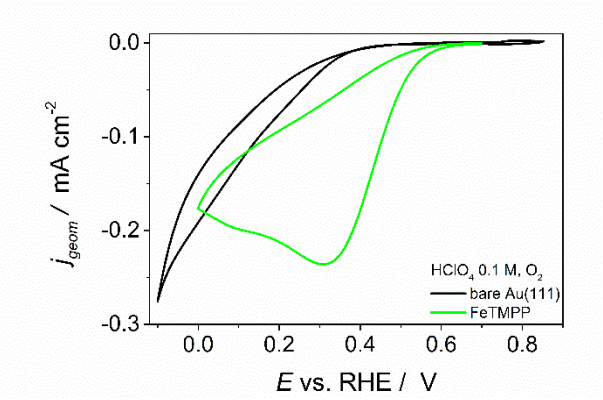

Figure 5.14: Comparison between Au(111) (black line) and Fe(III)TMPP-Cl-functionalised Au(111) (green line) electrodes in O_2 saturated 0.1 M $HClO_4$.

The CV in deaerated electrolyte shown that FeTMPP possesses the most negative Fe(III)/Fe(II) redox potential. Proven that the Fe(III)/Fe(II) has a serious concern in O_2 reduction electrocatalysis, one can expect FeTMPP to behave worse than Fe(II)Pc and Fe(III)Pc-Cl towards ORR. This is actually verified, since the reduction peak potential is found at E_p = 0.31 V. The CV interestingly retains the second peak that was previously observed in absence of O_2, with a shape which is no longer well resolved. The associated ring redox transition is in fact forced to occur at potentials close to the extensive process of O_2 reduction, and for this reason the detected potential appears cathodically shifted to E_p = 0.10 V, even if a clear peak potential could not be measured. The effect of the scan rate on the peak potential un current peak can be extended also to FeTMPP-Cl system.

To sum up, all the three FeN_4 systems were found to act as catalysts towards O_2 reduction, confirming the key-role of the central iron atom. Thanks to cyclic voltammetric investigations conducted in deaerated electrolyte, the redox behaviour of the Fe(III)/Fe(II) couple was confirmed. This is a crucial step that leads to the generation of the real active site for ORR, that is Fe(II). The peak potential detected in the cathodic scan of each molecular system in O_2 saturated electrolyte is slightly more negative (less than 100 mV) than the corresponding detected Fe(III)→Fe(II) redox peak potential in Ar saturated electrolyte. The nature of irreversibility for oxygen reduction reaction at the FeN_4-modified Au(111) electrode was explored through the expressions of a diffusion-limited system.

Fe(III)TMPP-Cl revealed to exhibit the lowest catalytic activity among the studied systems, whereas Fe(III)Pc-Cl turned out to be a better catalyst than Fe(II)Pc. The lower activity of Fe(III)TMPP-Cl can be explained in terms of a different chemical environment provided by the porphyrin ligand in lieu of the phthalocyanine ring, whose plausibility is confirmed by a more intense ring redox peak revealed at E_p = 0.20 V. Only Fe(III)-phthalocyanine chloride was in fact showing a similar feature, but at significantly higher scan rates.

5.4 Effect of chloride anions on the FeN_4 macrocycles electrochemical behaviour

From Figure 5.4a and 5.6a it can be noticed that Fe(II)-Phthalocyanine and Fe(III)-Phthalocyanine chloride possess a slightly different electrochemical behaviour, despite being characterised by the same molecular structure. The ligand is in fact exactly the same, i.e. phthalocyanine without any substituent. The initial oxidation state of iron is not considered a major issue, since also Fe(II)-phthalocyanine was found to undergo the Fe(III)→Fe(II) process even at the first scan. The only significant dissimilarity between Fe(II)Pc and Fe(III)Pc-Cl is then assigned to the presence of chloride as axial ligand of the iron centre. The initial oxidation state of iron is primarily the consequence of the presence of chloride in the molecular crystal structure, that affects the solubility properties of the complex. In fact, axial ligands are known to increase the solubility of metal-phthalocyanines and -porphyrins by modifying the π-electronic distribution upon introduction (or strengthening) of a dipole moment along the metal-axial bond [47,48].

The presence of an axial ligand may rise a great interest towards the O_2 reduction mechanism. The iron-phthalocyanine may be thought of as a plane, which adsorbs with flat geometry on the Au surface with whichever of the two moieties. It belongs to the D4h point group and it therefore possesses a symmetry plane embedding the isoindole groups as well as the iron centre. This is true for Fe(II)-phthalocyanine without axial substituents. If chloride is present as the fifth axial ligand, then the symmetry is reduced to C4v and differences may arise during the adsorption of Fe(III)Pc-Cl onto the Au surface. One might think that phthalocyanine adsorbs with the remaining free moiety, favoured by the retention of a planar arrangement at the gold surface. It must be recalled that chloride is a strong-adsorbing species, even capable of specific adsorption on many single crystal surfaces [31]. Fe(III)Pc-Cl may therefore adsorb with a face down configuration, namely exposing Cl to the Au surface and causing the Fe centre to slightly protrude out of the molecular plane. A third possibility is that chloride is lost from the metal centre but adsorbs on the Au surface due to its strong tendency to specifically adsorb. This is why it is reasonable to consider the possibility of a different electrochemical response of Fe(III)Pc-Cl with respect to Fe(II)Pc when they are adsorbed on the gold electrode, both in terms of Fe(III)/Fe(II) redox behaviour and of O_2 reduction electrocatalysis.

In this regard, a special cyclic voltammetry experiment was dedicated to the exploration of a possible effect of chloride on the aforementioned properties. On the basis of the calculated molecular surface concentration, which is in the order of 10^{13} molecules/cm^2, an equal number of chloride anions was calculated. For 80 mL of 0.1 M $HClO_4$ introduced in the electrochemical cell, a concentration of $4.96 * 10^{-10}\ M$ in chloride needed to be realised. Hydrochloric acid was selected as chloride source, being a strong acid able to fully dissociate in water. Consecutive dilutions were performed with glass micro-syringe, which allow to pick up microliters of liquid avoiding contaminations, since glass can be cleaned with Piranha etching as described in section 3.2.4. The suitable aliquot of Cl^- was added after the introduction of the electrode in the electrolytic solution.

Figure 5.15 compares the CV curve obtained for bare Au(111) with the voltammogram recorded for the gold electrode functionalised with Fe(II)-phthalocyanine, to which $4.96 \cdot 10^{-10}$ M of HCl were added. This experimental condition is termed as "Fe(II)Pc + Cl^-". The cyclic voltammogram shows a cathodic peak with an onset at $E_{onset} \cong 0.65$ V and a poorly resolved peak at $E_p = 0.45$ V. For a better understanding, cyclic voltammograms were

compared, for Fe(II)Pc and Fe(II)Pc + Cl^-, and for Fe(II)Pc + Cl^- and Fe(III)Pc-Cl, in Figure 5.16a and b, respectively.

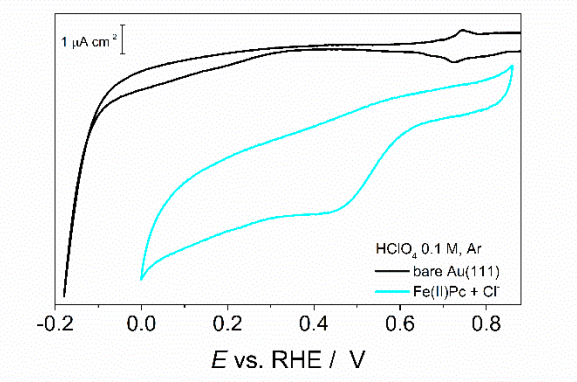

Figure 5.15: Comparison between Au(111) (black line) and Fe(II)Pc-functionalised Au(111) (azure line) electrodes in Ar purged 0.1 M $HClO_4$ + Cl^-.

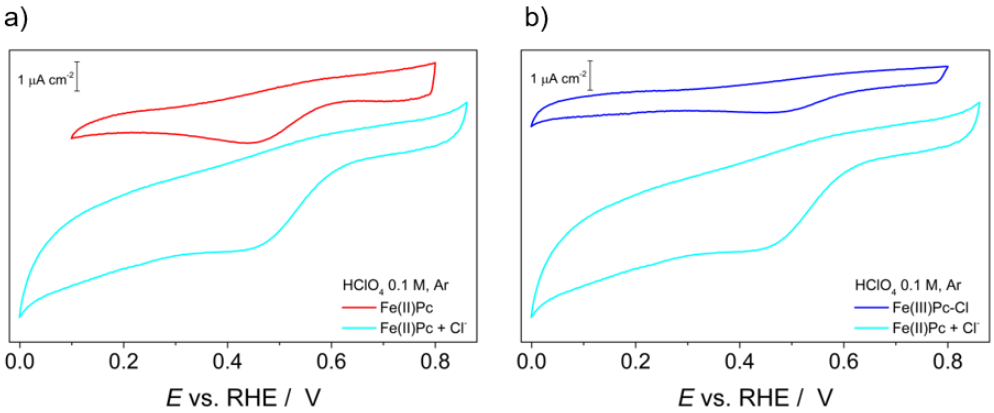

Figure 5.16: (a) Comparison between Fe(II)Pc-functionalised Au(111) electrodes in O_2 saturated 0.1 M $HClO_4$, in the presence and absence of Cl^-; (b) comparison between Fe(III)Pc-Cl-functionalised Au(111) and Fe(II)Pc + Cl^--functionalised Au(111) electrodes and in Ar purged 0.1 M $HClO_4$.

The obtained voltammogram for the Fe(II)Pc + Cl^- system is intermediate between those registered for Fe(II)Pc and Fe(III)Pc-Cl. This means that chloride is not innocent towards the redox behaviour of the Fe centre, even if at this stage it cannot be stated how its adsorption occurs in the presence of previously adsorbed Fe(II)Pc molecules.

The role of chloride on the iron-phthalocyanine catalytic activity towards ORR was evaluated also in O_2 saturate $HClO_4$ electrolyte and CV recorded at chloride-modified Fe(II)Pc adlayer on Au(111) is displayed in Figure 5.17.

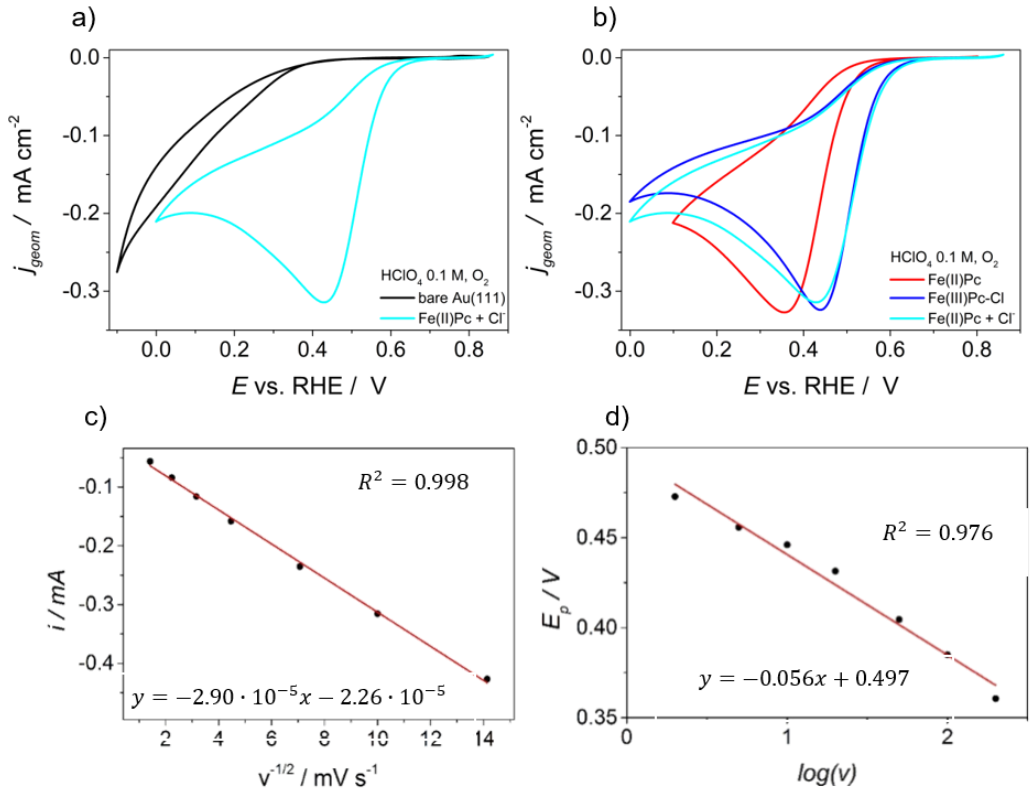

Figure 5.17: (a) Comparison between Au(111) (black line) and Fe(II)Pc-functionalised Au(111) (azure line) electrodes in O_2 saturated 0.1 M $HClO_4$ + Cl^-; (b) comparison between Fe(II)Pc, Fe(III)Pc-Cl and Fe(II)Pc + Cl^- electrodes in O_2 saturated 0.1 M $HClO_4$ + Cl^-; (c) i_p vs $v^{1/2}$ plot and (d) E_p vs log$v$ plot of O_2 reduction at Fe(II)Pc-functionalised Au(111) electrodes in 0.1 M $HClO_4$ + Cl^-.

It is confirmed that the presence of chloride, disregarding whether it still retains its axial ligand position or it is co-adsorbed, enhances the catalytic performances of the Fe(III)Pc-Cl adlayer with respect to the Fe(II)Pc one. This can simply be a consequence of a higher reduction potential detected for the Fe(III)/Fe(II) couple, determining also a more positive ORR peak. Another possibility is that the presence of chloride also acts by modifying the O_2 interaction with the active site, leading to a slightly enhanced ORR activity, in accordance with recent computational advances of Wang et al. [22] and of Arenz et al. [49]. The presence of an axial ligand causes the iron atom to retain a (III) oxidation state. In the case of cyanogen CN, the Fe(III) is predicted to have a less effective electron donation capability to the antibonding π^* orbitals of O_2, causing however only a small worsening effect onto ORR performances. Arenz et al. shown that strong anion-catalyst interaction does not automatically result in a worsening in ORR activity [49]. The Fe site activity is actually tuned by the presence of a fifth ligand in axial position and forces the reacting molecule (O_2) to interact with the unique free position of iron. Dihydrogen phosphate ($H_2PO_4^-$) and chloride (Cl^-) are both predicted to weaken the Fe-O bond, causing a more energetically unfavourable OOH formation than the OH removal. Note that OH is a key-species in the 4e$^-$ mechanism for the desired O_2 conversion to H_2O.

References

[1] D.R. Tackley, G. Dent, W.E. Smith, *Phthalocyanines: Structure and vibrations*, Phys. Chem. Chem. Phys., **2001**, *3*, 1419–1426.

[2] D.W. Oxtoby, H.P. Gillis, A. Campion, *Principles of Modern Chemistry*, 7th edition, Cengage Learning, **2012**.

[3] J.H. Zagal, M.T.M. Koper, *Reactivity Descriptors for the Activity of Molecular MN4 Catalysts for the Oxygen Reduction Reaction*, Angew. Chemie - Int. Ed., **2016,** *55*, 14510–14521.

[4] J.H. Zagal, F. Bedioui, J.P. Dodelet, *N4-Macrocyclic Metal Complexes*, Springer, **2006**.

[5] J. Masa, W. Schuhmann, *Systematic selection of metalloporphyrin-based catalysts for oxygen reduction by modulation of the donor-acceptor intermolecular hardness*, Chem. - A Eur. J., **2013**, *19*, 9644–9654.

[6] Y. Oliver Su, T. Kuwana, S.M. Chen, *Electrocatalysis of oxygen reduction by water-soluble iron porphyrins. Thermodynamic and kinetic advantage studies*, J. Electroanal. Chem., **1990**, *288*, 177–195.

[7] M. Shao, *Electrocatalysis in Fuel Cells*, **2015**.

[8] J.H. Zagal, S. Griveau, J.F. Silva, T. Nyokong, F. Bedioui, *Metallophthalocyanine-based molecular materials as catalysts for electrochemical reactions*, Coord. Chem. Rev.,**2010**, *254*, 2755–2791.

[9] J.H. Zagal, M.A. Paez, A.A. Tanaka, J.R.J. dos Santos, C.A. Linkous, *Electrocatalytic activity of metal phthalocyanines for oxygen reduction*, J. Electroanal. Chem., **1992**, *339*, 13–30.

[10] J.H. Zagal, *Metallophthalocyanines as catalysts in electrochemical reactions*, Coord. Chem. Rev., **1992**, *119*, 89–136.

[11] K. Liu, Y. Lei, G. Wang, *Correlation between oxygen adsorption energy and electronic structure of transition metal macrocyclic complexes*, J. Chem. Phys., **2013**, *139*, 204306, 1-9.

[12] S. Zheng, Z. Jiujun, *Density functional theory study of transitional metal macrocyclic complexes' dioxygen-binding abilities and their catalytic activities toward oxygen reduction reaction*, J. Phys. Chem. C., **2007**, *111*, 7084–7090.

[13] R.G. Pearson, *Absolute electronegativity and hardness correlated with molecular orbital theory.*, Proc. Natl. Acad. Sci. U. S. A., **1986**, *83*, 8440–8441.

[14] R.G. Parr, R.G. Pearson, *Absolute Hardness: Companion Parameter to Absolute Electronegativity*, J. Am. Chem. Soc., **1983**, *105*, 7512–7516.

[15] M. Savy, P. Andro, C.B. et G. Magner, *Etude de la reduction de l'oxygene sur les phthalocyanines monomeres polymeres-I. Principes fondamentaux, choix de l'ion central*, Electrochim. Acta., **1973**, *18*, 191–197.

[16] K. Wiesener, D. Ohms, V. Neumann, R. Franke, *N_4 macrocycles as electrocatalysts for the cathodic reduction of oxygen,* Mater. Chem. Phys., **1989**, *22*, 457–475.

[17] P. Vasudevan, Santosh, N. Mann, S. Tyagi, *Transition metal complexes of porphyrins and phthalocyanines as electrocatalysts for dioxygen reduction,* Transit. Met. Chem., **1990**, *15*, 81–90.

[18] J.A.R. van Veen, J.F. van Baar, H.A. Colijn, J.G.F. Coolegen, N. de Wit, *Oxygen Reduction on Transition-Metal Porphyrins in Acid Electrolyte I. Activity*, Berichte Der Bunsengesellschaft Für Phys. Chemie., **1981**, *85*, 693–700.

[19] J.A.R. van Veen, C. Visser, *Oxygen reduction on monomeric transition metal phthalocyanines in acid electrolyte*, Electrochim. Acta., **1979**, *24*, 921–928.

[20] J. Manassen, A. Bar-Ilan, *Metal complexes of phthalocyanine and α,β,γ,δ-tetraphenyl porphyrin as heterogeneous catalysts in oxidative dehydrogenation. Correlation between catalytic activity and redox potential*, J. Catal., **1970**, *17*, 86–92.

[21] R. Baker, D.P. Wilkinson, J. Zhang, *Electrocatalytic activity and stability of substituted iron phthalocyanines towards oxygen reduction evaluated at different temperatures*, Electrochim. Acta., **2008**, *53*, 6906–6919.

[22] Y. Wang, H. Yuan, Y. Li, Z. Chen, *Two-dimensional iron-phthalocyanine (Fe-Pc) monolayer as a promising single-atom-catalyst for oxygen reduction reaction: A computational study,* Nanoscale., **2015**, *7*, 11633–11641.

[23] T.S. Olson, S. Pylypenko, J.E. Fulghum, P. Atanassov, *Bifunctional Oxygen Reduction Reaction Mechanism on Non-Platinum Catalysts Derived from Pyrolyzed Porphyrins*, J. Electrochem. Soc., **2010**, *157*, B54.

[24] J. Perez, E.R. Gonzalez, H.M. Villullas, *Hydrogen Evolution Reaction on Gold Single-Crystal Electrodes in Acid Solutions*, J. Phys. Chem. B., **1998**, *102*, 10931–10935.

[25] K. Uosaki, G. Elumalai, H.C. Dinh, A. Lyalin, T. Taketsugu, H. Noguchi, *Highly Efficient Electrochemical Hydrogen Evolution Reaction at Insulating Boron Nitride Nanosheet on Inert Gold Substrate*, Sci. Rep., **2016**, *6*, 32217.

[26] A. Hamelin, *Cyclic voltammetry at gold single-crystal surfaces. Part 1. Behaviour at low-index faces*, J. Electroanal. Chem., **1996**, *407*, 1–11.

[27] H. Angerstein-Kozlowska, B.E. Conway, A. Hamelin, L. Stoicoviciu, *Elementary steps of electrochemical oxidation of single-crystal planes of Au Part II. A chemical and structural basis of oxidation of the (111) plane*, J. Electroanal. Chem., **1987**, *228*, 429–453.

[28] H. Angerstein-Kozlowska, B.E. Conway, A. Hamelin, L. Stoicoviciu, *Elementary steps of electrochemical oxidation of single-crystal planes of Au-I. Chemical basis of processes involving geometry of anions and the electrode surfaces*, Electrochim. Acta., **1986**, *31*, 1051–1061.

[29] S. Yoshimoto, A. Tada, K. Suto, K. Itaya, *Adlayer Structures and Electrocatalytic Activity for O 2 of Metallophthalocyanines on Au(111): In Situ Scanning Tunneling Microscopy Study*, J. Phys. Chem. B., **2003**, *107*, 5836–5843.

[30] S. Yoshimoto, A. Tada, K. Itaya, *In Situ Scanning Tunneling Microscopy Study of the Effect of Iron Octaethylporphyrin Adlayer on the Electrocatalytic Reduction of O2 on Au(111)*, J. Phys. Chem. B., **2004**, *108*, 5171–5174.

[31] O.M. Magnussen, *Ordered anion adlayers on metal electrode surfaces*, Chem. Rev., **2002**, *102*, 679–725.

[32] J.H. Zagal, M.A. Paez, J. Sturm, S. Ureta-Zanartu, *Electroreduction of Oxygen on Mixtures of Phthalocyanines co-adsorbed on a Graphite Electrode*, J. Electroanal. Chem., **1984**, *181*, 295–300.

[33] J.Y. Gu, Z.F. Cai, D. Wang, L.J. Wan, *Single Molecular Imaging of Iron-Phthalocyanine Catalyzed Oxygen Reduction Reaction by in situ Scanning Tunneling Microscopy*, ACS Nano., **2016**, 1–10.

[34] K. Suto, S. Yoshimoto, K. Itaya, *Electrochemical control of the structure of two-dimensional supramolecular organization consisting of phthalocyanine and porphyrin on a gold single-crystal surface*, Langmuir., **2006**, *22*, 10766–10776.

[35] S. Yoshimoto, J. Inukai, A. Tada, T. Abe, T. Morimoto, A. Osuka, H. Furuta, K. Itaya, *Adlayer Structure of and Electrochemical O2 Reduction on Cobalt Porphine-Modified and Cobalt Octaethylporphyrin-Modified Au(111) in $HClO_4$*, J. Phys. Chem. B., **2004**, *108*, 1948–1954.

[36] A. Alsudairi, J. Li, N. Ramaswamy, S. Mukerjee, K.M. Abraham, Q. Jia, *Resolving the Iron Phthalocyanine Redox Transitions for ORR Catalysis in Aqueous Media*, J. Phys. Chem. Lett., **2017**, *8*, 2881–2886.

[37] T. Kuwana, M. Fujihira, K. Sunakawa, T. Osa, *Catalytic Electroreduction Of Molecular Oxygen Using Water Soluble Iron Porphyrin*, J. Electroanal. Chem., **1978**, *88*, 299–303.

[38] K. Shigehara, F.C. Anson, *Electrocatalytic Activity of Three Iron Porphyrins in the Reductions of Dioxygen and Hydrogen Peroxide at Graphite Electrodes*, J. Phys. Chem., **1982**, *86*, 2776–2783.

[39] T. Ye, Y. He, E. Borguet, *Adsorption and electrochemical activity: An in situ electrochemical scanning tunneling microscopy study of electrode reactions and potential-induced adsorption of porphyrins*, J. Phys. Chem. B., **2006**, *110*, 6141–6147.

[40] S. Yoshimoto, E. Tsutsumi, K. Suto, Y. Honda, K. Itaya, *Molecular assemblies and redox reactions of zinc(II) tetraphenylporphyrin and zinc(II) phthalocyanine on Au(1 1 1) single crystal surface at electrochemical interface*, Chem. Phys., **2005**, *319*, 147–158.

[41] P. Atkin, J. Paula, *Physical Chemistry*, **2006**.

[42] https://goldbook.iupac.org/html/C/C00876.html.

[43] https://www.nature.com/subjects/heterogeneous-catalysis.

[44] P. Quaino, N.B. Luque, R. Nazmutdinov, E. Santos, W. Schmickler, *Why is gold such a good catalyst for oxygen reduction in alkaline media?*, Angew. Chemie - Int. Ed., **2012**, *51*, 12997–13000.

[45] P. Rodriguez, M.T.M. Koper, *Electrocatalysis on gold*, Phys. Chem. Chem. Phys., **2014**, *16*, 13583–13594.

[46] A.J. Bard, L.R. Faulkner, *Electrochemical Methods: Fundamentals and Applications, 2nd Editio*, Wiley, New York, **2001**.

[47] M.D. Maree, T. Nyokong, K. Suhling, D. Phillips, *Effects of axial ligands on the photophysical properties of silicon octaphenoxyphthalocyanine*, J. Porphyr. Phthalocyanines., **2002**, *6*, 373–376.

[48] Y. Chen, M. Hanack, W.J. Blau, D. Dini, Y. Liu, Y. Lin, J. Bai, *Soluble axially substituted phthalocyanines: Synthesis and nonlinear optical response*, J. Mater. Sci., **2006**, *41*, 2169–2185.

[49] K. Holst-Olesen, M. Reda, H.A. Hansen, T. Vegge, M. Arenz, *Enhanced Oxygen Reduction Activity by Selective Anion Adsorption on Non-Precious-Metal Catalysts*, ACS Catal., **2018**, *8*, 7104–7112.

Chapter 6

6 EC-STM investigations

In this chapter, the FeN_4 macrocycles are examined in their ability to physically adsorb on the Au(111) single crystal substrate to produce FeN_4-functionalised gold electrode surfaces. This allows first of all to study the structures of physisorption, namely if a monolayer, or multiple layers or clusters are formed at the gold surface. The studied molecules revealed to have a tendency to produce Self-Assembled Monolayers (SAM), even if precise electrochemical conditions were required for the SAM stability. This deals also with the purpose for which FeN_4-modified electrodes were conceived, namely Oxygen Reduction Reaction electrocatalysis. One major advantage of the EC-STM instrumentation lies in the ability to characterise the process of ORR catalysis occurring at Fe centres. The mechanism has already been introduced in section 5.1. A riveting aspect of EC-STM is the possibility to compare imaging data with electrochemical information coming from the "four-electrodes setup", in which the FeN_4-modified gold electrode plays as working electrode.

The procedure of functionalisation has already been described in section 3.3.2. In this section, details on the self-assembly process as well as the electrocatalytic activity at the single molecular sites are examined for each molecular system. First of all, Fe(II)-phthalocyanine was studied, then Fe(III)-phthalocyanine chloride was examined, since it provides exactly the same ligand environment, with a different initial oxidation state of the iron atom, as well as the presence of chloride species, which in principle could alter the macrocycle adsorption event and/or or the O_2 reduction catalysis. Finally, Fe(III)-tetramethoxyphenyl porphyrin chloride was characterised, essentially to evaluate the effect of substituents on molecular physisorption and the differences in the electrocatalytic activity based on the theoretical considerations of section 5.1.

6.1 Fe(II)-Phthalocyanine — Fe(II)Pc

Fe(II)-Phthalocyanine was found to adsorb on the Au(111) by forming SAM. Ar-saturation was initially performed on the 0.1 M $HClO_4$ electrolyte. The phthalocyanine (or porphyrin) solutions in DMF were also deaerated with Ar gas for at least 30 min (*Volume* = 25 mL). Gold was functionalised with hanging meniscus technique. It was then rinsed and transferred with a droplet of water sticking at the surface. This allows to avoid any O_2 contamination, since the first task was to evaluate molecular physisorption on the gold substrate, and not the ORR electrocatalysis. No significant evidences of bilayers or multi-layers were detected, showing instead ordered domains of molecules or at least disordered patterns. The obtained results in terms of SAM domains partially reflect some recent evidences for the same Fe(II)Pc/Au(111) system at the solid/electrolyte interface [1]**,** for which square symmetry was found to describe

the geometry of the ordered Fe(II)Pc domains. However, more careful investigations, linked to an optimised Au(111) functionalisation procedure, revealed the co-existence of ordered domains both with hexagonal and square symmetry. Unit cells and angles were all sketched with CorelDRAW and measurements were performed with CorelDRAW and as well with WSxM software, as described in section 3.5.3. Figures 6.1a and b clearly show that two types of domains are covering the gold surface. Square and hexagonal symmetry domains were revealed to characterise Fe(II)-phthalocyanine SAM, and they are termed Phase 1 and Phase 2, respectively. They are easily recognisable thanks to the angle formed by the two unit-cell vectors. Hexagonal symmetry is distinguished by 60° or 120° angles, depending which of many unit cell vectors couples was chosen. In this work, the smallest angle (60°) resulting with the shortest unit cell vectors was pursued. Square symmetry was assigned to ordered domains whose unit cell angle was approaching to 90°. Moreover, phase translation domains are observable and are denoted with yellow solid lines and the domain boundary between them marked by dashed yellow lines (Fig. 6.1a). Furthermore, rotational domains may be noticed, since the measured angle of rotation between adjacent domains is roughly compatible with the hexagonal symmetry of the (111) crystallographic face. However, it deviates from the expected 120° value due to the drift issue, which was affecting instrumentation during scanning.

The images in Figure 6.1 were collected at sufficiently positive working electrode potentials as indicated in the captions, in order to avoid the reduction of the Fe(III) centre to Fe(II). This redox behaviour was characterised by means of cyclic voltammetry in section 5.2.1, allowing to properly choose the initial applied potential when performing EC-STM.

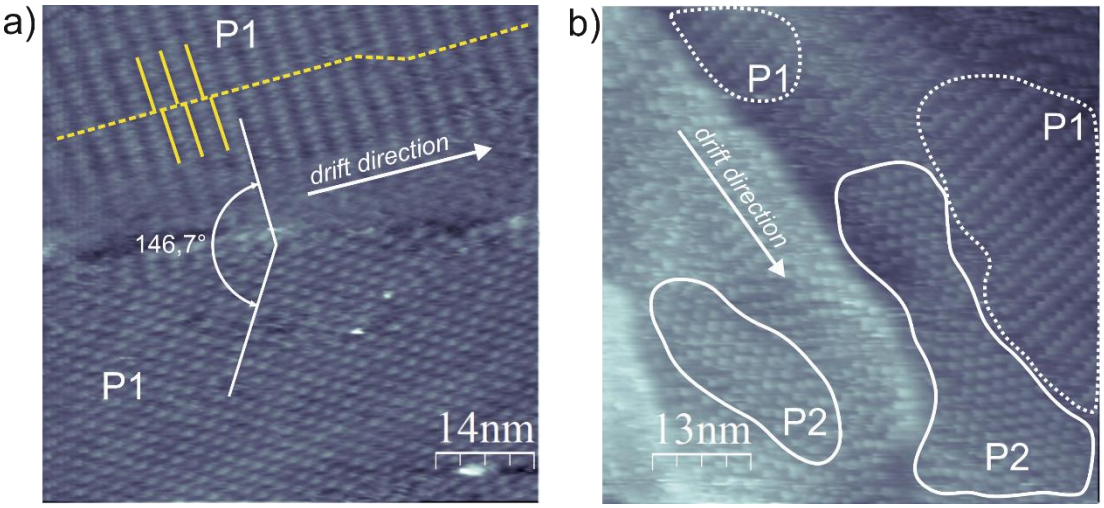

Figure 6.1: (a) I_t= 2.6 nA; U_b= –358 mV; E_{app}=625 mV vs. RHE; I = –0.0 µA; (b) I_t= 0.95 nA; U_b= –373 mV; E_{app}= 710 mV vs RHE; I = –0.0 µA.

Figures 6.1a and b are also two relevant examples of the "drift" issue affecting the EC-STM instrumentation, as already mentioned. The effect of drift consists in an unreal elongation or shortening of the image structures, which therefore appear different from what they really are. Molecules are therefore not visualised as symmetrical crosses, but rather as distorted or bended structures. This reflects on the geometrical studies performed on the imaged domains, which for example show discrepancies of few degrees among the unit cell vectors measured in the same image or in different images, or in deviations from the 60° (or 90°) expected value. Another effect is the different length of the two unit-cell vectors, even if

symmetrical structures like phthalocyanines are expected to regularly arrange on the surface, as demonstrated by many studies both in UHV and *in situ* environment [1–5]. These considerations are simply supported by experimental evidences gained by many imaging characterisations performed on the same typology of FeN_4-functionalised substrate. Image quality and instrumental drift are in fact revealed to improve after hours of use of the instrumentation. As described in section 2.1.3.1 and 3.2.1, the scanner unit is represented by a tube made of a piezoelectric material. This allows to scan the tip over an area of interest thanks to the piezoelectric properties of the tube. If, however, the piezoelectric material is subjected to many years of operation, alternated by periods of disuse, the material undergoes an aging effect. This turns into inappropriate functioning and misleading results. A component of thermal drift must not be neglected. For this reason, a definite system was characterised with many experiments performed in different days, in order to minimise the drift effect by averaging independent data. Thus, Fe(II)Pc was further characterised, and the following figure 6.2 was obtained.

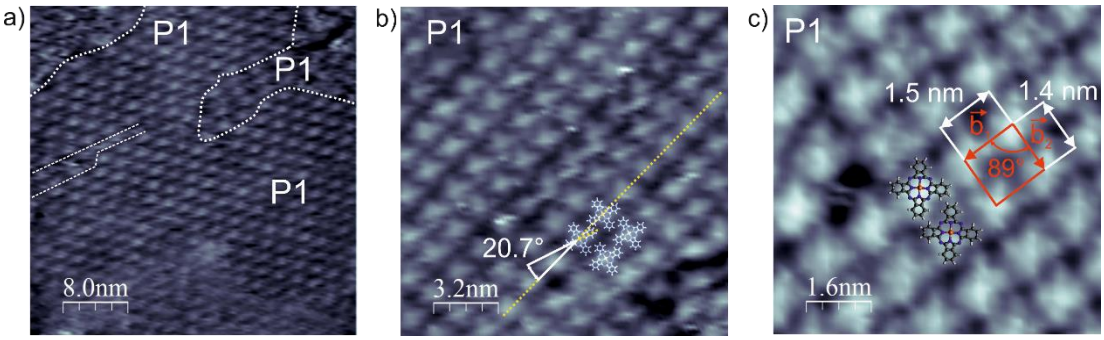

Figure 6.2: (a) I_t= 2.6 nA; U_b= –358 mV; E_{app}=625 mV vs RHE; I= –0 µA; (b) I_t= 1.95 nA; U_b= –384 mV; E_{app}=710 mV vs RHE; I= –0.0 µA; (c) I_t= 0.55 nA; U_b= –226 mV; E_{app}=625 mV vs RHE; I= –0.2 µA.

Square symmetry (P1) is revealed as in Fig. 6.2a and 6.2b, where the white dashed lines stand for separation borders of a large ordered molecular array from smaller areas of disordered molecules. In figure 6.2c are indicated the unit cell parameters for the imaged Fe(II)Pc SAM.

Figure 6.2c actually is an example of high-resolution EC-STM image. The resolution of an EC-STM image depends on many factors, among which a large impact is exerted by the tip, by the external noise and by the monolayer ordering and stability. The tip should in fact ideally terminate with a single atom to provide definite and stable-in-time tunnelling conditions, as pointed out in section 2.1.3.2. External noises must be suppressed otherwise streaks and artefacts will superimpose to the real image, making difficult their interpretation. The major sources of external disturbances have electromagnetic and mechanical nature, and their minimisation was described in sections 2.1.3.3 and 3.2 respectively. Finally, imaging of isolated molecules does not usually bring to satisfactory results, since single molecules are easily perturbed by the tunnelling phenomena. Ordered layers create a more stable surface towards tunnelling perturbations (section 2.2.2.5). When all these conditions are satisfied, high resolution is attained, and the features of a single molecule are well imaged. In Figure 6.2b and 6.2c, the ball-and-stick model of Fe(II)-phthalocyanine has also been superimposed to the recorded STM image, to show the correspondence between the expected structure and the imaged one. Thanks to the powerful resolution, it was also possible to determine the rotation angle of single molecules with respect to the row direction parallel to the unit cell vector $\overrightarrow{b_1}$,

which in this case is about 21°. The unit cell parameters (square symmetry, Phase I) are: $\overrightarrow{b_1} = (1.5 \pm 0.1)\ nm$; $\overrightarrow{b_2} = (1.4 \pm 0.1)\ nm$, measured angle $\measuredangle = (89 \pm 2)°$.

For the hexagonal Phase II, no high-resolution images were successfully recorded, and therefore the unit cell parameters are estimated on the basis of a large area image, which is however more sensitive to instrumentation drift. It is also less precise since molecules are imaged as circles rather than crosses and identifying a unique repeating point is trickier. Anyway, the measured parameters for Phase II are: $\overrightarrow{c_1} = (1.5 \pm 0.1)\ nm$; $\overrightarrow{c_2} = (1.4 \pm 0.1)\ nm$, measured angle $\measuredangle = (63 \pm 2)°$.

It is now worth to calculate the surface concentration of molecules. This is achieved with geometrical calculations based on the measured unit cell parameters. In any case, few assumptions must be made to simplify the calculation, hence the final number will be an estimation of the real surface concentration. One first issue is represented by the compresence of two different domains, and their distribution is surely not uniform since hexagonal domains (Phase II) were detected in a lower number of images with respect to square domains (Phase I), and in those images the two phases were coexisting. Therefore, it is now assumed that all the exposed Au(111) surface was covered with Fe-Phthalocyanine molecules with the Phase I arrangement. The fundamental mathematical relation between the Fe(II)Pc monolayer and the Au surface is provided by the following proportion:

$$1\ cell_{FePc} : X\ cells_{Au} = Totcells_{FePc} : Totcells_{Au} \qquad (6.1)$$

Namely, one Fe(II)Pc cell will be covering *X* cells of Au, with X > 1 since the phthalocyanine molecule is much larger than one Au atom, so will be their surface arrangement. Therefore, a total number of phthalocyanine molecules will be covering the total number of surface Au atoms, but the number of molecules and atoms are connected to the respective number of cells. Each unit cell of Fe(II)Pc contains one phthalocyanine molecule, whereas the number of surface atoms needs not to be specified for the purpose of this calculation. First of all, the left-hand side of the proportion is calculated. The area of the Fe(II)Pc, thanks to its tetragonal symmetry, is calculated as: $A_{cell}^{FePc} = \overrightarrow{b_1} \cdot \overrightarrow{b_2} = 2.1\ nm^2 = 2.1 \cdot 10^{-14}\ cm^2$. The area of one Au(111) unit cell, due to hexagonal symmetry, is calculated as:

$$A_{cell}^{Au} = \overrightarrow{a_1} \cdot \overrightarrow{a_2} \cdot \frac{\sqrt{3}}{2} = 0.07233\ nm^2 = 7.233 \cdot 10^{-16}\ cm^2 \qquad (6.2)$$

where $a_1 = a_2 = 0.289\ nm$. The *X* cells of Au underlying one cell of Fe(II)Pc are given by the ratio of the area of one Fe(II)Pc cell to the area of one Au unit cell.

$$X\ cells_{Au} = \frac{A_{cell}^{FePc}}{A_{cell}^{Au}} = 29.03 \qquad (6.3)$$

The total number of Au surface cells (*N*) is calculated as the exposed geometrical area of the gold single crystal to the area of one Au unit cell, assuming that the surface has zero roughness:

$$N_{cell}^{Au} = \frac{A_{geom}^{Au}}{A_{cell}^{Au}} = \frac{0.4 \cdot 0.4 \cdot \pi\ cm^2}{7.233 \cdot 10^{-16}\ cm^2} = 6.9494 \cdot 10^{14} \qquad (6.4)$$

The total number of Fe(II)Pc cells is obtained by multiplying one (that is, one Fe(II)Pc unit cell) with the total number of Au cells, dividing the result for the number of Au cells underlying one FePc cell, as follows:

$$N_{cell}^{FePc} = \frac{1 \cdot N_{cell}^{Au}}{X\ cells_{Au}} = 2.394 \cdot 10^{13} \quad (6.5)$$

Each unit cell of Fe(II)Pc contains one phthalocyanine molecule, therefore the total number of Fe(II)Pc cells is also the total number of Fe(II)Pc molecules. By dividing the total number of molecules for the exposed geometrical area of the Au sample, one obtains the surface concentration of Fe(II)Pc arranged with Phase 1 symmetry (d_{FePc}^{P1}):

$$d_{FePc}^{P1} = \frac{2.394 \cdot 10^{13}}{0.4 \cdot 0.4 \cdot \pi} = 4.762 \cdot 10^{13}\ \frac{molecules}{cm^2} \quad (6.6)$$

It is now possible to give a rough estimation of the surface coverage originated by the FePc molecules, if all the surface was covered with Phase 1 arrays. The coverage of Au is taken as reference, since it is the substrate on which molecules are lying. It is therefore set at $\theta_{Au} = 1$. The following proportion is then established:

$$Au\frac{atoms}{cm^2} :\ \theta_{Au} = Fe\frac{molecules}{cm^2} : \theta_{FePc} \quad (6.7)$$

The surface coverage of Fe(II)Pc is then:

$$\theta_{FePc} = \frac{Fe\frac{molecules}{cm^2} \cdot 1}{Au\frac{atoms}{cm^2}} = 0.034 \quad (6.8)$$

where $Au\frac{atoms}{cm^2}$ is the surface concentration of Au atoms, calculated as $\frac{1}{A_{Au}^{cell}} = 1.383 \cdot 10^{15}\ \frac{atoms}{cm^2}$.

If all the surface was covered with Phase 2 domains, surface concentration and coverage would have been the same due to very similar unit cell vectors.

6.1.1 Investigation of Fe(II)Pc in Ar purged electrolyte

The electrode potential is known to exert a major role in determining surface ordering/disordering phenomena. Changing the working electrode polarisation offers the ability to study the behaviour of the Fe(II)-phthalocyanine molecules at the solid/liquid interface. This would be extremely useful when studying the self-assembly processes and the forces and interactions that are governing it. This work aims to characterise the electrocatalytic effect exerted by FeN_4 towards the oxygen reduction reaction, being metal-phthalocyanines and -porphyrins a powerful alternative to PGM catalysts. The catalytic effect of Fe(II)-phthalocyanine, Fe(III)-phthalocyanine chloride and Fe(III)-tetramethoxyphenyl porphyrin chloride towards O_2 reduction had already been confirmed in section 5.2 by means of cyclic voltammetry. What it is still on debate is the dynamics involved in the reduction of the O_2 molecule. A crucial step in the electrocatalytic reduction of O_2 is represented by its adsorption on the active site. This is a typical concern of *heterogeneous catalysis*, for which the catalyst is held at a different phase (typically solid) with respect to reactants (usually in liquid or gaseous phase) [6]. The catalytic site is widely recognised in the central metal within the phthalocyanine (or porphyrin) cavity. It must be recalled that FeN_4 are herein physically adsorbed on the Au(111) surface. Hence the solid phase is actually represented by gold, and molecules are forming a thin monolayer on it. Moreover, as it will be shown in the following pictures, these molecules retain a certain degree of freedom on the surface, being able to change their position and undergo kind of ordering/disordering phenomena. For this reason,

the FeN_4-functionalised electrodes are at the same time peculiar systems deviating from the classical heterogenous catalyst concept and the expression of heterogeneous catalysis at its best. This is only an apparent contradiction and it can be overcome by remembering that the catalytic effect explicates with an adsorption process of O_2 on the Fe active site. This means that if there exists a technique able to resolve what is going on precisely on that single site, then the catalytic behaviour would be well understood, and that single site would have acted as heterogeneous catalyst. EC-STM is therefore the needed answer to the question on how the catalytic behaviour of FeN_4 centres occurs.

To systematically investigate the FeN_4-modified electrodes, potentiodynamic imaging was performed. This means that the working electrode potential (FeN_4-functionalised Au(111)) was subjected to potential step variations. More precisely, the image acquisition was started at fixed WE polarisation, which must be at a sufficiently positive potential to avoid any Faradaic process. For all the investigated systems, an initial $E_{app} > 0.6$ V (vs RHE) revealed to be a "safe" potential; both in Ar- and O_2-saturated electrolyte. This information came from the cyclic voltammogram recorded for each molecular system in the same electrochemical conditions used for EC-STM imaging. The potential was then allowed to vary, usually in cathodic direction, and concomitantly STM scanning was performed, allowing in principle to directly see the effect of polarisation within one image. It is worth noting that in many cases this procedure failed to prove substantial information, since the WE variations always induced a certain effect on the monolayer arrangement and/or on its activity, thus resulting in disturbed tunnelling conditions. In any case, to prevent undesired Faradaic current developing at the tip electrode, the tip potential was held constant with respect to reference electrode during potentiodynamic imaging. This is the proper mode of operation suggested by Wilms et al. [7]. Many images were collected at each stepped potential both in Ar and O_2 saturated, leaving the system to reach its dynamic equilibrium based on that potential. This gave also the possibility to evaluate order/disorder events. The potential was then stepped back to the original potential, allowing to restore the initial equilibrium condition and to notice any eventual changes on the monolayer assembly. Actually, what it was observed through STM imaging was even more advanced and clarifying.

6.1.2 Potentiodynamic investigation of Fe(II)Pc in Ar purged electrolyte

Figure 6.3 provides a high-resolution image of a Fe(II)Pc ordered domain. In section 5.2.1, cyclic voltammetric investigations demonstrated that iron is found at (III) oxidation state, therefore the notation Fe(II)Pc simply refers to the molecule in crystal form at the moment of dilution in DMF. Topographic profiles were extracted from Figure 6.3 with the use of *WSxM* software. Three lines (dashed lines in figure 6.3 1,2 and 3) were manually traced in order to cross the molecule in the centre, where the iron atom should lie. A brighter spot in centre of each molecule is visible by eye, however the colour scale and its brightness/darkness are intended to provide only a rough visual interpretation of the image. The actual quantitative information comes from the analysis of topographic profiles extracted by the image itself. The corresponding topographic profiles are displayed in Figures 6.3 and numbered accordingly and they show that the brighter central spot is actually emerging from the molecular plane with an average $\Delta Z = (0.26 \pm 0.10)$ Å. This topographic profile is associated with the iron atom at the (III) oxidation state, in accordance with the cyclic voltammograms (see section 5.2.1-2).

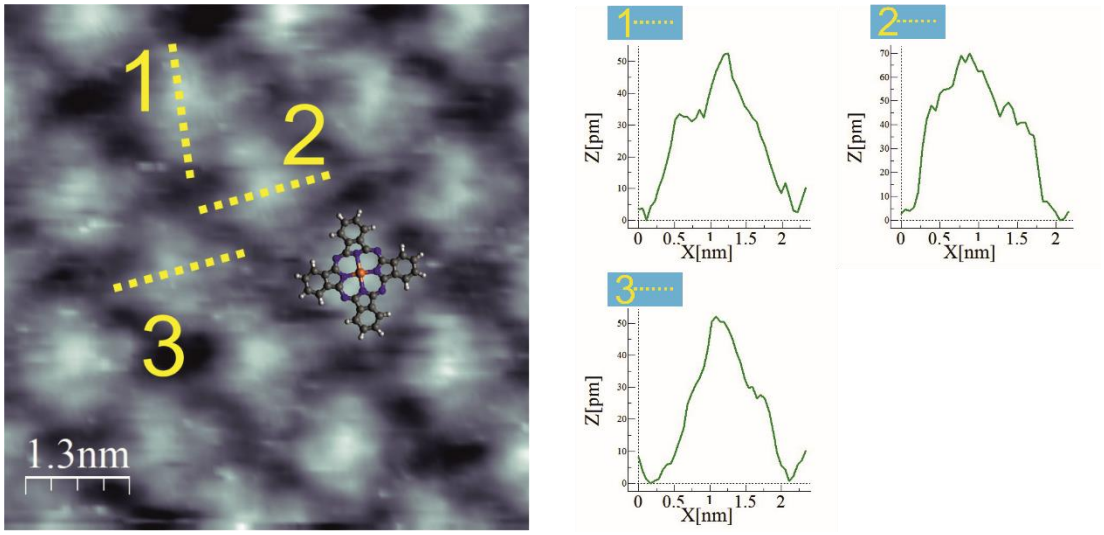

Figure 6.3: I_t= 1.05 nA; U_b= –3352 mV; E_{app}= 625 mV vs RHE; I = –0.2 µA**.** The topographic profiles corresponding to lines 1,2 and 3 are reported on the right side of the figure.

Potentiodynamic imaging (figure 6.4) was started at E_{app} = 600 mV, and a $\Delta Z = (0.26 \pm 0.10)$ Å was measured by the extracted topographic profiles along the dotted lines of figure 6.4a. At a WE polarisation of E_{app} = 350 mV, the image (Figure 6.4b) appears slightly different from the previous ones. First of all, the image looks more "fuzzed", being molecules irregurargly distributed on the surface. More noise also appears, causing stripes and lines or very bright/dark regions to appear. This is ascribed to an enhanced molecular mobility over the Au surface, whose origin may be found in a different phthalocyanine-gold non-covalent electrostatic interaction. As a consequence of the modified applied potential, an excess surface charge appears or changes in magnitude, therefore causing, in this case, a higher molecular mobility, accordingly to a physisorption molecule/substrate interaction. The tip is also enhancing this effect by perturbating molecules with a tunnelling current. These effects will be further elucidated for the case of Fe(III)-Pc chloride and Fe(III)TMPP, for which they had been found to produce more impacting consequences.

Even by a first glance, many "hollow" molecules were imaged. Topographic profile analysis (solid lines 1 and 2 in Figure 6.4b) prove that dips with an average depth of $\Delta Z_{dip} = (0.24 + 0.10)$ Å are characterising many molecules. There still exist few molecules with a full centre and an associated protrusion of $\Delta Z_{Fe(III)} = (0.28 + 0.10)$ Å. It is concluded that the hollow molecules are not caused by a demetallation process, since consecutive scan performed after many minutes were still exhibiting a redox activity. They are rather believed to be caused by the different oxidation state of the metal. This is not a new argument, since a difference in STM imaging features were revealed for cobalt-phthalocyanine with respect to copper-phthalocyanine both deposited on Au(111) [8]. The explanation was based on the different *d* orbital population. Indeed, Co(II) possesses a d^7 orbital occupation, namely $d_{xy}^2 d_{xz}^2 d_{yz}^2 d_{z^2}$, whereas Cu(II) has a configuration of $d_{xy}^2\ d_{xz}^2 d_{yz}^2 d_{z^2}^2 d_{x^2-y^2}^2$ [3]. Fe(II) has a d^6 occupation, resulting in a $d_{xy} d_{xz}^2 d_{yz} d_{z^2} d_{z^2}$ configuration [9]. The occupancy of *d* orbital therefore provides a great contribution to the STM image formation of a metal-phthalocyanine or -porphyrin [3]. Fe(II) was actually predicted to exhibit a protrusion, and therefore to appear as a bright spot in the STM image. This was however true for UHV investigation of Fe(II)-phthalocyanine on Au(111), but it had been shown in section 2.1.2 that the tunnelling through an electrolyte introduces significant deviations from UHV-STM. It is therefore suggested that

the reduction of Fe(III) to Fe(II) modifies the tunnelling path(s), resulting in a visible change in the STM images when passing from the (III) to (II) oxidation state.

By further reducing the applied potential to E_{app} = 250 mV, the image looks noisier than in Figure 6.4b. This is a consequence of an increased surface mobility derived by a change of non-covalent electrostatic interaction between molecule and substrate. Molecules are in fact barely recognisable or look distorted. In any case, most of the recognisable molecules show the hollow centre, as confirmed by two topographic profiles extracted in Figures 6.5a. The measured dips have an average depth of $\Delta Z_{dip} = (0.25 + 0.10)$ Å. This is coherent with the existence of iron in the (II) oxidation state, which was already hypothesised to show this different behaviour to STM.

When the potential was stepped even more negative up to E_{app} = 150 mV, molecules were hardly recognisable, as visible in the upper part of Figure 6.4d. Upon returning to a positive potential (E_{app} = 550 mV), the same image (figure 6.4d) became clearer and molecules were again resolved. Both hollow and full molecules were imaged. Being the applied potential sufficiently positive to induce the iron re-oxidation, it may be inferred that molecules with bright central spot possess an already oxidised Fe(III) atom, whereas the hollow molecules still exhibit a Fe(II) atom. In fact, the protrusion has a height of $\Delta Z_{Fe(III)} = (0.24 \pm 0.10)$ Å, whilst the hollow molecules return a dip with depth of $\Delta Z_{dip} = (0.31 \pm 0.10)$ Å. This experimental evidence would indicate a slow re-oxidation process, which is consistent with the electrochemical response observed with cyclic voltammetry in section 5.2.1 and with a similar redox behaviour of cobalt phthalocyanine [8].

Finally, the potential is stepped back to the original applied potential, that is E_{app} = 600 mV. The resulting image is displayed in Figure 6.4f. All the imaged molecules now exhibit a bright central spot, as it was at the beginning of potentiodynamic imaging. The extracted topographic profiles give an average protrusion of $\Delta Z_{Fe(III)} = (0.28 \pm 0.10)$ Å. Figure 6.4f also proves that having raised the applied potential to positive values causes the molecule to regain adsorption stability. Ordered domains were not detected, but at least short-range row of phthalocyanines are well visible in the right part of Fig. 6.4f.

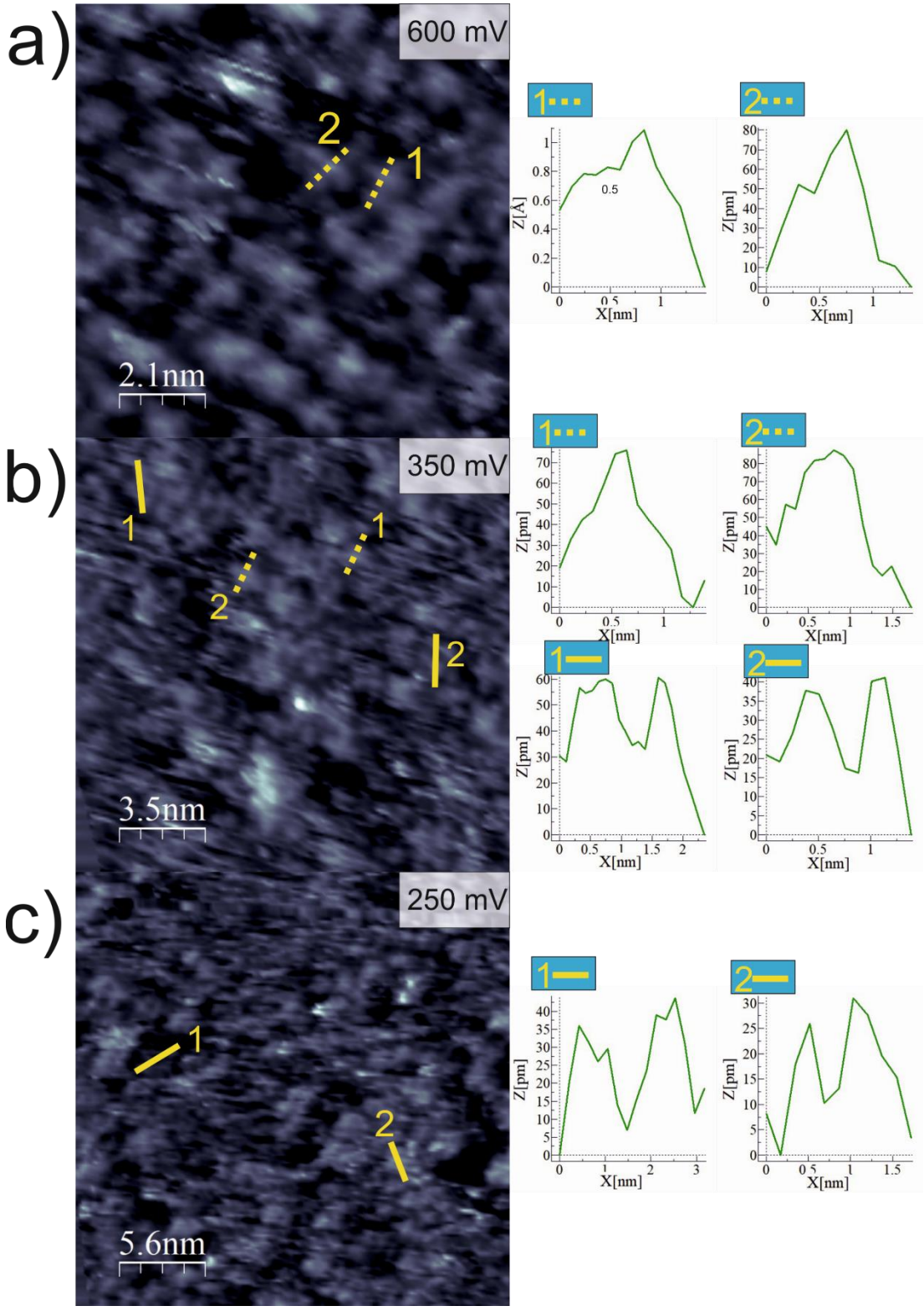

Figure 6.4: (a) I_t = 2.6 nA; U_b = –393 mV; E_{app} = 600 mV vs RHE; I = –0.3 µA; (b) I_t = 2.6 nA; U_b = –330 mV; E_{app} = 350 mV vs RHE; I = –2.1 µA; (c) I_t = 2.6 nA; U_b = –280 mV; E_{app} = 250 mV vs RHE; I = –2.4 µA.

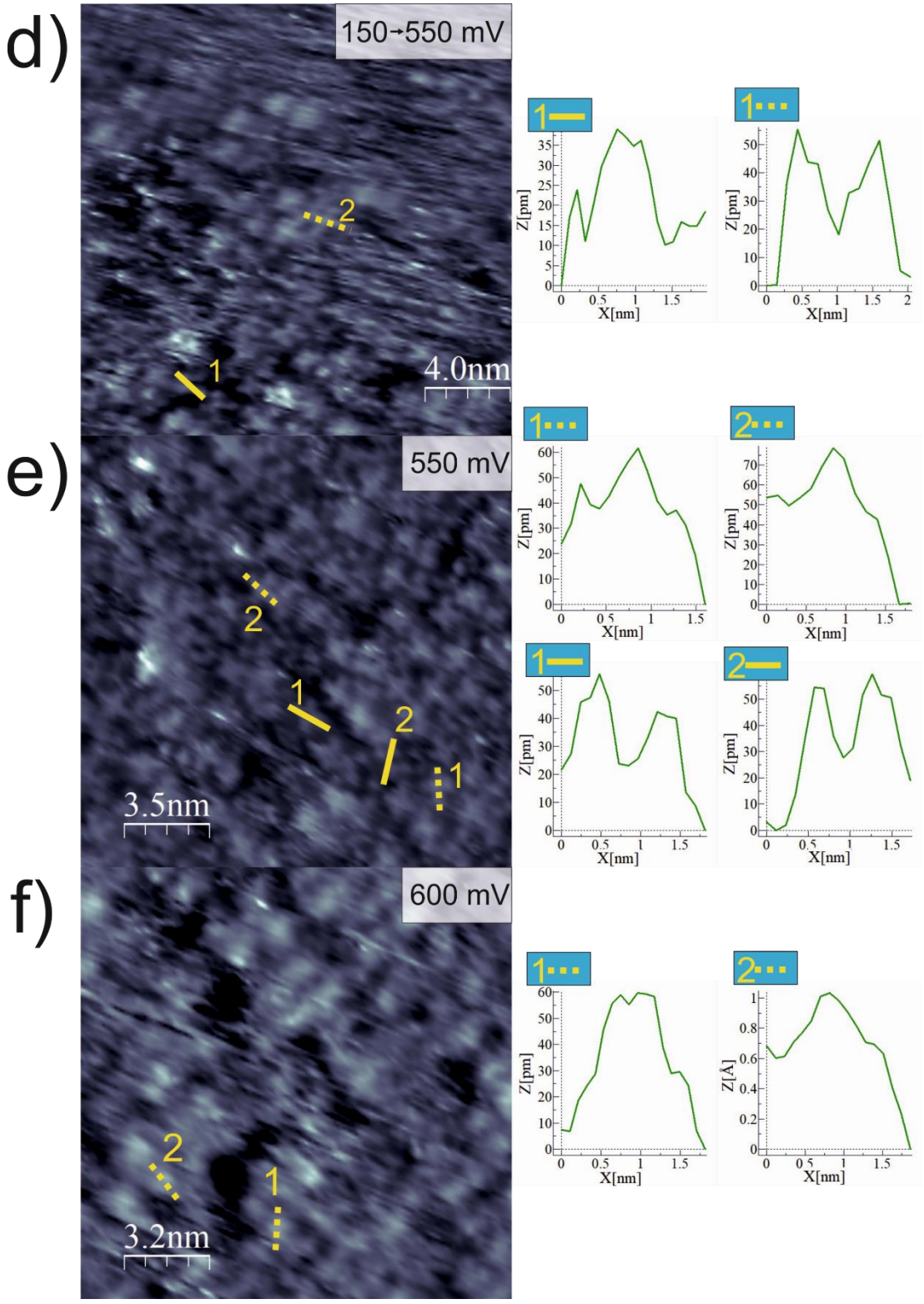

Figure 6.4: (d) I_t = 2.6 nA; U_b = –298 mV; E_{app} = from 150 to 550 mV vs RHE; I = from –1.5 to –0.5 µA; (e) I_t = 2.6 nA; U_b = –298 mV; E_{app} = 550 mV vs RHE; I = –0.5 µA; (f) I_t = 2.6 nA; U_b = –401 mV; E_{app} = 600 mV vs RHE; I = –0.2 µA.

6.1.3 Investigation of Fe(II)Pc in O_2 saturated electrolyte

The O_2 adsorption and reduction behaviours were analysed in a O_2 saturated 0.1 M $HClO_4$ electrolyte. First, the Fe(II)Pc layer was characterised in its ability to form stable monolayers in the O_2 saturated electrolyte. The results are shown in Figures 6.5a-c. Differently from the Ar saturated case, more hexagonal domains were revealed, even if both square and hexagonal phase (Phase I and II, respectively) were imaged, as shown in Figures 6.5c. Figure 6.5a is also a visual demonstration of the drift issue. Molecules appear stretched in oblique direction, and the two-unit cell vectors differ from each other even if two portions of the same image are considered. In fact, the rows of molecular phthalocyanines look bended because of the improper electrical response of the piezoelectric elements for the STM unit.

The unit cell parameters (square symmetry, Phase I) are: $\overrightarrow{b_1} = (1.5 \pm 0.1)\ nm$; $\overrightarrow{b_2} = (1.5 \pm 0.1)\ nm$, measured angle $\measuredangle = (88.2 \pm 2)°$. The unit cell parameters (hexagonal symmetry, Phase II) are: $\overrightarrow{c_1} = (1.5 \pm 0.1)\ nm$; $\overrightarrow{c_2} = (1.4 \pm 0.1)\ nm$, measured angle $\measuredangle = (64.7 \pm 2)°$.

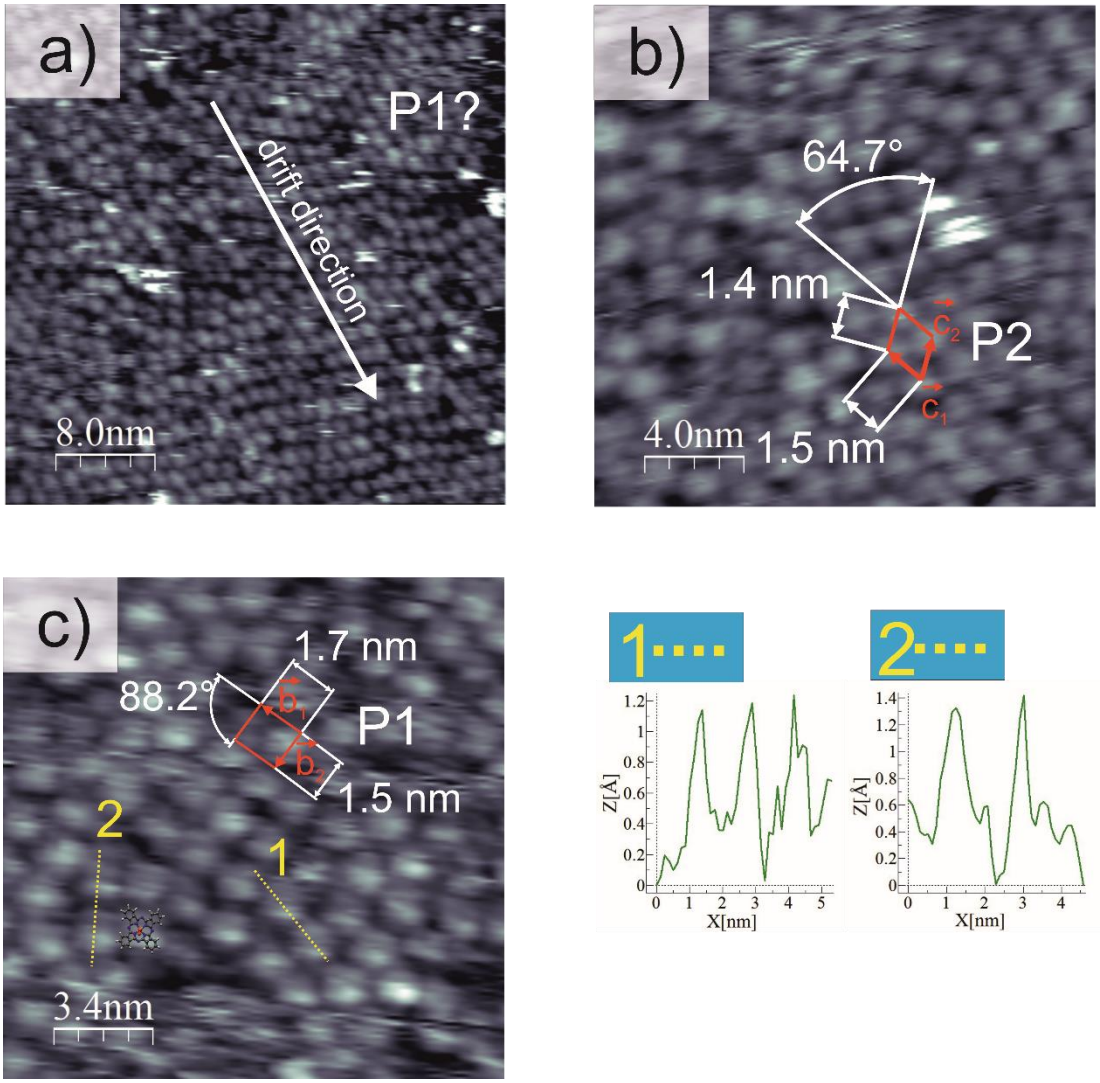

Figure 6.5: (a) I_t = 2.55 nA; U_b = –303 mV; E_{app} = 626 mV vs RHE; I = –1.5 µA; (b) I_t = 2.55 nA; U_b = –303 mV; E_{app} = 626 mV vs RHE; I = –1.5 µA; (c) I_t = 5 nA; U_b =–385 mV; E_{app} = 625 mV vs RHE; I = –1.2 µA. Topographic profiles along lines 1 and 2 of figure 6.5c are shown in the bottom right side.

Figure 6.5c differs from Figure 6.5a and 6.5b for the voltage bias and, in particular, the tunnelling current used to obtain each image. The variation of the tunnelling parameters causes the involvement of different molecular orbitals (and their combinations) in the tunnelling event. This explain why Figures 6.5a, 6.5b and 6.5c show different molecular shapes and features, even if they were obtained in the same measuring session, but according to different tunnelling parameters. This becomes of vital relevance when comparing images obtained in deaerated electrolyte with those obtained in O_2 saturated one.

Figure 6.5c allows to visualize O_2 adsorption onto the Fe centres. Molecules in fact retain an almost symmetrical shape, but a brighter spot is visible with a shifted position with respect to the molecular centre, i.e. iron. By extracting the topographic profiles along the dashed lines (1 and 2), it is evident that a larger ΔZ is found if compared to that obtained in deaereted electrolyte (Fig. 6.3 and 6.4a). Since the tunnelling parameters are similar to figure 6.4a obtained in deaereted delectrolyte, the new feature observed in O_2 saturated electrolyte is ascribed to the presence of the O_2 species adsorbed on the metal atom. The topographic profiles exhibit a larger vertical protrusion if compared to the Ar saturated case. Indeed, an average $\Delta Z_{O_2} = (0.85 \pm 0.10)$ Å had been measured. The shifted position of the bright spot may be demonstrative of the *end-on* adsorption geometry. The model of an O_2 *end-on* adsorbed molecule onto a Fe-phthalocyanine unit had been superimposed to the STM image in Figure 6.5c. For the sake of clarity, the same model is reported in the following Figures 6.6b and 6.6c with two different perspective angles, whereas the bare Fe-phthalocyanine molecule is reported in Figure 6.6a. For sake of comparison, in Figure 6.6d and 6.6e it is shown the *side-on* adsorption geometry.

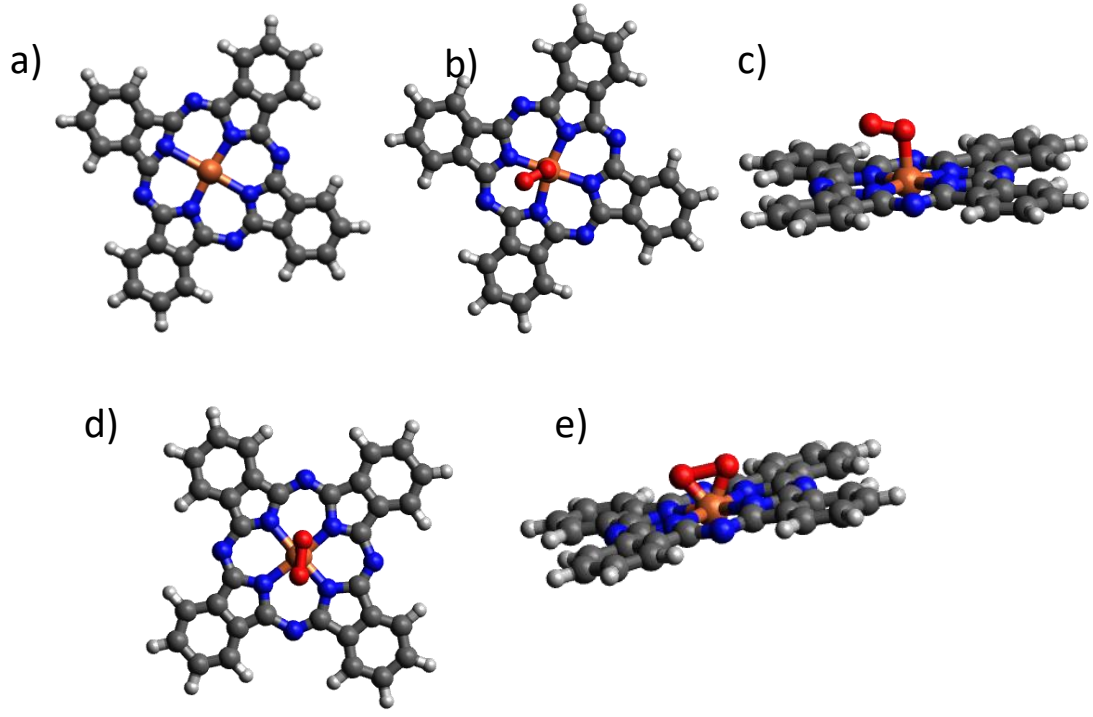

Figure 6.6: (a) Fe-phthalocyanine in deaerated electrolyte; (b) *end-on* O_2 adsorption; (c) *end-on* O_2 adsorption (side-view); (d) *side-on* O_2 adsorption; (e) *side-on* O_2 adsorption (side-view)

Figure 6.7a show that phase 1 and phase 2 can co-exist for Fe(II)Pc on Au(111), whereby figure 6.7b provides a high resolution image obtained for the O_2 saturation case. Molecular shape can clearly been identidfied, as well as a brighter spot starting from the

molecular centre but expanding in decentred position, as seen in the previous figures 6.5c. The topographic profiles collected along the dashed lines (1 and 2) confirm that a protrusion exist, and its magnitude is $\Delta Z_{O_2} = (0.95 \pm 0.10)$ Å, which is compatible with the previous ΔZ_{O_2} value.

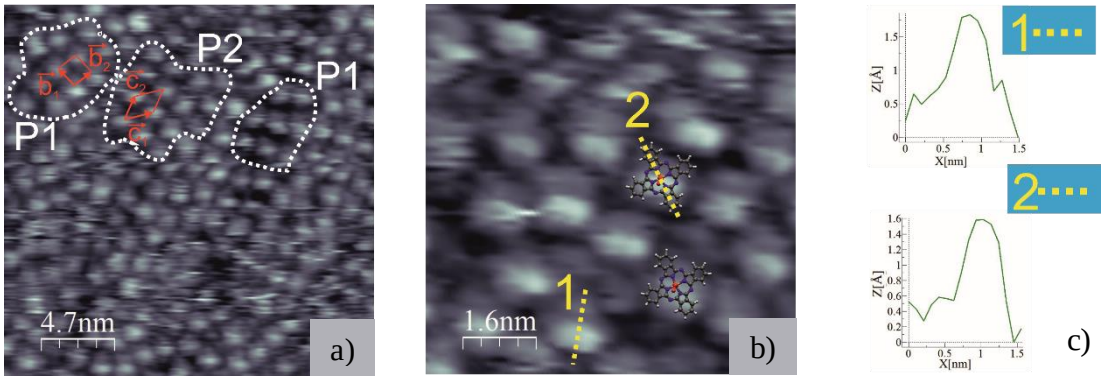

Figure 6.7: (a) I_t = 5 nA; U_b = –385 mV; E_{app} = 625 mV vs RHE; I =–1.2 µA; (b) high resolution image I_t = 5 nA; U_b = –385 mV; E_{app} = 625 mV vs RHE; I = –1.2 µA; (c) topographic profiles corresponding to lines 1 and 2 of fig. 6.9(b).

It must be noticed that the observed O_2 adsorbed molecule seems in proportion much larger than the expected dimensions. The model structures of figures Figure 6.6b and 6.6c are suitable examples about it. However, two explanations may be adducted. First of all, the STM is a probe towards the local density of states, and the presence of a new molecule (O_2) is certainly altering it and introducing new molecular orbitals as well as new molecular orbitals superpositions. New tunnelling pathways would therefore have been created, or old ones would have been modified. Another aspect concerns the O_2 adsorption geometry. The *end-on* configuration states that only one oxygen atom is bonded to the Fe atom, whereas the remaining O atom is not. The resulting Fe-O σ bond is therefore free to rotate and vibrate, especially considering that a significant perturbation is applied to the Fe-O bond through the tunnelling phenomenon. There are not enough experimental evidences to prove whether the first or the second hypothesis may be accepted, or at least to discriminate which is prevailing. Thus, both aspects must be accepted as the major responsible for the peculiar topographic profiles and image shape detected.

Anyway, the obtained images represent a remarkable result because they succeeded in characterising the first fundamental step of O_2 reduction catalysis, namely its adsorption on the catalytic active site.

6.1.4 Potentiodynamic investigation of Fe(II)Pc in O_2 saturated electrolyte

The study was further pursued by performing potentiodynamic imaging on the Fe(II)Pc-functionalised Au(111) crystal. The same procedure of potential step variation performed in deaerated electrolyte was then repeated with O_2 saturated one, to study how the oxygen reduction occurs at the single molecular site. As a confirmation, the adsorption step was evaluated with a new set of images, and a representative result is shown in Figure 6.8. The applied potential was set at E_{app} = 600 mV, which was found to be near the onset potential for ORR in the CV curves registered ex-situ (section 5.2.2). As expected, the O_2 adsorption is recognisable by a brighter spot shifted from the centre of the molecule, in accordance with the

end-on adsorption geometry. The extracted topographic profiles along the three dashed lines gave back an average $\Delta Z_{O_2} = (0.93 \pm 0.10)$ Å, in accordance with previous determinations.

The potential was then carefully stepped in cathodic direction, stopping at E_{app} = 500 mV. This potential was found to exert a remarkable activity towards ORR, even if the peak current was revealed at even more negative potential (see section 5.3.1). At the tip electrode, no Faradaic current could develop since the TE potential was fixed with respect to the RE potential. However, at the WE the Faradaic current due to ORR increases, and the proof is that the STM image got noisier. In any case, most of the imaged molecules still show the brighter spot ascribed to O_2 adsorption and confirmed by topographic profile of $\Delta Z_{O_2} = (0.87 \pm 0.10)$ Å.

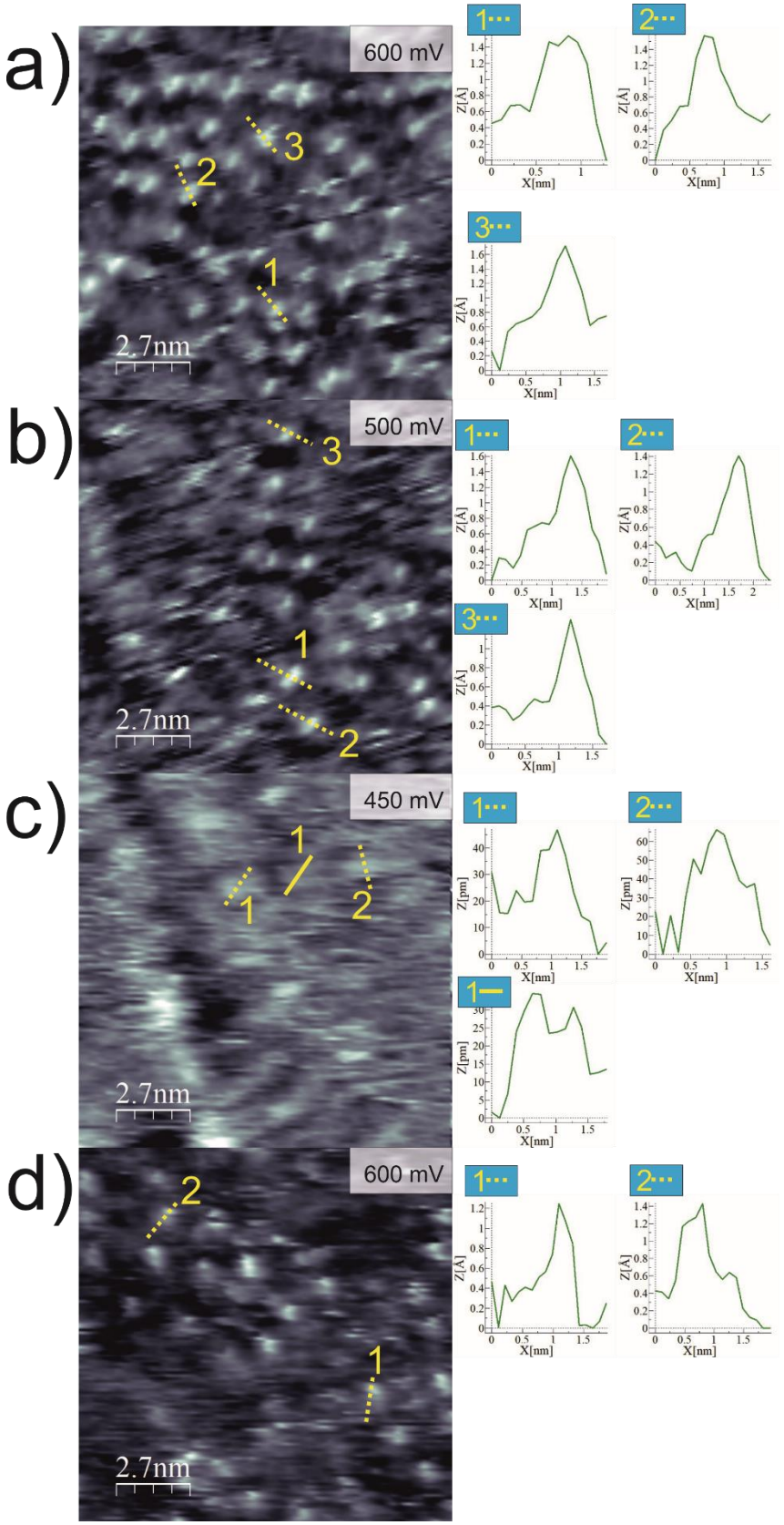

Figure 6.8: (a) I_t = 3.4 nA; U_b = +309 (vs RHE) mV; E_{app} = 600 mV vs RHE; I = –1.1 µA; (b) I_t = 3.4 nA; U_b=+309 (vs RHE) mV; E_{app} = 500 mV vs RHE; I = –4.9 µA; (c) I_t = 3.4 nA; U_b = +309 vs RHE mV; E_{app} = 450 mV vs RHE; I = –5.1 µA; (d) I_t = 3.4 nA; U_b = +309 mV vs RHE mV; E_{app} = 600 mV vs RHE; I = –0.3 µA.

The potential was then stepped to E_{app} = 450 mV, very close to the peak potential previously detected (section 5.3.1), consequently the tunnelling current was heavily disturbed. Moreover, from Ar potentiodynamic measurements it was revealed a pronounced surface mobility of phthalocyanine over the Au surface. This phenomenon is also expected to affect image quality. Anyway, few molecules were imaged, and the extracted topographic profiles reveal that no oxygen was adsorbed at the moment of scanning. In fact, of three analysed molecules, two exhibit a central hole, whereas one shows a small protrusion. This would indicate that the hollow molecule (solid line 1) feature the iron atom in the (II) oxidation state, since the topography leads to $\Delta Z_{dip} = (0.11 \pm 0.10)$ Å. The full molecules (dashed lines 1 and 2) have a protrusion of $\Delta Z = (0.26 \pm 0.10)$ Å, which according to the previous experimental results would indicate that the Fe atom possess the (III) oxidation state. It must to be stressed that at this applied potential, the reaction proceeds much faster than the time required for registering a STM image. Therefore, the EC-STM visualises a mean information at each molecular site, which is believed to undergo many catalytic cycles at sufficiently large overpotentials.

Finally, by returning to a positive potential equal to E_{app} = 600 mV, the image regains a better resolution and nitidity, and many molecules can be imaged (figure 6.8d). The surface mobility was in fact substantially lowered, in agreement with Ar potentiodynamic measurements. Moreover, the potential is sufficiently positive to avoid further oxygen reduction. It is not surprising that high protrusions are detected, since O_2 is expected to adsorb but not react at that potential. Indeed, the measured topographic profile is equal to $\Delta Z = (0.83 \pm 0.10)$ Å, which is comparable to the protrusion measured before (ΔZ_{O_2}) letting the FePc-modified electrode to undergo O_2 reduction.

6.2 Fe(III)-Phthalocyanine chloride — Fe(III)Pc-Cl

Fe(III)-Phthalocyanine chloride was investigated as mean of comparison with Fe(II)-Phthalocyanine. Section 5.2.2 was fully dedicated to cyclic voltammetric investigation of Fe(II)Pc-modified Au electrode with the addition of Cl^- since a sensitive different electrochemical response emerged by comparing Fe(II)Pc- and Fe(III)Pc chloride-Au(111) electrodes. Therefore, a different behaviour is also expected when performing EC-STM analysis. The investigation on Fe(III)-Phthalocyanine was conducted by taking the previously studied Fe(II)Pc as guiding model. This is also justified by the fact that Fe(II)Pc and Fe(III)Pc-Cl share many common aspects, above all the central metal atom and the N_4 macrocyclic ligand. However, a major difference exists, and it is the presence of chloride as fifth axial ligand for iron.

EC-STM measurements were first performed in deaerated electrolyte to study both the surface arrangement and its changes in consequence of an applied potential variations. Figure 6.9 represent the best results with Fe(III)Pc-Cl in terms of ordered monolayers. Despite having the same molecular architecture of Fe(II)Pc, the self-assembly process did not bring to a successful result. Few short-range ordered domains were discovered. Pseudo-square and pseudo-hexagonal domains were detected, in accordance with the Fe(II)Pc system, but providing an estimation of their unit cell parameters would lead to untrustworthy results also in terms of surface concentration and coverage.

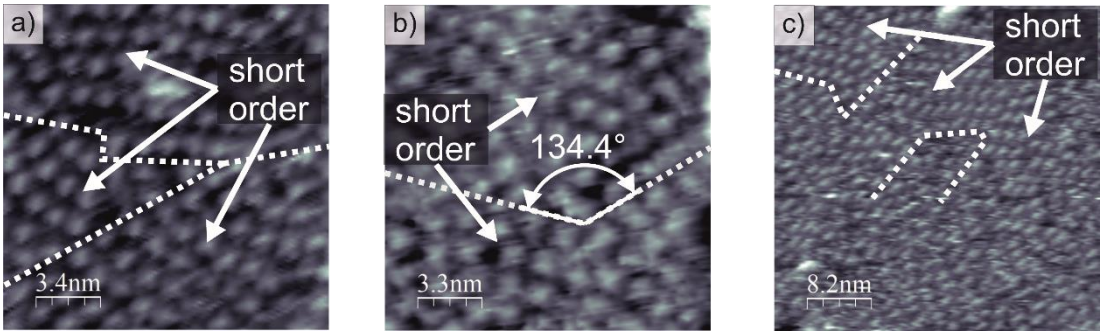

Figure 6.9: (a) I_t = 1 nA; U_b = –313 mV; E_{app} = 630 mV vs RHE, I = –0.4 μA; (b) I_t = 1 nA; U_b = –313 mV; E_{app} = 630 mV vs RHE, I = –0.4 μA; (c) I_t = 1.75 nA; U_b = –286 mV; E_{app} = 670 mV vs RHE, I = –0.2 μA.

Albeit having followed the identical procedure for the sample functionalisation used with Fe(II)Pc, the results were significantly worse. Since the only major difference with Fe(II)Pc had already been identified as the presence of Cl^-, it is inferred that Cl^- does exert a role in the adsorption behaviour of Fe(III)Pc-Cl. An interesting point concerns how this role explicates in determining a different electrochemical response and a different adsorption behaviour if compared to Fe(II)Pc. Further information may be brought by potentiodynamic imaging in Ar saturated electrolyte.

6.2.1 Potentiodynamic investigation of Fe(III)Pc-Cl in Ar purged electrolyte

As already done for Fe(II)Pc, potentiodynamic imaging was performed by stepping the potential from a sufficiently positive value (E_{app} = 675 mV) where no Faradic reactions take place to the peak potential (or close values) according to the corresponding cyclic voltammetry. The corresponding image collected at this potential is reported in figure 6.10a.

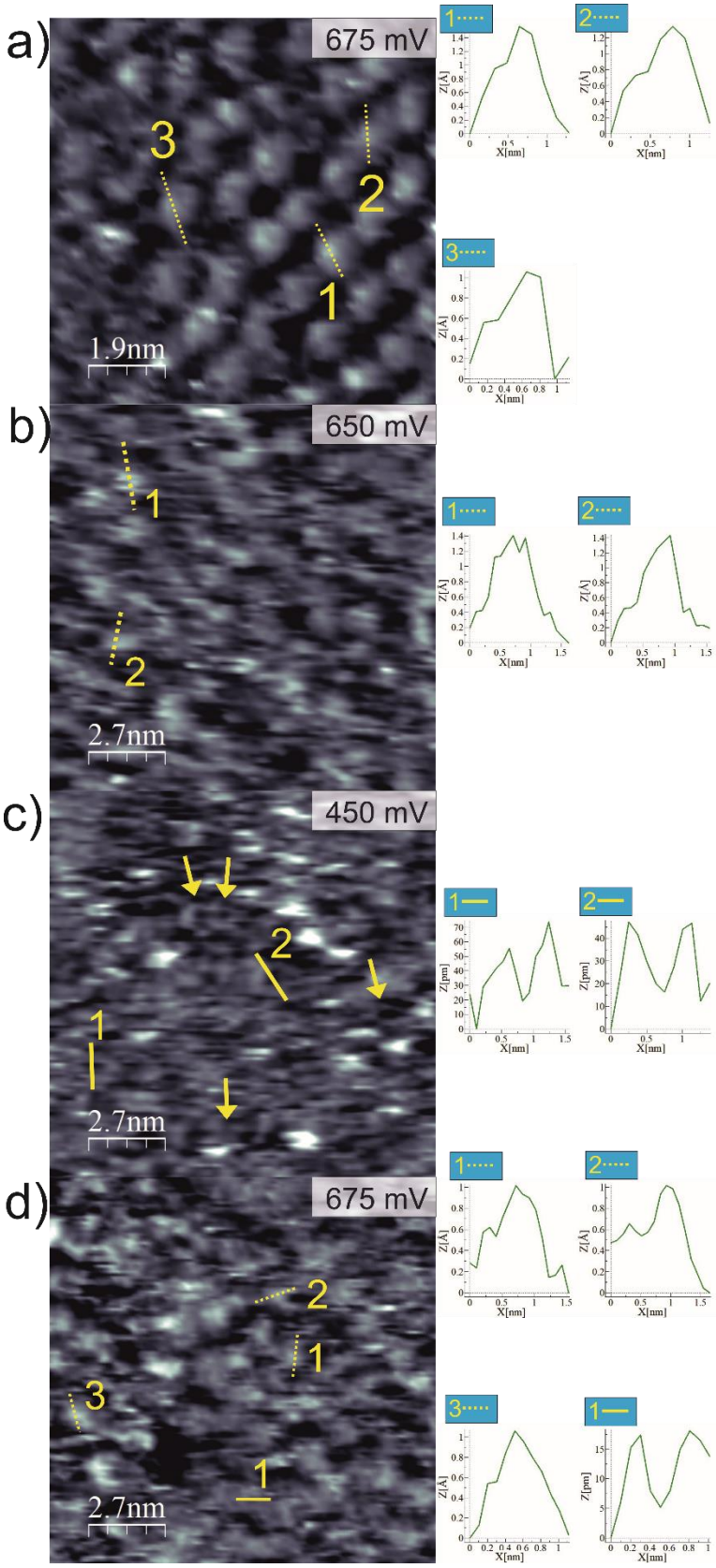

Figure 6.10: (a) I_t = 1.95 nA; U_b = +324 mV (vs RE) mV; E_{app} = 675 mV vs RHE; I = –0.1 µA; (b) I_t = 1.95 nA; U_b = +324 mV (vs RE) mV; E_{app} = 650 mV vs RHE; I = –0.2 µA; (c) I_t = 1.95 nA; U_b =+309 mV (vs RE) mV; E_{app} = 450 mV vs RHE; I = –1.6 µA; (d) I_t = 1.95 nA; U_b = +309 mV (vs RE) mV; E_{app} = 675 mV vs RHE; I = –0.1 µA.

A small ordered domain was observed, and all the molecules show a central brighter spot, even if their shape appears distorted, probably as a consequence of a drift component. Topographic profiles were extracted, and the average protrusion was equal to $\Delta Z = (0.52 \pm 0.10)$ Å. At this point, a possible contradiction arises. In fact, when $E_{app} > E_{onset}$ Fe(II)Pc was found to undergo the same (III)→(II) redox process on the Fe atom, and the protrusion detected in EC-STM was assigned to the presence of iron as Fe(III). The same mechanism is expected to occur for Fe(III)-Pc-Cl, accordingly with the cyclic voltammetric investigations. At this point, the role of chloride can be invoked to explain the apparent difference in topographic profiles for two molecular systems which are in principle identical. Indeed, if chloride is predicted to be found nearby the iron atom, its presence would be somehow revealed by means of tunnelling microscopy. In fact, a higher topographic profile was encountered when chloride was present together with phthalocyanine, even if at $E_{app} > E_{onset}$ both with Fe(II)Pc and Fe(III)Pc-Cl iron should be present as Fe(III). Nonetheless, it cannot be stated whether Fe still retains chloride as a fifth axial ligand when FePc is adsorbed on the Au(111) substrate, or if chloride is lost at the moment of adsorption, or even if chloride was lost in the FePc/DMF solution but then co-adsorbed when functionalising the gold substrate. The hypothetical scenario can be further complicated if one thinks that chloride is capable of a strong specific adsorption on gold [10], and that FePc retains the chloride but adsorb facing with the chloride atom towards the surface, or that free chloride adsorbs on gold and FePc binds on it though the iron atom. In all the considered cases, the result might explain the enhanced protrusion revealed with respect to Fe(II)Pc.

The applied potential was first shifted to E_{app} = 650 mV (figure 6.10b) and then to E_{app} = 450 mV (figure 6.10c), which roughly corresponds to the peak potential as determined by cyclic voltammetry (section 5.2.2). It seems clear that the cathodic potential shift caused an enhanced molecular mobility, since molecules appear distorted and an overall noise is affecting the image. Very bright spots are ascribed to temporary bi-layer molecular arrangements, in the sense that the tunnelling tip embraces the marked mobility and perturbs some molecules so that they are swept over the existing phthalocyanine monolayer by the tip [11]. The enhancing of molecular mobility is often encountered when performing *in situ* STM under electrochemical control. This is a key-point that requires further explanation. The ordering/disordering character is known to be mainly determined by the manipulation of adsorbates/substrate and adsorbates/adsorbates interactions under electrochemical conditions through modification of the applied potential [12–14]. In particular, strong adsorbates/substrate interactions will reduce molecular mobility, since molecules will be stuck to the surface due to the strong interaction. The interaction can however be modified by a change in surface charge density prompted by a variation of the applied potential [13]. Phthalocyanines and porphyrins possess large delocalised π systems, and they are good candidates for adsorbates/substrate interaction modification. High electrode potential will result in a positive surface charge density, whereas a lower electrode potential will realise a negative surface charge density [12]. Depending on substituents of the macrocyclic ring, a positive surface charge will result in an increased adsorbates/substrate interaction or vice versa. Moreover, the presence of a metal centre with a definite oxidation state must also be considered in this case, therefore resulting in a very complex system to be modelized *a priori*. In particular, according to the experimental evidences for Fe(III)Pc-Cl, it appeared that lowering the electrode potential (more negative surface charge) resulted in an increased mobility and hence in a decreased adsorbates/substrate interaction.

An interesting feature of the same figure 6.10c is the detection of many hollow molecules. This behaviour was similarly observed in the case of Fe(II)Pc. The measured depth of the empty regions is equal to $\Delta Z = (0.33 \pm 0.10)$ Å. This value is in accordance with those obtained for the Fe(II)Pc system. Therefore, the same speculation of Fe(II)Pc is now recalled for explaining such profound change in the imaged molecules. Namely, the iron centre had undergone the redox transition from Fe(III) to Fe(II), and the STM imaged had changed accordingly due to the different electronic configuration, as hypothesised for Fe(II)Pc.

When the potential was then swept back to the original E_{app} = 675 mV potential, molecules clearly lose their mobility due to a stronger molecule-substrate interaction promoted by the restored positive potential, as previously discussed. Figure 6.10d shows that, in the STM image taken at that WE potential, the most part of the recognisable molecules possess a bright centre with an associated height of $\Delta Z = (0.48 \pm 0.10)$ Å. This would signify that those metal centre underwent re-oxidation. Fewer molecules appear hollow, with a depth of $\Delta Z = (0.13 \pm 0.10)$ Å.

The bright spots are then ascribed to Fe(III) atoms, whereas the hollow molecule would refer to Fe atoms still at the (II) oxidation state. This is however not surprising, since the same slow re-oxidation phenomenon was observed with Fe(II)Pc as well as with CoPc [8].

6.2.2 Investigation of Fe(III)Pc-Cl in O_2 saturated electrolyte

To examine the Fe(III)Pc-Cl activity towards ORR, the 0.1 M $HClO_4$ electrolytic solution was saturated with O_2 gas. As already observed in the case of Ar saturated electrolyte, Fe(III)Pc-Cl is less prone than Fe(II)Pc to form SAM also in O_2 saturated electrolyte. Only small domains resembling to square symmetry (as Phase 1 of Fe(II)Pc) were detected (figure 6.11), but unit cell parameters were not calculated, being the detected domains composed by a limited number of molecules. This means that the unit cell parameters determination would lead to an untrustworthy result.

Differently from Fe(II)Pc, at a first glance the Fe(III)Pc-Cl system seems to not clearly exhibit the O_2 adsorption, even if O_2 reduction was clearly observed in the CV at Fe(III)-Pc-Cl-Au(111) electrode, even showing the best catalytic activity with respect to the other FeN_4 examined system. For this reason, further investigations were performed by subjecting the Fe(III)Pc-Cl modified Au(111) crystal to EC-STM potentiodynamic imaging.

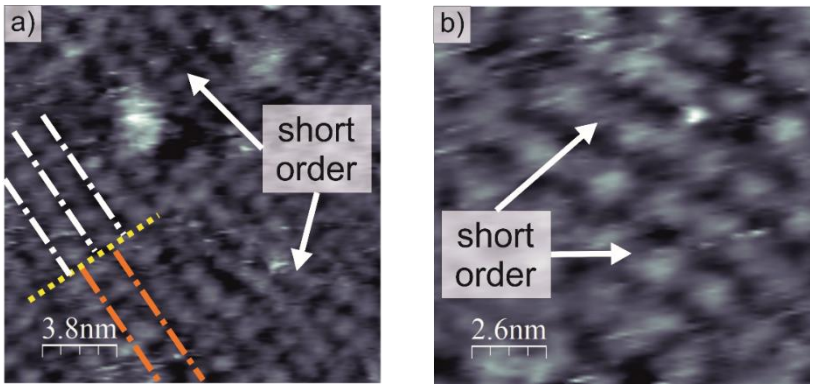

Figure 6.11: (a) I_t = 1.65 nA; U_b = –268 mV mV; E_{app} = 660 mV vs RHE; I = –0.6 µA; (b) I_t = 1.15 nA; U_b = –268 mV; E_{app} = 660 mV vs RHE; I =–0.3 µA.

6.2.3 Potentiodynamic investigation of Fe(III)Pc-Cl in O_2 saturated electrolyte

The applied potential was manually varied starting by E_{app} = 670 mV, which roughly corresponds to the onset potential for O_2 reduction, as determined by cyclic voltammetric investigation (section 5.3.2). The most part of molecules were imaged with an enlightened central spot, without any particular shape. The topographic profiles reveal that the protrusion extends of $\Delta Z = (0.78 \pm 0.10)$ Å, which is approximately ≈0.30 Å higher than the previously determined Fe(III) centre. This could indicate that O_2 was in some way interacting with the Fe(III)Pc-Cl adlayer. Since the STM images are substantially different from the *end-on* adsorbed O_2 molecule on the Fe(II)Pc system, it is speculated that in the case of Fe(III)Pc-Cl the O_2 molecule is *side-on* adsorbed. The *side-on* adsorption geometry was depicted in figure 6.8d and 6.8e. The stability or at least the possible existence of *end-on* or *side-on* adsorption geometries is somewhat tricky to state, since computational studies are often in contrast and do not always corroborate the experimental evidences, and vice versa. Wang et al. used spin-polarised DFT computations to predict the *end-on* adsorption of O_2 on a FePc monolayer as the only stable configuration [15]. Other studies reported by Zagal et. al. showed that in Fe-phthalocyanine can exhibit both *end-on* and *side-on* adsorption geometries [16].

Wang et al. performed interesting DFT calculations of the O_2 adsorption onto FePc single molecules [17]. They found that both *end-on* and *side-on* adsorption structures are stable on FePc, but also that the *side-on* geometry allows more charge transfer from FePc to O_2 itself. Moreover, O-O bond length is predicted to be 7.3% larger than in *end-on* configuration, and 11.6% larger than the isolated dioxygen molecule. This would suggest that the O-O bond is weaker in the *side-on* configuration and that the adsorbed O_2 molecules are more prone to follow reduction [17]. This would in principle justify the slightly increased ORR activity shown by Fe(III)Pc-Cl with respect to Fe(II)Pc, but clear computational evidences are missing and furthermore all this study does not take into account the presence of chloride and its eventual implication in varying the O_2 adsorption geometry [17].

However, Arenz et al. performed DFT calculation of selective anion adsorption on FeN_4C_{12} moieties, showing that anions like Cl^- and $H_2PO_4^-$ are able to weaken the Fe-O bond, making the OOH formation more difficult to occur with respect to OH removal, so that the ORR activity of iron macrocycles increases (at least with $H_2PO_4^-$), but the selectivity toward the tetraelectronic mechanism decreases. In fact, OOH and OH species are involved in the $2e^-$ and $4e^-$ mechanism catalysis, respectively (see section 5.4) [18].

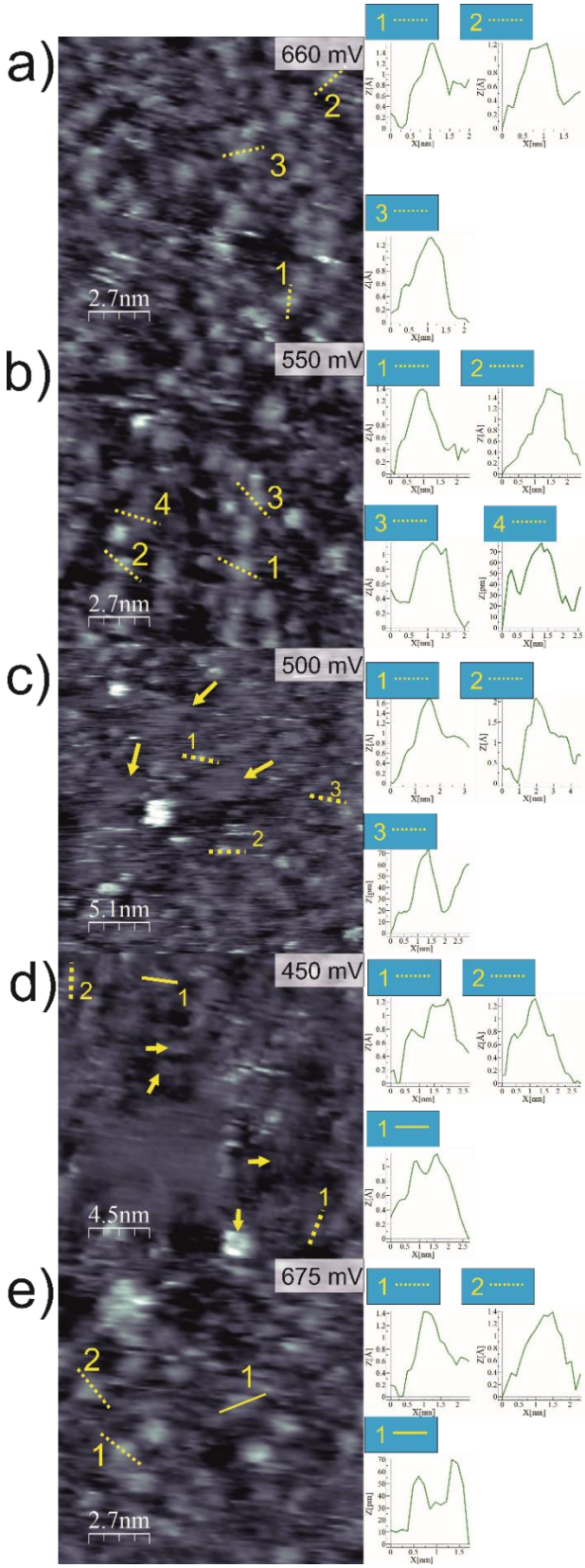

Figure 6.12: (a) I_t = 2.3 nA; U_b =+303 mV (vs RHE) mV; E_{app} = 660 mV mV vs RHE; I = –0.3 µA; (b) I_t = 2.3 nA; U_b =+303 mV (vs RE) mV; E_{app} = 550 mV vs RHE; I = –5.1 µA; (c) I_t= 2.3 nA; U_b = +303 mV (vs RHE) mV; E_{app} = 500 mV vs RHE; I = –7.0 µA; (d) I_t = 2.3 nA; U_b = +303 mV (vs RE) mV; E_{app} = 450 mV vs RHE; I = –5.2 µA; (e) I_t = 2.3 nA; U_b =+303 mV (vs RE) mV; E_{app} = 675 mV vs RHE; I = –0.2 µA.

From the initial $E_{app} = 670\ mV$, the applied potential was slowly swept to E_{app} = 550 mV, which still produces a weak ORR Faradaic current. In fact, molecules are still quite well resolved (figure 6.12b), and the corresponding topographic profiles confirm a protrusion of $\Delta Z = (0.80 \pm 0.1)$ Å that is the characteristic value found for the metallic centre of each molecule.

At the applied potential of E_{app} = 500 mV (figure 6.12c), the Fe(III)Pc-Cl adlayer underwent a profound change in arrangement. Molecules were indeed greatly mobile, and the solid arrows of figure 6.12c indicate "islands" of not resolved molecules. These islands have actually a colour contrast similar to molecules, but they appear as uniformly coloured without any detailed feature. This behaviour is anyway frequent and as it observed also in literature with iron-porphyrin monolayers at a copper/electrolyte interface [11]. It was also observed that scanning with "drastic tunnelling conditions" (more than 3 nA and 200 mV differences in tunnelling current and voltage bias, respectively) causes the adlayer to be significantly damaged and consequently the image to become unclear. However, some molecules where managed to be imaged, and their topographic profiles led to two results: (*i*) O_2-FePc complexes were still present due to the already known protrusion of $\Delta Z = (0.85 \pm 0.1)$ Å (dashed lines 1 and 2; (*ii*) a shorter protrusion of $\Delta Z = (0.53 \pm 0.1)$ Å (dashed line 3) was also measured, indicating the presence of some non-O_2-coordinated iron sites, in accordance with an applied potential which is still enough positive for not causing high reductive current.

When the WE electrode is polarized to a value close to the peak potential for the ORR, E_{app} = 450 mV (figure 6.12d), the islands previously detected at E_{app} = 500 mV appear to enlarge into a bigger unique one, confirming the effect of the WE potential in enhancing molecular mobility. Notwithstanding the increased mobility, some molecules were imaged, showing both protrusions and hollow spots, with a height of $\Delta Z = (0.54 \pm 0.10)$ Å (dashed line 1 and 2) and a depth of $\Delta Z = (0.28 \pm 0.10)$ Å (solid line 1), respectively. Moreover, besides the distortion caused by the surface mobility, many hollow molecules can be visualised, as indicated by the arrows in figure 6.12d.

Finally, upon returning to a positive potential of E_{app} = 675 mV (figure 6.12e), molecular mobility ceased, allowing to notice many bright molecules, as it was evident in the initial image (figure 6.12a) where O_2 adsorption was hypothesised on Fe centres. The bright spots correspond in fact to a protrusion of $\Delta Z = (0.85 \pm 0.10)$ Å (dashed lines 1 and 2), confirming the same results obtained at the beginning of potentiodynamic imagine, namely that O_2 is adsorbed probably with *side-on* geometry onto Fe(III)Pc-Cl. Hollow molecules with a $\Delta Z = (0.29 \pm 0.10)$ Å are also noticeable (solid line 1).

6.3 Fe(III)-Tetramethoxyphenyl porphyrin chloride — Fe(III)TMPP-Cl

Fe(III)-tetramethoxyphenyl porphyrin chloride (abbreviated Fe(III)TMPP-Cl) was the third FeN_4 macrocyclic system to be analysed. Like phthalocyanines, porphyrins exhibit remarkable activity towards ORR [16,19–21]. Transition metal porphyrins are however more susceptible to oxidation and possess lower thermal stability than the parent transition metal phthalocyanines [20]. Nevertheless, it is of great scientific interest to study the possible modifications to ORR electrocatalysis exerted by a different chemical environment. Indeed, porphyrins still are well-known representative of N4 chelates able to coordinate a transition metal thanks to their suitable central hole, with the four coordinating N atoms pointing inwards the cavity. The porphyrin herein investigated not only provided a different macrocyclic ligand in terms of number of nitrogen and carbon atoms, but also presents *meso*-substituents. In particular, *para*-methoxyphenyl groups are occupying the *meso* positions of the porphyrin ring. Methoxyphenyl is regarded as an electron-donating substituent [21], which is therefore expected to cause a cathodic shift the O_2 reduction peak. These concepts are well described in terms of intermolecular hardness, as done in section 5.1. Electron-donating substituents supply electron density to the metal centre. This will make the iron centre more difficult to be reduced, shifting the Fe(III)/Fe(II) redox potential to more negative values. The HOMO-LUMO gap between the metal and the O_2 molecule will also increase, thereby enlarging the intermolecular hardness. A cathodic shift in the ORR will be in the end produced, therefore worsening the catalytic activity of the FeN_4 system [16,21].

The substituents have also effects on other properties, for example solubility. In fact, Fe(III)TMPP-Cl was found to fully dissolve in DMF without forming any precipitation even after days. Masa and Schumann indeed performed UV-VIS spectrophotometry and shown that the Soret band, which is most intense for porphyrins, undergoes significant shifts depending on the nature of the ligand and its substituents [21].

Another remarkable aspect concerns the presence of chloride as counterion linked to the Fe atom in the crystal form of the compound. Having already determined an effect of Cl^- on both the electrochemical response and the adsorption behaviour on Au(111) for Fe(III)-phthalocyanine chloride, a similar one is expected also for Fe(III)-tetramethoxyphenyl chloride, even if the corresponding Cl^- free compound was not tested, being not commercially available.

Fe(III)TMPP-Cl was found to have a pronounced tendency to self-assembly, since highly-ordered domains counting also hundreds of molecules are visible, so that domains are even larger than the scanned area, which was frequently set at 40 nm x 40 nm. This is a striking difference if compared to the previously studied phthalocyanines and its origin should be ascribed to a different non-covalent interaction with the surface. Indeed, the substituents are implied in a molecular distortion phenomenon, for which the molecular plane of the bare porphyrin is warped by the methoxyphenyl groups. The distortion can be qualitatively predicted by using simple structure design software such as *Avogadro*, which compute the most energetically favourable molecular structure. The result is shown in figure 6.13.

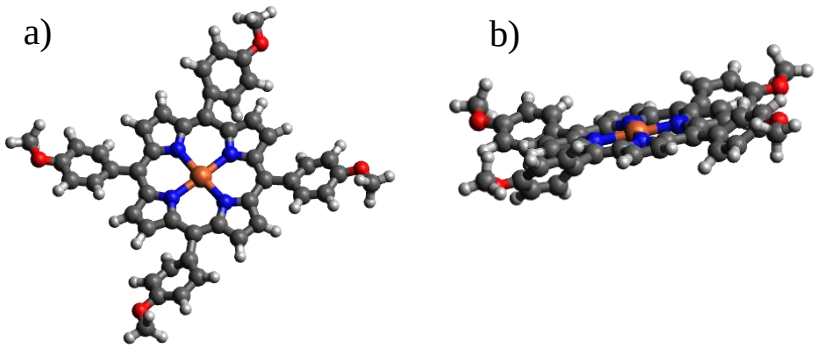

Figure 6.13: (a) and (b) Models of Fe(III)TMPP-Cl and side view (distorted plane).

This roughly means that non-directional interactions are more hindered due to the non-uniform molecular geometry, and the resulting physisorbed monolayer is therefore expected to be more labile [22]. Imaging was started at an applied potential of E_{app} = 610 mV, since the previously recorded cyclic voltammograms (section 5.2.3) have shown no significant Faradaic current. The resulting image is displayed in figure 6.14.a, which also features the sketched unit cell parameters and the superimposed model structure of Fe(III)TMPP-Cl. Additionally, hexagonal-symmetry domains were also found, as shown in figure 6.14b.

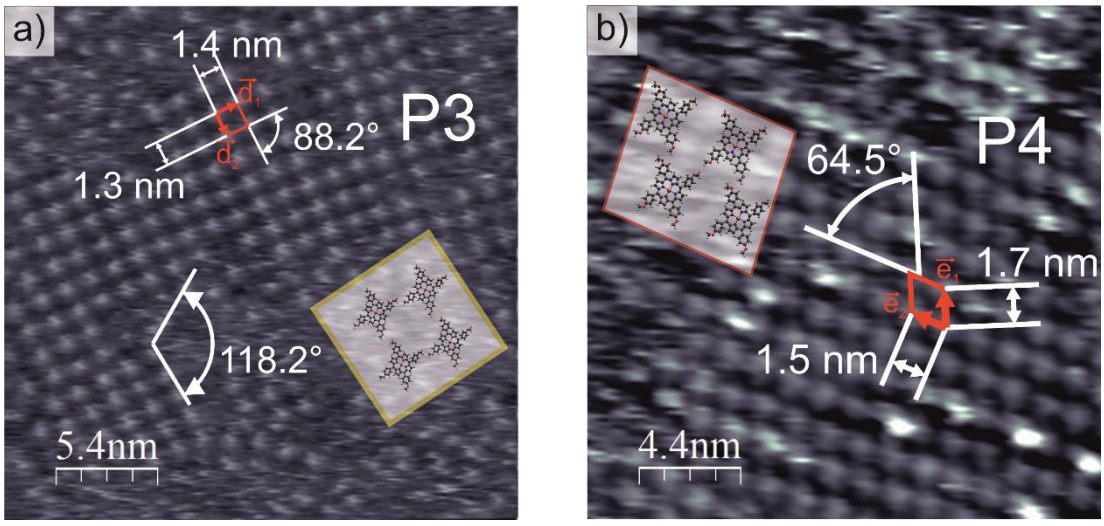

Figure 6.14: (a) I_t= 1 nA; U_b = -300 mV; E_{app} = 610 mV vs RHE; I = –0.0 µA**; (b)** I_t = 1 nA; U_b = –318 mV; E_{app} = 610 mV vs RHE; I = –0.0 µA

Figure 6.14a shows an almost unique square symmetry domain, denoted as Phase 3 (to diversify it from the square Phase 1 of Fe(II)Pc). The derived unit cell parameters are: $\vec{d}_1 = (1.4 \pm 0.1)\ nm$, $\vec{d_2} = (1.3 \pm 0.1)\ nm$, measured angle $\measuredangle = (88 \pm 2)$ °. The corresponding surface concentration is: $5.510 \cdot 10^{13}\ \frac{molecules}{cm^2}$, while the surface coverage is $\theta_{FeTMPP}^{P3} = 0.040$.

On the contrary, in figure 6.14b displays an almost unique hexagonal domain (Phase 4), with the following unit cell parameters: $\vec{e_1} = (1.7 \pm 0.1)\ nm$, $\vec{e_2} = (1.5 \pm 0.1)\ nm$ measured angle $\measuredangle = (65 \pm 2)°$. The resulting surface concentration is: $3.922 \cdot 10^{13}\ \frac{molecules}{cm^2}$, while the surface coverage is $\theta_{FeTMPP}^{P4} = 0.0328$.

6.3.1 Fe(III)TMPP-Cl bi-layer formation

Fe(III)TMPP-Cl exhibited a peculiar adsorption behaviour if compared to the previously examined Fe-phthalocyanines. In fact, it formed regions with a bi-layer coverage. In those regions, molecules were arranged by forming two layers over the Au surface, therefore deviating from the monolayer coverage conditions. This is known to occur for other metal-phthalocyanine and -porphyrin compounds [9]. The formation of a bi- or multiple-layer arrangement is a consequence of numerous factors and cannot be rigorously predicted. The main factors influencing the Au functionalisation concern both physical chemical properties of the porphyrin and some external factor like concentration of the Fe(III)TMPP-Cl/DMF solution, Au terraces smoothness, functionalisation time, etc. Physical chemical properties are fixed once chosen a definite system, however external factors can seriously alter the functionalisation process. Bi-layers were in fact only occasionally revealed, whilst they were involving a large number (>100) of ordered molecules. Few images are in any case analysed, as shown in figure 6.15.

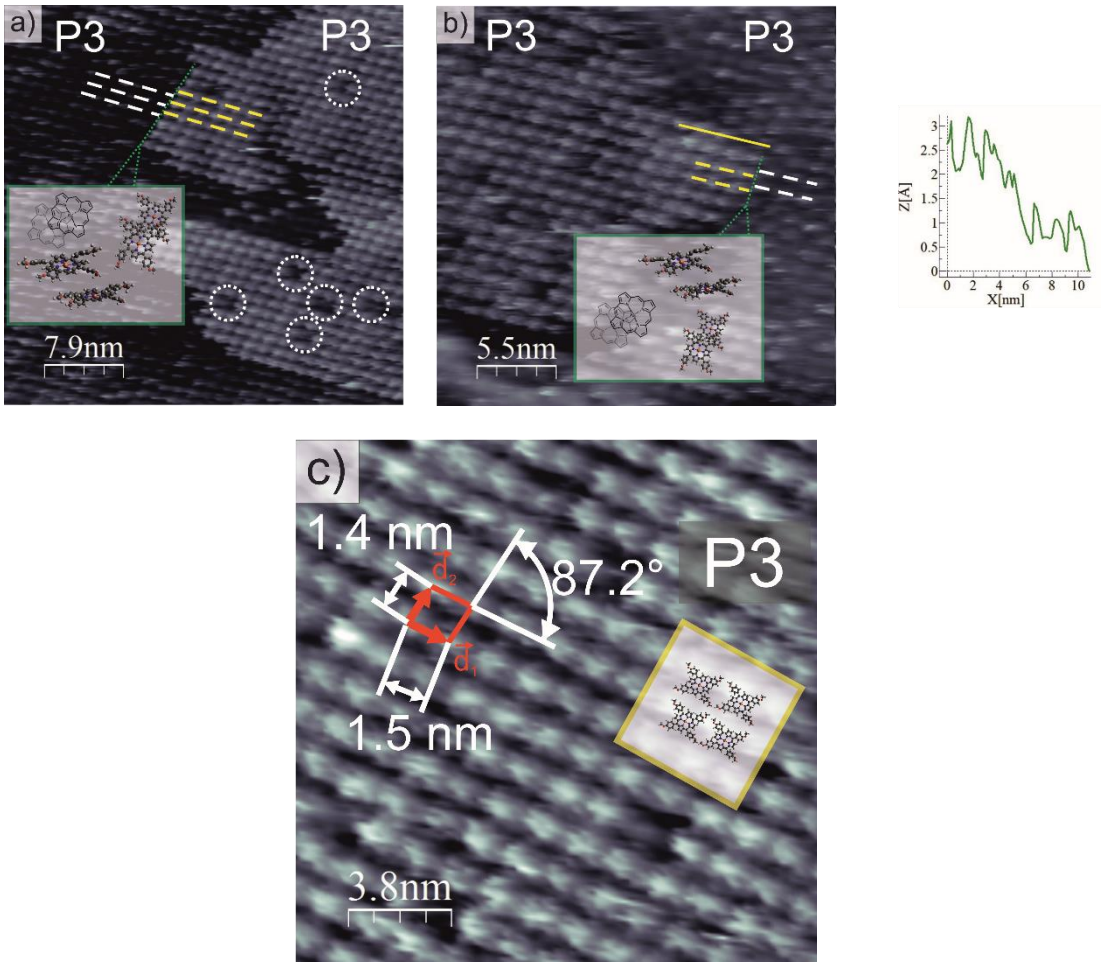

Figure 6.15: (a) I_t = 0.48 nA; U_b = –443 mV; E_{app} = 720 mV vs RHE; I = –0.0 µA; **(b)** I_t = 0.48 nA; U_b = –443 mV; E_{app} = 720 mV vs RHE; I = –0.0 µA**; (c)** I_t = 0.48 nA; U_b = –443 mV; E_{app} = 720 mV vs RHE; I = –0.0 µA**.**

By a detailed analysis of figures 6.15a and 6.15b, the structure of the bi-layer stacking can be observed. The second-layer is displayed with a brighter contrast in both figures. Molecular

rows are better visualised by tracing white and yellow dashed lines at the border of the upper layer. In this way, it can be noticed that the rows of the second layer are misaligned with respect to the rows of the first layer. This is coherent with the molecular stacking depicted in figure 6.16.

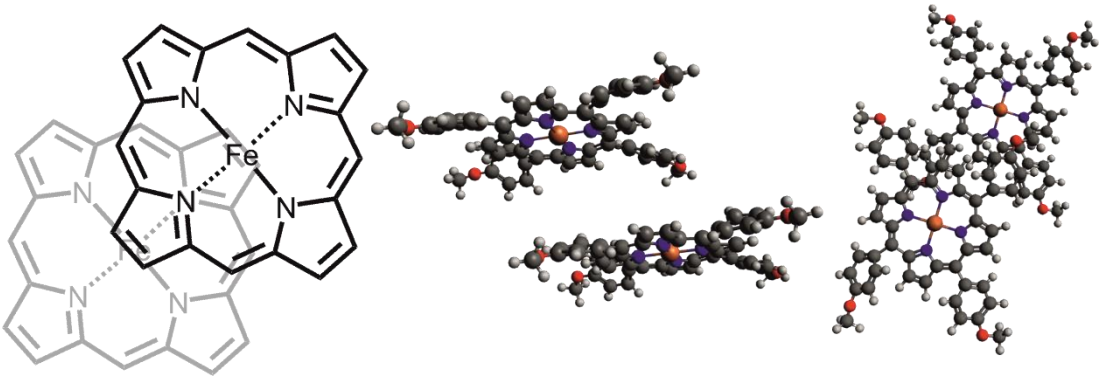

Figure 6.16: Depictions of bi-layer arranged Fe(III)TMPP molecules.

A similar arrangement was encountered with Zn-phthalocyanine [9]. Metals in the cavity of porphyrins generally favours their stacking in a face-to-face geometry, as depicted in figure 6.16 [23]. This means that the positive charge density located on the metal atom establishes a favourable interaction with the porphyrin system π on the pyrrolic units [23]. The presence of a 2nd molecular layer could in principle be confused with an Au step edge, but the topographic profiles extracted by the solid line of figure 6.15b returned a height of $\Delta Z = (1.57 \pm 0.10)$ Å, which is significantly lower than the expected 2.4 Å assigned to the Au step edge (see section 4.1.2).

Some missing 2nd layer molecules are encircled with a dashed line in figure 6.15a. This corroborates the observation of a molecular bi-layer.

Figure 6.15c is a high-resolution image performed exclusively on a portion of the bilayer island shown in figure 6.15a. The detected symmetry is ascribed to Phase 3 and the extracted unit cell parameters are: $\overrightarrow{d_1} = (1.5 \pm 0.1)\ nm, \overrightarrow{d_2} = (1.4 \pm 0.1)\ nm$ angle $\measuredangle = (87 \pm 2)°$. The corresponding surface concentration is $4.762 \cdot 10^{13}\ \frac{molecules}{cm^2}$, whereas the surface coverage is $\theta_{FeTMPP}^{P3-bilayer} = 0.034$.

6.3.2 Potentiodynamic investigation of Fe(III)TMPP-Cl in Ar purged electrolyte

Potentiodynamic imaging was first and foremost performed in deaerated 0.1 M $HClO_4$, as did for the previous systems, to evaluate the eventual effect of the electrode potential on the surface ordering and also on the central iron atom. The first set of measurement were focused to the first peak up to 400 mV vs. RHE. Imaging was started at a E_{app} = 620 mV, since the recorded CV for the Fe(III)TMPP-Cl/Au(111) electrode shown no substantial Faradaic contribution at that potential. The obtained STM image is reported in figure 6.17a, together with the topographic profile extracted along the dotted line. The image shows greatly ordered Fe(III)TMPP-Cl domains. The 40 nm x 40 nm scan size achieves a medium resolution picture, and the greatly ordered domains allow to trace a longer topographic profile line, noticing profile changes of many molecules all at once. At E_{app} = 620 mV the average topographic

profile is equal to $\Delta Z = (1.00 \pm 0.10)$ Å. This value is actually higher than the corresponding one measured for Fe(II)Pc and Fe(III)Pc-Cl, but the resolution is, as just mentioned, lower due to a higher scan size, making the identification of any eventual central protrusion unattainable. Namely, the STM is still sensitive at the molecular level, but not at sub-molecular one, as it did with previous high-resolution images.

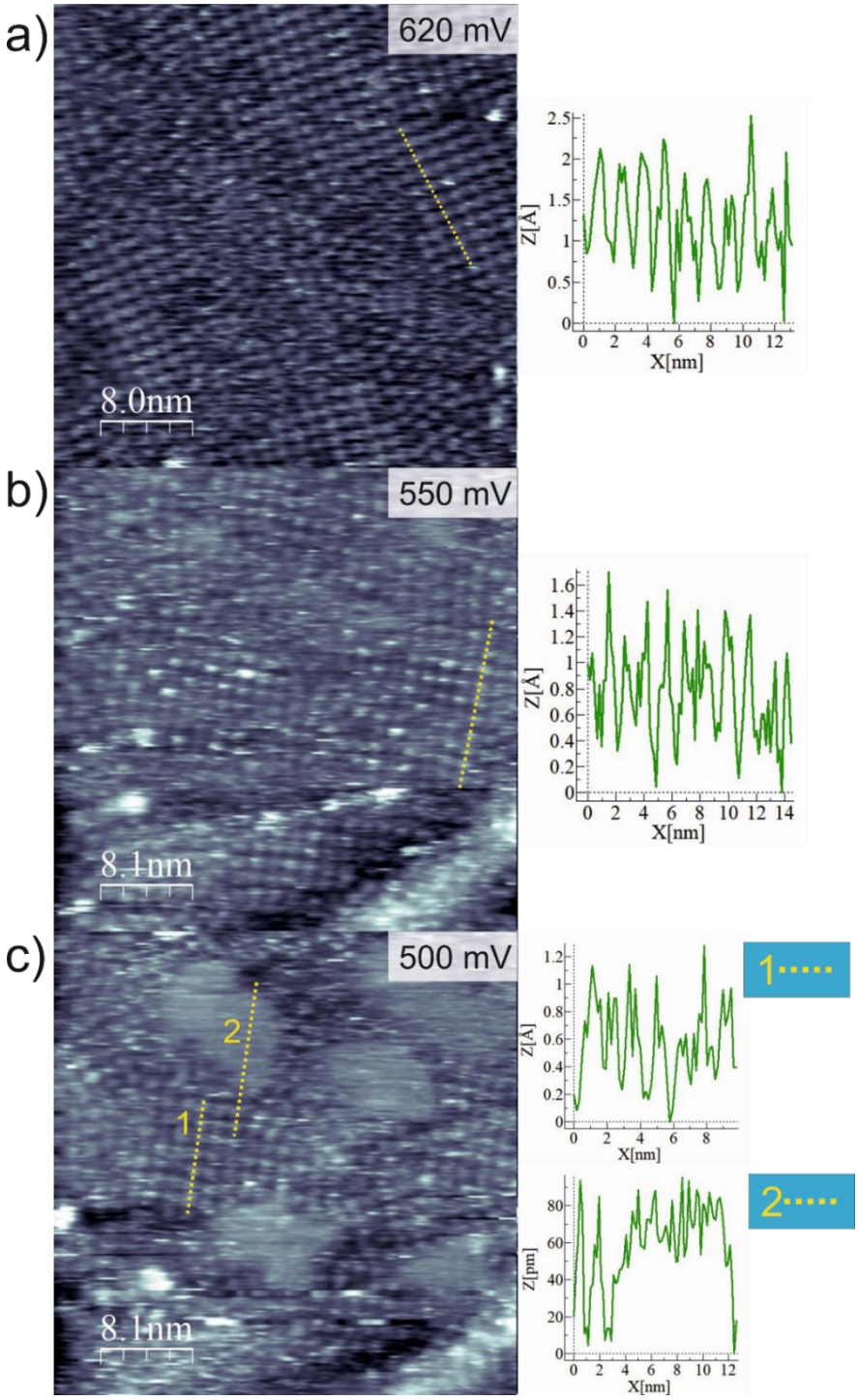

Figure 6.17: (a) I_t = 0.60 nA; U_b =+175 mV (vs RHE) mV; E_{app} = 620 mV vs RHE; I = –0.0 µA; (b) I_t = 0.60 nA; U_b = +175 mV (vs RHE) mV; E_{app} = 550 mV vs RHE; I = –0.1 µA; (c) I_t = 0.60 nA; U_b = +175 mV (vs RHE) mV; E_{app} = 500 mV vs RHE; I = –0.2 µA. The dotted lines express the regions from which the topographic profiles were got.

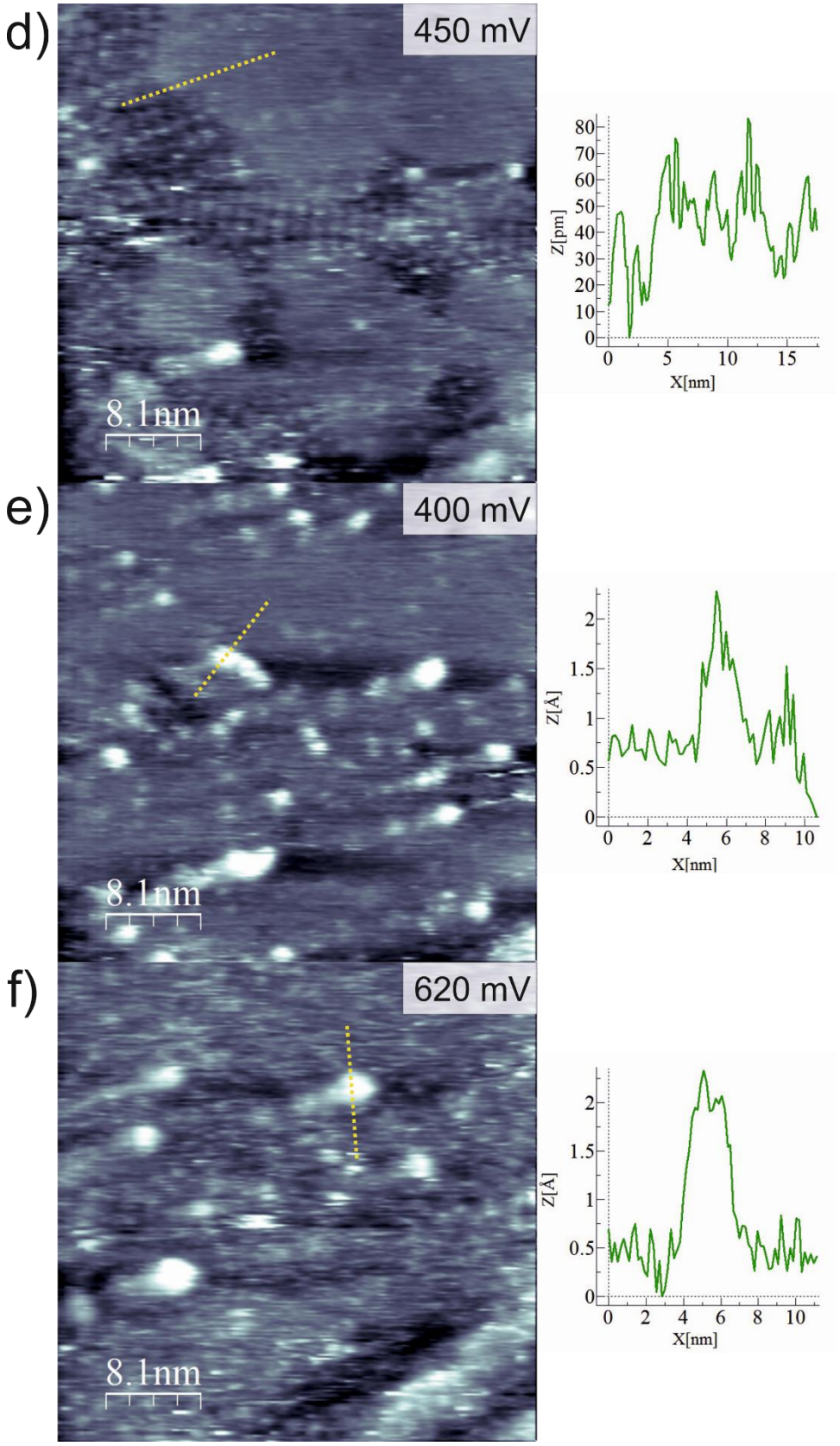

Figure 6.17: (d) I_t = 0.60 nA; U_b = +175 mV (vs RHE) mV; E_{app} = 450 mV vs RHE; I = –0.6 µA; (e) I_t = 0.60 nA; U_b = +175 mV (vs RHE) mV; E_{app} = 400 mV vs RHE; I = –1.0 µA; (f) I_t = 0.60 nA; U_b = +175 mV (vs RHE) mV; E_{app} = 620 mV vs RHE; I = –0.0 µA. The dotted lines express the regions from which the topographic profiles were got.

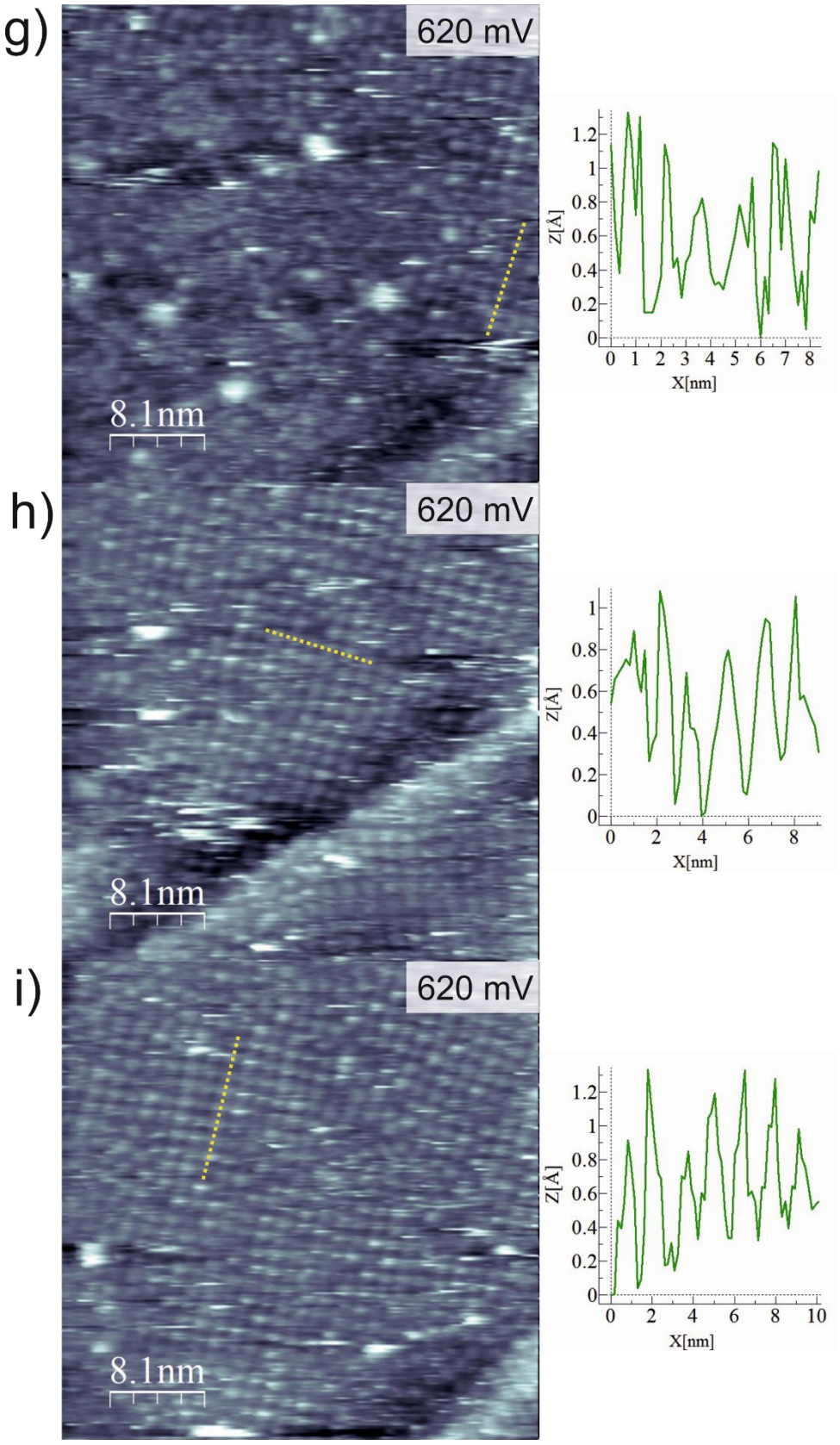

Figure 6.17: (g) I_t = 0.60 nA; U_b = +175 mV (vs RHE) mV; E_{app} = 620 mV vs RHE; I = –0.0 µA; (h) I_t = 0.60 nA; U_b = +175 mV (vs RHE) mV; E_{app} = 620 mV vs RHE; I = –0.0 µA; (i) I_t

= 0.60 nA; U_b = +175 mV (vs RHE) mV; E_{app} = 620 mV vs RHE; I = –0.0 µA. The dotted lines express the regions from which the topographic profiles were got.

Potential steps of 50 mV were covered in cathodic direction to explore the effect of the applied potential. Figure 6.17b shows the image obtained at E_{app} = 550 mV, where ordered domains still exhibit a substantial integrity, but some bad resolved regions start to appear. The topographic profile is still showing protrusions around 1 Å, $\Delta Z = (1.00 \pm 0.10)$ Å.

At E_{app} = 500 mV (fig. 6.17c), the islands became wider and more definite, but ordered domains still co-existed. Two topographic profiles were extracted, one accounting for molecules in an ordered row, the other considering both molecular row and an island. Both topographic profiles were comparable and shown a $\Delta Z = (1.00 \pm 0.10)$ Å. This means that the undefined islands should be associated to molecules in a very mobile state due to a mobility-enhancing applied potential. Indeed, the effect of potential modulation on surface charge density were already correlated to modifications of adsorbates/substrate interaction when describing the Fe(III)Pc-Cl system (section 6.2).

The tunnelling tip also exerts a perturbation, since under certain circumstances it can act as a brush, sweeping molecules away from the scanned surface [11]. The circumstances are determined by the chosen tunnelling parameters. Usually, higher tunnelling currents and lower voltage biases are known to represent "drastic tunnelling conditions" which can significantly alter the molecular adlayer [11]. Analysing by EC-STM the Fe(III)TMPP-Cl adlayer meant to use smaller tunnelling current and higher bias to achieve a satisfactory resistance of the Fe(III)TMPP-Cl adlayer to the tunnelling perturbation. In this way, the tip was farther from the adlayer, and the current flowing through them was lower. The lower resistance to tunnelling perturbation of Fe(III)TMPP-Cl with respect to the studied phthalocyanines is mainly a product of the different ligand, which diminishes the adsorbates/substrate interaction and increases the adlayer lability.

The EC-STM image recorded at E_{app} = 450 mV is showed in Figure 6.17d, where it is evident how islands continued to expand, still maintaining a similar topographic profile with respect to the previous ones: $\Delta Z = (0.90 \pm 0.10)$ Å. Note that the most part of the image is occupied by non-resolved islands, and the ordered layer looks very confined.

At E_{app} = 400 mV (figure 6.17e), the surface is barely recognisable. This potential nearly corresponds to the Fe(III)/Fe(II) potential observed with cyclic voltammetry (section 5.2.3). However, no information can be gathered by STM microscopy, since molecules are found to be greatly mobile on the surface at this potential.

By sweeping back the potential to E_{app} = 620 mV, the following figure 6.17f was obtained. It can be noticed that the previously not resolved areas now start to exhibit dots, which are associated to sufficiently less mobile molecules. Very bright spots are still present, with a $\Delta Z = (2.25 \pm 0.10)$ Å.

Anyway, by continuously scanning the same area, an ordering phenomenon was observed, as shown in figure 6.17g, and a topographic profile of $\Delta Z = (1.00 \pm 0.10)$ Å was regained. It is worth to briefly take into account the effect of the tunnelling tip in breaking the surface ordering, or in retarding its re-assembly. In fact, figure 6.17h was collected immediately after figure 6.17.g and after having moved the scanner few nanometres on the right, showing that areas adjacent to the previously scanned one already feature well-ordered domains. Furthermore, by returning to the original position (figure 6.17i), order was finally re-established. Since this area was not subjected to tunnelling scanning anymore, ordering could complete without external perturbation, demonstrating that the tunnelling phenomenon does play a role in damaging the order and/or in retarding re-ordering.

The second set of measurements was focused to the second peak up to 200 mV vs. RHE, with the aim to collect potentiodynamic images at potentials close to the most intense peak showed in the CV (figure 5.8a). For this reason, the applied potential was swept from 620 mV to 300 mV, as shown in figure 6.18a and as expected, the perfectly ordered surface undergoes a rapid worsening when the more negative potential was reached, starting to form the characteristic islands. The measured height of line 1 is $\Delta Z = (0.91 \pm 0.10)$ Å, in agreement with figure 6.17a. Line 2 embraces both an ordered line of molecules and a small island, where it shows a slightly higher topographic profile than the molecular row, probably arising by the greatly mobile molecules.

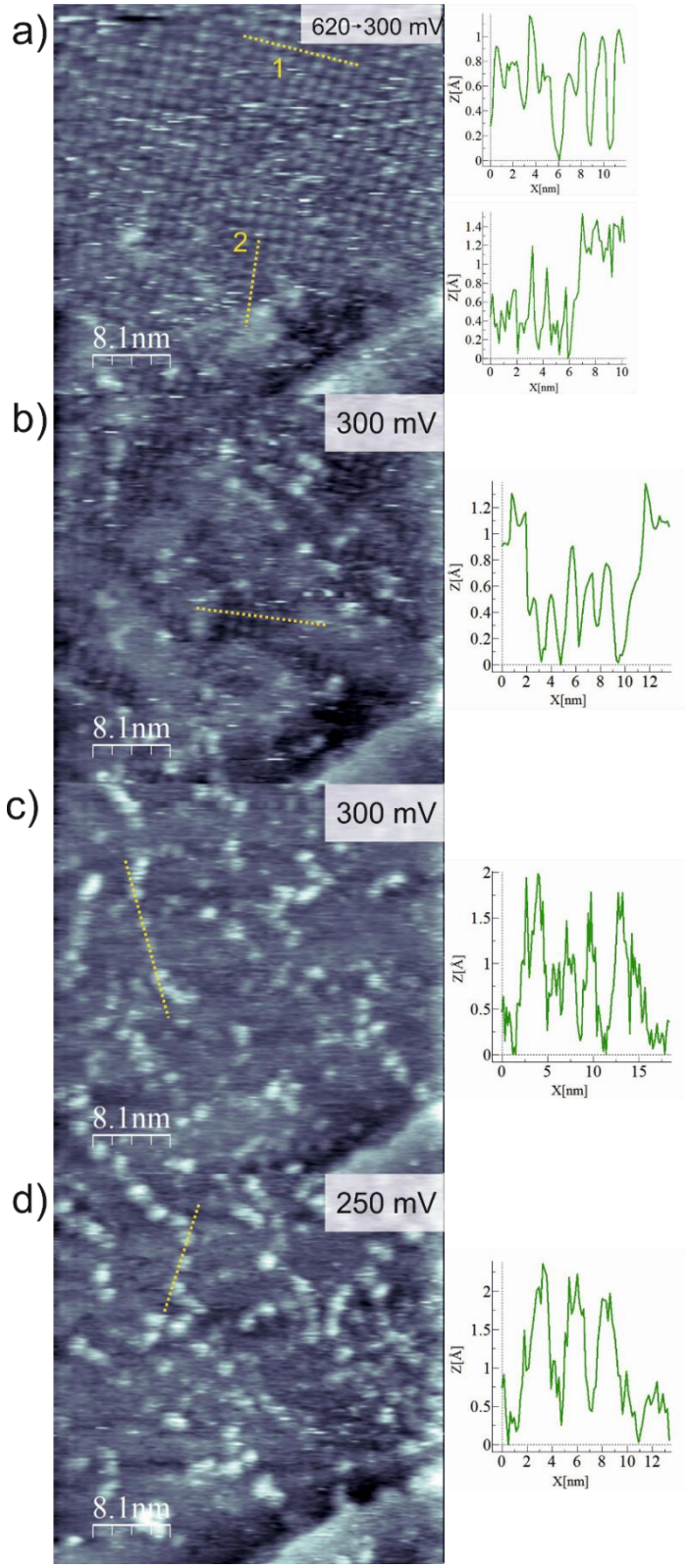

Figure 6.18: (a) I_t = 0.60 nA; U_b = +175 mV (vs RHE) mV; E_{app} = from 620 to 300 mV vs RHE; I = from 0.0 to –3.0 µA; (b) I_t = 0.60 nA; U_b = +175 mV (vs RHE) mV; E_{app} = 300 mV vs RHE; I = –2.1 µA; (c) I_t = 0.60 nA; U_b = +175 mV (vs RHE) mV; E_{app} = 300 mV vs RHE; I= –1.9 µA; (d) I_t = 0.60 nA; U_b = +175 mV (vs RHE) mV; E_{app} = 250 mV vs RHE; I= –2.2 µA.

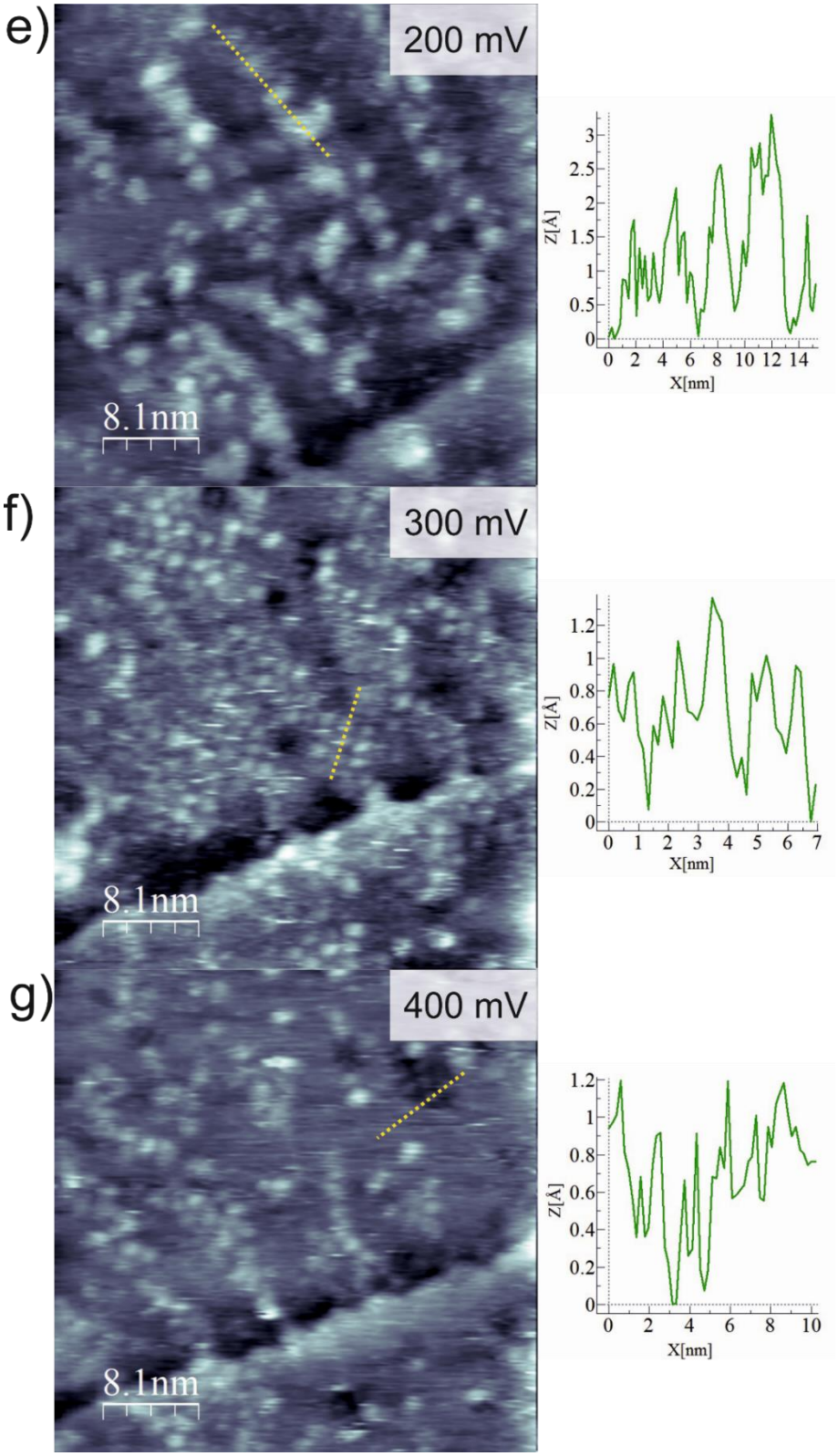

Figure 6.18: (e) I_t = 0.60 nA; U_b = +175 mV (vs RHE) mV; E_{app} = 200 mV vs RHE; I = –1.1 µA; (f) I_t = 0.60 nA; U_b = +175 mV (vs RHE) mV; E_{app} = 300 mV vs RHE; I = –0.6 µA; (g) I_t = 0.60 nA; U_b = +175 mV (vs RHE) mV; E_{app} = 400 mV vs RHE; I = –0.2 µA.

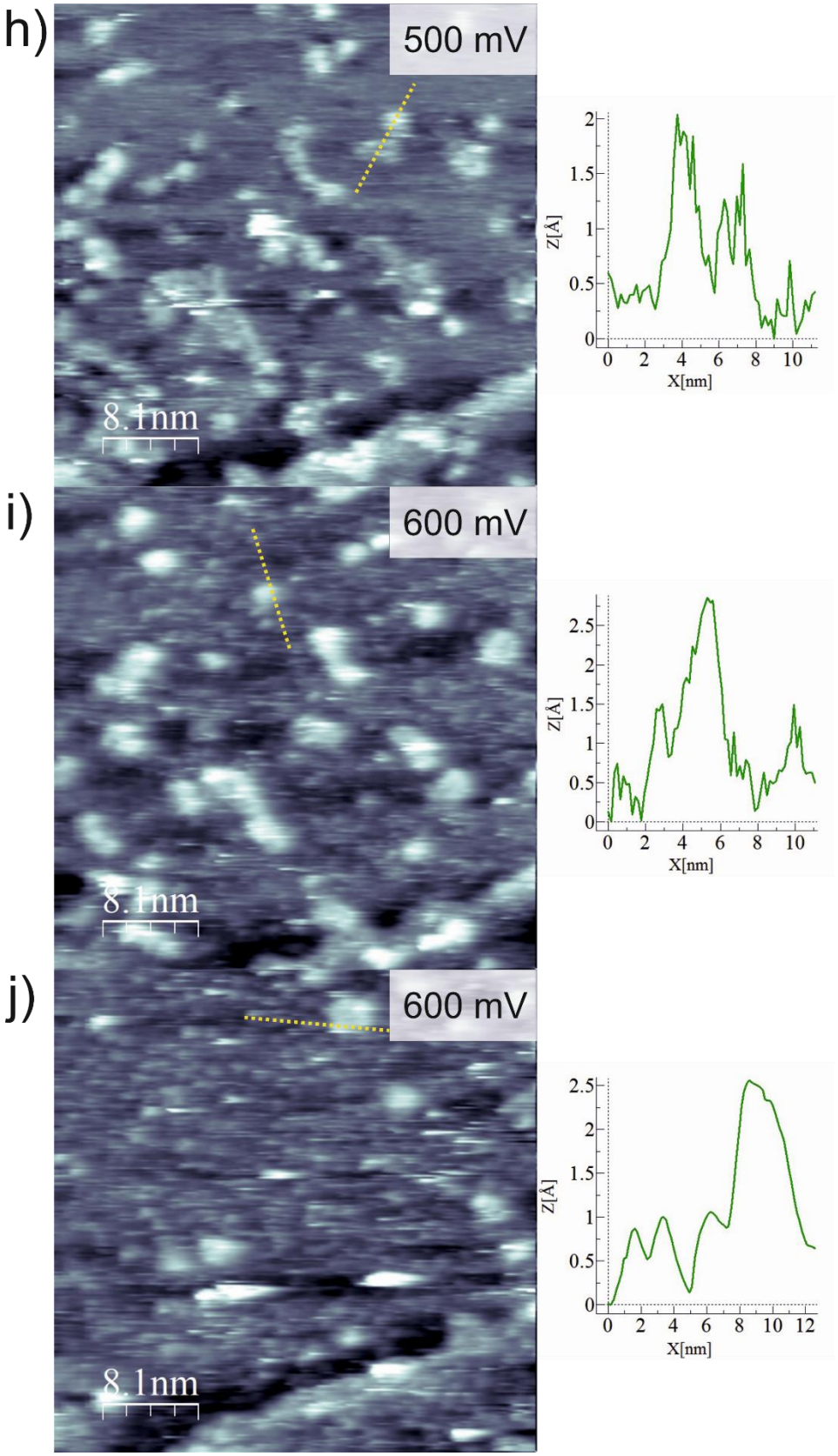

Figure 6.18: (h) I_t = 0.60 nA; U_b = +175 mV (vs RHE) mV; E_{app} = 500 mV vs RHE; I = –0.1 µA; (i) I_t = 0.60 nA; U_b = +175 mV (vs RHE) mV; E_{app} = 600 mV vs RHE; I = +0.0 µA; (j) I_t = 0.60 nA; U_b = +175 mV (vs RHE) mV; E_{appV}= 600 mV vs RHE; I = –0.0 µA.

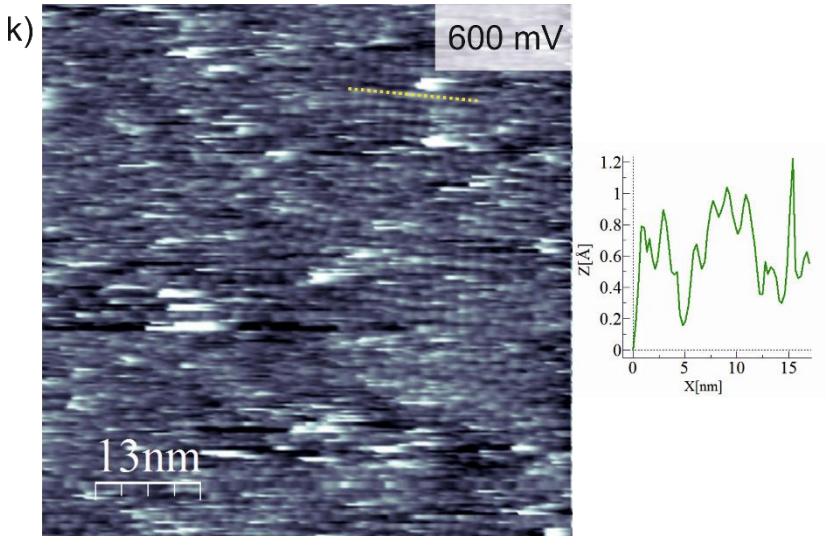

Figure 6.18: (k) I_t = 0.60 nA; U_b = +175 mV (vs RHE) mV; E_{app} = 600 mV vs RHE; I = –0.0 µA.

By holding the potential at E_{app} = 300 mV (figure 6.18b), islands considerably enlarge, leaving only small portions of ordered domains. The topographic profile shows that the islands are around 0.2 Å higher than the ordered molecular row, as already noticed in figure 6.18a.

If the potential is kept at E_{app} = 300 mV even for longer time, the surface appeared completely unresolved (figure 6.18c), with brighter spot which are reconducted to temporary 2nd layer molecules as confirmed by the measured profile that resulted nearly doubled with respect to the ordered domain profile, that is $\Delta Z = (1.81 \pm 0.10)$ Å.

At more negative potential E_{app} = 250 mV no substantial changes are noticeable, with probable by-layer molecules still being imaged with a $\Delta Z = (2.02 \pm 0.10)$ Å (figure 6.18d).

Finally, a potential of E_{app} = 200 mV was reached (figure 6.18e). The extracted topographic profile exhibits an even larger height of $\Delta Z = (2.27 \pm 0.10)$ Å. It could be ascribed to a triple layer of Fe(III)TMPP-Cl molecules, but at this stage it cannot be stated whether it is a peculiar behaviour of the Fe(III)TMPP-Cl adlayer at this potential or just a consequence of the perturbation with the tunnelling tip on the highly mobile Fe(III)TMPP-Cl adlayer.

By sweeping back the applied potential, at E_{app} = 300 mV a temporary ordering behaviour was encountered, and background island seems to show overlying ordered molecules (figure 6.18f). The topographic start to show again a smaller height, in this case equal to $\Delta Z = (1.00 \pm 0.10)$ Å.

However, this effect seemed to be temporary, since at E_{app} = 400 mV molecules regained mobility, showing a completely unresolved surface with usual 2nd layer molecules (figure 6.18g). Only a small portion with five apparently ordered molecules is visible. The trace dotted line shows that the topographic profile is substantially the same both on the ordered domain and on the island, further corroborating the hypothesis of the greatly mobile Fe(III)TMPP-Cl monolayer, that can occasionally result in a bi-layer, explaining the brighter spots.

The situation did not improve by reaching E_{app} = 500 mV (figure 6.18h), as confirmed by the topographic profile of $\Delta Z = (1.78 \pm 0.10)$ Å.

When E_{app} = 600 mV was reached (figure 6.18i), the large island started to be better defined by small spots ascribed to single molecules, thereby maintaining intense bright spots associated to 2nd layer molecules.

Figure 6.18j shows that keeping a positive potential for a sufficient time leads to a progressively ordering surface adlayer. Indeed, the number of brighter spot decrease, and low-range ordered domains start to appear.

After few minutes at E_{app} = 600 mV, a large area picture (figure 6.18k) confirms the reordering phenomenon, with a regained topographic profile of $\Delta Z = (0.88 \pm 0.10)$ Å.

The Fe(III)TMPP-Cl/Au(111) system was probed under potentiodynamic conditions in deaerated electrolyte. The two features observed in the corresponding cyclic voltammetry were in particular investigated, by varying the applied potential up to the two revealed peak potentials, namely 400 mV and 200 mV, respectively. STM basically provided structural information, since high mobility was observed when the potential was scanned in negative direction. Therefore, no significant information about the Fe oxidation state was gained. The same behaviour is then expected for the O_2 saturation case, hence being not able to identify the adsorption step due to very labile Fe(III)TMPP-Cl adlayer.

6.3.3 Investigation of Fe(III)TMPP-Cl in O_2 saturated electrolyte

Figure 6.19 shows that O_2 saturation did not cause a decrease in Fe(III)TMPP-Cl ordered self-assembly, in fact in the large size STM image two highly-ordered and wide domains are visible. The two domains are characterised by different symmetry elements. The left domain possesses square symmetry (Phase 3), whereas the domain on the right possesses hexagonal symmetry (Phase 4). Both phases where already characterised for the case of Ar purged electrolyte. A ~120° domain boundary is also highlighted in figure 6.19b, as well as a unique 2nd layer molecule is encircled in the top-tight part of the same figure 6.19b.

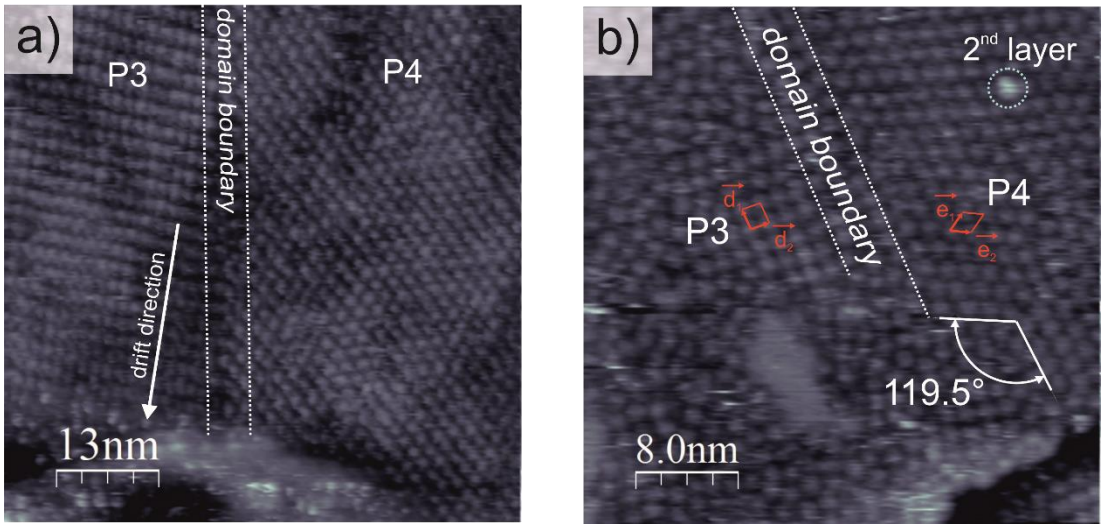

figure 6.19: (a) I_t = 0.55 nA; U_b = –484 mV; E_{app} = 720 mV vs RHE; I = –0.0 µA; (b) I_t = 0.48 nA; U_b = –358 mV E_{app} = 620 mV vs RHE; I = –0.3 µA.

The two types of domains are compresent in several figures (figure 6.19a and 6.19b), with similar measured unit cell parameters.

High-resolution images were collected and reported in figure 6.20. A topographic profile was extracted for each picture following the traced dotted line. In both cases, phase 3 was detected, as shown with the superimposed Fe(III)TMPP-Cl ball-and-stick model in figure 6.20a.

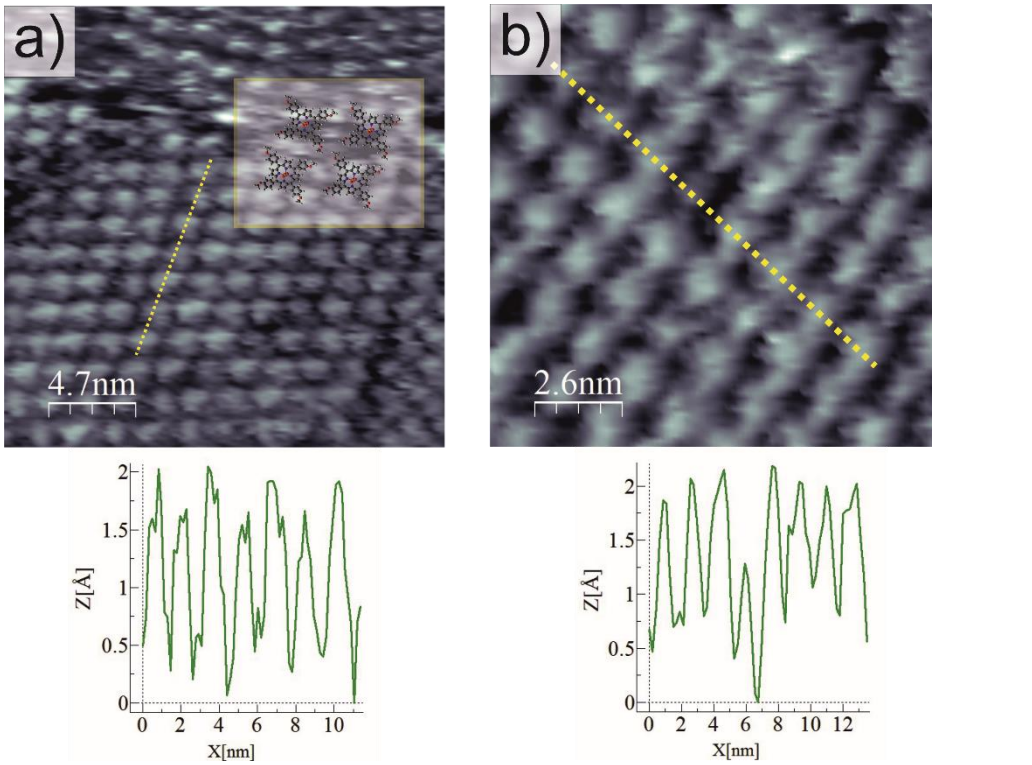

Figure 6.20: (a) I_t = 0.55 nA; U_b = –520 mV (+100 mV vs RHE); E_{app} = 620 mV vs RHE; I = 0.0 µA; the lower part features the topographic profile extracted by the dotted line (b) I_t = 0.55 nA; U_b = –451 mV (+169 mV vs RHE); E_{app} = 620 mV vs RHE; I = –0.0 µA; the lower part features the topographic profile extracted by the dotted line.

Both figures 6.20a and 6.20b show higher protrusions if compared to those revealed in the Ar saturated case (figure 6.17a). In fact, an average $\Delta Z = (1.51 \pm 0.10)$ Å was acquired, which is ~0.5 Å higher than the corresponding Ar saturated case (figure 6.17a) at the same applied potential (E_{app} = 620 mV) and at similar tunnelling conditions (the internal bias was also referenced to RHE in the captions). Being the brighter central spot not clearly distinguished, is it hypothesised that O_2 is *side-on* adsorbed, as it had been speculated for Fe(III)Pc-Cl in consequence of the presence of chloride. Fe(III)TMPP-Cl, has Cl^- species as fifth axial ligand in the crystal form of the molecule. Therefore, the possible effect of chloride is plausible also with the Fe(III)TMPP-Cl system. A model visualisation of the O_2 *side-on* adsorption is displayed in figure 6.21a and 6.21b with a top-view and side-view perspective, respectively.

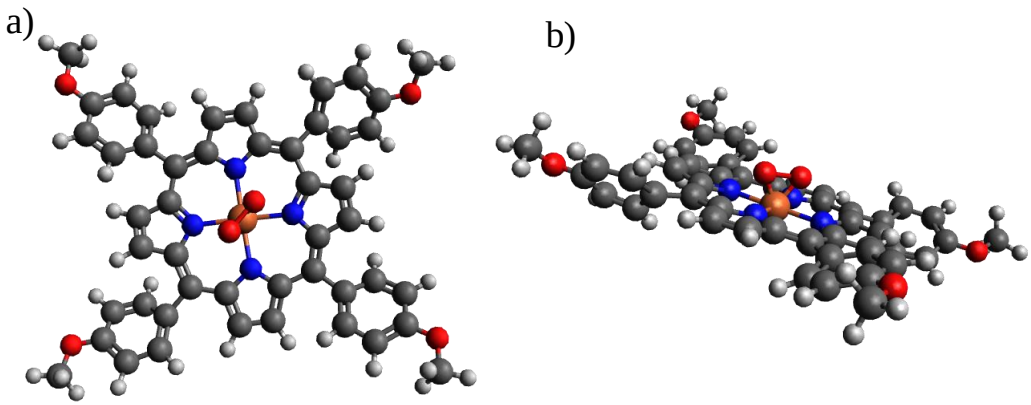

Figure 6.21: (a) top view and (b) side-view of Fe(III)TMPP-Cl with O_2 adsorbed with *side-on* geometry.

6.3.4 Potentiodynamic investigation of Fe(III)TMPP-Cl in O_2 saturated electrolyte

As done for the deaerated electrolyte case, the Fe(III)TMPP-Cl/Au(111) electrode underwent two sets of potentiodynamic imaging series. The first one aimed to reach a potential close to the firs peak potential as revealed by cyclic voltammetry reported in figure 5.14. The second set reached the potential of the second peak at around 200 mV, which correspond to an intense peak in the Ar saturation case, and to a weakly distinguishable peak in the case of O_2 saturation (Figure 5.14).

The starting potential was set at E_{app} = 620 mV, which is near the onset potential determined by the the corresponding CV (figure 5.14). The topographic profile running along the dashed line of figure 6.22a returns a $\Delta Z = (1.32 \pm 0.10)$ Å. As already stated for figure 6.20, this topographic profile is assigned to the presence of O_2 adsorbed on the iron site with a *side-on* geometry.

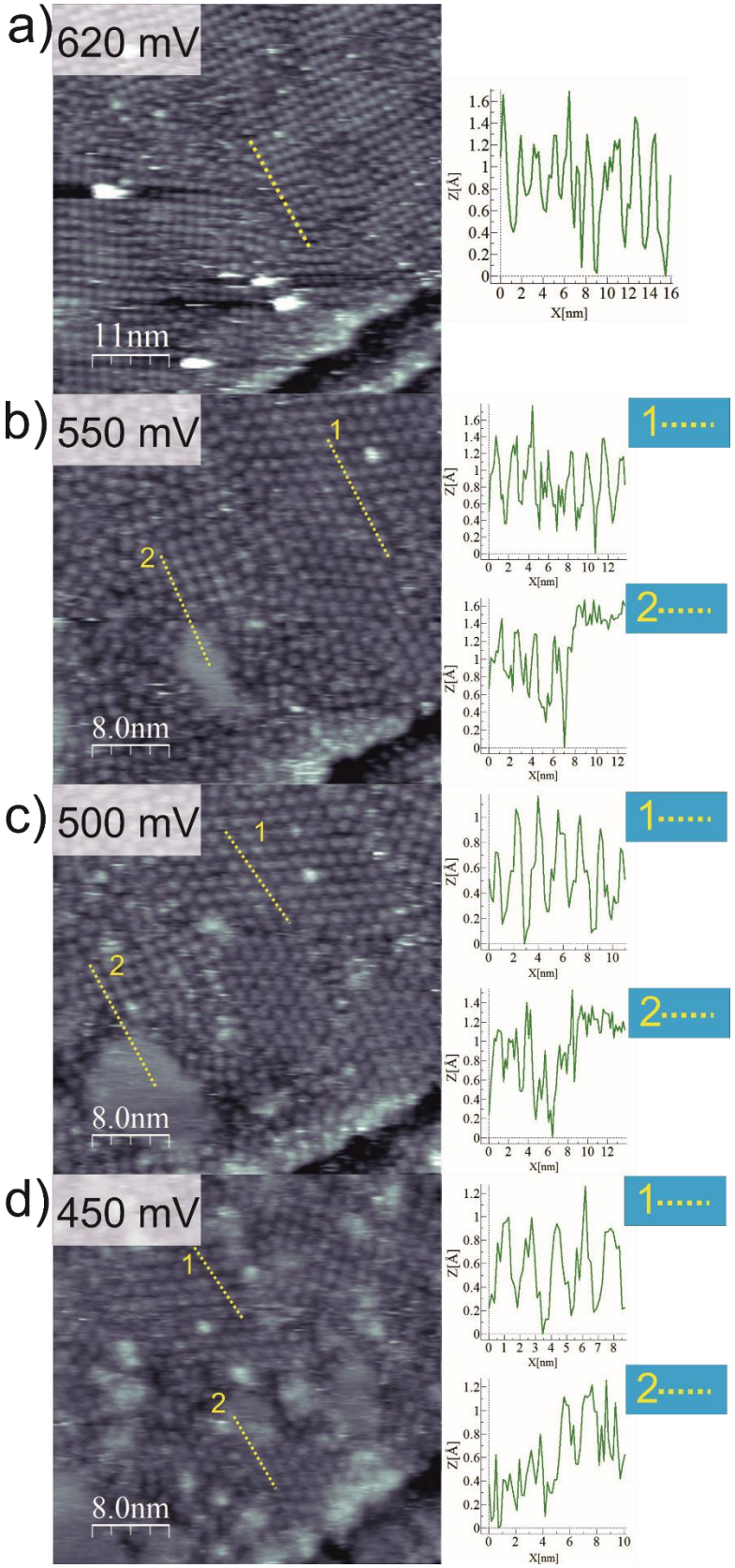

Figure 6.22: (a) I_t = 0.48 nA; U_b = +204 mV (vs RHE) mV; E_{app} = 620 mV vs RHE; I = 0.0 µA; (b) I_t = 0.48 nA; U_b = +204 mV (vs RHE) mV; E_{app} = 550 mV vs RHE; I = –0.3 µA; (c) I_t = 0.48 nA; U_b = +204 mV (vs RHE) mV; E_{app} = 500 mV vs RHE; I = –1.0 µA; (d) I_t = 0.48 nA; U_b = +204 mV (vs RHE) mV; E_{app} = 450 mV vs RHE; I = –3.3 µA.

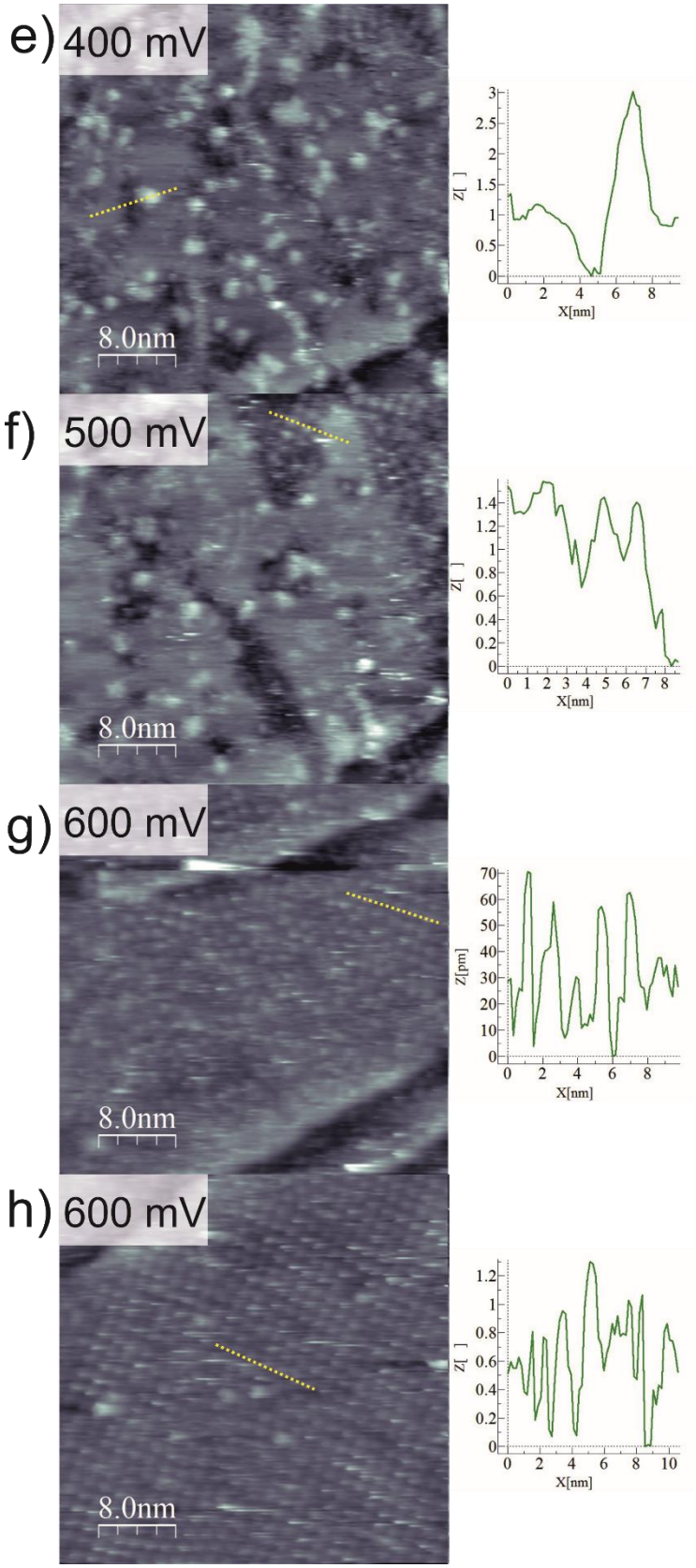

Figure 6.22: (e) I_t = 0.48 nA; U_b = +204 mV (vs RHE) mV; E_{app} = 400 mV vs RHE; I = –3.3 µA; (f) I_t = 0.48 nA; U_b = +204 mV (vs RHE) mV; E_{app} = 500 mV vs RHE; I = –0.6 µA; (g) I_t = 0.48 nA; U_b = +204 mV (vs RHE) mV; E_{app} = 600 mV vs RHE; I = –0.0 µA; (h) I_t = 0.48 nA; U_b = +204 mV (vs RHE) mV; E_{app} = 600 mV vs RHE; I = –0.0 µA.

When the applied potential was shifted to E_{app} = 550 mV (figure 6.22b), molecules seemed to have rearranged in hexagonal domains, whilst maintaining only smaller square-symmetry domains. Moreover, a small island with non-resolved molecules has been evaluated with the dashed line 2, showing that the topographic profile does vary less than 0.2 Å. As noticed in the Ar saturation case, this island is ascribed to the molecular mobility as a consequence of both the applied potential and the tunnelling tip.

Upon lowering the applied potential to E_{app} = 500 mV, figure 6.22c was obtained. The surface still retains a good ordering degree, with molecules most likely to be found in hexagonal arranged domains. However, the portion of non-resolved image started to enlarge, whilst maintaining a monolayer-like topographic profile.

At E_{app} = 450 mV, the picture (figure 6.22d) started to undergo a general disordering phenomenon. The ordered hexagonal domains were in fact frequently interrupted by the usual islands, where molecules were mobile and probably swept by the tunnelling tip. The topographic profile is coherent with the corresponding Ar case (figure 6.17d).

The first set of potentiodynamic imaging in O_2 saturated electrolyte were stooped at E_{app} = 400 mV, as shown in figure 6.22e. The ORR peak potential was measured at ~0.31 V (figure 5.14), but STM imaging was stopped few tens of mV more positive to avoid the excessive Faradaic current that would have arisen at the peak potential. Anyway, figure 6.22e shows that the adlayer undergoes to an even larger disordering process due to the high molecule mobility. 2nd and 3rd layer-packed molecules were detected, with $\Delta Z = (3.00 \pm 0.10)$ Å.

Returning to E_{app} = 500 mV, mobility was sensitively decreased, leading to figure 6.22f. Small ordered areas were regained, and the topographic profile embracing both an ordered portion and a non-resolved island shows that no significant differences in the Z profile are noticeable.

At E_{app} = 600 mV, islands had almost disappeared, showing a more stationary adlayer. The topographic profile along the dotted line of figure 6.22g exhibits a slightly lower ΔZ than expected: $\Delta Z = (0.63 \pm 0.10)$ Å. This is however ascribable to the results of a profoundly changing surface adlayer as response of the applied potential. In fact, by continuing imaging for few minutes at $E_{app} = 600\ mV$, figure 6.22h was collected, with a corresponding topographic profile of $\Delta Z = (0.94 \pm 0.10)$ Å.

The second set of potentiodynamic images aimed to reach an applied potential of 200 mV, where a second minor peak was detected, as visible in the cyclic voltammogram of figure 5.14.

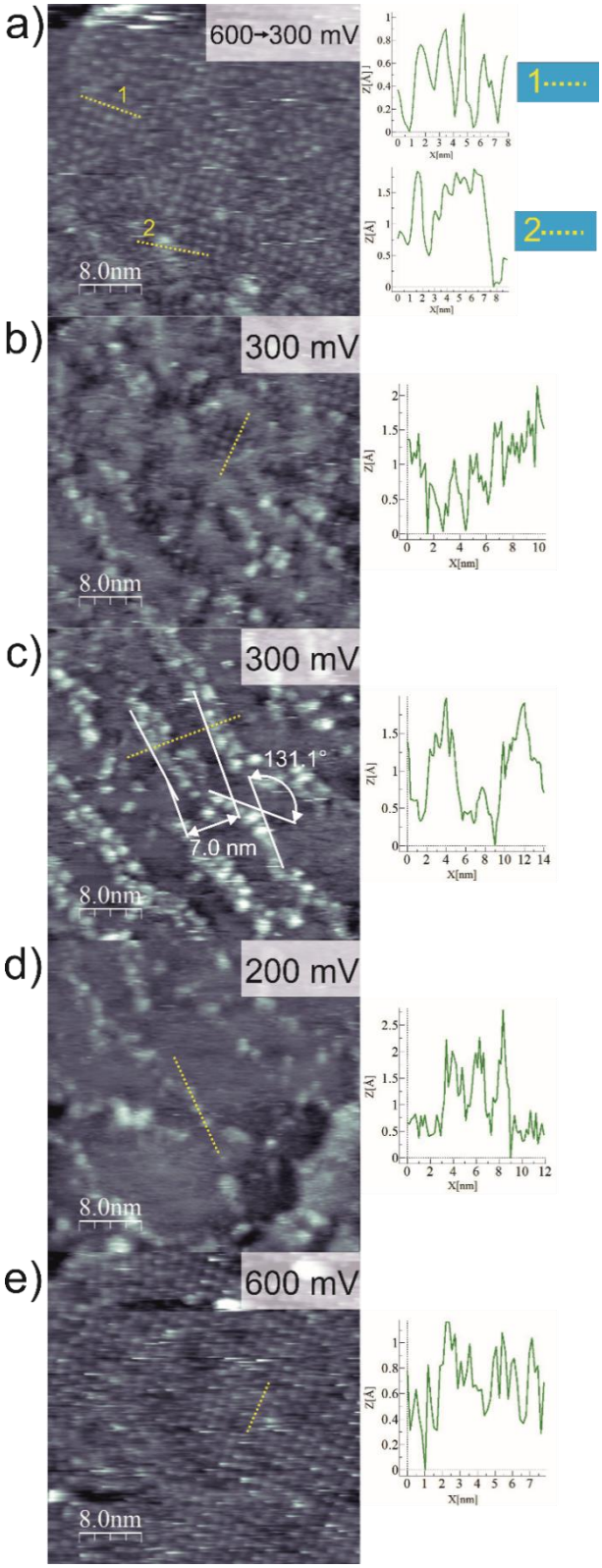

Figure 6.23: (a) I_t = 0.48 nA; U_b = +204 mV (vs RHE) mV; E_{app} = from 600 to 300 mV vs RHE; I =from 0.0 to –11.4 µA; (b) I_t = 0.48 nA; U_b = +204 mV (vs RHE) mV; E_{app} = 300 mV vs RHE; I = –6.5 µA; (c) I_t = 0.48 nA; U_b = +204 mV (vs RHE) mV; E_{app} = 300 mV vs RHE; Iv= –4.3 µA; (d) I_t = 0.48 nA; U_b = +204 mV (vs RHE) mV; E_{app} = 200 mV vs RHE; I = –6.3 µA; (e) I_t = 0.48 nA; U_b = +204 mV (vs RHE) mV; E_{app} = 600 mV vs RHE; I = –0.0 µA.

Figure 6.23a was obtained by varying (in the same image) the applied potential from 600 mV to 300 mV, as done for potentiodynamic imaging performed in deaerated electrolyte. No additional information was discovered, since the system underwent the usual disordering process. The extracted topographic profiles are in agreement with those obtained in Ar saturated electrolyte (figure 6.17 and 6.18).

Upon fixing the E_{app} = 300 mV, the adlayer underwent the usual disrupting due to the enhanced mobility, with 2nd and multiple-layer formation (figure 6.23b).

Figure 6.23c interestingly shows that the 2nd layer molecules (see the topographic profile for confirmation) seems to align along herringbone reconstruction ridges. In fact, the measured distance between two rows is ~7 nm, which is very close to the expected herringbone periodicity of 6.35 nm, as discussed in chapter 4.

Finally, the E_{app} = 200 mV was realised (figure 6.23d). Molecules, as expected, are completely unrecognisable, and the 2nd layer molecules are not properly images as well.

By returning to 600 mV and continuing imaging for few minutes, order is restored, as demonstrated by figure 6.23e and its corresponding topographic profile of ~1 Å.

The Fe(III)TMPP/Au(111) system had been probed in O_2 saturated electrolyte, but the results were similar to those obtained in deaereted electrolyte. Namely, Fe(III)TMPP possesses an intrinsic high surface mobility due to a substantial distortion of the molecular plane induced by the *meso* substituents. This results in weaker adsorbate-substrate interactions, which favour self-assembly but limit the potential window of the adlayer stability. For these reasons, the O_2 reduction mechanism could not be characterised as did for the iron phthalocyanine systems, and its adsorption could not be fully confirmed.

References

[1] J.-Y. Gu, Z.-F. Cai, D. Wang, L.-J. Wan, Single-*Molecule Imaging of Iron-Phthalocyanine-Catalyzed Oxygen Reduction Reaction by in Situ Scanning Tunneling Microscopy*, ACS Nano., **2016**, *10*, 8746–8750.

[2] O. Snezhkova, F. Bischoff, Y. He, A. Wiengarten, S. Chaudhary, N. Johansson, K. Schulte, J. Knudsen, J. V. Barth, K. Seufert, W. Auwärter, J. Schnadt, *Iron phthalocyanine on Cu(111): Coverage-dependent assembly and symmetry breaking, temperature-induced homocoupling, and modification of the adsorbate-surface interaction by annealing*, J. Chem. Phys., **2016**, *144*.

[3] X. Lu, K.W. Hipps, *Scanning Tunneling Microscopy of Metal Phthalocyanines: d ^{6} and d ^{8} Cases*, J. Phys. Chem. B., **1997**, *101*, 5391–5396.

[4] Z.H. Cheng, L. Gao, Z.T. Deng, Q. Liu, N. Jiang, X. Lin, X.B. He, S.X. Du, H.J. Gao, *Epitaxial growth of iron phthalocyanine at the initial stage on Au(111) surface*, J. Phys. Chem. C., **2007**, *111*, 2656–2660.

[5] Z.H. Cheng, L. Gao, Z.T. Deng, N. Jiang, Q. Liu, D.X. Shi, S.X. Du, H.M. Guo, H.-J. Gao, *Adsorption Behavior of Iron Phthalocyanine on Au(111) Surface at Submonolayer Coverage*, J. Phys. Chem. C., **2007**, *111*, 9240–9244.

[6] M.E. Davis, R.J. Davis, *Fundamentals of Chemical Reaction Engineering*, **2003.**

[7] M. Wilms, M. Kruft, G. Bermes, K. Wandelt, *A new and sophisticated electrochemical scanning tunneling microscope design for the investigation of potentiodynamic*

processes, Rev. Sci. Instrum., **1999**, *70*, 3641–3650.

[8] S. Yoshimoto, A. Tada, K. Suto, K. Itaya, *Adlayer Structures and Electrocatalytic Activity for O_2 of Metallophthalocyanines on Au(111): In Situ Scanning Tunneling Microscopy Study*, J. Phys. Chem. B.,**2003**, *107*, 5836–5843.

[9] S. Yoshimoto, E. Tsutsumi, K. Suto, Y. Honda, K. Itaya, *Molecular assemblies and redox reactions of zinc(II) tetraphenylporphyrin and zinc(II) phthalocyanine on Au(1 1 1) single crystal surface at electrochemical interface*, Chem. Phys., **2005**, *319*, 147–158.

[10] O.M. Magnussen, *Ordered anion adlayers on metal electrode surfaces,* Chem. Rev., **2002**, *102*, 679–725.

[11] T.H. Phan, K. Wandelt, *Redox-activity and self-organization of iron-porphyrin monolayers at a copper/electrolyte interface*, J. Chem. Phys., **2015**, *142*, 101917.

[12] Y. He, T. Ye, E. Borguet, *Porphyrin self-assembly at electrochemical interfaces: Role of potential modulated surface mobility*, J. Am. Chem. Soc., **2002**, *124*, 11964–11970.

[13] J. Lipkowski, L. Stolberg, D.F. Yang, B. Pettinger, S. Mirwald, F. Henglein, D.M. Kolb, *Molecular Adsorption At Metal Electrodes*, Electrochim. Acta., **1994**, *39*, 1045–1056.

[14] S. Yoshimoto, N. Yokoo, T. Fukuda, N. Kobayashi, K. Itaya, *Formation of highly ordered porphyrin adlayers induced by electrochemical potential modulation*, Chem. Commun.,**2006,** 500–502.

[15] Y. Wang, H. Yuan, Y. Li, Z. Chen, *Two-dimensional iron-phthalocyanine (Fe-Pc) monolayer as a promising single-atom-catalyst for oxygen reduction reaction: A computational study*, Nanoscale., **2015,** *7*, 11633–11641.

[16] J.H. Zagal, F. Bedioui, J.P. Dodelet, *N_4-Macrocyclic Metal Complexes*, Springer, **2006**.

[17] G. Wang, N. Ramesh, A. Hsu, D. Chu, R. Chen, *Density functional theory study of the adsorption of oxygen molecule on iron phthalocyanine and cobalt phthalocyanine*, Mol. Simul., **2008**, *34*, 1051–1056.

[18] K. Holst-Olesen, M. Reda, H.A. Hansen, T. Vegge, M. Arenz, *Enhanced Oxygen Reduction Activity by Selective Anion Adsorption on Non-Precious-Metal Catalysts*, ACS Catal., **2018**, *8*, 7104–7112.

[19] J.H. Zagal, M.T.M. Koper, *Reactivity Descriptors for the Activity of Molecular MN_4 Catalysts for the Oxygen Reduction Reaction*, Angew. Chemie - Int. Ed., **2016**, *55*, 14510–14521.

[20] R. Baker, D.P. Wilkinson, J. Zhang, *Electrocatalytic activity and stability of substituted iron phthalocyanines towards oxygen reduction evaluated at different temperatures*, Electrochim. Acta., **2008,** *53*, 6906–6919.

[21] J. Masa, W. Schuhmann, *Systematic selection of metalloporphyrin-based catalysts for oxygen reduction by modulation of the donor-acceptor intermolecular hardness*, Chem. - A Eur. J., **2013**, *19*, 9644–9654.

[22] J. Otsuki, *STM studies on porphyrins*, Coord. Chem. Rev., **2010**, *254*, 2311–2341.

[23] C.A. Hunter, J.K.M. Sanders, *The Nature of π-π Interactions*, J. Am. Chem. Soc, **1990,** *112*, 5525–5534.

Chapter 7

Conclusions

Three molecular systems featuring FeN_4 sites were studied in their electrochemical response by means of electrochemical scanning tunnelling microscopy and cyclic voltammetry, namely Fe(II)-phthalocyanine (Fe(II)Pc), Fe(III)-phthalocyanine chloride (Fe(III)Pc-Cl) and Fe(III)-tetramethoxyphenyl porphyrin (Fe(III)TMPP). The FeN_4 macrocycles are able to catalyse the oxygen reduction reaction thanks to the transition metal atom, which is regarded as the active site involved in the reduction reaction. At this purpose, FeN_4 compounds in crystal form were dissolved in DMF to functionalise a flame-annealed Au single crystal exposing the (111) crystallographic face. Cyclic voltammetry of FeN_4-modified Au electrodes in Ar purged electrolyte shown that the iron atom undergoes a (III)→(II) transition in oxidation state, and the Fe(II) formation had been observed at potentials of ≈ 0.4 V vs. SCE. As electrolyte, a 0.1 M $HClO_4$ aqueous solution was employed, since perchlorate had been verified to barely specifically adsorb on Au single crystals [1,2]. By further registering cyclic voltammograms of FeN_4/Au electrodes in O_2 saturated electrolyte, a clear reduction peak was observed at potentials close to the previously found Fe(III)→Fe(II) peak potentials. Therefore, a "redox-catalysis" mechanism holds, in which the reduction of the metal centre from (III) oxidation state to (II) is first required to then allow the O_2 reduction [3–6]. The metal in the M-O_2 adduct regains the (III) oxidation state and reduces the O_2 molecule to water (preferably) or hydrogen peroxide, freeing the active site with its (III) oxidation state.

Potentiodynamic EC-STM measurements in argon allowed to visualize the formation and the stability of FeN_4 macrocycle domains, where molecules organized in both hexagonal and square symmetry. The topographic profiles extracted by the STM images and corresponding to the brighter central spot of the single molecule is associated with the iron atom in the (III) oxidation state $\Delta Z_{Fe(III)} = (0.26 \pm 0.10)$ Å, in accordance with the cyclic voltammograms. Moving to more cathodic potentials, with respect to the open circuit potential, many "hollow" molecules were imaged, where the topographic profile is consistent with formation of Fe(II) centres $\Delta Z_{dip} = (0.24 + 0.10)$ Å. However, the effect of the potential is not only the change in the redox state of the catalytic site but also to increase the surface mobility of FeN_4 macrocycles due to a change of non-covalent electrostatic interaction between molecule and substrate and, as a consequence, ordered organisation is lost.

In the presence of O_2 a larger ΔZ is found $\Delta Z_{O_2} = (0.85 \pm 0.10)$ Å, if compared to that obtained in deaereted electrolyte, and this was ascribed to the presence of the O_2 species adsorbed on the metal atom. However, when the potential is allowed to reach a sufficient cathodic value, where ORR occurs, topographic profiles reveal that no oxygen was adsorbed at the moment of scanning since they exhibit a central hole $\Delta Z_{dip} = (0.11 \pm 0.10)$ Å, indicating that the iron atom is in the (II) oxidation state.

O_2 adsorption explicates through the formation of a Fe-O_2 adduct, which is attained after an adsorption step of O_2 on the Fe atom. The Fe-O_2 adduct can exhibit two main geometrical configurations, namely *end-on* or *side-on* [4,5]. This translates into a different molecular orbital superposition between the FeN_4 macrocycle and the O_2 orbitals [6]. The adsorption geometry may be influenced by the transition metal and its orbitals, as well as the nature of the ligand and its substituents. Generally, FeN_4 are expected to exhibit both the adsorption geometries [5]. The EC-STM technique succeeded in revealing the adsorption configuration of O_2 on the FeN_4 molecules. In particular, the *end-on* geometry was observed for the Fe(II)pc system, whereas the *side-on* geometry was assigned to Fe(III)-Pc-Cl and FeTMPP. These significantly different EC-STM results, especially between Fe(II)Pc and Fe(III)Pc-Cl, may be correlated to the absence/presence of Cl^-. Chloride is the counterion and axial ligand of Fe(III) in the crystal form of Fe(III)Pc-Cl. It could not be stated whether chloride still remained the fifth axial ligand of iron even when Fe(III)Pc-Cl was adsorbed on Au(111) or it was lost. In the latter case, the released chloride anions could co-adsorb in different ways together with phthalocyanines. In any case, an effect of chloride was explored also through dedicated cyclic voltammetry experiments. It emerged that the voltammograms obtained for a Fe(II)Pc-modified electrode with the addition of a highly diluted HCl solution to the 0.1 M $HClO_4$ electrolyte became similar to those obtained for Fe(III)Pc-Cl, where chloride was directly provided by the molecule. This resemblance was encountered both in Ar and O_2 purged electrolyte.

References

[1] H. Angerstein-Kozlowska, B.E. Conway, A. Hamelin, L. Stoicoviciu, *Elementary steps of electrochemical oxidation of single-crystal planes of Au Part II. A chemical and structural basis of oxidation of the (111) plane*, J. Electroanal. Chem., **1987,** *228*, 429–453.

[2] M. Hugelmann, W. Schindler, *Tunnel barrier height oscillations at the solid/liquid interface*, Surf. Sci., **2003**, *541*, L643–L48.

[3] K. Wiesener, D. Ohms, V. Neumann, R. Franke, *N_4 macrocycles as electrocatalysts for the cathodic reduction of oxygen*, Mate. Chem. Phys., **1989**, *22*, 457–475.

[4] J.H. Zagal, F. Bedioui, J.P. Dodelet, *N_4-Macrocyclic Metal Complexes*, Springer, **2006**.

[5] M. Shao, *Electrocatalysis in Fuel Cells*, **2015**.

[6] J.H. Zagal, *Metallophthalocyanines as catalysts in electrochemical reactions*, Coord. Chem. Rev., **1992**, *119*, 89–136.

Appendix

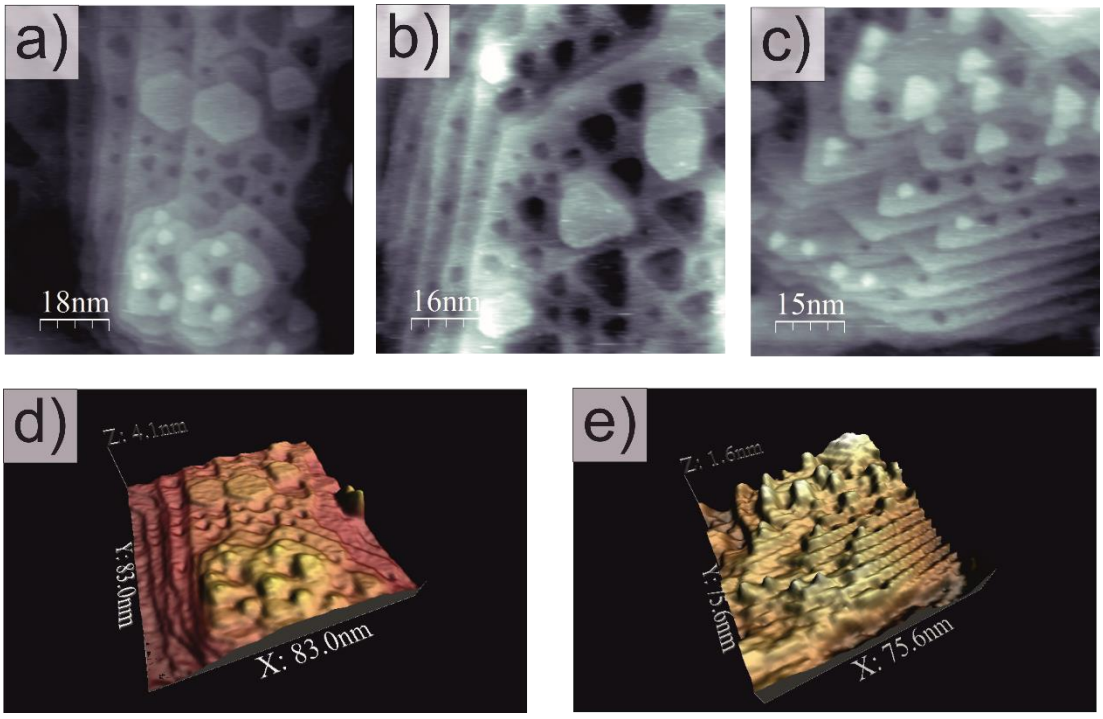

Figure 1: Images of a roughened bare Au(111) surface resulting from repetitive potential cycling up to oxidative potentials. Figure 1d is the 3D projection of figure 1a; figure 1e is the 3D projection of figure 1c.

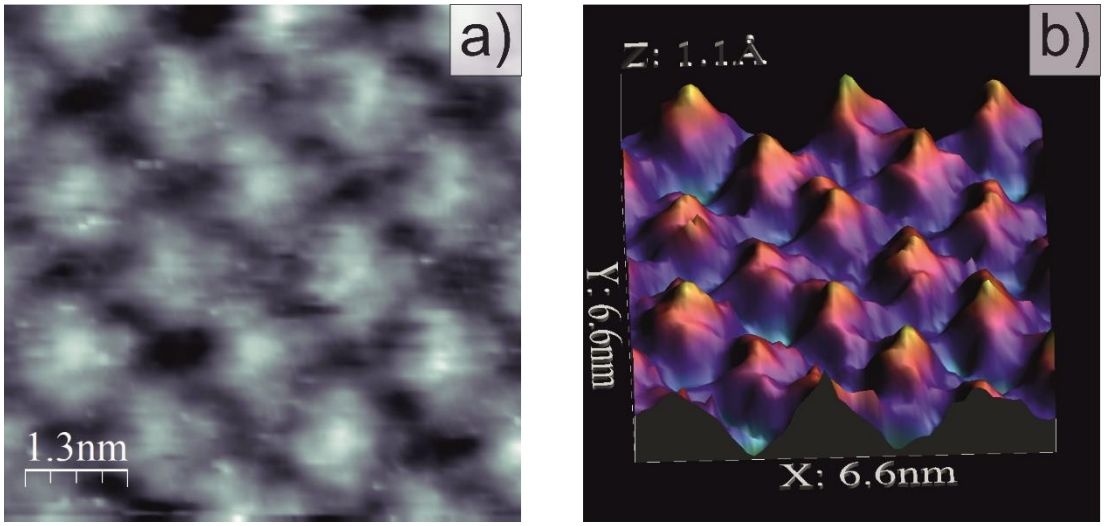

Figure 2: (a) self-assembled monolayer of Fe(II)Pc molecules and (b) its corresponding 3D projection**.**

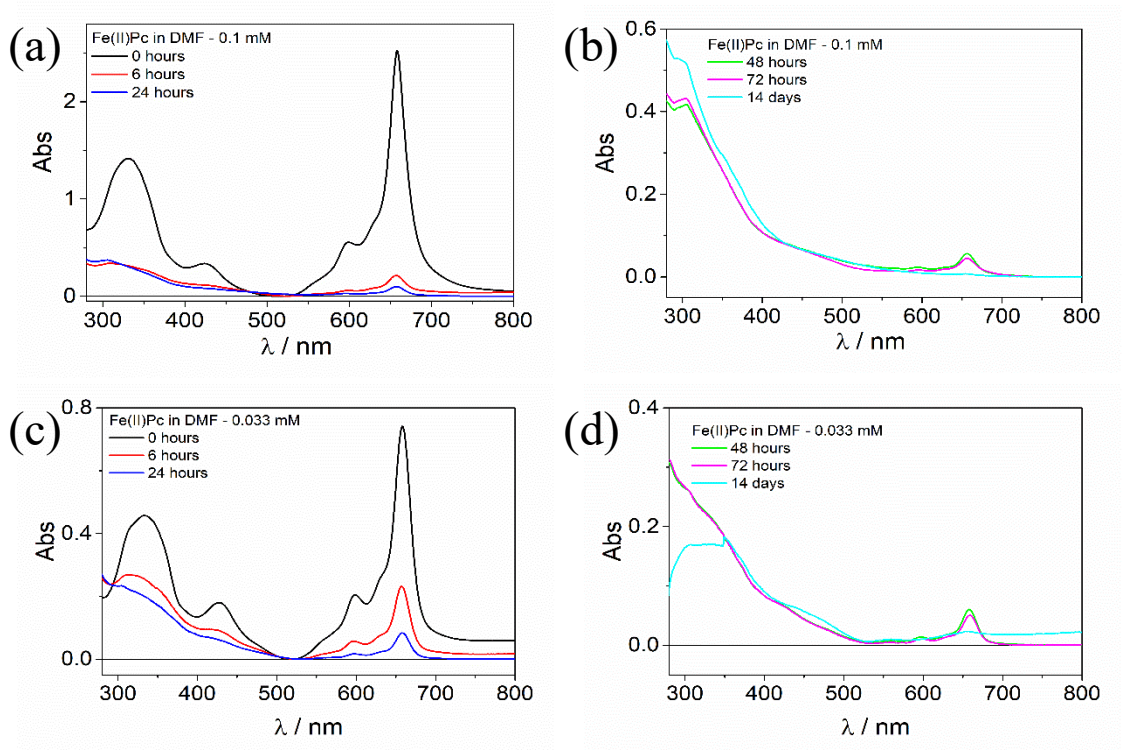

Figure 3: UV-Vis spectra aging of Fe(II)Pc in DMF from 0 to 14 days of (a,b) 0.1 mM solution and (c,d) 0.033 mM solution**.**

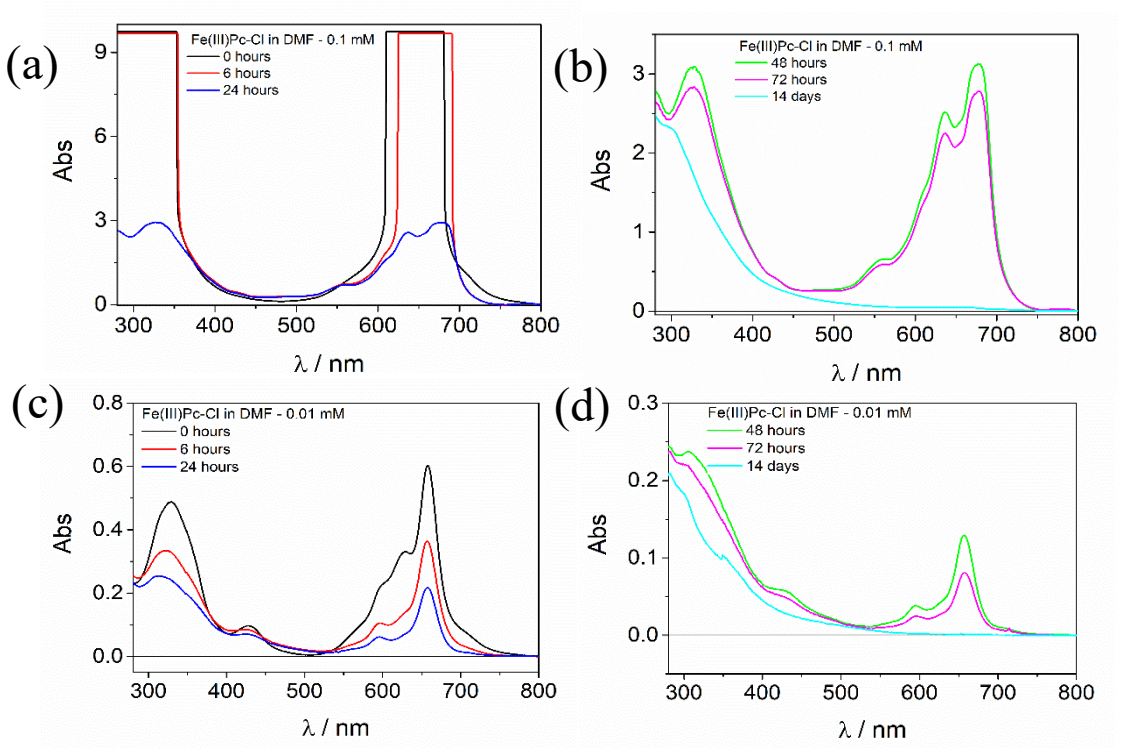

Figure 4: UV-Vis spectra aging of Fe(III)Pc-Cl in DMF from 0 to 14 days of (a,b) 0.1 mM solution and (c,d) 0.01 mM solution**.**

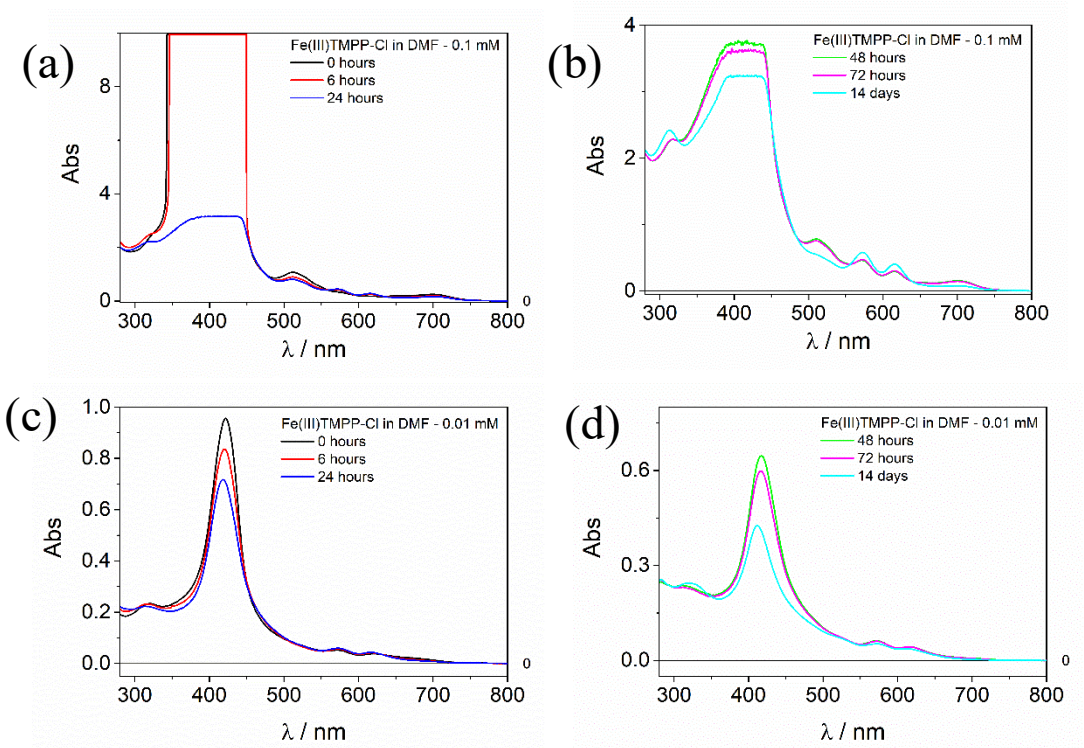

Figure 5: UV-Vis spectra aging of Fe(III)TMPP-Cl in DMF from 0 to 14 days of (a,b) 0.1 mM solution and (c,d) 0.01 mM solution**.**

Aknowledgement

In Primis, I would like to thank Prof. Dr. Armando Gennaro, for giving me the opportunity to carry out my master's thesis by the Electrocatalysis and Applied Electrochemistry Group at the University of Padua.

My sincere gratitude goes also to Prof. Christian Durante, for teaching me the basis of electrochemistry during the 5th year of university, as well as for having been a tireless and inspiring master's thesis Supervisor.

I would reserve special thanks to Dr. Denis Badocco, as examiner of this master's thesis and for the suggestions he gave me early in the morning, before the laboratory activity.

I sincerely thank Dr. Tomasz Kosmala, for teaching me how to handle with EC-STM, from switching on the bipotentiostat to managing with advanced experimental procedures, as well as for helping me whenever I needed.

Grazie Giorgia, for encouraging me to improve every day.

I express my thanks to all colleagues working by the EAEG for their help throughout my thesis project.

I finally thank my parents for supporting and bearing me, in a time which flied and brought me here, at the end of these acknowledgements, at the end of five years, at the end of this breath-taking experience.

Ora sono Libero,

un Uomo,

Oltre.